
**International Committee for Future Accelerators**

Sponsored by the Particles and Fields Commission of IUPAP

# Beam Dynamics Newsletter

**No. 48**

**Issue Editor:**
**M. E. Biagini**

**Editor in Chief:**
**W. Chou**

**April 2009**

# Contents

# 1 Foreword

## 1.1 From the Chairman

Weiren Chou, Fermilab
Mail to: chou@fnal.gov

The International Committee for Future Accelerators (ICFA) met on February 12-13, 2009 at KEK. Atsuto Suzuki, Director General of KEK and the new Chair of ICFA, chaired this meeting.

The ILCSC gave a report on the status of the ILC. It has been decided to not pursue the γ-γ collider because a 230 GeV $e^+e^-$ collider for early Higgs studies would be a better choice than a 180 GeV γ-γ collider, and the cost saving of a γ-γ collider compared to the $e^+e^-$ option is insignificant. Since the term of the current ILCSC Chair, Enzo Iarocci will end soon, ICFA approved the appointment of Jonathan Bagger (Johns Hopkins University, U.S.A.) as the next ILCSC Chair, for a two-year term beginning about October 2009. The ILCSC mandate has also been reviewed and revised. Toshiki Tajima, Chair of the International Committee for Ultra Intense Lasers (ICUIL) was invited to the meeting. He proposed forming a collaboration with ICFA, since one of the uses of very intense lasers is exploration of laser acceleration of particles. ICFA endorsed his proposal and charged the ICFA Panel on Advanced and Novel Accelerators to work with ICUIL and provide suggestions for joint activities.

Reports from about 20 laboratories were presented. Some highlights follow. Several U.S. laboratories (Fermilab, SLAC, BNL and JLab) reported significant additional funding will come from the government stimulus package, which is a big help to the U.S. HEP and science program. Fermilab has proposed to the DOE to run the Tevatron through 2011. SLAC expects first light from the LCLS for experiments in late summer 2009. BNL has begun construction of NSLS II and also expects a factor of 5 increases in the RHIC luminosity thanks to stochastic cooling of the 100 GeV gold beams. TRIUMF has submitted a new 5-year plan, starting in 2010, which includes a 50 MeV high intensity e-linac for isotope production using 1.3 GHz ILC SRF technology. Frascati has completed the FEL commissioning and laser light was seen for the first time on the night prior to this meeting. The LAL Orsay will operate a new 10 MeV electron linac in 2009. CERN has 21 member states now. Its highest priority is LHC. The magnet repair is ongoing and the machine will begin operation this fall and run over the 2009/2010 winter. DESY has started civil construction for the XFEL and will conduct a review of its 5-year particle physics plan. The BEPC in China has seen a luminosity increase of 15 over what it was before the upgrade with a goal of 100. The Shanghai light source will begin operation for users in April 2009. The CSNS project has received government approval. The IHEP in Protvino operates a 70 GeV accelerator and uses bent crystals for beam extraction and beam splitting. PSI has the world's most powerful neutron spallation source, which achieved 1.3 MW on target and will be upgraded to 1.8 MW over the next two years. JLab has an IRFEL with an energy

recovery linac (ERL), and commissioning of the 12 GeV upgrade of CEBAF will begin in 2013. The 2008 Nobel Prize had a positive effect on the Japanese particle physics budget. A compact ERL will be constructed at KEK. J-PARC is being commissioned and most of the experimental halls have received beam.

Four ICFA panels presented reports at the meeting. Approved were two advanced beam dynamics workshops (ABDW): the 46th, *HB2010*, which will take place from September 27 to October 1, 2010 at Morschach, Switzerland; and the 47th, *the Physics and Applications of High Brightness Electron Beams,* to be held from November 16-19, 2009 in Maui, Hawaii. The latter will be jointly sponsored by this Panel and the Panel on Advanced and Novel Accelerators. ICFA also approved three new Beam Dynamics Panel members: Wolfram Fischer from BNL, Mark Palmer from Cornell University, and Rick Baartman from TRIUMF. A list of current panel members can be found on the last page of this newsletter.

After a number of years of valuable service, Jie Wei decided to step down from the panel. I thank him for his many contributions to this panel, including editing the ICFA BD Newsletter and organizing ICFA workshops.

*The Fourth International Accelerator School for Linear Colliders* will be held from September 7-18, 2009 at Hotel Jixian in Huairou near Beijing, China. The host is the Institute of High Energy Physics (IHEP). Please see Section 2 for the announcement. The school web address is http://www.linearcollider.org/school/2009/.

This panel will have a biennial meeting on May 6, 2009 at the Fairmont Hotel in Vancouver during PAC09. The meeting minutes will be published in the next issue of this newsletter.

The editor of this issue is Dr. Marica Biagini, a panel member and a senior scientist from LNF-INFN, Italy. Marica collected 27 excellent articles in the theme section "$e^+e^-$ Colliders: Past and Present Experiences and Future Frontiers." These articles give a comprehensive review of this very important accelerator field by experts from all over the world. It will no doubt serve as a valuable reference for every accelerator physicist who works or plans to work on $e^+e^-$ colliders. The total number of pages in this issue approaches 300, a record number for this newsletter. This is a reflection of strong interest and vigorous activity in the lepton energy frontier. I thank Marica for editing and producing a newsletter of excellent quality and great value.

## 1.2 From the Editor

M. E. Biagini, INFN-Laboratori Nazionali di Frascati
Mail to: marica.biagini@lnf.infn.it

As editor of the April 2009 issue I spent sometime thinking about the theme I wanted to choose. In spite of the many new topics arising in our field, I felt the need to make a sort of summary on the performances of $e^+e^-$ circular colliders, a field that has been extremely important for elementary particle physics, and now seems to suffer from lack of money and support from the funding agencies. The last issue on this topic was No. 31 edited by Funakoshi-san back in 2003. So I chose the theme "**$e^+e^-$ Colliders: Past and Present Experiences and Future Frontiers**". The aim was to collect papers on the experience of commissioning and running high luminosity colliders (past and

present) as well as descriptions of new principles and R&D for future ones. The result, as you can see, is a rich (27 papers!) issue.

I divided the contributions following a straightforward classification. First of all are presented the "Fruitful Factories", the most successful colliders at the moment in terms of luminosity reached: the Φ-Factory DAΦNE at LNF (Frascati, Italy); the two B-Factories PEP-II (SLAC, US) and KEKB (Tsukuba, Japan), which have both exceeded their design peak and integrated luminosity and provided a huge amount of good data to the experiments.

For DAΦNE, C. Milardi has written a summary of past performances and a description of the upgraded machine, which has recently achieved records in peak luminosity after the implementation of the "large Piwinski angle and crab waist" collision scheme, and described also by M. Zobov, with a comparison of beam-beam simulations and measurements. More specific contributions are by A. Drago on measurements and cures of the horizontal instability limiting the positron current; by M. Boscolo on the simulation of Touschek backgrounds and lifetime, a problem common to low energy beams, and by T. Demma with an overview of the electron cloud instability, including simulations and measurements, which plagues all high intensity positron rings.

From PEP-II, we have an exhaustive overview by J. Seeman, followed by a paper on the design of the asymmetric Interaction Region with a discussion on operational issues related to the IR design. U. Wienands contributed with a detailed report on the high beam intensity related vacuum problems, and J. Ng has reported on very important experiments on electron cloud mitigation carried out at PEP-II.

For KEKB, H. Fukuma has reported on the electron cloud instability as observed in KEKB, with simulation studies for SuperKEKB; Y. Suetsugu describes the vacuum system for high current $e^+e^-$ colliders, while K. Akai gives a very interesting report on the KEKB RF system, including crab cavities used for colliding head-on even in presence of a crossing angle geometry.

The other subsections are devoted respectively to the Past, the Present and the Future of $e^+e^-$ circular colliders.

In the "Past Glories" subsection we start with a report on CESR (Cornell, US) beautifully written by D. Rice and D. Rubin, an extensive review of the collider performances and issues.

From VEPP-4M (BINP, Novosibirsk, Russia) I received six papers on different topics, all of them very interesting. I'm grateful to Eugene Levichev who has coordinated this effort. A. Bogomyagkov has submitted an interesting paper on the beam energy measurements by resonant depolarization technique, used for precise instantaneous energy calibration. Another approach to the beam energy and energy spread measurement by Compton backscattering of laser radiation, has been described by N. Muchnoi. O. Meshkov has contributed with the study of a fast electron beam profile with multi-anode photomultiplier, providing a turn-by-turn measurement of transverse beam profile for beam diagnostics. P. Piminov has written a paper on the study of beam dynamics during the crossing of resonance. The passage of a beam through the betatron resonances and the corresponding loss of particles, or beam distribution degradation, have been extensively studied in the past, and recently became popular again because of the FFAG synchrotron projects. This issue could be important for $e^+e^-$ accelerators with extremely low emittances such as the Linear Collider damping rings, or the Super Factories. A different topic was addressed by S. Nikitin, with the

study on the possibility of increasing the accuracy of CPT invariance test in $e^+e^-$ storage rings, based on a precise comparison with an accuracy of ~ $10^{-10}$ of spin precession frequencies of electrons and positrons simultaneously circulating. Finally V. Smaluk has reported on the commissioning of the VEPP-4M longitudinal feedback system, a mode-by-mode feedback developed to suppress the longitudinal multi-bunch instability.

This subsection could not be complete without the experience of LEP (CERN, Switzerland). I'm particularly indebted with Helmut Burkhart and John Jowett, whom I contacted only at the last moment, since my idea at first was to focus just on the most recent machines. I appreciate very much that they have responded immediately in spite of their busy schedule, and have written their paper taking an interesting look back from the perspective of what is now known from the latest generation of colliders.

The subsection on the "Exciting Present" has two reports on machines which have started their commissioning in the past two years: the BEPC-II (IHEP, China) accelerator at the $\tau$ energy, and the new conception $\Phi$- Factory at BINP (Novosibirsk, Russia). J. Wang from IHEP has written a detailed report on the commissioning issues of BEPC-II (Beijing), which has reached a luminosity of $1.85\times10^{32}$ $cm^{-2}s^{-1}$ and provided stable operation for high energy physics experiment. Work is continuing to reach the design luminosity and improve the diagnostics and beam dynamics. I. Koop from BINP has described the initial commissioning of the first accelerator designed to work with round beams, a collision scheme debated for decades.

Proposal for upgrades, in order to achieve about two order of magnitude larger luminosity, are in progress both in Japan and Europe, so in the "Challenging Future" subsection three new projects are presented: an European *SuperB* (by myself) and SuperKEKB (by Y. Ohnishi) at the B mesons production energy, and a new generation "c-$\tau$ Factory" (by E. Levichev) at BINP. All three (in a way or another) rely on the novel approach of the "Crab Waist" collision scheme developed by P. Raimondi at LNF, Frascati (Italy). K. Ohmi presents also a study of various collision schemes for SuperKEKB, which includes the Crab Waist developed for *Super*B.

For the section dedicated to the International Linear Collider we have the announcement of the 4th International Accelerator School for Linear Collider, which will be held in Beijing, China, from September 7 to 18, 2009, following the series started in 2006.

We have two reports in Section 4 on previous Workshops: the 40th ICFA Advanced Beam Dynamics Workshop on high luminosity $e^+e^-$ Factories, a topic related to the theme of this issue, held at BINP, Russia in April 2008, and the Mini-Workshop on laser assisted H-beam stripping, held at the SNS in Oak Ridge in February 2009.

Three doctoral theses are reported in Section 5, on "Application of the Frequency Map Analysis to Analyze Beam Dynamics in the Ring Accelerator" by Yi Jiao and on "The Study of Fringe Field Effects of Magnet in the Synchrotron" by Yuan Chen, both from IHEP, Beijing, China, and on "Emittance Control in High Power LINACs", by Mohammad Eshraqi, CERN, Switzerland.

We also have announcements of five beam dynamics events in Section 6:

- COOL9 – Workshop on beam cooling and related topics in Lanzhou, China
- ICAP09 – 10th International Computational Accelerator Physics Conference in S. Francisco, Ca, US
- LLRF09 – Low level RF Workshop at KEK, Tsukuba, Japan

- Workshop on Physics Application of High Brightness Electron Beam in Maui, Hawaii, US
- Workshop on the Future Directions of Accelerator R&D at Fermilab, Batavia, Il, US.

Finally, I wish to deeply thank all authors for responding so enthusiastically to my requests, even if I was sometimes "pushy". Their contributions have created this rich and complete issue, I hope readers will enjoy it as much as I did.

I would also like to thank Manuela Giabbai, administrative assistant of the LNF Accelerator Division, for her professional editing of this "fat" Newsletter.

# 2 International Linear Collider (ILC)

## 2.1 Fourth International Accelerator School for Linear Colliders

Jiuqing Wang, IHEP, Beijing, China
Mail to: wangjq@ihep.ac.cn

We are pleased to announce the *Fourth International Accelerator School for Linear Colliders*. This school is a continuation of the series of schools started three years ago. The first school was held in 2006 at Sokendai, Hayama, Japan, the second one in 2007 at Erice, Sicily, Italy and the third one in 2008 at Oak Brook, Illinois, U.S.A. The school is organized by the International Linear Collider (ILC) Global Design Effort (GDE), ILC Steering Committee (ILCSC) and the International Committee for Future Accelerators (ICFA) Beam Dynamics Panel. The school this year will take place at Huai Rou near Beijing, China from September 7 to 18, 2009. It is hosted by the Institute of High Energy Physics (IHEP) and sponsored by a number of funding agencies and institutions around the world including U.S. DOE, U.S. NSF, Fermilab, SLAC, CERN, DESY, INFN, IN2P3, CEA, Oxford University, KEK, CHEP/KNU and POSTECH.

The school will take place at the Jixian Villa (http://www.bjjxsz.com.cn/main.asp). There are a total of 10 school days, which are divided as follows: 2 days for required courses, 1 day for an excursion, 6 days for elective courses, 0.5 day for a site visit to IHEP and 0.5 day for study time for preparation for the final exam. The first two days will be an introductory course with an overview of proposed future lepton colliders (ILC, CLIC and the muon collider). This will be followed by two elective courses, one on accelerator physics and the other on RF technology. Both of these will run in parallel for 6 days. Each student is required to take the introductory course and one of the electives. A complete description of the program is attached below and can also be found on the school web site (http://www.linearcollider.org/school/2009). There will be homework assignments and a final examination but no university credits.

We encourage young physicists (graduate students, post doctoral fellows, junior researchers) to apply to the school. In particular we welcome those physicists who are considering changing to a career in accelerator physics. This school is adopting a new, in-depth approach. Therefore, former students are welcome to apply if they have a

compelling reason to do so. The school will accept a maximum of 70 students from around the world. Students will receive financial aid covering their expenses for attending the school including travel (full or partial). There will be no registration fee. Each applicant should complete the online registration form and submit a curriculum vita as well as a letter of recommendation from his/her supervisor (in electronic form, either PDF or MS WORD). The deadline for application is June 1, 2009. For more information, please contact: Tiejun Deng, IHEP, P.O. Box 918, Beijing 100049, P.R. China, phone: +86-21-88235014, fax: +86-10-88233374, e-mail: dengtj@ihep.ac.cn.

Organizing Committee

Barry Barish (GDE/Caltech, Co-Chair)
Shin-ichi Kurokawa (KEK, Co-Chair)
Alex Chao (SLAC)
Hesheng Chen (IHEP)
Weiren Chou (ICFA BD Panel/Fermilab)
Jean-Pierre Delahaye (CERN)
Paul Grannis (Stony Brook Univ.)
In Soo Ko (PAL)
Nick Walker (DESY)
Kaoru Yokoya (KEK)

Curriculum Committee

Weiren Chou (Fermilab, Chair)
William Barletta (USPAS)
Daniel Brandt (CERN)
Alex Chao (SLAC)
Jie Gao (IHEP)
Shin-ichi Kurokawa (KEK)
Carlo Pagani (INFN/Milano)
Junji Urakawa (KEK)
Andrzej Wolski (Univ. of Liverpool)

Local Committee

Jiuqing Wang (IHEP, Chair)
Jie Gao (IHEP)
Tongzhou Xu (IHEP)
Chuang Zhang (IHEP)

**Fourth International Accelerator School for Linear Colliders Curriculum**
(v.3, 03/25/2009)

September 7-18, 2009, Beijing, China

Daily Schedule

| | |
|---|---|
| Breakfast | 08:00 – 09:00 |
| Morning | 09:00 – 12:30, including ½-hour break |
| Lunch | 12:30 – 14:00 |
| Afternoon | 14:00 – 17:30, including ½-hour break |
| Dinner | 17:30 – 19:00 |
| Tutorial & homework | 19:00 – 22:00 |

List of Courses (black: required, red and blue: elective)

| | Morning | Afternoon | Evening |
|---|---|---|---|
| September 7 | | *Arrival, registration* | *Reception* |
| September 8 | Introduction | ILC | Tutorial & homework |
| September 9 | CLIC | Muon collider | Tutorial & homework |
| September 10 | Joint lecture: Linac basics | Course A: Accelerator physics<br>Course B: RF technology | Tutorial & homework |
| September 11 | Course A: Accelerator physics<br>Course B: RF technology | | Tutorial & homework |
| September 12 | *Excursion* | *Excursion* | *Free time* |
| September 13 | Course A: Accelerator physics<br>Course B: RF technology | | Tutorial & homework |
| September 14 | Course A: Accelerator physics<br>Course B: RF technology | | Tutorial & homework |
| September 15 | Course A: Accelerator physics<br>Course B: RF technology | *Site visit to IHEP* | Tutorial & homework |
| September 16 | Course A: Accelerator physics<br>Course B: RF technology | | Tutorial & homework |
| September 17 | Course A: Accelerator physics<br>Course B: RF technology | Study time | Tutorial & homework |
| September 18 | Final exam | *Free time* | *Banquet; Student Award Ceremony* |
| September 19 | *Departure* | | |

| | Tuesday, September 8 | Wednesday, September 9 | Thursday, September 10 | Friday, September 11 |
|---|---|---|---|---|
| Morning<br>09:00 – 12:30 | **Opening remarks**<br>**Hesheng Chen** (IHEP)<br><br>**Lecture 1 – Introduction** (3 hrs)<br>**Barry Barish** (GDE/ Caltech)<br>• Tera scale physics<br>• ILC and LHC<br>• Layout of the ILC<br>• Parameter choices & optimization<br>• Other possible future lepton colliders: CLIC and the muon collider<br>• Detectors | **Lecture 3 – CLIC** (3 hrs)<br>• Klystron vs. beam driven acceleration<br>• CLIC layout<br>• Parameter choices & optimization<br>• Driver beam stability<br>• Comparison of the CLIC and ILC<br>• Technical challenges | **Joint lecture of Courses A & B:**<br>**Linac basics** (3 hrs) | **Course A: Accelerator physics**<br>**Lecture A1 – Linac** (cont'd)<br><br>**Course B: RF technology**<br>**Lecture B1 – Room temperature RF** (cont'd) |
| Afternoon<br>14:00 – 17:30 | **Lecture 2 – ILC** (3 hrs)<br>**Barry Barish** (GDE/ Caltech)<br>• e- and e+ sources<br>• Bunch compressors and spin rotators<br>• Damping rings<br>• Main linac<br>• Beam delivery system<br>• Civil construction issues | **Lecture I4 – Muon collider** (3 hrs)<br>**Bob Palmer** (BNL)<br>• Muon collider basics<br>• Machine layout<br>• Major sub-systems<br>• Challenges | **Course A: Accelerator physics**<br>**Lecture A1 – Linac** (9 hrs)<br><br>**Course B: RF technology**<br>**Lecture B1 – Room temperature RF** (12 hrs) | **Course A: Accelerator physics**<br>**Lecture A1 – Linac** (cont'd)<br><br>**Course B: RF technology**<br>**Lecture B1 – Room temperature RF** (cont'd) |
| Evening<br>19:00 – 22:00 | Tutorial & homework | Tutorial & homework | Tutorial & homework | Tutorial & homework |

| | Saturday, September 12 | Sunday, September 13 | Monday, September 14 | Tuesday, September 15 |
|---|---|---|---|---|
| Morning<br>09:00 – 12:30 | **Excursion** | **Course A: Accelerator physics**<br>**Lecture A2 – Sources** (6 hrs)<br><br>**Course B: RF technology**<br>**Lecture B1 – Room temperature RF** (cont'd) | **Course A: Accelerator physics**<br>**Lecture A3 – Beam delivery system and beam-beam** (6 hrs)<br><br>**Course B: RF technology**<br>**Lecture B2 – Superconducting RF** (cont'd) | **Course A: Accelerator physics**<br>**Lecture A4 – Damping rings** (12 hrs)<br>**Andy Wolski** (U. of Liverpool)<br><br>**Course B: RF technology**<br>**Lecture B2 – Superconducting RF** (cont'd) |
| Afternoon<br>14:00 – 17:30 | **Excursion** | **Course A: Accelerator physics**<br>**Lecture A2 – Sources** (cont'd)<br><br>**Course B: RF technology**<br>**Lecture B2 – Superconducting RF** (12 hrs) | **Course A: Accelerator physics**<br>**Lecture A3 – Beam delivery system and beam-beam** (cont'd)<br><br>**Course B: RF technology**<br>**Lecture B2 – Superconducting RF** (cont'd) | **Site visit to IHEP** |
| Evening<br>19:00 – 22:00 | *Free time* | Tutorial & homework | Tutorial & homework | Tutorial & homework |

| | Wednesday, September 16 | Thursday, September 17 | Friday, September 18 | Saturday, September 19 |
|---|---|---|---|---|
| Morning<br>09:00 – 12:30 | **Course A: Accelerator physics**<br>**Lecture A4 – Damping rings** (cont'd)<br>**Andy Wolski** (U. of Liverpool)<br><br>**Course B: RF technology**<br>**Lecture B3 – LLRF & high power RF** (9 hrs) | **Course A: Accelerator physics**<br>**Lecture A4 – Damping rings** (cont'd)<br>**Andy Wolski** (U. of Liverpool)<br><br>**Course B: RF technology**<br>**Lecture B3 – LLRF & high power RF** (cont'd) | **08:00 – 12:30 Final exam** (4.5 hrs) | **Departure** |
| Afternoon<br>14:00 – 17:30 | **Course A: Accelerator physics**<br>**Lecture A4 – Damping rings** (cont'd)<br>**Andy Wolski** (U. of Liverpool)<br><br>**Course B: RF technology**<br>**Lecture B3 – LLRF & high power RF** (cont'd) | **Study time** | *Free time* | |
| Evening<br>19:00 – 22:00 | Tutorial & homework | Tutorial & homework | Banquet;<br>Student Award Ceremony | |

Notes on the Program:

1. This year's program contains major changes from what was done in previous years. Excluding the arrival day (September 7) and the final examination day (September 18), there are a total of 10 school days. The time is divided as follows: 2 days for required courses, 1 day for an excursion, 6 days for elective courses, 0.5 day for a site visit to IHEP and 0.5 day for study time for preparation for the final exam.
2. The required course consists of four lectures: Introduction, ILC, CLIC and the muon collider. Every student must take this course.
3. There are two elective courses: Course A (the red course) is accelerator physics, Course B (the blue course) is RF technology. They will run in parallel. Each student will choose one of these.
4. The accelerator physics course consists of lectures on four topics: (1) linac, (2) sources, (3) beam delivery system and beam-beam effects, and (4) damping rings.
5. The RF technology course consists of lectures on three topics: (1) room temperature RF, (2) superconducting RF, and (3) LLRF and high power RF.
6. There is a half-day joint lecture on linac basics for students taking both Courses A and B.
7. There will be homework assignments, but homework is not counted in the grade. There will be a final examination. Some of the exam problems will be taken from the homework assignments. The exam papers will be graded immediately after the exam and results announced in the evening of September 18 at the student award ceremony.
8. There is a tutorial and homework period every evening. It is part of the curriculum and students are required to attend. Lecturers will be available in the evening of their lecture day during this period.
9. Lecturers have been asked to cover the basics as well as possible. Their teaching material will be made available online to the students well ahead of time (~ 1 month prior to the school). Students are strongly encouraged to study this material prior to the beginning of the school.
10. Lecturers of the elective courses are required to provide a lecture outline as soon as possible in order to help students make their selection.
11. All lecturers are responsible for the design of homework and exam problems as well as the answer sheet. They are also responsible for grading the exams.
12. The award ceremony will honor the top (~10) students based on their exam scores.

# 3 Theme Section: $e^+e^-$ Colliders: Past and Present Experiences and Future Frontiers

## 3.1 Crab Waist Collision at DAΦNE

Catia Milardi on behalf of the DAΦNE Team[1]
LNF-INFN, Via Enrico Fermi 40, Frascati 00044 Italy
Mail to: Catia.Milardi@lnf.infn.it

### 3.1.1 Introduction

DAΦNE [2, 3] is an accelerator complex consisting of a double ring lepton collider working at the c.m. energy of the Φ-resonance (1.02 GeV) and an injection system. In its original configuration the collider consisted of two independent rings, each ~ 97 m long, sharing two 10 m long interaction regions (IR1 and IR2) where the KLOE [4] and FINUDA [5] or DEAR [6] detectors were respectively installed. A full energy injection system, including an S-band linac, 180 m long transfer lines and an accumulator/damping ring, provides fast and high efficiency electron positron injection also in topping-up mode during collisions.

Recently the DAΦNE collider has been upgraded in order to implement a new collision scheme based on large Piwinski angle and cancellation of the synchro-betatron resonances by means of electromagnetic sextupoles (*Crab-Waist* compensation). The novel approach has proved to be effective in improving beam-beam interaction and collider luminosity.

### 3.1.2 Physics at DAΦNE

The interest in the Φ resonance relies on the production of monochromatic and quasi-colinear KK pairs; in fact Φ mesons are produced almost at rest and their main decay modes are $K_S K_L$ ( ~ 34% B.R.) and $K^+ K^-$ ( ~ 49% B.R.).

The very large number of $K_S K_L$ correlated pairs is a powerful tool for the measurement of CP and CPT asymmetry and, more in general, to study neutral kaon decays and quantum interference.

A high luminosity Φ-factory is also suitable to study Λ-hypernuclei formation and decay. Very low energy and monochromatic $K^-$ can be stopped in thin nuclear targets, yielding a small energy straggling of the outgoing $\pi^-$ and consequently increasing the resolution on the hypernuclear levels measurements. Moreover, since $K^+$ and $K^-$ are produced in pairs, $K^+$ detection can be used for tagging and calibration procedures improving the hypernuclear decay measurements. DAΦNE is, by now, the most intense source available of low energy, monochromatic $K^-$, which also allows experiments aimed at studying the kaonic atom spectroscopy.

These topics are the main field of interest of the KLOE, FINUDA and DEAR experiments respectively.

### 3.1.3 Luminosity before the Upgrade

#### *3.1.3.1 Achievements*

Since 2001 the DAΦNE collider has been delivering luminosity to three experiments, improving, at the same time, its performances in terms of luminosity (see Fig. 1).

The DEAR experiment has been completed in less than five months during 2002-2003, collecting ~ 200 $pb^{-1}$, with a peak luminosity of 0.7 $\cdot 10^{32}$ $cm^{-2}s^{-1}$. The KLOE experimental program ended in 2006, logging 3.0 $fb^{-1}$ integrated luminosity [7] on the peak of the Φ resonance, and more than 0.25 $fb^{-1}$ off-resonance, to carry out a high statistics energy scan and measurements unaffected by resonant background from the Φ itself. The highest peak luminosity achieved has been 1.5 $\cdot 10^{32}$ $cm^{-2}s^{-1}$, with a maximum daily integrated luminosity ~ 10 $pb^{-1}$.

The FINUDA experiment logged 1.2 $fb^{-1}$ [8, 9] of which 1.0 $fb^{-1}$ during the last six months of operation in 2006-2007. In this period a 1.6 $\cdot 10^{32}$ $cm^{-2}$ $s^{-1}$ peak luminosity, and a maximum daily integrated luminosity comparable with that of the KLOE run has been achieved with lower beam currents, lower number of bunches and higher beta functions at the collision point. However, these performances were the best obtainable with the DAΦNE original collision scheme.

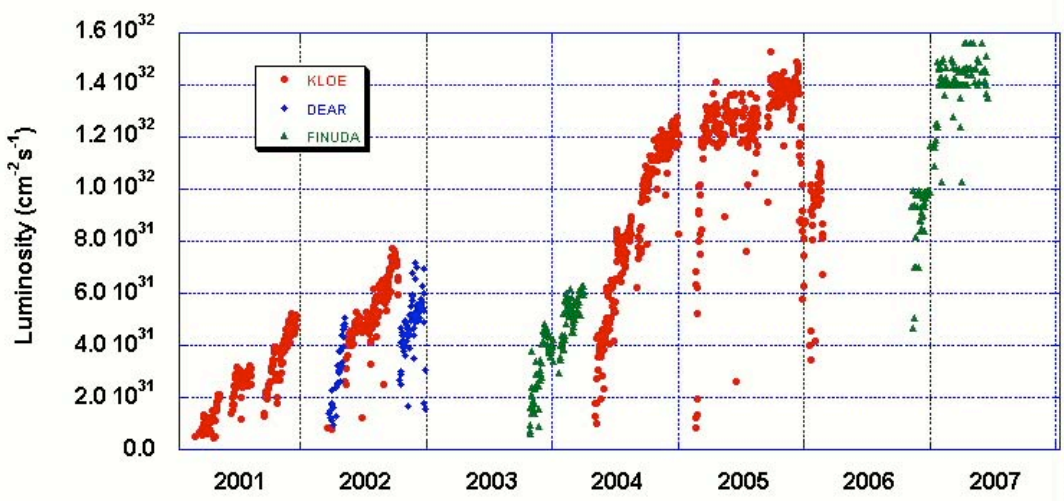


**Figure 1:** Daily peak luminosity trend.

#### *3.1.3.2 Limiting Factors*

The experimental activity on DAΦNE outlined the following factors limiting any further relevant luminosity improvement.

Long-range beam-beam interactions [10] (parasitic crossings) occurring in the two 10 m long interaction regions led to a substantial lifetime reduction of both beams in collision, limiting the maximum storable current and, as a consequence, the achievable peak and integrated luminosity.

The colliding bunches transverse spot size at the IP depends on the local values of the transverse betatron functions $\beta^*_{x,y}$. It is well known that reducing $\beta^*_y$ is beneficial to

the luminosity. However the minimum value of $\beta^*_y$ is set by the bunch overlap area, to avoid the detrimental effects arising from the hourglass effect. For head-on or small angle collisions the overlap area is comparable with the longitudinal bunch length, which in DAΦNE, after a careful optimization of the main rings coupling impedance [11], was ~ 2.5 cm for both beams at the operating bunch current (~ 15 mA).

The positron beam showed a threshold in the maximum storable current due to a fast horizontal instability, faster than the synchrotron period, depending on the injection conditions, on the stored current and on the beam fill pattern, compatible with an e-cloud driven instability. The current threshold appeared after the 2003 shut down, when the beam emittance and the nonlinear contributions coming from the eight wiggler magnets installed in the colliding rings have been reduced. The instability was mitigated by: using transverse feedbacks, reducing strength and pulse length of the injection kickers and tuning the phase advance between the two injection kickers.

All these limitations required a new conceptual approach to push the luminosity towards $10^{33}$ $cm^{-2}$ $s^{-1}$. After long studies and discussions involving the Accelerator Division Team and the high energy physics community of the laboratory, a new collision scheme based on large Piwinski angle and *Crab-Waist* has been adopted for the DAΦNE collider.

### 3.1.4 DAΦNE Upgrade

Existing factories, designed more than ten years ago, rely on flat multibunch beams colliding under a horizontal angle θ and having a normalized crossing angle ψ (also known as Piwinski angle) much less than 1, according to Eq. (1) where $\sigma^*_z$ and $\sigma^*_x$ are the r.m.s. longitudinal and horizontal bunch sizes at the IP respectively.

$$\psi = \frac{\sigma_z^*}{\sigma_x^*}\frac{\theta}{2} << 1. \qquad (1)$$

This criterion is intended to cope with the synchro-betatron resonances arising from the horizontal angle, which is required to minimize secondary bunch crossings around the IP. In this context, to increase the luminosity it is necessary to reduce the vertical betatron function $\beta_y$ at the IP and the vertical beam emittance $\varepsilon_y$, and to increase the beam intensity I, the horizontal beam size $\sigma_x$ and the horizontal emittance $\varepsilon_x$, the last condition being required to keep under control the beam-beam effects. This approach meets severe limitations; in fact $\beta_y$ can not be much smaller than the bunch length $\sigma_z$, high intensity currents stored circular rings require relevant radio frequency power to compensate the beam losses due to the synchrotron radiation emission and short bunches carrying high currents are affected by instabilities, which become more harmful as the currents increase.

A new collision scheme with a large Piwinski angle, obtained by increasing the horizontal crossing angle and reducing the horizontal beam size at the IP, has been proposed and implemented at DAΦNE [12]. The large Piwinski angle provides several advantages: it reduces the beam-beam tune shift in both planes, shrinks the longitudinal size of the overlap between colliding bunches, thus allowing for a lower $\beta_y$ at the IP and cancels almost all the parasitic crossings: in the case of DAΦNE it becomes possible to completely separate the vacuum chambers of the two beams just after the first low-β

quadrupole in the IR. A couple of *Crab-Waist* sextupoles, installed in symmetric position with a proper phase advance with respect to the IP, suppresses the betatron and sinchro-betatron resonances coming from the vertical motion modulation due to the horizontal oscillation.

According to the simulations this new collision scheme was expected to increase the luminosity by more than a factor 3 with the same bunch length and moderate colliding currents.

**Table 1:** DAΦNE beam parameters.

| | ***DAΦNE (KLOE run)*** | ***DAΦNE Upgrade Achieved (Nominal)*** |
|---|---|---|
| $I_{bunch}$ (mA) | 13.0 | 13.0 |
| $N_{bunch}$ | 110 | 105 (110) |
| $\beta^*_y$ (cm) | 1.7 | 0.9 (0.65) |
| $\beta^*_x$ (cm) | 170. | 25. (20.) |
| $\sigma^*_x$ (μm) | 700. | 200. |
| $\sigma^*_y$ (μm) | 7. | 4. (2.6) |
| $\sigma^*_z$ (mm) | 25. | 17. (20.) |
| $\theta^*_{cross}/2$ (mrad) | 12.5 | 25. |
| ψ (mrad) | 0.6 | 1.9 |
| ε (mm mrad) | 0.34 | 0.26 |
| Luminosity • $10^{32}$ ($cm^{-2}$ $s^{-1}$) | 1.5 | 4.36 (~ 5.) |

The evolution of the main DAΦNE parameters are summarized in Table 1 while the changes in the mechanical and magnetic layout of the IR1 [13] are presented in Fig. 2. The second unused interaction region has been eliminated and replaced by a ring crossing section where the two vacuum chambers are vertically separated (see Fig. 2).

The SIDDHARTA experiment [14] (an evolution of DEAR) has been installed on the new IR. It is a compact device without solenoidal field providing a simple environment to test the effectiveness of the new collision scheme.

The DAΦNE upgrade included several other improvements and modifications. Some devices, such as bellows and injection kickers have been redesigned in order to improve their performances and to reduce their contribution to the ring total coupling impedance [15, 16, 17]. A bunch length of 1.7 cm has been measured for both beams at 10 mA/bunch, which, for the electron beam, is consistent with a 20% bunch length reduction.

The four electron and positron transverse feedbacks have been upgraded by adopting a new generation feedback unit [18], which beyond its stabilization function provides a variety of diagnostic tools. Two new different monitors have been built to measure the luminosity [19]. Moreover the kaon counting rate is yielded by the SIDDHARTA experiment trigger system.

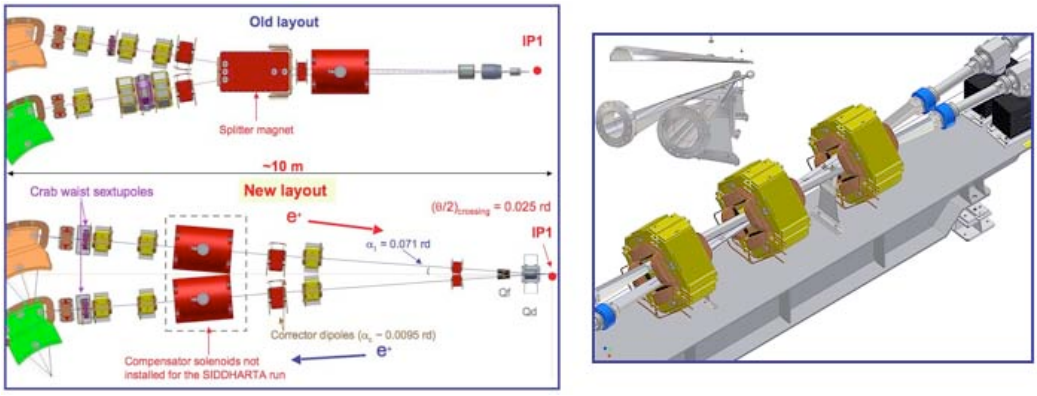


**Figure 2:** View of half IR1 old (top-left) and new (bottom-left) layout. New ring crossing region (bottom-right) and new vacuum chamber design (top-right).

### 3.1.5 DAΦNE Commissioning after the Upgrade

DAΦNE operation restarted at the end of November 2007 with the aim to test the new devices, set the beam parameters accordingly to the upgrade nominal values, verify the *Crab-Waist* collision scheme and provide luminosity to the SIDDHARTA experiment.

#### *3.1.5.1 Colliding Rings Optics*

The *low-beta* section in the SIDDHARTA IR is based on permanent magnet quadrupole doublets. The quadrupoles are made of SmCo alloy and provide gradients of 29.2 T/m and 12.6 T/m for the first one from the IP and the second one respectively. The first is horizontally defocusing and is shared by the two beams; due to the off-axis beam trajectory, it provides strong beam separation. The second quadrupole, the focusing one, is installed just after the beam pipe separation and is therefore on axis (see Fig. 2). The new configuration almost cancels the problems related to beam-beam long range interactions, because the two beams experience only one parasitic crossing inside the defocusing quadrupole where, due to the large horizontal crossing angle, they are very well separated ($\Delta x \sim 40\ \sigma_x$). It is worth reminding that in the old configuration the colliding beams had 24 parasitic crossing in the IRs and in the main one the separation at the first crossing was $\Delta x \sim 7\ \sigma_x$ [20].

The DAΦNE main rings have been commissioned using a detuned optics, with $\nu_x$ slightly above 5, $\nu_y$ above 4, and without *Crab-Waist* sextupoles in order to speed up beam injection, put the diagnostics in operation and perform a satisfactory machine modeling. The beam closed orbit has been minimized together with the steering magnet strengths relying also on beam based procedures to point out and fix misalignment errors. The vertical dispersion has been minimized by global vertical orbit correction and by centering the beam vertical position in the arc sextupoles. Once a reliable machine model has been defined (presently the agreement between computed and measured twiss parameters is better than 10%), the ring optics has been moved progressively towards the nominal one with both tunes above 5. The β functions are

now $\beta^*_{y,x} \sim 0.009/0.25$ m at the IP, slightly larger than the *Crab-Waist* design values ($\beta^*_{y,x} \sim 0.0065/.20$ m).

The transverse betatron coupling has been corrected mainly by correcting rotation errors in the low-β focusing quadrupoles, now independent for the two rings. The best value obtained so far is $\kappa \sim 0.4\%$ for both beams measured at the synchrotron light monitor after a careful calibration.

The *Crab-Waist* sextupoles are electromagnetic devices; their strength depends on the values of the horizontal crossing angle and of the betatron functions at the IP and at the sextupole according to:

$$k_s = \frac{1}{2\theta}\frac{1}{\beta_y^* \beta_y^{sext}}\sqrt{\frac{\beta_x^*}{\beta_x^{sext}}}\,. \qquad (2)$$

The nominal strength with the present parameters is larger than the maximum available with our sextupoles, which now provide slightly more than half the required value. The *Crab-Waist* sextupoles compensate exactly each other and do not add any contribution to the ring chromaticity. The transverse beam trajectory in the *Crab-Waist* sextupoles must be carefully aligned to avoid any tune and betatron coupling variation which, in turn, might influence the luminosity and the background hitting the experimental detector.

#### *3.1.5.2 High Currents Issues*

In the early stage of the commissioning high current operations have been limited by the maximum achievable positron current that was affected by a transverse horizontal instability observed even before the upgrade, but with a lower grow rate. Several studies have been aimed at ruling out trapped high order modes and anomalous wake fields as possible sources of the positron current limit. The measurements indicate the e-cloud instability as a possible explanation for the observed behaviour. The current limit has been overcome by halving the damping time of the transverse horizontal feedback used to cope with the instability. A second feedback system has been implemented, kicking the beam by using two out of the four injection kickers striplines powered by spare hardware. The effects of the two systems add up linearly and the horizontal instability is damped in less than 15 turns (~ 5 μsec). In this way it has been possible to store more than 1.1 A of positron in a stable beam with the correct transverse beam dimensions.

Eventually a faulty behaviour of a RF cavity subsystem, intended for damping the beam barycentric coherent motion, which was affecting the current and luminosity performances, has been corrected. Both electron and positron currents benefited from reducing the noise in the DAΦNE equipotential network, that was affecting RF and feedback subsystems.

#### *3.1.5.3 Luminosity Achievements*

The most relevant results obtained after the DAΦNE upgrade concern the luminosity and the background shower hitting the experimental detector.

Commissioning has been completed in six months. In May 2008 a luminosity considerably higher (~30%) with respect to the past had already measured, as can be seen comparing the green data presented in Fig. 3 with the ones (yellow, red and blue) taken while operating DAΦNE with the original collision scheme. It is worth noticing that in May the luminosity given by the Bhabha monitor was underestimated (~ 15%) due to the insertion of new background shields around the IP, which was not yet accounted for.

The impact of the Piwinski angle had already been tested during the KLOE experiment data taking in 2005 when ψ was doubled and $\beta^*_y$ considerably reduced resulting in an almost doubled peak luminosity (red and blue curve in Fig. 3).

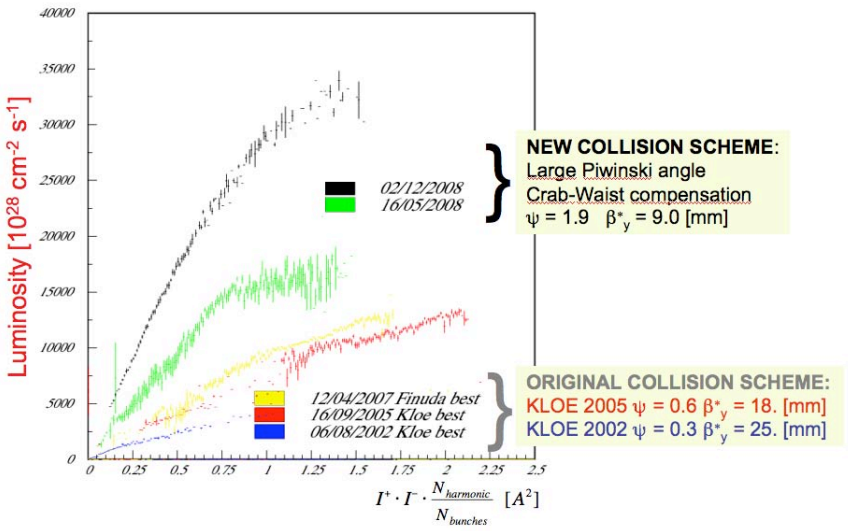


**Figure 3:** Luminosity versus the product of the colliding currents normalized to the number of colliding bunches. Data refer to runs acquired before (bottom) and after (top) implementing the new collision scheme.

The peak luminosity has been progressively improved by tuning the collider and increasing the beam currents; the maximum value achieved by now is $4.36 \cdot 10^{32}$ cm$^{-2}$ s$^{-1}$ measured in several runs (see Fig. 4) with good luminosity to background ratio. As a result of working point optimization, transverse and longitudinal feedback tuning, *Crab-Waist* sextupole adjustment and vertical dispersion reduction, it has been also possible to mitigate the luminosity saturation at high currents. However a residual effect cannot be avoided since in Large Piwinski Angle & *Crab-Waist* regime the luminosity depends inversely on the bunch length, which in turn is affected by the ring impedance. The present peak luminosity is satisfactorily close to the nominal one predicted by theoretical simulations [21].

The highest single bunch luminosity achieved so far is L ~ $5 \cdot 10^{30}$ cm$^{-2}$ s$^{-1}$ obtained with 20 bunches in collision.

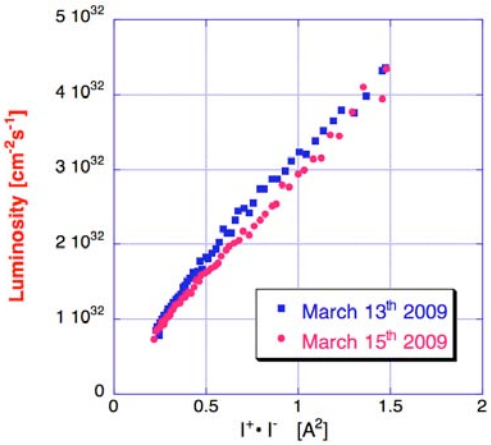


**Figure 4:** Luminosity versus the product of the colliding currents during two of the best runs returning a peak luminosity in excess of 4.36 ·10$^{32}$ cm$^{-2}$ s$^{-1}$.

The impact of the *Crab-Waist* sextupoles has been studied and discussed in detail [22, 23]. It can be recognized at glance comparing runs taken with *Crab-Waist* sextupoles on and off (see Fig. 5). At low current the luminosity is the same in the two cases, and it is significantly higher than the one measured during the operation with the DAΦNE original collision scheme. As the product of the stored currents exceeds 0.5 A the luminosity measured with the *Crab-Waist* sextupoles off becomes lower and a correspondent transverse beam size blowup and beam lifetime reduction are observed as a consequence of the uncompensated beam-beam resonances.

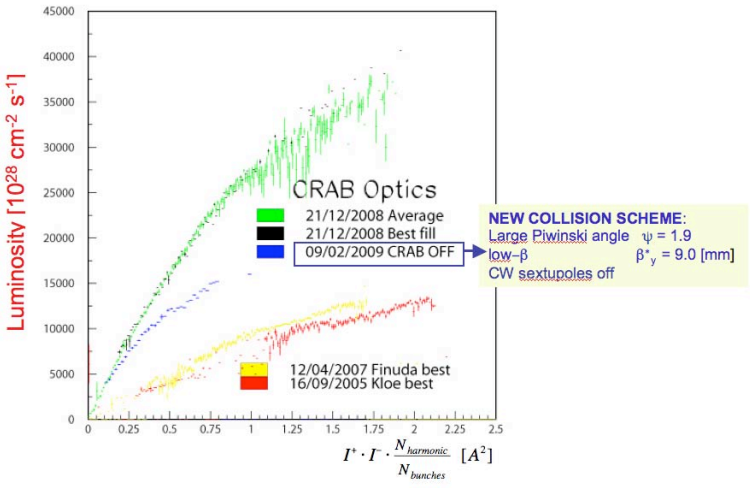


**Figure 5:** Luminosity measured with *Crab-Waist* sextupoles off (blue dots) and on (green dots).

The integrated luminosity profited from implementing a new software procedure to switch the injection system from electrons and positrons and the other way round. The switch time has been reduced by a factor three and is now in the range 50 – 80 sec. A continuous switching regime provides $L_{\int 1\ hour} \sim 1.0$ pb$^{-1}$ hourly integrated luminosity (see Fig.6), which is not compatible with the SIDDHARTA experiment data taking since the acquisition is vetoed during injection. Nevertheless it opens important

perspectives for the next DAΦNE runs with the KLOE experiment that is presently scheduled to start by the end of 2009. Scaling this best integrated luminosity already measured over two hours it is reasonable to expect a daily integrated luminosity larger than 20 $pb^{-1}$, and assuming 80% collider uptime, as during the past runs, a monthly integrated luminosity of ~ 0.5 $fb^{-1}$ can be foreseen.

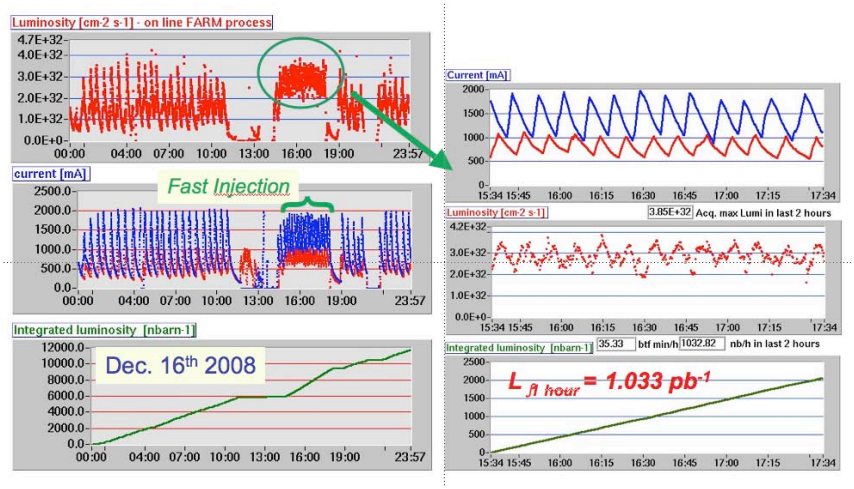


**Figure 6:** Integrated luminosity in continuous switch regime.

A satisfactory integrated luminosity has been obtained also in a moderate injection regime compatible with the SIDDHARTA operation with a ~50% duty cycle. In this context the best hourly and daily integrated luminosity measured by now are: $L_{\int 1\ hour}$ ~ 0.79 $pb^{-1}$ averaged over two hours, and $L_{\int day}$ ~ 15 $pb^{-1}$ (see Fig 7). Luminosity achievements are even more relevant since they have been obtained letting in collision lower currents stored in less bunches than in the past.

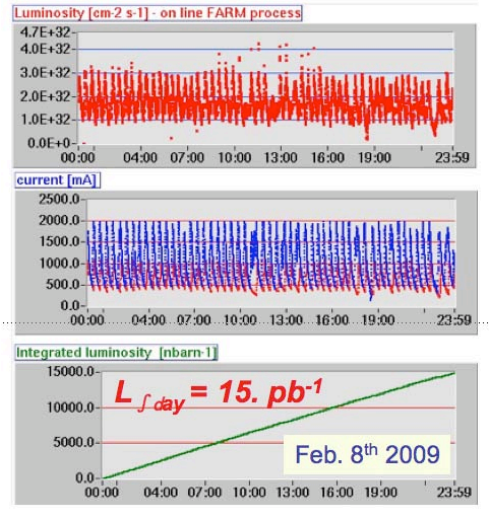


**Figure 7:** Best daily integrated luminosity.

Further luminosity gains are expected from improving vacuum conditions to shrink the gap in the electron beam necessary to avoid the ion trapping instability, and future developments to reduce the impact of the e-cloud instability on the storable positron current.

The present DAΦNE performances are summarized, and compared with the old ones, in Table 2.

**Table 2:** DAΦNE present achievements.

| | ***DAΦNE Upgrade*** | ***DAΦNE (KLOE run)*** | ***DAΦNE (FINUDA run)*** |
|---|---|---|---|
| $L_{peak} \cdot 10^{32}$ ($cm^{-2}$ $s^{-1}$) | 4.36 | 1.5 | 1.6 |
| $L_{\int 1\ hour}$ ($pb^{-1}$) | 1.03 | 0.44 | 0.5 |
| $L_{\int day}$ ($pb^{-1}$) | 14.98 | 9.8 | 9.4 |
| $I^-$ at $L_{peak}$ (A) | 1.4 | 1.4 | 1.5 |
| $I^+$ at $L_{peak}$ (A) | 1.0 | 1.2 | 1.1 |
| $N_{bunches}$ | 105 | 111 | 106 |

Background conditions have been constantly improved by: minimizing closed orbit and corrector strengths, improving the beam lifetime, tuning the beam position in the ring crossing region, optimizing the scrapers insertion and installing additional shields around the IR to improve signal/noise ratio on the silicon drift detectors of the SIDDHARTA setup. In this way the background has been reduced by a significant amount and meets the SIDDHARTA experiment requirements.

### 3.1.6 Conclusions

The new collision scheme based on large Piwinski angle and *Crab-Waist* implemented on DAΦNE worked as expected according to the preliminary studies and theoretical simulations.

The principle of *Crab-Waist* compensation has been recognized as a major advance in the field of the beam-beam interaction in lepton colliders.

The present luminosity achievements have opened new perspectives for the DAΦNE collider, and a new run for the KLOE experiment has been planned starting by the end of 2009.

The new collision scheme is the main design concept for a new project aimed at building a Super-B factory [24] that is expected to achieve a luminosity of the order of $10^{36}$ $cm^{-2}$ $s^{-1}$ and it has been also taken into account to upgrade one of the LHC interaction regions.

### 3.1.7 References

1. D.Alesini, M.E.Biagini, C.Biscari, R.Boni, M.Boscolo, F.Bossi, B.Buonomo, A.Clozza, G.Delle Monache, T.Demma, E.Di Pasquale, G.Di Pirro, A.Drago, A.Gallo, A.Ghigo, S.Guiducci, C.Ligi, F.Marcellini, G.Mazzitelli, C.Milardi, F.Murtas, L.Pellegrino, M.Preger, L.Quintieri, P.Raimondi, R.Ricci, U.Rotundo, C.Sanelli, M.Serio, F.Sgamma, B.Spataro, A.Stecchi, A.Stella, S.Tomassini, C.Vaccarezza, M.Zobov LNF-INFN, Frascati, Italy; I.Koop, E.Levichev, P.Piminov, D.Shatilov, BINP SB RAS, Novosibirsk, Russia; V.Smaluk BINP, Novosibirsk, Russia; S.Bettoni, CERN, Geneva,

Switzerland; M.Schioppa INFN- Cosenza, Cosenza, Italy; P.Valente, INFN-Roma1, Roma, Italy; K.Ohmi, KEK, Ibaraki, Japan; N.Arnaud, D.Breton, L. Burmistrov, A.Stocchi, A.Variola, B.F.Viaud, LAL, Orsay, France; M.Esposito, University La Sapienza, Roma, Italy; E.Paoloni, University of Pisa and INFN, Pisa, Italy; P.Branchini, INFN-Roma3, Rome, Italy; D.Teytelman SLAC, Menlo Park, USA.

2. G. Vignola et al., Frascati Phys. Ser. 4:19-30,1996; G. Vignola et al., PAC93, p. 1993.
3. C. Milardi et al., Frascati Phys. Ser.16:75-84,1999.
4. KLOE Collab., Nucl. Inst. Meth. A 482, 363-385 (2002).
5. FINUDA Collab., Proc. HYP2000, Torino, 2000, Italy.
6. DEAR Collab., Physics Letters B, Vol. 535, (2002) 52.
7. A. Gallo et al., DAΦNE Status Report, EPAC06, p. 604-606, Edinburgh, UK.
8. C. Milardi et al., DAΦNE Operation with the FINUDA Experiment, EPAC04, Lucerne, Switzerland.
9. C. Milardi et al., DAΦNE Setup and Performances during the second FINUDA Run, PAC07, p. 1457, Albuquerque, USA.
10. C. Milardi et al., DAΦNE Lifetime Optimization with Compensating Wires and Octupoles, arXiv:0803.1544v3.
11. M.Zobov et al., Impact of Ion Clearing Electrodes on beam dynamics in DAΦNE, JINST 2, P08002, 2007.
12. P. Raimondi et al., Beam-Beam Issues for Colliding Schemes with Large Piwinski Angle and Crabbed Waist, physics/0702033.
13. C. Milardi et al., DAΦNE Interaction Regions upgrade, arXiv:0803.1450v1, e-print: physics/0408073.
14. SIDDHARTA Collab., Eur. J. Phys. A 31 (2007) 537-539.
15. F. Marcellini et al., Coupling Impedance of DAΦNE Upgraded Vacuum Chamber, EPAC08, p. 1661, Genoa, Italy.
16. S. Tomassini et al., A New RF Shielded Bellows for the DAΦNE Upgrade, EPAC08, p. 1661, Genoa, Italy.
17. D. Alesini et al., DAΦNE Tech. Note I-17, 2006.
18. A. Drago et al., Commissioning of the iGp Feedback System at DAΦNE, EPAC08, p. 3251, Genoa, Italy
19. M. Boscolo et al., Luminosity measurement at DAΦNE for crab waist scheme**,** EPAC08, p. 1203, Genoa, Italy.
20. C. Milardi et al., Wire Compensation of Parasitic Crossings in DAΦNE, e-Print: physics/0607129.
21. M. Zobov et al., this issue of ICFA Beam Dynamics Newsletters.
22. C. Milardi et al., "Present status of the DAΦNE upgrade and perspectives", Int.J.Mod.Phys.A24:360-368, 2009.
23. C. Milardi et al., DAΦNE setup and operation with the Crab-Waist collision scheme, EPAC08, p. 1203, Genoa, Italy.
24. M. Biagini et al., this issue of ICFA Beam Dynamics Newsletters.

## 3.2 Beam Dynamics in Crab Waist Collisions at DAΦNE

M. Zobov, C. Milardi, P. Raimondi, INFN, Laboratori Nazionali di Frascati, Italy
E. Levichev, P. Piminov, D. Shatilov, Budker Institute of Nuclear Physics, Russia
K. Ohmi, KEK, Tsukuba, Japan
Mail to: Mikhail.Zobov@lnf.infn.it

### 3.2.1 Introduction

In high luminosity colliders with standard collision schemes the key requirements to increase the luminosity are: very small vertical beta function $\beta_y$ at the interaction point (IP), high beam intensity and large horizontal emittance $\varepsilon_x$ and beam size $\sigma_x$. However, $\beta_y$ can not be much smaller than the bunch length $\sigma_z$ without incurring in the "hour-glass" effect. It is, unfortunately, very difficult to shorten the bunch in a high current ring without exciting instabilities. In turn, the beam current increase may result in high beam power losses, beam instabilities and remarkable enhancement of the wall-plug power. These problems can be overcome with the recently proposed Crab Waist (CW) scheme of beam-beam collisions [1] where a substantial luminosity increase can be achieved without bunch length reduction and with moderate beam currents.

The CW scheme has been already successfully tested at DAΦNE, the Italian Φ-factory [2, 3] and the most recent results of the experiment are reported in the present issue of the Newsletters [4]. The main purpose of this paper is to compare the obtained experimental data with numerical simulation results. This is required in order to accomplish the following tasks:

- to prove that the crab waist concept works as predicted by numerical simulations,
- to benchmark existing numerical codes versus experimental measurements.

Such tasks are particularly important for the design of the future e+e- factories based on the crab waist idea, such as the SuperB factory in Italy [5], the Tau-Charm factory in Novosibirsk [6] and others.

In the following we will briefly introduce the CW idea and show some numerical examples demonstrating the beam-beam coupling resonance's suppression with crab waist sextupoles. A comparison of the experimental results with those obtained numerically is given in the second part of the paper.

### 3.2.2 Crab Waist Concept

The Crab Waist scheme of beam-beam collisions can substantially increase collider luminosity since it combines several potentially advantageous ideas. Let us consider two bunches colliding under a horizontal crossing angle $\theta$ (as shown in Fig. 1a). Then, the CW principle can be explained, somewhat artificially, in the three basic steps. The **first one** is large Piwinski angle. For collisions under a crossing angle $\theta$ the luminosity $L$ and the beam-beam tune shifts scale as [7]:

$$L \propto \frac{N\xi_y}{\beta_y^*}; \quad \xi_y \propto \frac{N\sqrt{\beta_y^*/\varepsilon_y}}{\sigma_z\theta}; \quad \xi_x \propto \frac{N}{(\sigma_z\theta)^2} \tag{1}$$

with $N$ being the number of particles per bunch. Here we consider the case of flat beams, small horizontal crossing angle $\theta << 1$ and large Piwinski angle $\phi >> 1$, defined as:

$$\phi = \frac{\sigma_z}{\sigma_x} tg\left(\frac{\theta}{2}\right) \approx \frac{\sigma_z}{\sigma_x}\frac{\theta}{2} \tag{2}$$

The idea of colliding with a large Piwinski angle is not a new one (see, for example, [8]). It has been also proposed for hadron colliders [9, 10] to increase the bunch length and the crossing angle. In such a case, if it were possible to increase $N$ proportionally to $\sigma_z\theta$, the vertical tune shift $\xi_y$ would remain constant, while the luminosity would grow proportionally to $\sigma_z\theta$, see (1). Moreover, the horizontal tune shift $\xi_x$ drops like $1/\sigma_z\theta$. However, differently from [9, 10], in the crab waist scheme described here the Piwinski angle is increased by decreasing the horizontal beam size and increasing the crossing angle. In this way we can gain in luminosity as well, and the horizontal tune shift decreases. Moreover, parasitic collisions (PC) become negligible since with higher crossing angle and smaller horizontal beam size the beam separation at the PC becomes larger in terms of $\sigma_x$. But the most important effect is that the overlap area of the colliding bunches is reduced, since it is proportional to $\sigma_x/\theta$ (see Fig. 1).

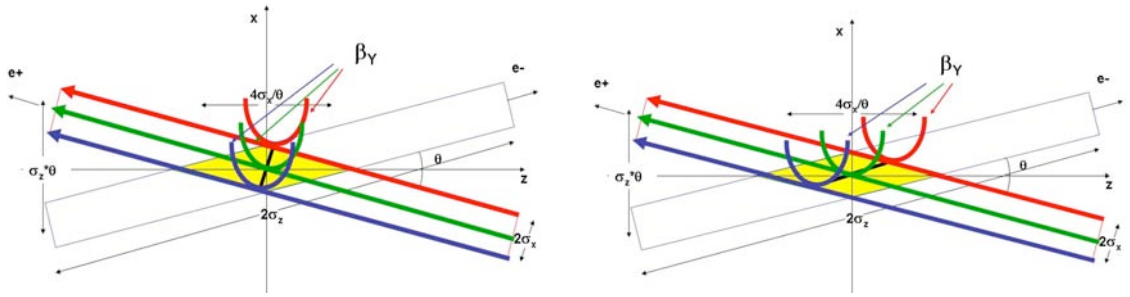


a) b)

**Figure 1:** Crab waist collision scheme.

Then, as the **second step**, the vertical beta function $\beta_y$ can be made comparable to the overlap area size (i.e. much smaller than the bunch length):

$$\beta_y^* \approx \frac{\sigma_x}{\theta} << \sigma_z \tag{3}$$

It is worth remarking that usually it is assumed that $\xi_y$ (see the expression for $L$ in (1)) always reaches the maximum allowed value, the so called "beam-beam limit". So, reducing $\beta_y$ at the IP gives us several advantages:

- Luminosity increase with the same bunch current.
- Possibility of bunch current increase (if it is limited by $\xi_y$), thus farther increasing the luminosity.

- Suppression of vertical synchrobetatron resonances [11].
- Reduction of the vertical tune shift with synchrotron oscillation amplitude [11].

Besides, there are additional advantages in such a collision scheme: there is no need of decreasing the bunch length to increase the luminosity as proposed in standard upgrade plans for B- and Φ-factories. This will certainly help solving the problems of HOM heating, coherent synchrotron radiation of short bunches, excessive power consumption, etc.

However, large Piwinski angle itself introduces new beam-beam resonances which may strongly limit the maximum achievable tune shifts (see [12], for example). At this point the crab waist transformation enters the game boosting the luminosity. This is the **third step**. As it can be seen in Fig. 1b, the beta function waist of one beam is oriented along the central trajectory of the other one. In practice the CW vertical beta function rotation is provided by sextupole magnets placed on both sides of the IP in phase with the IP in the horizontal plane and at π/2 in the vertical one (as shown in Fig. 2).

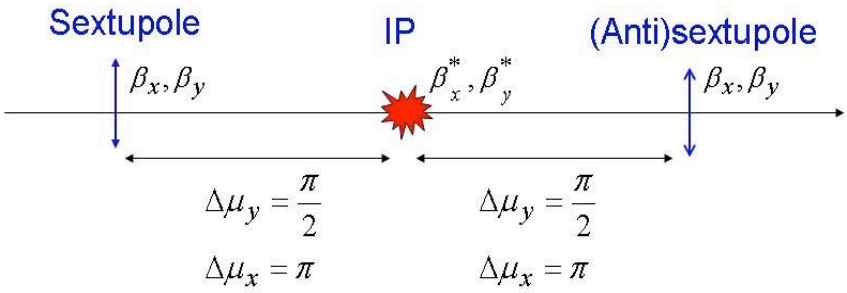


**Figure 2**: Crab sextupole locations.

The crab sextupole strength should satisfy the following condition depending on the crossing angle and the beta functions at the IP and the sextupole locations:

$$K = \frac{1}{\theta}\frac{1}{\beta_y^*\beta_y}\sqrt{\frac{\beta_x^*}{\beta_x}} \tag{4}$$

The crab waist transformation gives a small geometric luminosity gain due to the vertical beta function redistribution along the overlap area. It is estimated to be of the order of several percent [13]. However, the dominating effect comes from the suppression of betatron (and synchrobetatron) resonances arising (in collisions without CW) due to the vertical motion modulation by the horizontal betatron oscillations [14, 15, and 16].

We have carried out many beam-beam simulations which confirmed advantages of the Crab Waist scheme and demonstrated suppression of the betatron coupling resonances. As an example, in Fig. 3 one can see two luminosity tune scans performed for the SuperB set of parameters [17]. The "geographical map" colors were used: red corresponds to the maximum luminosity, blue to the minimum. One can see a clear resonance suppression and "good" areas expansion when the Crab sextupoles are switched on. It is worth to note that the bunch current in Fig. 3 b) is higher by a factor

2.5! One more example is given in Fig. 4, where the beam tails and vertical blowup (r.m.s. beam size which affects the luminosity) for one of the good working points are shown versus the bunch current. The vertical size blow up and beam distribution tails are strongly reduced with the crab sextupoles on.

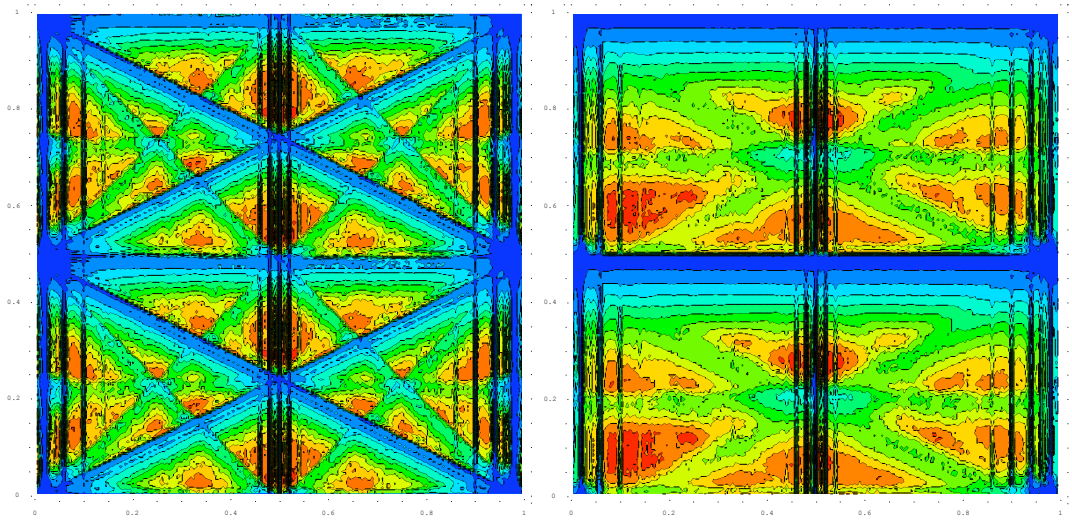

a) b)

**Figure 3:** Luminosity tune scan with CW off (a) and on (b).

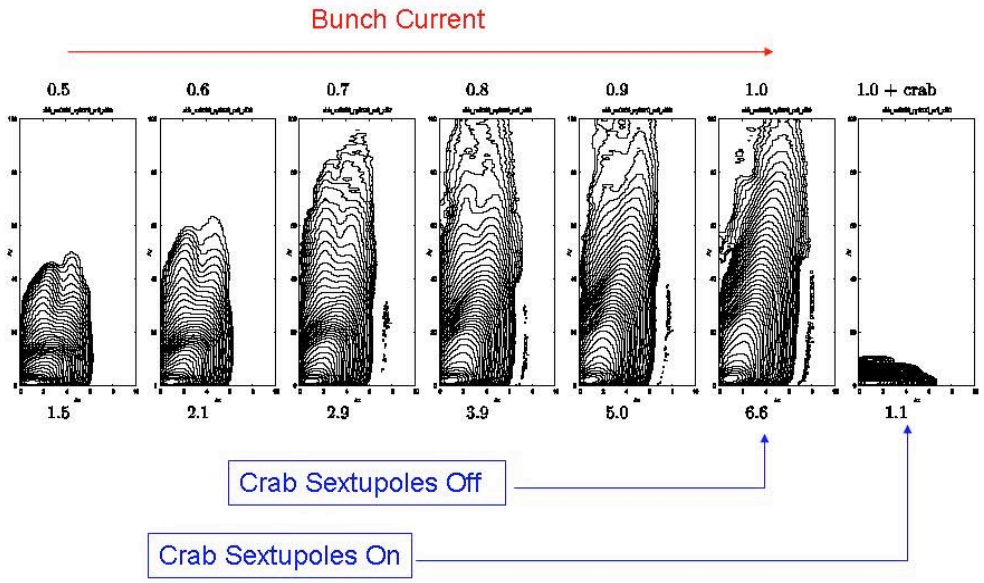


**Figure 4:** Beam distribution tails and vertical size blow up (numbers at the bottom) versus bunch current with crab sextupoles on and off. Each plot represents equilibrium density in the space of normalised betatron amplitudes where successive contour levels are at a constant ratio $e^{1/2}$ below each other.

### 3.2.3 Numerical Simulations versus Experimental Results

#### *3.2.3.1 Achieved Results*

Table 1 summarizes the luminosity and corresponding parameters at the interaction point (IP) for the best DAΦNE luminosity runs for the three main experiments carried out on the collider. The first and the second column correspond to the results achieved with the KLOE [18] and FINUDA [19] detectors before the DAΦNE upgrade based on the crab waist concept. The third column shows results obtained during the current run with the SIDDHARTA experiment after the collider upgrade [4].

As one can see from Table 1, the best present luminosity is by almost a factor 3 higher than in the previous runs before the upgrade. The obtained luminosity of $4.4 \times 10^{32}$ $cm^{-2}s^{-1}$ is already very close to the upgrade design value of $5 \times 10^{32}$ $cm^{-2}s^{-1}$, and work is still in progress to achieve this ultimate goal.

Partly the luminosity gain has been reached due to implementation of the "micro-beta" collision optics – the high Piwinski angle with the smaller vertical beta function comparable to the small collision area (step 1 and step 2). Another factor in the luminosity increase comes from improvements in beam dynamics, first of all due to beam-beam resonance suppression in the crab waist collisions. Indeed, as it can be seen in the last row of Table 1 the vertical tune shift parameter has been significantly improved and now it is as high as 0.042. It is worth mentioning that in weak-strong collisions when the electron beam current is much higher than the positron one the tune shift has exceeded 0.06.

**Table 1:** DAΦNE luminosity and IP parameters for 3 experimental runs.

| *Parameter* | *KLOE* | *FINUDA* | *SIDDHARTA* |
|---|---|---|---|
| Date | September 2005 | April 2007 | March 2009 |
| Luminosity, $cm^{-2}$ $s^{-1}$ | $1.5 \times 10^{32}$ | $1.6 \times 10^{32}$ | $4.4 \times 10^{32}$ |
| e- current, A | 1.38 | 1.50 | 1.47 |
| e+, current, A | 1.18 | 1.10 | 1.00 |
| Number of bunches | 111 | 106 | 105 |
| $\varepsilon_x$, mm mrad | 0.34 | 0.34 | 0.25 |
| $\beta_x$, m | 1.5 | 2.0 | 0.25 |
| $\beta_y$, m | 1.8 | 1.9 | 0.95 |
| Crossing angle, mrad | 2x12.5 | 2x12.5 | 2x25 |
| $\xi_y$ | 0.025 | 0.029 | 0.042 |

#### *3.2.3.2 Comparison with Ideal Simulations*

In order to benchmark the numerical codes that have been used for the crab waist collision studies for the DAΦNE [20] upgrade and SuperB CDR [17] we have compared the DAΦNE experimental data with numerical results. For this purpose we have used both weak-strong and strong-strong beam-beam numerical simulations.

First preliminary simulations with the weak-strong code LIFETRAC [21] have shown that for present DAΦNE parameters (tunes, bunch length, crab waist sextupole strength etc.) both beams are blown up that correspond to experimental observations. For this reason we have passed to strong-strong simulations with the BBSS [12] code. Some of the simulation results are shown in Fig. 5 and Fig. 6. The single bunch luminosity with CW sextupoles on (red curve) and off (blue curve) as a function of the number of revolution turns is shown in Fig. 5. Here we remind that the radiation damping time is very long for DAΦNE (110.000 turns). In turn, the corresponding vertical size blow up for the electron (blue) and positron (red) beams for the cases with CW sextupoles on (left picture) and off (right picture) are shown in Fig. 6.

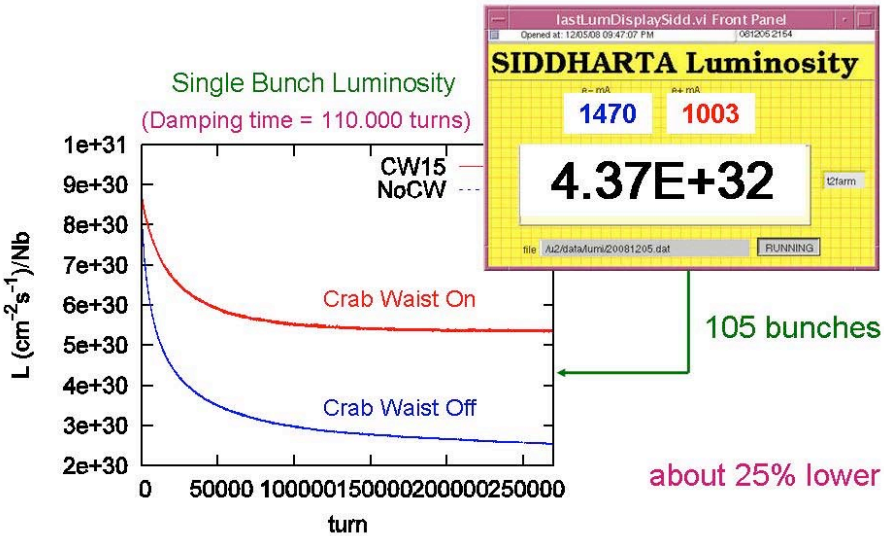


**Figure 5:** Simulated DAΦNE luminosity for CW on (red curve) and off (blue curve) versus number of revolution turns.

As we can see, a high luminosity gain is predicted by the simulations with the crab sextupoles on. However, even with CW on both beams are remarkably blown up and the blow up becomes dramatic when the CW sextupoles are off.

Comparing the numerical result with the best single bunch luminosity of $4.16 \times 10^{30}$ $cm^{-2}s^{-1}$ achieved in collision with 105 bunches, we see that the experimental result is by about 25% lower than the numerical one. In our opinion, this is a good agreement since the very ideal single bunch simulations do not take into account many other factors, both single- and multibunch, affecting the luminosity such as: lattice nonlinearities, e-cloud effects, trapped ions, wake fields, gap transients, hardware noise etc. Indeed, when colliding 20 bunches instead of nominal 105 in order to decrease the influence of the multibunch high current effects we have measured a higher single bunch luminosity of $4.4 \times 10^{30}$ $cm^{-2}s^{-1}$, closer to the ideal simulations.

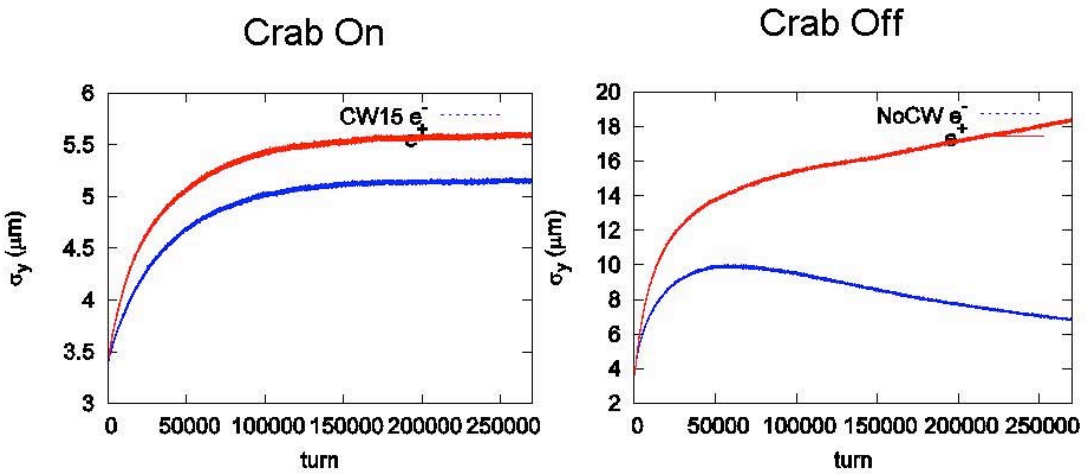


**Figure 6:** Vertical size blow up for CW on (left picture) and CW off (right picture).

Anyway, the maximum luminosity achieved experimentally with the CW sextupoles on is by a factor 1.7 higher that the ideal one predicted numerically for the case of CW sextupoles switched off. This is a clear proof that the crab waist concept works. However, in order to complete the studies we have dedicated several hours tuning the collider with the CW sextupoles off. Fig. 7 shows a comparison of the luminosity as a function of beam current product obtained with crab sextupoles on and off. The maximum single bunch luminosity reached in the latter case was of the order of 1.6-1.7x$10^{30}$ $cm^{-2}s^{-1}$. This result is also consistent with numerical predictions. However, another limitation becomes very important in collision without crab waist sextupoles: besides much bigger vertical blow up, a sharp lifetime reduction is observed already at single bunch currents of 8-10 mA. That is why the blue curve in Fig. 7 is interrupted at much lower currents. A reasonable explanation of the lifetime reduction is given in the next paragraph.

#### *3.2.3.3 Beam-Beam Simulation in a Realistic Lattice*

According to the past DAΦNE experience we learned that both luminosity and especially beam lifetime can be affected by a crosstalk between lattice nonlinearities and beam-beam interactions [22]. In particular, dedicated octupoles installed in DAΦNE in order to correct cubic lattice nonlinearities have been found to be very useful for lifetime improvement in beam-beam collisions [23].

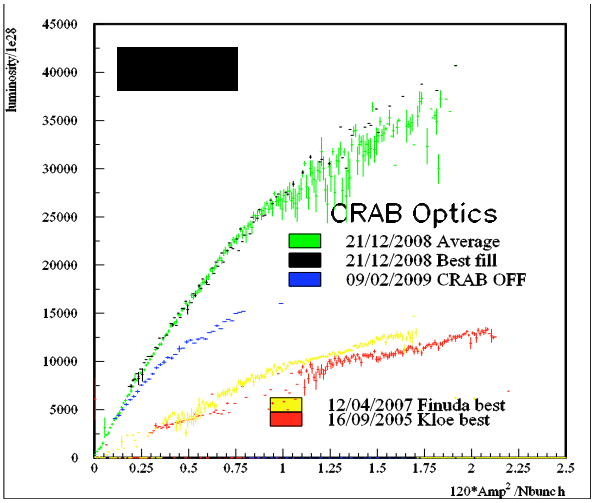


**Figure 7:** DAΦNE measured luminosity as a function of beam current product.

So, in order to estimate the impact of machine nonlinearities on the luminosity performance in the crab waist scheme, we have carried out computer simulations of beam dynamics and luminosity at DAΦNE with a realistic lattice including crab and chromatic sextupoles, damping wigglers, magnet fringe fields etc. During this study the beam-beam interaction simulation was provided by the LIFETRAC code. A tracking of the particles ensemble along the lattice was performed by another software called ACCELERATICUM [24] allowing particles to pass through the variety of storage ring lattice elements in a symplectic way.

Initially we have performed a detailed study of the DAΦNE nonlinear lattice without beam collisions to better understand particle's motion with nonlinear perturbations. In particular, dynamic aperture scans for on- and off-energy particles have been performed in some area around the nominal tune point. As an example, the horizontal (left) and vertical (right) dynamic aperture scans for on-energy particles are shown in Fig. 8.

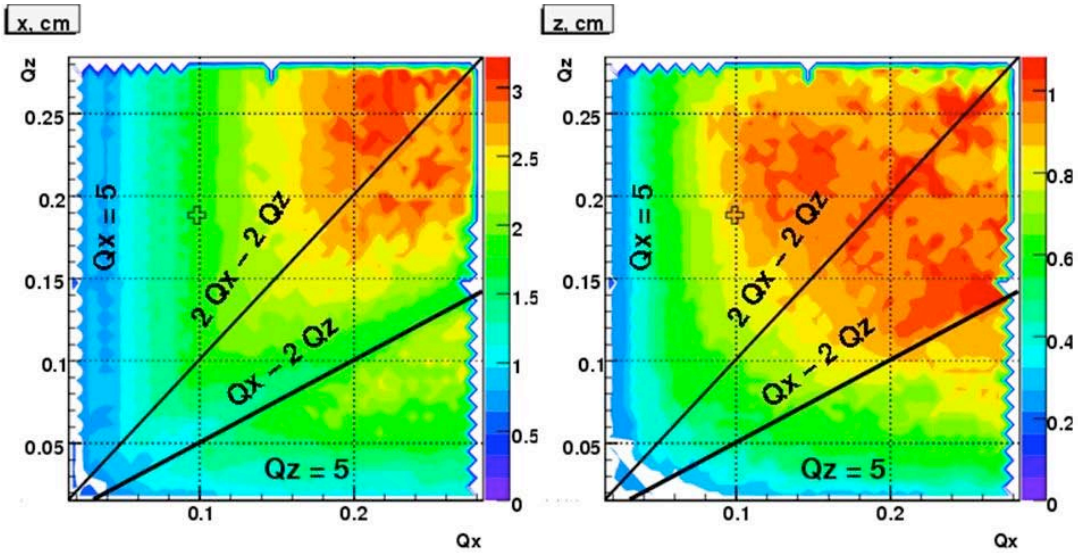


**Figure 8:** Horizontal (left) and vertical (right) DAΦNE dynamic aperture scans (calculated). The numbers on the right side of the scans correspond to the dynamic aperture in cm.

Here we can distinguish typical sextupole-induced resonances Qx = 5, Qx – 2Qy = n, 3Qx = 15, 2Qx – 2Qy = n. The last resonance is not a linear coupling one (there is no coupling errors in the lattice model) but the second order sextupolar coupling resonance coinciding with the linear one. Fortunately, in the vicinity of the present working point marked by a small cross there are no dangerous resonances and the dynamic aperture is reasonably large in both planes, see Fig. 9. As can be seen, the on-energy dynamic aperture exceeds 12 $\sigma_x$, while the vertical one is about 80 $\sigma_y$. The aperture remains reasonable also for energy deviations of +-0.3% corresponding to +-7.5 $\sigma_E$.

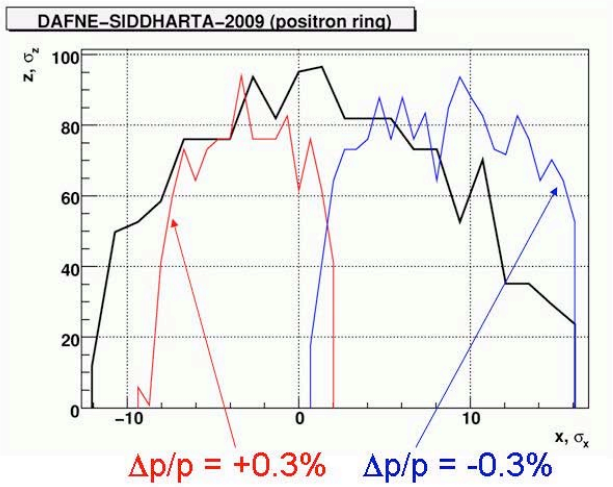


**Figure 9:** DAΦNE on- and off-energy dynamic apertures for the nominal working point (positron beam).

By including beam-beam interactions in the simulation we see that the effect of the lattice nonlinearities is not dramatic for the case of the crab sextupoles on (see Fig. 10). The beam size blow up is only by about 8% higher with respect to the ideal simulations. The beam distribution tails propagate to somewhat higher amplitudes, but still remain confined within the dynamic aperture. No lifetime reduction is indicated by the simulations.

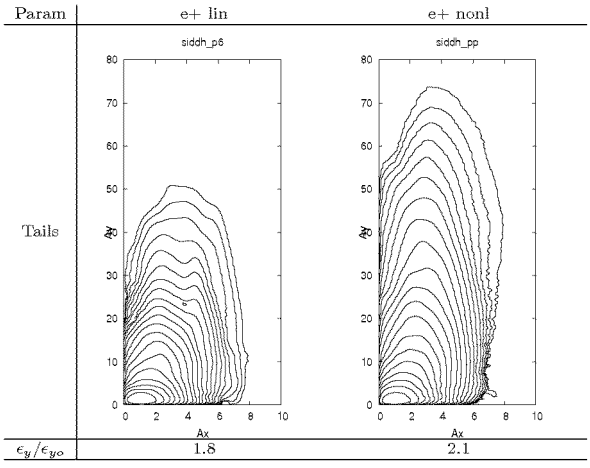


**Figure 10:** Equilibrium densities in the space of normalized betatron amplitudes for linear lattice (left) and realistic nonlinear lattice (right) with crab sextupoles on. Numbers below indicate the vertical emittance blow up.

Instead, in the case of the CW sextupoles off the beam tails are much longer for the nonlinear lattice exceeding 80 $\sigma_y$ in the vertical plane (see Fig. 11) that was estimated to be the dynamic aperture limit. Already at 10 mA per bunch the calculated lifetime sharply drops down in agreement with our experimental observations. However, the luminosity and the vertical emittance blow up still remain comparable for linear and nonlinear lattices even in this case.

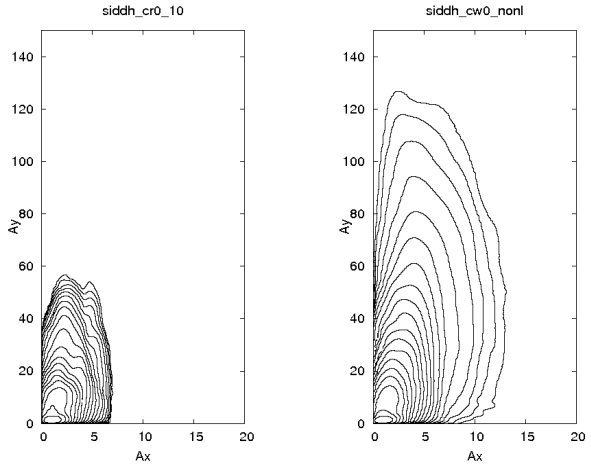


**Figure 11:** Equilibrium densities in the space of normalized betatron amplitudes for linear lattice (left) and realistic nonlinear lattice (right) with crab sextupoles off.

### 3.2.4 Conclusions

Several conclusions can be drawn from these studies:

- The crab waist concept has been proved to work. The ideal strong-strong beam-beam simulations agree within 25% with the results (luminosity) achieved experimentally at DAΦNE. One can expect even better agreement if other factors affecting the luminosity such as: e-cloud, ions, impedances, space charge, errors, noise etc., are included in the simulations.
- Much lower luminosity is achieved with the crab sextupoles off. Besides stronger beam size blow up, a sharp lifetime reduction is observed for bunch currents > 8-10 mA. This is in agreement with beam-beam simulations taking into account the realistic DAΦNE nonlinear lattice.
- The existing beam-beam simulations codes are quite reliable in reproducing and predicting beam-beam performance in present and future e+e- colliders.

### 3.2.5 References

1. P. Raimondi, talk presented at 2nd SuperB Workshop, Frascati, March 2006.
2. C. Milardi et al., "Present status of the DAΦNE upgrade and perspectives", Int.J.Mod.Phys.A24:360-368, 2009.
3. D. Alesini et al., “DAΦNE upgrade status”, Nucl.Phys.Proc.Suppl.181-182:385-389, 2008.
4. C. Milardi et al., this issue of ICFA Beam Dynamics Newsletters.
5. M. Biagini et al, “An introduction to the SuperB accelerator project”, ICFA Beam

Dyn.Newslett.46:193-201, 2008.
6. E. Levichev, “The project of a Tau-Charm factory with crab waist in Novosibirsk”, Phys.Part.Nucl.Lett.5:554-559, 2008.
7. D. Shatilov and M. Zobov, “Beam-beam collisions with an arbitrary crossing angle: analytical tune shifts, tracking algorithm without Lorentz boost, crab-crossing”, ICFA Beam Dyn.Newslett.37:99-109, 2005.
8. K. Hirata, “Analysis of beam-beam interactions with a large crossing angle”, Phys.Rev.Lett.74:2228-2231, 1995.
9. K. Takayama et al, “Superbunch hadron colliders”, Phys.Rev.Lett.88:144801, 2002.
10. F. Ruggiero and F. Zimmermann, “Luminosity optimization near the beam-beam limit by increasing bunch length or crossing angle”, Phys.Rev.ST Accel.Beams 5:061001, 2002.
11. D. Pestrikov, “Vertical synchrobetatron resonances due to beam-beam interaction with horizontal crossing”, Nucl.Instrum.Meth.A336:427-437, 1993.
12. K. Ohmi et al., “Luminosity limit due to the beam-beam interactions with or without crossing angle”, Phys.Rev.ST Accel.Beams 7:104401, 2004.
13. I. Koop, private communications.
14. P. Raimondi, D. Shatilov and M. Zobov, “Beam-Beam Issues for Colliding Schemes with Large Piwinski Angle and Crabbed Waist”, e-Print: physics/0702033.
15. P. Raimondi, D. Shatilov, M. Zobov, “Suppression of beam-beam resonances in crab waist collisions”, in Proceedings of 11th European Particle Accelerator Conference (EPAC 08), Magazzini del Cotone, Genoa, Italy, 23-27 June 2008, pp.2620-2622 (CONFP,C0806233,WEPP045).
16. D. Shatilov, “Beam-Beam Resonances for Different Collision Schemes”, presented at 40th ICFA Advanced Beam Dynamics Workshop on e+e- Factories, BINP, Novosibirsk, Russia, 14-16 April 2008. e-Print: arXiv: 0806.4070 [physics.acc-ph]
17. M. Bona et al., “SuperB: A High-Luminosity Asymmetric e+ e- Super Flavor Factory. Conceptual Design Report”, e-Print: arXiv:0709.0451 [hep-ex].
18. M. Zobov et al., “DAΦNE status and upgrade plans”, Phys.Part.Nucl.Lett.5:560-565, 2008.
19. C. Milardi et al., “DAΦNE operation with the FINUDA experiment”, e-Print: physics/0408073.
20. P. Raimondi, D. Shatilov and M. Zobov, “Beam-beam simulations for particle factories with crabbed waist”, in Proceedings of Particle Accelerator Conference (PAC 07), Albuquerque, New Mexico, 25-29 Jun 2007, pp. 1469-1471.
21. D. Shatilov, “Beam-beam simulations at large amplitudes and lifetime determination”, Part.Accel.52:65-93, 1996.
22. M. Zobov, “Crosstalk between beam-beam effects and lattice nonlinearities in DAΦNE”, e-Print: physics/0311129.
23. C. Milardi et al., “DAΦNE Lifetime Optimization with Compensating Wires and Octupoles”, e-Print: arXiv:0803.1544 [physics.acc-ph].
24. P. Piminov, Master’s Thesis, 2001 (in Russian).

## 3.3 The New DAΦNE Kickers

Fabio Marcellini, David Alesini
INFN- Laboratori Nazionali di Frascati, Via E. Fermi 40, 00044 Frascati, Italy
Mail to: Fabio.Marcellini@lnf.infn.it

### 3.3.1 Introduction

New kickers have been realized for the injection upgrade of the Φ-factory DAΦNE. The main features of these kickers, compared to the previous ones, are:

a) much shorter pulse (≈12 ns instead of ≈150 ns);
b) better uniformity of the deflecting field;
c) lower impedance.

They have been designed to operate with new very fast pulsers (a) and thanks to an accurate shaping of their single components (b) and (c) were obtained [1].

In DAΦNE the much shorter pulse allows perturbing only the injected bunch and the two adjacent ones. This improvement can increase the current threshold of the transverse instability in the DAΦNE rings.

The better uniformity of the deflecting field can increase the injection efficiency at high currents and reduce the background to experiments during injection.

The broadband impedance, according to calculations and measurements, is reduced by a factor 3 with respect to the previous kickers. Moreover, since the new kickers have been designed with the same beam pipe cross section of the dipoles, no taper transition are needed between the dipoles and the kicker and this also contributes to the reduction of the machine impedance.

The new injection system at DAΦNE is, at the same time, a test and a R&D activity of one of the most challenging issues of the International Linear Collider (ILC): the injection/extraction kickers for the damping rings (DR) [2], [3]. The bunch distance in the DR and therefore the choice of the DR circumference are related to the kicker pulse duration; moreover the stability of the beam position at the IP depends also on the kicker pulse stability. Common requirements of ILC DR kickers and DAΦNE kickers are: ultra short rise and fall times, high integrated strength, good uniformity of the deflecting field, and impedances of the structure as low as possible.

Therefore the operation of these new kickers at DAΦNE is an important test for the ILC project, since it should demonstrate with beam measurements the achievement of the system performances.

### 3.3.2 Kicker Design

The kicker has been designed as a two stripline structure (see Fig. 1). The stripline and the surrounding vacuum chamber are properly tapered and each transverse section has constant 50 Ω impedance to match the output impedance of the high voltage pulse generator. Thanks to this geometry and in particular to the stripline tapering, the following results have benn obtained:

a) reduction of the broadband beam coupling impedance and beam transfer impedance of the device;
b) better deflecting field quality with a more uniform transverse deflection as a function of the transverse coordinate (horizontal in particular);
c) improved matching between the generator and the kicker structure at high frequency.

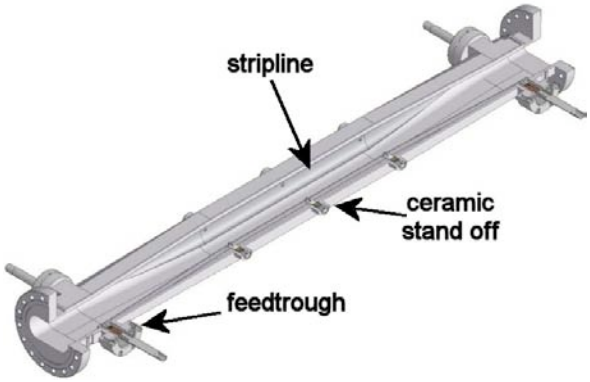


**Figure 1:** Stripline kicker.

The longitudinal and transverse beam coupling impedances have been calculated by simulating the wire method technique of measurement [7]. The longitudinal and the transfer impedance are reported in the Figures 2a and 2b. From the transfer impedance it is possible to evaluate the peak voltage and the average power induced by the beam into the kicker ports for a given beam current. The maximum induced peak voltage on the upstream (output) ports is of the order of 100 V with a 6 nC bunch while the average power induced on the ports is of the order of few tens of Watts with a 2A beam. In longitudinal and horizontal planes there is no evidence of trapped HOMs and the longitudinal loss factor is ~$5 \cdot 10^{-3}$ V/pC for 1 cm bunch length. In vertical plane four trapped HOM ($TE_{11n}$) are found having impedance of the order of few tens of kV per meter. These modes could give, in the worst case of full coupling with beam spectrum lines, growth rates of the order of 1 $ms^{-1}$ at a total current of 2A that are about two orders of magnitude lower than the damping rates provided by the DAΦNE vertical feedback system.

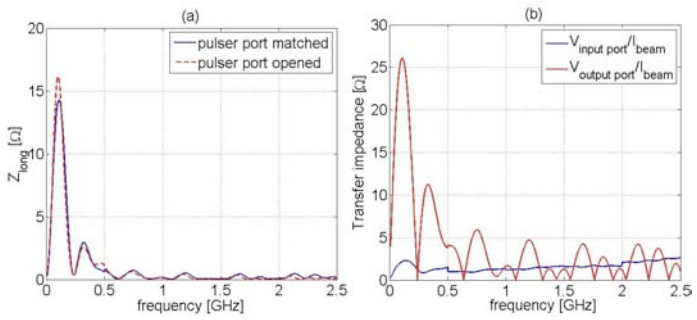


**Figure 2:** (a) longitudinal beam coupling impedance and beam transfer impedance (b) calculated by HFSS [5].

The uniformity of the deflecting field in a generic transverse plane of the kicker depends on the geometry and on the coverage angle of the stripline. As shown in Fig. 3 the coverage angle varies for different section along the stripline taper. Therefore it is possible to optimize the length of the tapers with respect to the stripline straight section to obtain a uniform integrated deflecting field along the horizontal coordinate.

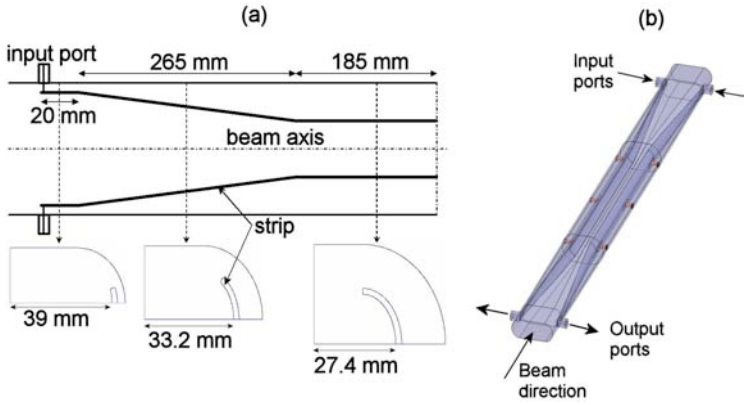


**Figure 3:** Stripline taper coverage angle.

The deflecting field variation as a function of the horizontal and vertical coordinates, as shown in Figures 4(a) and 4(b), is within ±2% over the kicker horizontal aperture (±2.7 cm) and less than 10 % over ±1 cm along the vertical axis.

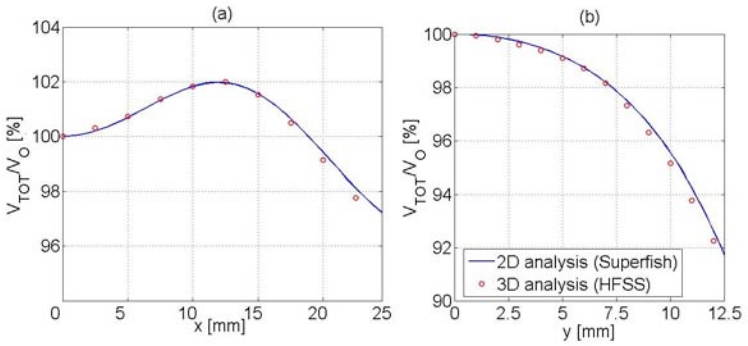


**Figure 4:** Deflecting field as a function of the horizontal (a) and vertical (b) coordinates.

Finally a good matching between the pulse generator and the kicker structure is assured by reducing the stripline section and placing it very close to the kicker vacuum chamber in the coaxial-stripline transition region. This geometry contributes to reduce the longitudinal and transfer impedance of the kicker [4].

### 3.3.3 Operational Experience with the Kicker

After construction, the new kicker was tested and measured in laboratory: Figure 5(a) and 5(b) below show the signal detected at the stripline output when the input was connected respectively with the old long pulse generator, already used with the previous kicker, and with the fast pulse generator produced by FID[6].

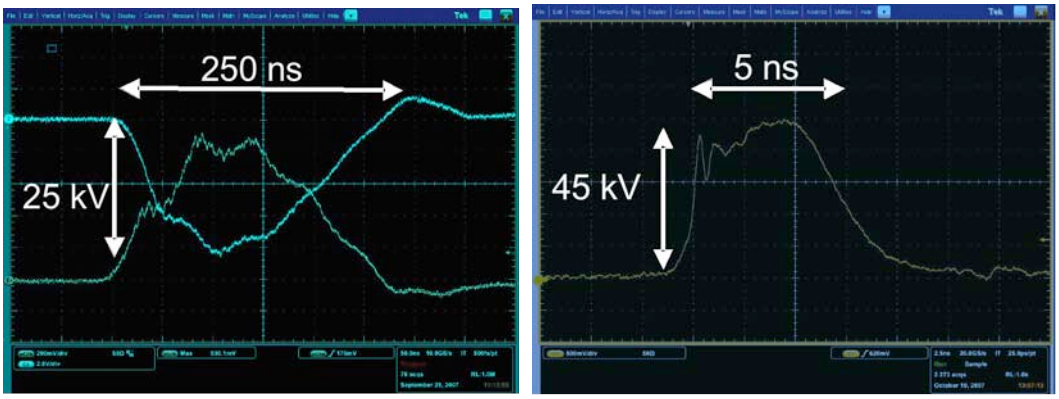


**Figure 5:** (a) stripline signal with input connected with old, long pulse generator (b) stripline signal with input connected with new, fast pulse generator.

The kicker has been designed to be used with the two different generators and the test results confirmed this possibility.

Four new kickers have been installed since November '07 in the DAΦNE storage rings. They always worked properly and never gave problems. For great part of the operation time, they worked with the old long pulse generators in both the rings.

As a matter of fact, the FID fast pulse generators has shown very poor reliability, even after repair and substitution of damaged parts with upgraded ones. For this reason we never had the possibility to use, at the same time, the four FID pulsers on the 2 kickers of the positron ring as scheduled for 2008.

Nevertheless, different "hybrid" configurations were tested, where the two kinds of pulsers were used together, even on the same kicker, connecting each one to a different stripline. Figure 6 illustrate this scheme, while Figure 7 is a snapshot of a scope display where each signal is the sum of the pulses detected at the two stripline outputs. The difference in length between the old generator and the FID pulses results very clearly, while the relative amplitudes are no significant because of the different attenuations on the two channels.

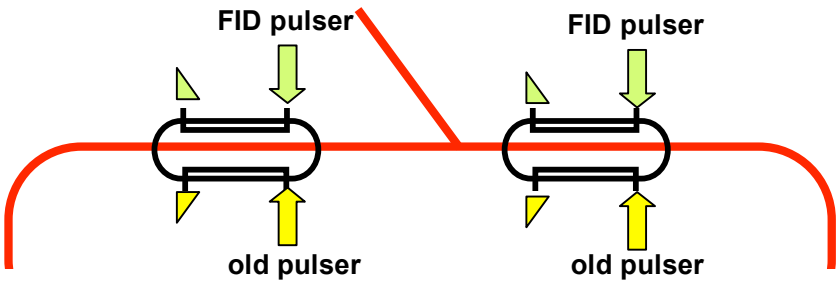


**Figure 6:** The hybrid scheme.

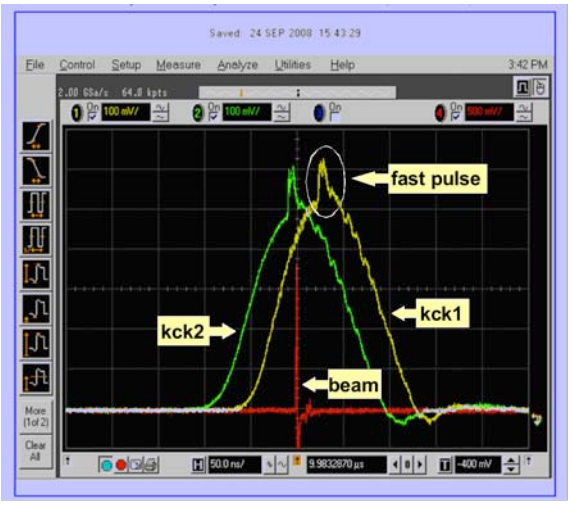


**Figure 7:** Snapshot of a scope display where each signal is the sum of the pulses detected at the two stripline outputs.

Two main results have been obtained testing the hybrid system:

- the injection was successfully tested;
- the perturbation of the fast pulse on the stored beam was measured. The plot in Fig. 8, obtained with the horizontal digital feedback diagnostics, shows the r.m.s. oscillation amplitude of 100 stored bunches with kicker pulse centered on bunch 50. As expected the bunches 49 and 51 takes approximately half the kick maximum amplitude while bunches 48 and 52 are only very little perturbed.

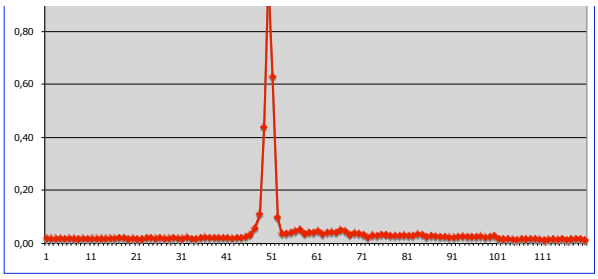


**Figure 8:** r.m.s. oscillation amplitude of 100 stored bunches with kicker pulse centered on bunch 50.

With the aim to overcome the problems related to the FID pulser reliability, it was decided to try a different and more compact FID model. It produces an output pulse having the same shape but a reduced amplitude from 45kV to 24kV. The injection with this lower kick voltage is possible as well, increasing ß function in the kicker region and changing the beam orbit in the septa. Two 24kV units were installed in the electron ring according to the hybrid scheme. Unfortunately, after a month of successfully operation, they also broke. At the moment FID is working on an upgraded version of this pulser that will be tested on DAΦNE as soon as possible.

The new stripline kicker has been also used as an additional kicker for the horizontal feedback. Both the kickers of the DAΦNE positron ring have, at present, one stripline

connected with the old pulser for beam injection and the remaining stripline connected to the amplifiers of the feedback system. Thanks to this configuration we are able to inject the beam and to improve the feedback performance at the same time.

### 3.3.4 Conclusions

The design of the new, fast, stripline kickers for the injection upgrade of the DAΦNE Φ-factory is based on stripline tapering to simultaneously obtain low impedance and an excellent uniformity of the deflecting field. These characteristics are essential also for the Damping Ring of the ILC, then the experience done with the new DAΦNE injection system is and will be, at the same time, an R&D on the Damping Ring injection system.

In DAΦNE the injection with the new kickers has been demonstrated, both using the old long pulse generator and a hybrid system where fast and old pulser are combined. A not yet solved problem concerns the reliability of the fast pulse generators. Work to substantially increase it is in progress.

### 3.3.5 References


1. D. Alesini, et al, DAΦNE Tech. Note I-17, EUROTeV-Report-2006-025, (2006).
2. S. Guiducci, Proc. of PAC05, Knoxville, (USA), (2005).
3. A. Wolski, et al., LBNL–59449, (2006).
4. D.A. Goldberg and G.R. Lambertson, LBL-31664 ESG-160, (1992).
5. http://www.ansoft.com/
6. http://www.fidtechnology.com
7. F. Caspers, "Impedance determination: bench measurements", in Handbook of Accelerator Physics and Engineering edited by A.W. Chao and M. Tigner, World Scientific, 1999.


## 3.4 Horizontal Instability Measurements and Cure in DAΦNE


Alessandro Drago
Istituto Nazionale di Fisica Nucleare,
Laboratori Nazionali di Frascati,
Via E.Fermi, 40 - 00044 Frascati (RM) – Italy
Mail to: Alessandro.Drago@lnf.infn.it


### 3.4.1 Introduction

As well known, DAΦNE is a positron - electron collider working at low energy (1.02 Gev in the center-of-mass) and active since 1997 at Frascati, Italy. DAΦNE has a linac, an accumulator ring, two transfer lines and two ~100 m main rings with 1 or 2 interaction points.

After removing the I.C.E. (Ion Clearing Electrodes) used for the electrons, the two main rings are perfectly symmetric but the storable maximum beam currents are always been very different. No evident limit found for the e- current (I-> 2.4A), whereas the positron current was limited by a strong horizontal instability to ~1.1A (single beam), or

<1.4 A (in collision) in the past years. During this 2008 run, moreover the e+ current has been limited to less than 800mA.

Of course this anomalous behavior has requested new investigations. Measurements have been carried on in many ways but especially using the feedback systems as diagnostics tools to estimate different machine conditions. A solution to control the beam instability has been found and analyzed in the following paragraphs.

### 3.4.2 System and Measurements Description

#### *3.4.2.1 Generality*

In DAΦNE, the positron beam has always shown peculiar characteristics respect to the electron one. In the past year the impedances of the two rings were different due the installation of the I.C.E. in the e- ring. After removal of these devices, the maximum storable beam current has continued to show a strong difference in spite of identical rings. The beam current limit was apparently due to a strong horizontal instability producing loss of e+ current at the end of the bunch train during injection. [1], [2]. This effect has never been shown by the e- beam and moreover during 2008 the positron current limit has become even lower. To try to solve the problem, many measurements have been considered and carried on, but the only really useful technique was to measure the modal grow rates of the positron beam.

This technique could be implemented using a regular spectrum analyzer, but it is much quicker to use the feedback system itself as diagnostic tool, together with offline post-processing software programs developed during the longitudinal bunch-by-bunch feedback collaboration started in the nineties of the last century. They were developed in particular by Shyam Prabhakar [3] for his PhD thesis at SLAC.

The last version of the bunch by bunch feedback system used for the horizontal e+ plane in DAΦNE is the “iGp” (Integrated Gigasample Processor) system, initially developed by a collaboration KEK-SLAC-LNF [4], [5]. This system can download data files [6] that are compatible with the off-line analysis software tools. In the Fig. 1, a real time EPICS [7] plot shows the correct turning off / turning on of the feedback loop during data taking (in the square at the top on the right).

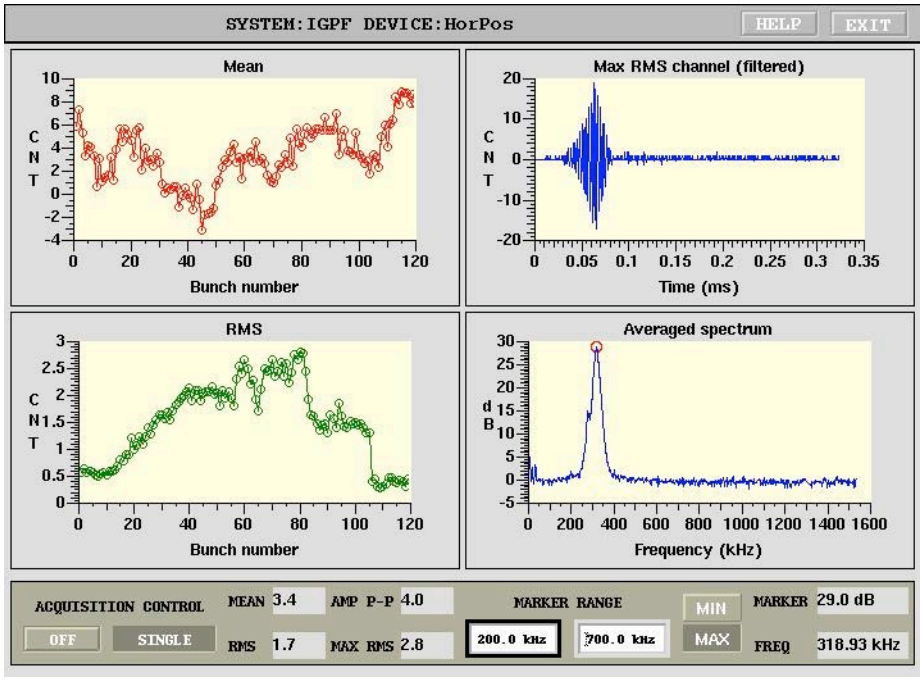


**Figure 1:** Positron grow-damp record made switching off the horizontal feedback, I=575mA, 105/120 bunch [October 14, 2008].

In the Fig. 2, the off-line program output shows the analysis results of the previous grow-damp measurement. In the fourth square the unstable mode is identified as the 119-th mode (i.e. -1 mode) and its grow rate (=63.5 $ms^{-1}$) is estimated. In the sixth square the feedback damping rate is also evaluated (=95 $ms^{-1}$). These data are taken in steady state (stored beam) for a ring with regular optic, whereas during the injection, that is done by horizontal kicks, the instability in the same plane can be even worst.

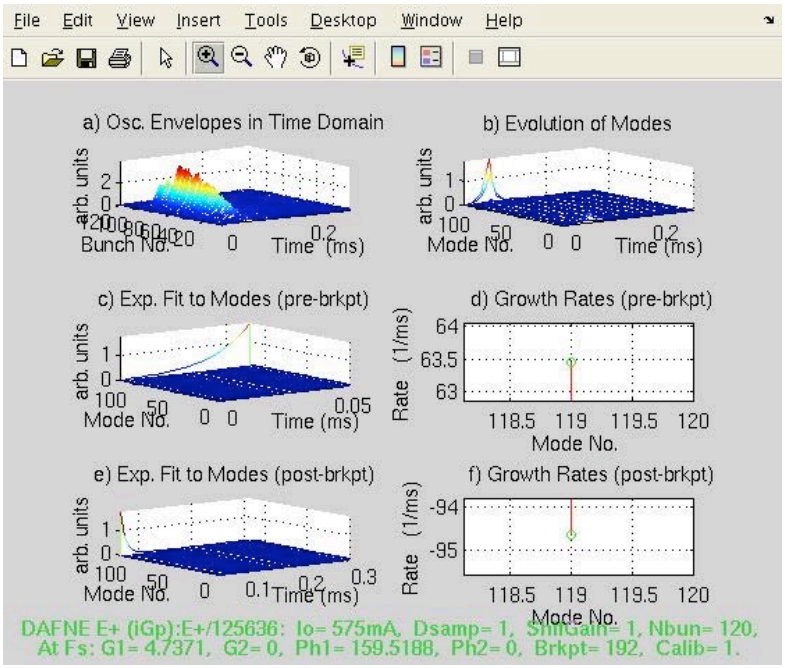


**Figure 2:** Horizontal e+ grow-damp analysis, I=575mA, 105/120 bunches [October 14, 2008].

#### *3.4.2.2 Positron versus Electron Ring Measurements*

Looking at Fig. 3, the horizontal instability behavior versus total beam current is linear in the large range with the same unstable mode. In the past years, troubles were much smaller and the instability grow rates, measured in same conditions, showed 15ms$^{-1}$ at 630 mA in the year 2004 and 25 ms$^{-1}$ at 900 mA in the 2005.

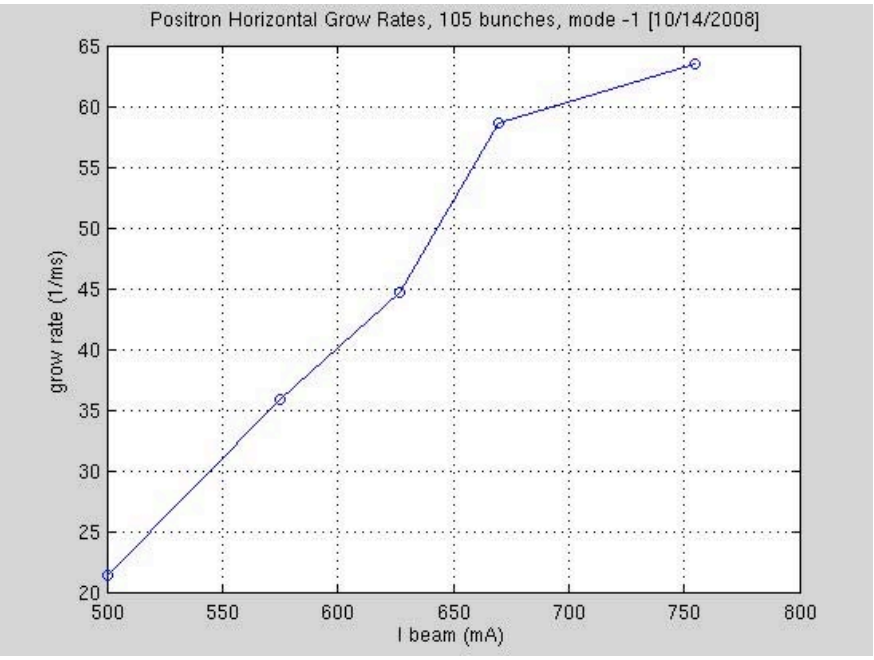


**Figure 3:** horizontal instability grow rate versus positron current.

In the electron ring the measurement system has shown different and much slower unstable mode compared with e+ beam. The Fig. 4 shows the behavior of the instability. The grow rates are much slower and again they are linear versus beam current. At 1500mA the instability grow rate is less than 7 ms$^{-1}$, whereas the feedback system is identical in power and components as well as in measured damping rate to the positron one. In the e- ring the unstable horizontal mode is the number 1. The vertical data (in the same plot, presented by the asterisk) are even slower than the horizontal grow rates. Since impedances and hardware of the two rings are equivalent, the source of such strong instability should be found in the nature of the positron beam that, from models and theory, is foreseen to be sensitive to the e-cloud in the vacuum chamber.

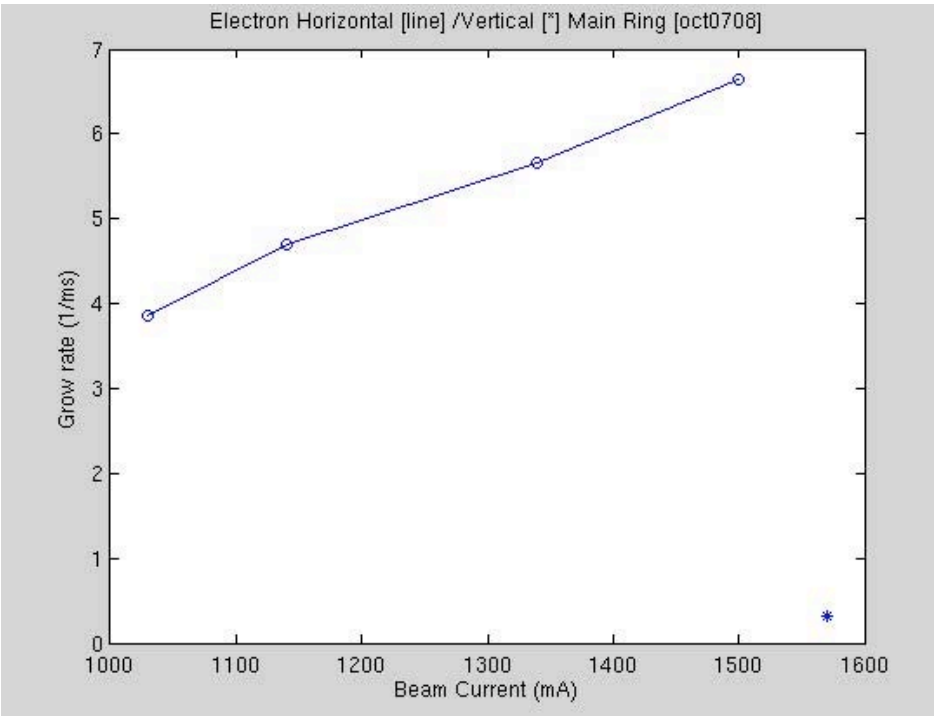


**Figure 4:** Electron horizontal instability grow rates versus beam current [October 7, 2008].

#### *3.4.2.3 Positron Ring Measurements versus Machine Parameters*

To characterize better the e+ instability, understanding not only the anomalous behavior but also the causes, studies to restrict the possible sources of instability have been carried on, in particular grow-rate measures in the following conditions:

- Solenoids turned on/ turned off [Oct 03 2008]
- Varying the βx in the RF cavity [Oct 23 2008]
- Increasing Δνx in PS1-PS2 zones, by +0.5 [Nov 04 2008]
- Increasing Δνx in RCR zone, with a total of +1 [Nov 05 2008]
- Varying the orbit in the dipoles [Nov 10 2008]

First of all, switching off the solenoids installed in the positron ring, the grow rates of the e+ instability does not change. This can be due to the fact that in DAΦNE solenoids have been installed only in straight section for the limited space and not in the wigglers and the dipoles, so they seems ineffective, at least in the horizontal plane. Vertical measurements for this condition have not been done.

As second test, the βx in the RF cavity was halved, passing from 4 m to 2 m, to test the hypothesis of a high order mode eventually driven by the radiofrequency system. Also in this case, no variations were measured for the instability grow rates.

The following tests have been done about variations of the horizontal tune. In particular the e+ instability grow rates have been measured versus Δνx in PS1-PS2 and RCR ring zones with the following optic condition (see Fig. 5):

- Collision (regular) optic ➔ mode m = -1 (blue)
- Δνx = + 0.5 (PS1÷PS2) , νx = νy ➔ mode m = 0 (red)
- Δνx = + 1.0 (0.5 in PS1÷PS2 0.5 in RCR), νx = νy ➔ mode m = -1 (cyan)

This is to study the e+ instability as a function of the relative betatron phase advance between the wigglers. As shown in the Fig. 5, no evident behavior variations have been found.

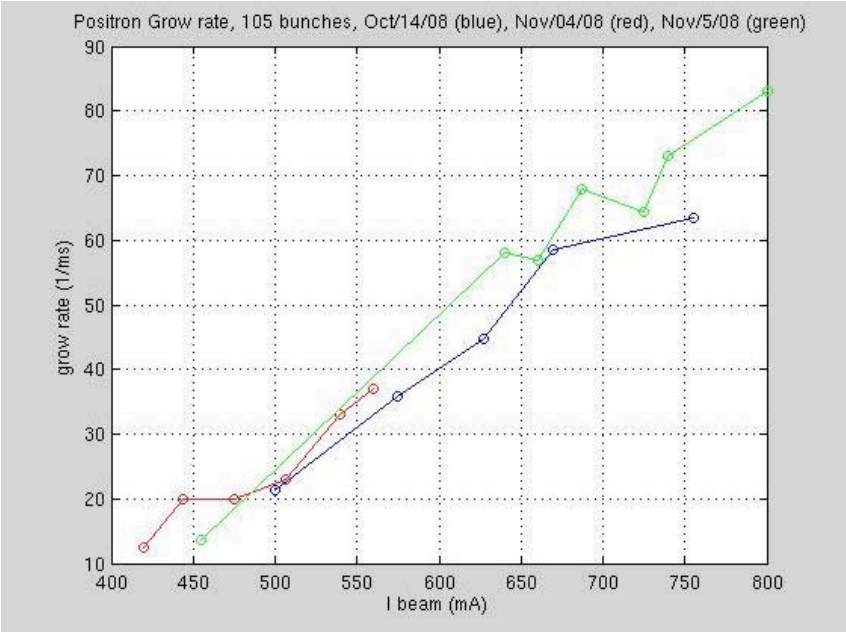


**Figure 5:** e+ instability grow rates versus Δνx in PS1-PS2 and RCR.

Then the e+ instability grow rates versus orbit in the main ring dipoles have been evaluated. The orbit variation is performed applying a closed orbit bump in the dipoles and recovering the beam energy variation by the RF frequency (Fig. 6).

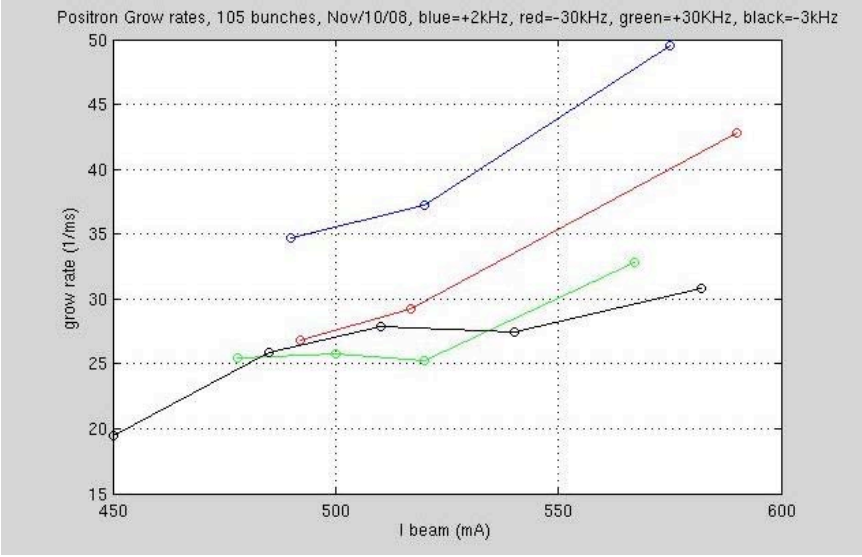


**Figure 6:** e+ instability grow rates versus orbit in the main ring dipoles.

In this case, the e+ instability grow rates show huge and meaningful differences versus orbit in the main ring dipoles that were slightly rotated in the last year. The e-cloud hypothesis seems to be confirmed and the source is just inside the dipole zones.

### 3.4.3 An Effective Cure

The measurements done have shown the linear behavior of the horizontal instability, that is >70 $ms^{-1}$ for beam current >800mA. Considering the further energy given to the instability by the injected charge, kicked in the horizontal plane, the measurement results seem to give a clear indication to increase the feedback power. Using the spare power amplifiers it was possible to double final stage from 500W to 1kW, but the power combiners to join other two 250W amplifiers were to be ordered. Moreover the simple doubling of the output power is not equal to double the feedback effect in term of damping rate. In alternative, a much more promising choice was to test another pickup (to see if less noisy) and to use the spare striplines of the injection kickers with the new power amplifiers.

Of course in this way, the feedback betatron phase advance would have been different from the first system, and it has been necessary to use a second horizontal feedback processing unit to elaborate the bunch by bunch correction signal. Besides to double effectively the voltage applied to the positron beam, this approach has the advantage to kick two times in a turn making a quicker correction. The Fig. 7 shows the performances of the two systems.

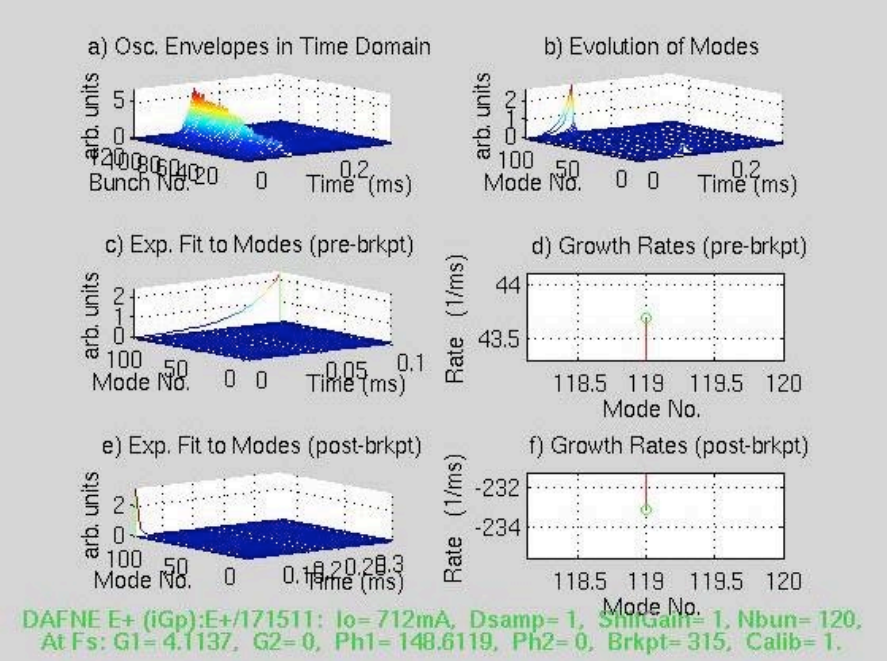


**Figure 7:** Double horizontal e+ feedback performance.

With this implementation, the feedbacks show that:

- The damping times of the two feedbacks add up linearly
- The damping times measured are:
- ~127 ms-1 (1 FBKs) ➔ fb damps in ~25 revolution periods (~8 us)
- ~233 ms-1 (2 FBKs) ➔ fb damps in ~13 revolution periods (~ 4.3 us)

A result that could seem apparently trivial but that, on the contrary, is very important from a practical point of view for the applications to new feedback designs and to manage new unexpected instabilities.

### 3.4.4 Conclusions

The HOM problems (RF cavity, Bellows Scrapers etc...) seem ruled out. It seems evident that the beam current limit in the e+ ring is due to an e-cloud induced instability. The instability strength is reduced by optimizing the orbit in the new dipoles.

The instability grow rates show a good agreement with e-cloud model and simulations.

More power on the horizontal e+ feedbacks help in keeping e+ current as higher as possible, reached 1.1A well controlled. Two separate feedback systems for the same oscillation plane work in perfect collaboration doubling the damping time. The feedback damping time has achieved 4.3 microsecond corresponding at ~13 revolution turns.

Further investigations at even higher beam currents can improve the knowledge of the instability behavior. The beam current does not seem limited by the horizontal instability. Grow rates at higher e+ current have shown that the unstable mode changes and becomes slower, as in the Fig. 8.

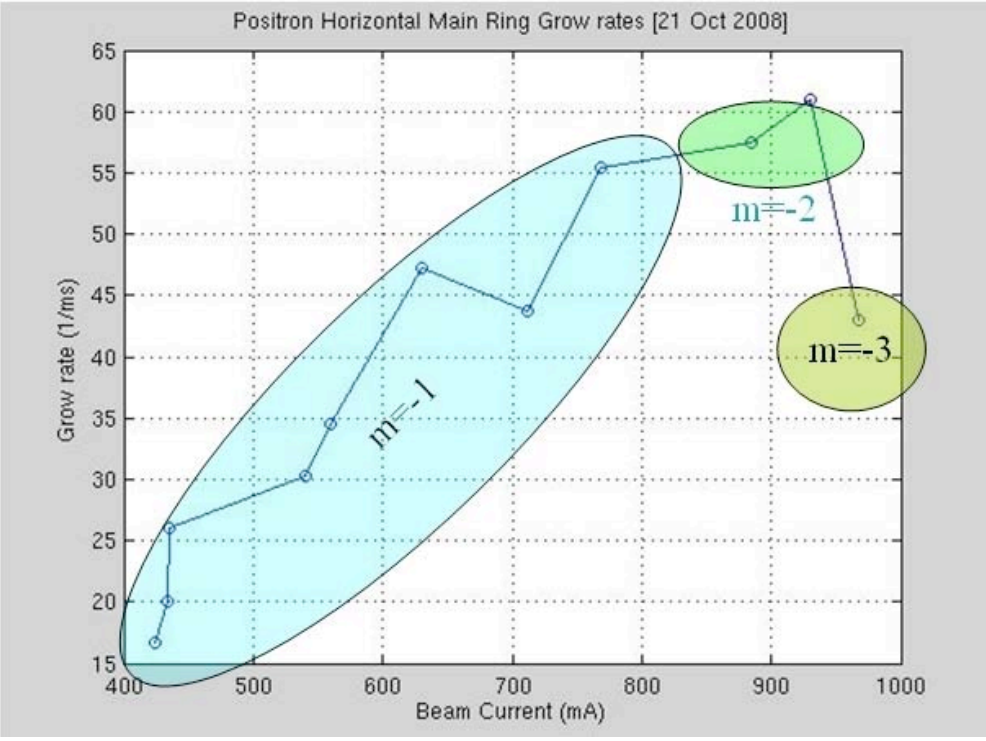


**Figure 8:** e+ horizontal modes and grow rates.

### 3.4.5 Acknowledgements

Concluding this paper, the author wants to thank all the DAΦNE Team, and especially M. Zobov, P. Raimondi, C. Milardi, D. Alesini, F. Marcellini, T. Demma, S. Guiducci, M. Biagini, M. Boscolo, C. Vaccarezza, A. Stella, A. Gallo, O. Coiro, and many many others.

The author wants to remember also all the researcher involved in the last 15 years in the bunch by bunch feedback collaboration, two or three different design generations from SLAC, KEK, DAΦNE/Frascati, ALS/Berkeley, Bessy: in particular Shyam Prabhakar and Dmitry Teytelman, John Fox, Makoto Tobiyama, F. Marcellini, W. Barry, J. Olsen, Claudio Rivetta, J. Flanagan, Shaukat Khan, and many others.

### 3.4.6 References

1. Alessandro Drago: "Horizontal Instability and Feedback Performance an DAΦNE e+ Ring", LNF-04/18(P), 30/07/04. EPAC-2004. -THPLT056, Oct 2004. 3pp. In the proceedings of 9th European Particle Accelerator Conference (EPAC 2004), Lucerne, Switzerland, 5-9 Jul 2004. Published in Proceedings of EPAC 2004, Lucerne, Switzerland:2610-2612,2004.
2. A. Drago, M. Zobov, INFN-LNF; Dmitry Teytelman, SLAC: "Recent Observations on a Horizontal Instability in the DAΦNE Positron Ring", Presented at the 2005 Particle Accelerator Conference (PAC2005), Knoxville, Tennessee, USA - May 16-20, 2005. Published in 2005 Particle Particle Accelerator Conference: Proceedings. pp. 1841-1843. LNF-05/26 (P), 20/12/2005. SLAC-PUB-11654, PAC-2005-MPPP024, Nov 2005. 3pp.
3. Shyam Prabhakar, "New Diagnostics and Cures for Coupled-Bunch Instabilities", PhD Thesis, SLAC-Report-554, pp. 191, August 2001.
4. Dmitry Teytelman, "Architectures and Algorithms for Control and Diagnostics of Coupled-Bunch Instabilities in Circular Accelerators", PhD Thesis, SLAC-Report-633, pp. 181, June 2003.
5. D. Teytelman, R. Akre, J. Fox, A.K. Krasnykh, C.H. Rivetta, D. Van Winkle (SLAC, Menlo Park), A. Drago (INFN/LNF, Frascati), J.W. Flanagan, T. Naito, M. Tobiyama (KEK, Ibaraki): "Design and Testing of Gproto Bunch-by-bunch Signal Processor", THPCH103, contributed to European Particle Accelerator Conference (EPAC 06), Edinburgh, UK, 26-30 Jun 2006. Published in *Edinburgh 2006, EPAC* 3038-3040.
6. Dmitry Teytelman, "iGp-120F Signal Processor- Technical User Manual", Rev.1.6. Dimtel, Inc., Sept.19, 2008. S.Jose', CA, USA. http://www.dimtel.com/support/manuals/igp
7. http://www.aps.anl.gov/epics/

## 3.5 Touschek Backgrounds Experience at DAΦNE

Manuela Boscolo
INFN, Laboratori Nazionali di Frascati, Via E. Fermi 40, 00044 Frascati, Italy
Mail to: manuela.boscolo@lnf.infn.it

### 3.5.1 Introduction

The DAΦNE machine induced backgrounds into the experiments as well as the beam lifetime are dominated by the Touschek effect, due to the dense beams at relatively low energy. It consists of a single Coulomb scattering which leads to an immediate loss of the two colliding particles due to the energy transfer from the transverse to the longitudinal direction with the relativistic effect of momentum change amplification. Off-momentum particles can exceed the momentum acceptance given by the radio-frequency (RF) bucket, or may hit the aperture when displaced by dispersion.

A dedicated simulation for the Touschek scattering has been developed for handling both the lifetime and the backgrounds dominated by this effect. In the following paragraph there is a brief description of this simulation code.

A discussion on Touschek lifetime with the crab waist (CW) configuration scheme and a description of how Touschek background has been minimized in the SIDDHARTA detector is done in the last section.

### 3.5.2 Simulation Tool for the Touschek Effect

The Touschek simulation code is based on the Monte Carlo technique and it has been developed for handling DAΦNE lifetime and particle losses, resulting very useful for understanding the critical beam parameters and optics knobs [1-2].

The generation of the scattering events in the simulation code is done continuously all over the ring, averaging the Touschek probability density function on every three machine elements. Touschek particles are extracted randomly within one transversely Gaussian bunch with the proper energy spectra and beam sizes, and then tracked over many turns or until they are lost, checking at every turn whether they exceed the RF or the physical acceptance. If the scattered particle is lost during tracking then its transverse positions and divergences are recorded all the way from the longitudinal position where the scattering takes place to where it gets lost. Particle tracking is usually performed for many machine turns.

An accurate analysis of the critical positions where Touschek particles are generated –mainly dispersive regions- can be performed, together with the optimization of collimators, both for finding the optimal longitudinal position along the ring and the optimal radial jaw position. In fact, in DAΦNE, each collimator has an external and an internal jaw that can be separately inserted in the vacuum pipe.

An accurate analysis can be done on the IR particle losses, determining for example upstream and downstream rates, transverse phase space and energy deviation of these off-energy particle losses as a function of different beam parameters, of different optics and for different sets of movable collimators.

The Touschek lifetime can be evaluated straightforwardly from the ratio between the initial number of particles per bunch N and the total particle losses $\dot{N}$, i.e. $\tau = N/\dot{N}$.

A realistic tracking of the off-energy particles should include the main non-linear terms present in the magnetic lattice. This is particularly true for machines with long damping time like DAΦNE, due to the low energy and small length, as resonances that may be excited by nonlinearities can have an effect on the beams for a long time. In benchmarking the simulation code with measurements it has been found that not only sextupoles have to be included in the tracking but also strong non linear terms. With the present CW lattice tracking simulation takes into account the decapole and dodecapole term present in wigglers poles, as obtained by fitting the wigglers magnetic measurements [3].

**Table 1:** Beam parameters for KLOE (2006) and SIDDHARTA (2008-2009) runs.

| *Parameters* | *Standard scheme (KLOE run)* | *CW scheme (Nominal)* |
|---|---|---|
| $\beta_x$*(m) | 1.5 | 0.2 |
| $\beta_y$*(mm) | 18 | 6 |
| $\sigma_x$(μm) | 700 | 200 |
| $\sigma_y$(μm) | 15 (blow-up) | 2.4 |
| $\sigma_z$ (cm) (for $I_b$=13 mA) | 2.5 | 2.0 |
| $\varepsilon_x$ (mm mrad) | 0.3 | 0.2 |

### 3.5.3 Touschek Effect with the Crab Waist Scheme

The important features from the Touschek effect point of view for the new CW lattice are the smaller emittance and the smaller beam sizes especially at the IP. In fact, lifetime scales linearly with bunch dimensions: $\tau \propto \sigma_l \sigma_x \sigma_y$. Table 1 shows the parameters for the standard scheme during the KLOE run and for the nominal CW collision configuration. Touschek measured lifetime is now shorter than before, as confirmed also by simulations. Moreover, also particle losses inducing backgrounds result higher; the remedies to counteract this effect on the detector are discussed below.

**Table 2:** Latest beam parameters with the CW scheme relevant to Touschek scattering.

| $N_{part}$/*bunch* | $2 \cdot 10^{10}$ |
|---|---|
| $I_{bunch}$ (mA) | 10 |
| $\varepsilon_x$ (mm·mrad) | 0.26 |
| $\sigma_z$ (cm) | 1.6 |
| Coupling (%) | 0.1-1.1 |
| $\beta_x$*(m) | 0.27 |
| $\beta_y$*(mm) | 9 |

During the summer 2008 the CW scheme has been implemeted in DAΦNE [4]. First simulations of Touschek scattering have been performed with an ideal CW optics [5]. Simulations predicted for the two IR collimators new positions with higher efficiency in rejecting scattered particles according to the new lattice. The IR1 collimator has been

placed at 8 m upstream the IP, while the IR2 collimator has been moved downstream the old IP2, at a position with low $\beta_x$ and high horizontal dispersion, both resulting very efficient as expected.

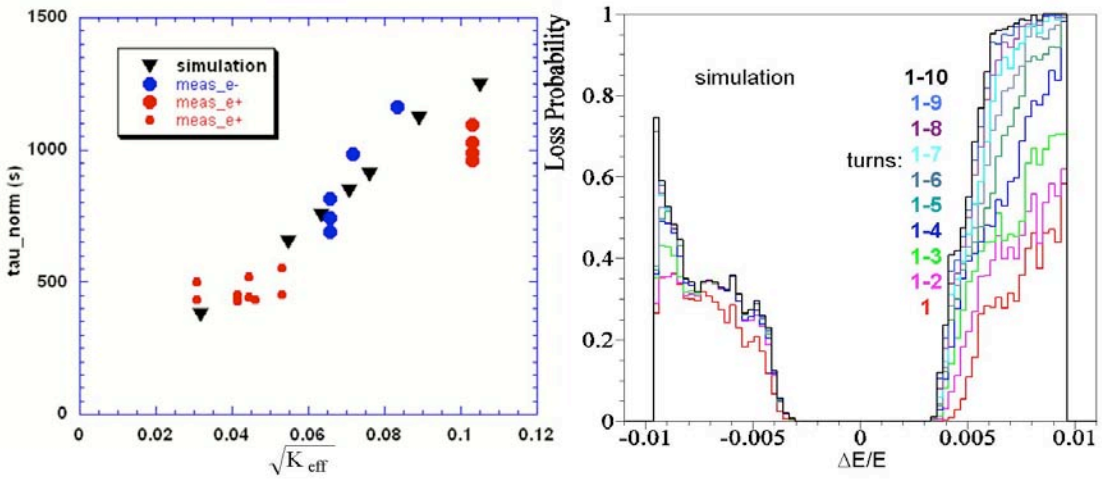


**Figure 1:** Left plot: comparison of the calculated (black dots) and measured lifetime for e+ and e- (red and blue markers, respectively) for different coupling values. Total beam current was Itot ≅ 100 mA with 10 bunches. Right plot: energy acceptance of Touschek particles resulting from simulation for the different machine turns, from the first to the tenth one.

New simulation studies have been performed with the actual beam parameters (see table 2) and with the latest CW optics used during high luminosity runs, including sextupoles at the set current and the nonlinear kick in wigglers central poles, as discussed in the previous paragraph.

The resulting simulated Touschek lifetime is as short as $\tau \cong 840$ s for a 0.5% beam coupling. This result is in agreement with measurements, as appears from left plot of Figure 1, which shows the normalized measured lifetime for both beams and the calculated one as a function of the square root of the effective beam coupling. Black markers refer to simulation while blue and red ones to electrons and positrons measured lifetimes, respectively. Larger and smaller markers refer to larger and smaller coupling. The plotted lifetime is normalized to the total current: $\tau_{norm} = \tau_{mis}(I/I_0)^{2/3}$, according to the scaling law $\tau \propto \sigma_l \sigma_x \sigma_y / I$ where $\sigma_l$ is the current dependent bunch length $\sigma_l \propto I^{1/3}$. Beam coupling is evaluated at the synchrotron light monitor from the measured transverse sizes and from the ratio $\beta_y/\beta_x$=2.25, as indicated by the MAD [6] optical model. The effective vertical beam size used for the evaluation of the effective coupling $K_{eff}$ takes into account its measurement resolution of 80 μm [7].

Right plot of figure 1 shows the simulated energy acceptance of the Touschek particles tracked for ten turns for the corresponding lifetime plotted by the black markers on the left plot.

Many efforts have been put in the Touschek background reduction during the runs of all the experiments that have been taking data at DAΦNE: KLOE, FINUDA, DEAR and presently SIDDHARTA, a gas detector sensitive also to low energy photons shown in Figure 2 together with the luminosity monitors.

For counteracting the background induced by the high rates of particle losses in the detector, shieldings have been successfully implemented between the IP and QD0, outside the beam pipe as shown in left plot of Figure 3.

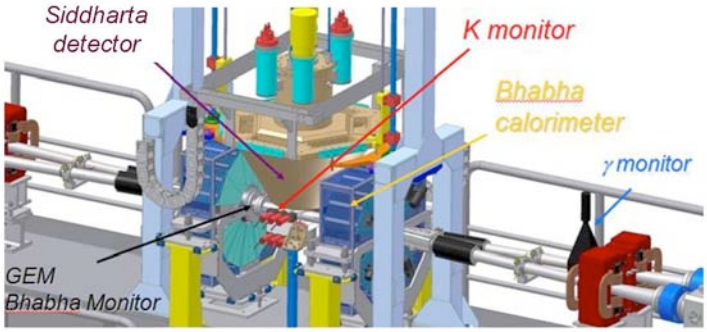


**Figure 2:** Overview of the upgraded DAΦNE IR1 showing the SIDDHARTA detector together with the various luminosity detectors.

They consist of two parts: one is made of lead and has a *soyuz* shape and a second one made of tungsten with *sputnik* shape. They have been very effective. Additional lead shielding has been added vertically above the IP (shown in right plot of figure 3) to mask residual secondaries reaching the gas target. Moreover, lead bricks in front of the IR1 collimator have been added to prevent showers from rejected particles to reach the IR. Finally, a signal to noise ratio of the order of 12 has been obtained, that is a better value than what obtained during the DEAR run.

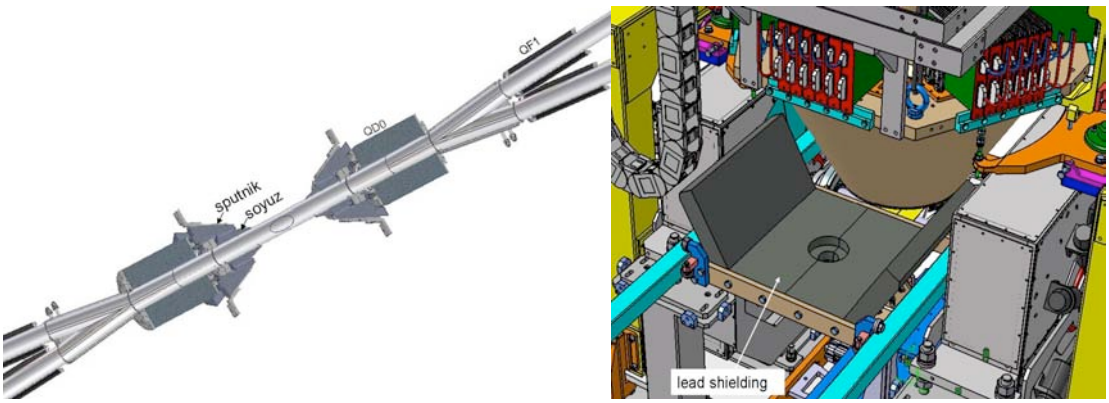


**Figure 3:** Left plot: Section of the IR: it is shown the lead soyuz and tungsten sputnik shielding between QD0 and IP. Right plot: lead shielding between IP and SIDDHARTA.

Together with a careful design of the shielding around the IR pipe, in order to be efficient in cutting secondaries from Touschek particle losses without reducing detector acceptance, adiabatic adjustments of the optical parameters, sextupoles tuning and orbit optimization, especially at the IR, are always important knobs to handle backgrounds.

Background is also an issue for the luminosity measurements. Two detectors, a gamma monitor and a Bhabha calorimeter (shown in figure 2), are used to measure single Bremsstrahlung and small angle Bhabha rates, respectively [8]. Dedicated studies have been performed for these detectors, to measure accurately luminosity and backgrounds, with particular care for the gamma monitor, being set along the beamline.

Touschek background particles have been tracked with GEANT4 from the loss point in the beam pipe (see these IR losses in left plot of figure 4) to the gamma monitors for a full simulation, in order to compare simulated rates to measured ones [9]. Preliminary analysis gives an agreement between measured rates at the gamma monitor and GEANT4 simulations within 50%. Upper right plot of figure 4 shows the full trajectories particles eventually lost at the IR with the collimators inserted in red and below plot shows the distribution of total losses, indicating collimators efficiency.

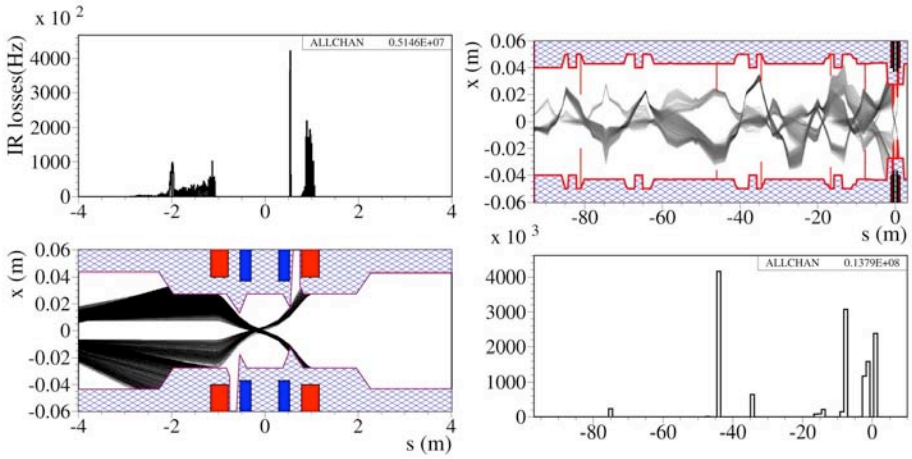


**Figure 4:** Left: Distribution (upper) and trajectories (below) of Touschek particles lost at IR. Right: full trajectories of Touschek particles lost at IR (upper) and full distribution of losses indicating collimators efficiency (below).

Future plan foresees the KLOE roll back in next fall 2009. Studies of the proper shielding to prevent background contamination in the physics events are in good progress.

### 3.5.4 References


1. M. Boscolo, S. Bertolucci, C. Petrascu, S. Guiducci, G. von Holtey, “Experience with Beam Induced Backgrounds in the DAΦNE Detectors”, Proceedings of the 2001 IEEE Particle Accelerator Conference, Chicago, USA (2001), p.2032.
2. M. Boscolo, M. Antonelli, S. Guiducci, “Simulations and Measurements of the Touschek Background at DAΦNE”, Proceedings of the 8th European Particle Accelerator Conference (2002) p.1238.
3. DAΦNE Technical Note MM-34, January 2004.
4. C. Milardi, this issue.
5. M. Boscolo, M. Biagini, S. Guiducci and P. Raimondi, “Touschek Background and Beam Lifetime Studies for the DAΦNE Upgrade”, Proceedings of the 2007 Particle Accelerator Conference, Albuquerque, USA (2007) p. 1454.
6. CERN Report CERN/SL 90-13 (AP) (1995).
7. DAΦNE operation logbook 2/4/2008 p.58.
8. M. Boscolo et al, "Luminosity Measurement at DAΦNE for Crab Waist Scheme", Proceedings of EPAC08, Genoa, Italy (2008), p. 1203.
9. Work in progress in collaboration with the *LUMI* group.

## 3.6 Electron Cloud Simulations for DAΦNE

Theo Demma
Istituto Nazionale di Fisica Nucleare-Laboratori Nazionali di Frascati,
Via E. Fermi 40, I-00044 Frascati (Rome) Italy
Mail to: Theo.Demma@lnf.infn.it

### 3.6.1 Introduction

After the 2003 shutdown for the FINUDA detector installation, and some optics and hardware modifications, the appearance of a strong horizontal instability for the positron beam at a current I ≈ 500mA, triggered the study of the e-cloud effect in the DAΦNE collider. Experimental observations that seem to provide an evidence that the electron cloud effects are present in the DAΦNE positron ring can be summarized as follow: a larger positive tune shift is induced by the positron beam current [1]; the horizontal instability rise time cannot be explained only by the beam interaction with parasitic HOM or resistive walls and increase with bunch current [2]; the anomalous vacuum pressure rise with beam current in positron ring [3], bunch-by-bunch tune shifts measured along the DAΦNE bunch train present the characteristic shape of the electron cloud build-up [4]. There are also indications that wigglers play an important role in the instability, since the main changes after the 2003 shutdown were the modification of the wiggler poles, and lattice variation which gave rise to an increase of the horizontal beta functions in wigglers [5]. To better understand the electron cloud effects and possibly to find a remedy, a detailed simulation study is undergoing. In this paper we present recent simulation results relative to the build up of the electron cloud in the DAΦNE wiggler and in straight sections in presence of a solenoid magnetic field. Then we estimate the electron cloud induced multi-bunch instability in the DAΦNE positron ring. When possible, simulation results are compared to experimental observations. Conclusions follow in the last section.

### 3.6.2 Electron Cloud Build Up

Photoemission and/or ionization of the residual gas in the beam pipe produces electrons, which move under the action of the beam field, their own space charge, and any magnetic field . These primary electrons are accelerated by the beam, gain energy, and strike the chamber again, producing more electrons. The secondary electron yield, the number of emitted electrons per impinging electron (SEY) of typical vacuum chamber materials, can be larger than 1 even after surface treatment, leading to an amplification of the cascade. This amplification is counterbalanced by the action of the own space charge of the electrons, and a saturation is reached.

A number of sophisticated computer simulation codes, (e.g., PEI[8], POSINST[9], and ECLOUD [10]), have been developed to study the e-cloud effect, and their predictions have been compared with experimental observations. To study the build up of the electron cloud in the DAΦNE positron ring the code ECLOUD has been used.

The input parameters for ECLOUD are collected in Table 1. The reflectivity and photo-emission yield values have been obtained by measurements performed on Al samples with the same finishing of the actual vacuum chamber [11]. The secondary emission yield (SEY) curve model used is the one described in [12] scaled to an elastic reflection probability at zero electron energy of 0.5 [13], and with a maximum value $\delta_{max} = 1.9$ as were found for technical Al surfaces after electron conditioning [14].

**Table 1:** DAΦNE beam and pipe parameters used as input for ECLOUD simulations.

| *Parameter* | *Unit* | *Value* |
|---|---|---|
| bunch population $N_b$ | $10^{10}$ | 2.1 |
| number of bunches N | … | 100 |
| missing bunches $N_{gap}$ | … | 20 |
| bunch spacing $L_{sep}$ | m | 0.8 |
| bunch length $\sigma_z$ | mm | 18 |
| bunch horiz. size $\sigma_x$ | mm | 1.4 |
| bunch vert. size $\sigma_y$ | mm | 0.05 |
| hor./vert. betatron tunes $_x/\nu_y$ | … | 5.1/5.1 |
| hor./vert. average beta functions $\beta_x/\beta_y$ | m | 4.1/1.1 |
| wiggler cham. horiz. aperture $2h_x$ | mm | 120 |
| wiggler cham. vert. aperture $2h_y$ | mm | 20 |
| straight sections radius | mm | 44 |
| primary photo-emission yield $d\lambda/ds$ | … | 0.0088 |
| photon reflectivity | … | 50% |
| maximum SEY $\delta_{max}$ | … | 1.9 |
| energy for max. SEY $E_{max}$ | eV | eV 250 |

#### *3.6.2.1 Build Up in the Wiggler*

The wiggler magnetic field characterization was performed measuring the vertical magnetic field component $B_y$, over a rectangular point matrix on the x-z plane [6]. Starting form these values a spline fit was performed and the obtained coefficients were used for the field reconstruction as showed in [3]. This method has been applied to build three models of the wiggler field, the first corresponding to the wiggler before the pole modification in 2003, the second corresponding to the field after the pole modification (currently installed at DAΦNE), and the third corresponding to a further modification of the wiggler recently proposed to improve field quality and reduce nonlinearities [7].In Figure 1 the field reconstruction results are reported for the three different models.

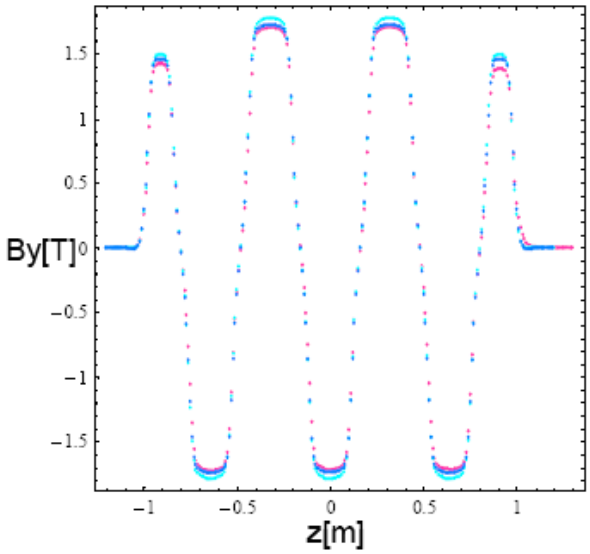


**Figure 1:** Vetical component of the magnetic field along the longitudinal axis for the old (blue), current (red), and recently proposed (cyan) wiggler.

Using these models of the DAΦNE wiggler field, the electron build-up was simulated. It has to be noted that the presence of the slots has been taken into account considering only the photon flux that is not intercepted by the antechamber (~5%). With this prescription part of the electrons are emitted at the position of the antechamber slots. However, since in a dipole magnetic field these electrons contribute little to the multipacting and the electron build up, this approximation does not introduce any noticeable error.

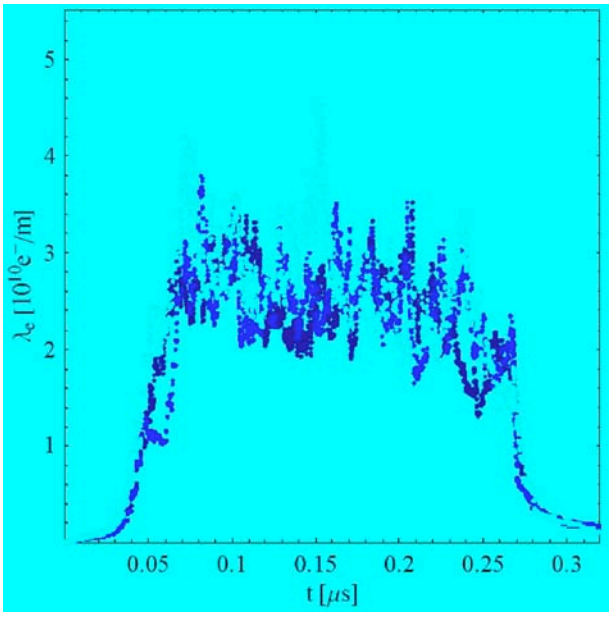


**Figure 2:** Electron cloud build up along a DAΦNE bunch train for the old (blue),current (red), and recently proposed (cyan) wiggler.

In Figure 2 the electron cloud linear density evolution is reported for the three wiggler magnetic field models discussed above, showing a negligible dependence of the build up on the magnetic field model.

#### *3.6.2.2 Build Up in Solenoid Field*

At the startup after the recent shutdown for the setup of the crab waist collision scheme [13] the instability threshold dropped to I ≈ 270mA for the positron current, with the vertical feedback switched off. In the attempt to find a remedy solenoids were installed in the field free regions of DAΦNE, leading to an increase of the threshold to I ≈ 400mA. Simulations followed to better understand this mechanism. Here we focus our attention on the electrons accumulated through the secondary emission from the beam pipe in the straight sections. In the simulation, we generate a large number of electrons only at the first bunch passage and let electron cloud develops by the secondary emission process. The electron cloud density build up along the train is shown in Figure 3, for different values of the solenoidal field Bz.

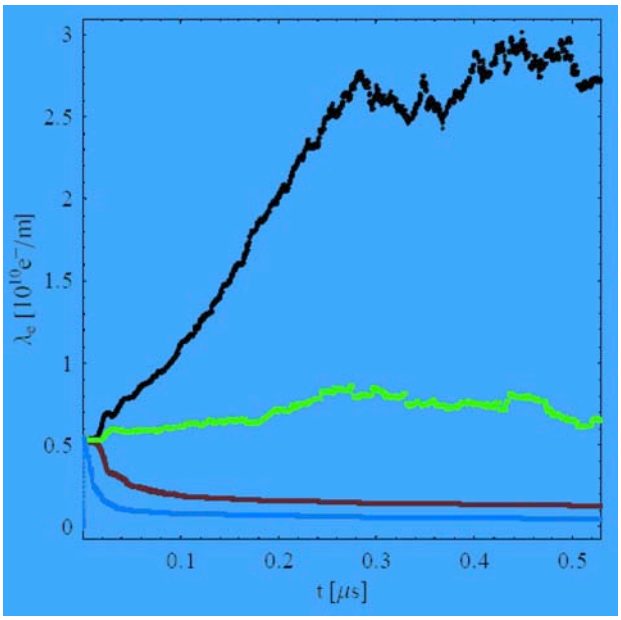


**Figure 3:** Density of electron cloud as a function of time for different solenoid settings: $B_z$ = 0G (black), $B_z$ = 20 G (green), $B_z$ = 40 G (red), $B_z$ = 60 G (blue).

Without solenoids (black curve in Figure 3) the average density grows along the train and saturates due to the balance between the space charge and secondary yield. For $B_z$ > 20 G the electron density decrease very quickly after the passage of the first bunch. A resonance is expected when the time between two consecutive collisions of the electrons in the cloud with the beam pipe surface, that is about half of the electrons cyclotron period $T_c$, is equal to the time interval between two bunch passage. For the DAΦNE parameters, this condition reads to the following resonance condition for the magnetic field:

$$B_z^c = \frac{\pi m_e c^2}{e L_{sep}} \approx 66G\,. \qquad (1)$$

However there is a threshold value of bunch population, related to the energy gain of the electrons in the cloud during the passage of a bunch and independent of the bunch spacing [14], above which the resonance takes place. As shown in Figure 4, simulations for DAΦNE exhibit a threshold $N_b$=5 $10^{10}$ for both single and double bunch spacing that is above the currently operated current.

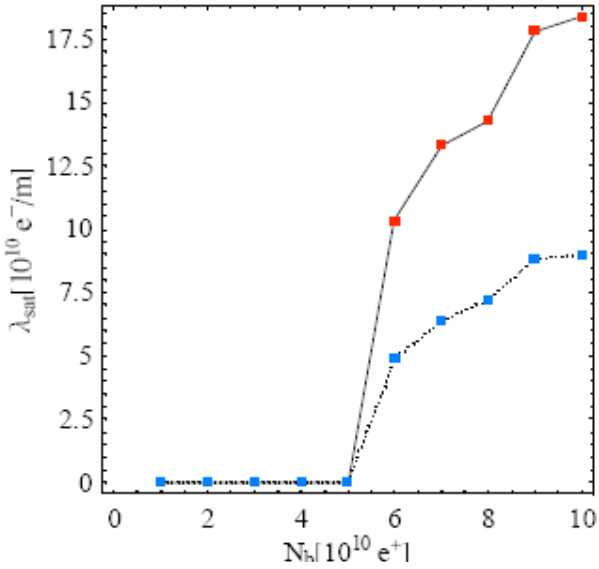


**Figure 4:** Saturated density as a function of the bunch population. Red dots represent the case of Lsep spacing and 66G field. Blue dots represent 2Lsep spacing and 33G field.

The effectiveness of solenoids in reducing the electron cloud density has also been checked by monitoring the vacuum behaviour for the positron beam. The vacuum pressure read-out is reported in Figure 5 for the solenoid ON-OFF cases as recorded by a vacuum gauge located in a region of the positron ring where solenois are installed. The pressure reduction in the region with solenoids is clear.

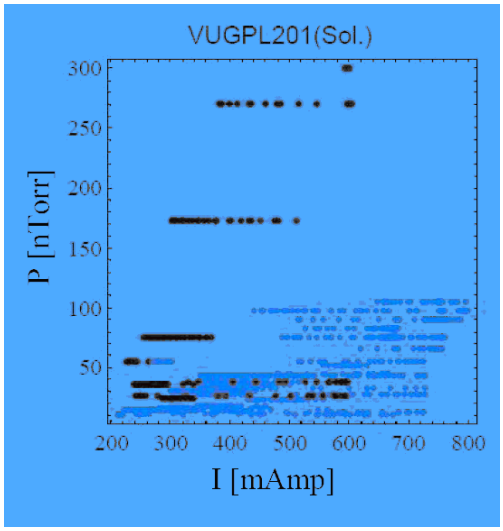


**Figure 5:** Vacuum pressure read-out vs. total current as recorded in a straight section of the positron ring where a 40 G solenoidal field was turned on (blue dots) and off (red dots).

### 3.6.3 Electron Cloud Induced Coupled-Bunch Instability

Once the electron cloud is formed, the beam passing through the cloud interacts with it. The motion of bunches become correlated with each other if the memory of a previous bunch is retained in the electron cloud, i.e. a small displacement of a bunch creates a perturbation of the electron cloud, which affects the motions of the following bunches, with the result that a coupled-bunch instability is caused. A complete discussion of the electron cloud induced multi-bunch instability formalism is outside the aim of this paper. The reader is referred to [17] for a detailed presentation of the subject.

Experimental observations [1-5] show that the horizontal instability affecting the DAΦNE positron beam is a multi-bunch instability. The observed oscillation mode of the instability is always a very slow frequency mode and can be identified as the -1 mode (i.e., the mode that has a line closest to the frequency origin (zero frequency) from the negative part of the spectrum). The same behaviour has been observed even after the solenoid installation. For this reasons the attention has been focused on the interaction of the beam with the cloud in wigglers and bending magnets where the solenoids are not effective.

#### *3.6.3.1 Tracking of the Coupled-Bunch Instability*

A positron bunch can be characterized by its transverse and longitudinal position (dipole moment) as a function of s, ignoring the internal structure of the bunch. Interactions between bunches and electrons in a cloud are determined by the transverse and longitudinal profiles of the bunches. The profiles are assumed to be Gaussian with standard deviation determined by the emittance and the average beta function in the transverse and longitudinal directions. The motion of each bunch is determined by the transformation representing lattice magnets and the interactions with electrons, while the motions of the electrons are determined by the interactions with the bunches, space charge forces between the electrons, and any magnetic field. The equations of motion are written as

$$\frac{d^2\mathbf{x}^p}{ds^2} + K(s)\mathbf{x}^p = \frac{r_e}{\gamma}\sum_{e=1}^{N}\mathbf{F}(\mathbf{x}^p - \mathbf{x}^e)\delta_p(s - s^e) \tag{2}$$

$$\frac{d^2\mathbf{x}^e}{dt^2} = 2r_e c^2\sum_{p=1}^{N_p}\mathbf{F}(\mathbf{x}^e - \mathbf{x}^p)\delta_p[t - t^p(s^e)] + \frac{e}{m_e}\frac{d\mathbf{x}^e}{dt}\times\mathbf{B} - 2r_e c^2\frac{\partial\Phi}{\partial\mathbf{x}} \tag{3}$$

where subscripts $p$ and $e$ of $\mathbf{x}$ denote positron and electron, respectively, $r_e$ is the classical electron radius, $m_e$ is the electron mass, $c$ is the speed of light, $e$ is the electron charge, $\Phi$ is the electric potential due to electrons, $\delta_P$ is the periodic delta function for the circumference, and $\mathbf{F}$ is the Coulomb force in two-dimensional space given by the Bassetti-Erskine formula [18].

To estimate the multi-bunch instability induced by the electron cloud in the arcs of the DAΦNE positron ring the code PEI-M [8], [16] has been used. The code computes the transverse amplitude of each bunch as a function of time by solving equations (2), and (3), while evolving the build-up of the electron cloud self-consistently. To save

computation time, the Poisson equation for the space charge potential Φ is solved only once for zero beam amplitude, and is used as a constant field in tracking simulation. The beam and chamber parameters used in the simulation are collected in Table 1. A uniform vertical magnetic field $B_z$=1.7 T was used to model the motion of the electrons both in wigglers and dipoles, and a circular chamber of radius R=45mm is used instead of the real chamber geometry in order to solve analytically the Poisson equation for Φ. The instability mode spectrum is obtained by taking the Fourier transform of the transverse amplitude of each single bunch as computed by the code, and the grow-rate is obtained by an exponential fit to the beam signal envelope. In Figure 6 are reported the beam signal (the horizontal position of each bunch as a function of time expressed in turns), the beam signal envelope, and the mode spectrum obtained for a bunch train of 120 equi-spaced bunches filled with a beam current of 1.2 A. It is clearly seen that the most unstable mode, obtained by the simulation is mode 114, corresponding to the -1 mode.

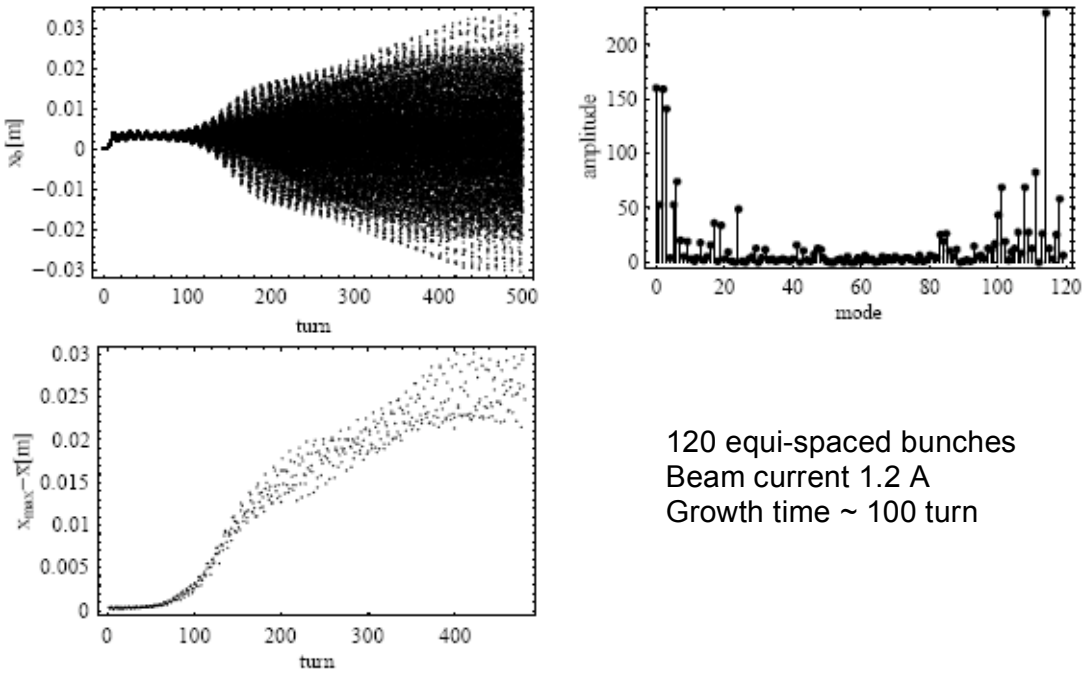


**Figure 6:** Beam signal (a), beam envelope (b), and mode spectrum (c) for a completely filled DAΦNE bunch train.

Experiments on coupled-bunch instabilities have been extensively performed using the DAΦNE fast feedback system to perform grow-dump measurements [2], [4]. Measured grow-rate are compared to simulation results in Table 2 for different beam currents, showing a good agreement.

**Table 2:** Measured and simulated instability growth rate for different beam current, most unstable mode is always -1.

| ***Measurment*** | | ***Simulation*** | |
|---|---|---|---|
| I[mA]/nb | τ/T0 | I[mA]/nb | τ/T0 |
| 1000/105 | 73 | 1200/120 | 100 |
| 750/105 | 56 | 900/120 | 95 |
| 500/105 | 100 | 600/120 | 130 |

### 3.6.4 Conclusions

Simulations for the DAΦNE wiggler show a negligible dependence of the build up on the magnetic field model, and a build-up variation with bunch filling pattern that is compatible with experimental observations. Simulations for the build up in solenoidal field show that a small field is effective in reducing the electron cloud density in straight section, and that the threshold for the cyclotron resonance is above the bunch population currently available in DAΦNE. Also in this case there is a qualitative agreement with observations. Coupled-bunch instability simulations are in good agreement with the experimental observations, and indicate that the observed horizontal instability is compatible with a coupled bunch instability induced by the presence of an electron cloud in the arcs of the DAΦNE positron rings. Work is in progress to include more realistic models for the space charge potential and the chamber boundaries in the simulation code.

### 3.6.5 References


1. C. Vaccarezza, et al, ECLOUD04, Napa Valley proc.
2. A.Drago et al., Proceedings of PAC05, p.1841.
3. C.Vaccerezza et al., Proceedings of PAC05, p.779.
4. A.Drago, proc. of the 40th ICFA Beam Dynamics Workshop on High Luminosity e+e- Factories.
5. A.Drago et al., DAΦNE Tech. Notes, G-67.
6. M. Preger, DAΦNE Tech. Notes, L-34.
7. S.Bettoni et al., Proceedings of PAC07, p. 1463.
8. K. Ohmi, Phys. Rev. Lett. **75**, 1526 (1995).
9. M. A. Furman and M. T. F. Pivi, Phys. Rev. ST Accel. Beams **5**, 124404 (2002).
10. F. Zimmermann, CERN, LHC-Project-Report-95, 1997; G. Rumolo and F. Zimmermann, CERN, SL-Note-2002-016, 2002.
11. N.Mahne et al., Proceedings of PAC05, p.817.
12. R. Cimino et al., PRL93, 014801, 2004.
13. D.Schulte et al., PAC-2005-FPAP014, 2005.
14. F. Le Pimpec et al., SLAC-PUB-10894 (2004).
15. C.Milardi et al.,WEPP036, EPAC 06.
16. Y.Cai et al., Phys. Rev. ST-AB 7, 024402 (2004).
17. S. S. Win et al., Phys. Rev. ST Accel. Beams 8, 094401 (2005).
18. M. Bassetti and G. Erskine, CERN Technical Report No. ISR TH/80-06, 1980.

## 3.7 Parameters for the PEP-II B-Factory at SLAC in 2008

J. Seeman, R. Akre, P. Bellomo, K. Bertsche, Y. Cai, R. Chestnut, J. Clendenin, S. DeBarger, F.-J. Decker, J. Dorfan, S. Ecklund, R. Erickson, A. Fisher, J. Fox, S. Heifets, T. Himel, R. Iverson, R. Humphrey, J. Irwin, L. Klaisner, D. Kharakh, W. Kozanecki, A. Kraznyk, A. Kulikov, N. Kurita, R. Larsen, P. McIntosh, S. Metcalfe, A. Novokhatski, C. Pearson, M. Petree, N. Reeck, C. Rivetta, P. Schuh, H. Shoaee, H. Schwarz, A. Sheng, M. Stanek, M. Sullivan, D. Teytelman, D. Van Winkle, M. Weaver, U. Wienands, W. Wittmer, Y. Yan, G. Yocky, M. Zurawel
SLAC, Menlo Park, CA 94025 USA
W. Barry, J. Corlett, T. Elioff, M. Furman, M. Zisman, LBNL, Berkeley, CA, USA
M. Biagini, P. Raimondi, LNF, INFN, Frascati, Italy
Mail to: seeman@slac.stanford.edu

### 3.7.1 Introduction

The PEP-II B-Factory [1] at SLAC (3.1 GeV $e^+$ x 9.0 GeV $e^-$) operated from 1999 to 2008, delivering luminosity to the BaBar experiment. The design luminosity was reached after one and a half years of operation. In the end PEP-II surpassed, by four times, its design luminosity reaching 1.21 x $10^{34}$ $cm^{-2}s^{-1}$. It also set world stored beam current records of 2.1 A $e^-$ and 3.2 A $e^+$. Continuous injection was implemented with BaBar successfully taking data. The total delivered luminosity to the BaBar detector was 557.4 $fb^{-1}$ spanning five upsilon resonances. PEP-II was constructed by SLAC, LBNL, and LLNL with help from BINP, IHEP, the BaBar collaboration, and the US DOE OHEP.

### 3.7.2 PEP-II Timeline

1987: Particle physicists determine that asymmetrical beam energies are preferred.
1991: First PEP-II CDR.
1993: Second PEP-II CDR.
1994: Construction started.
1997: First HER stored beam 6:30 am June 5.
1998: First LER stored beam 2:49 am July 16.
1998: First collisions 12:05 pm July 23.
1999: BaBar placed on beam line in May.
1999-2008: Collisions for BaBar.
2000: Design luminosity achieved ($3x10^{33}$) Oct. 29.
2006: Luminosity $1.2x10^{34}$ achieved 8 pm Aug. 17.
2008: PEP-II turned off 23:22 pm April 7.

**Table 1:** PEP-II parameters at peak luminosity.

| *Parameter* | *Units* | *Design* | *April 2008 Best* | *Gain Factor Over Design* |
|---|---|---|---|---|
| I+ | mA | 2140 | 3213 | x 1.50 |
| I- | mA | 750 | 2069 | x 2.76 |
| Number bunches | | 1658 | 1732 | x 1.04 |
| $\beta_y$* | mm | 15-25 | 9-10 | x 2.0 |
| Bunch length | mm | 15 | 10-12 | x 1.4 |
| $\xi_y$ | | 0.03 | 0.05 to 0.065 | x 2.0 |
| Luminosity | $10^{34}$ /cm$^2$/s | 0.3 | 1.2 | x 4.0 |
| Int luminper day | pb$^{-1}$ | 130 | 911 | x 7.0 |

### 3.7.3 PEP-II Parameters

In PEP-II the Low Energy Ring (LER) is mounted 0.89 m above the High Energy Ring (HER) in the 2.2 km tunnel as shown in Figure 1. The PEP-II hardware devices are shown in Figures 2-5. The interaction region is shown in Figure 6 where the beams are collided head on. Figure 7 shows the Be vacuum chamber inside the detector with the permanent magnet dipoles on either side. The interface cone angle at the IR between BaBar and PEP-II was 300 mrad. To bring the beams into collision, LER is brought down 0.89 m to the HER level and then with horizontal deviations for both rings the beams are made to collide as shown in Figure 6. Since both rings have the same circumference, each bunch in one ring collides with only one bunch in the other ring. There are small parasitic collision effects as the bunches separate near the interaction point but at full currents these only reduce the luminosity a few percent.

The luminosity in a flat beam collider is given by

$$L = 2.17x10^{34}\frac{n\xi_y EI_b}{\beta_y^*}$$

where n is the number of bunches, $\xi_y$ is the vertical beam-beam parameter limit, E is the beam energy (GeV), $I_b$ is the bunch current (A), and $\beta_y$* is the vertical beta function value at the collision point (cm). This equation holds for each beam separately. These parameters for PEP-II are shown in Table 1 with the design and best values. PEP-II exceeded all design parameters, in particular the luminosity by a factor of 4 and the integrated luminosity per day by a factor of 7.

**Figure 1**: PEP-II tunnel with LER above the HER.


**Figure 2:** PEP-II LER magnet and vacuum chamber hardware.

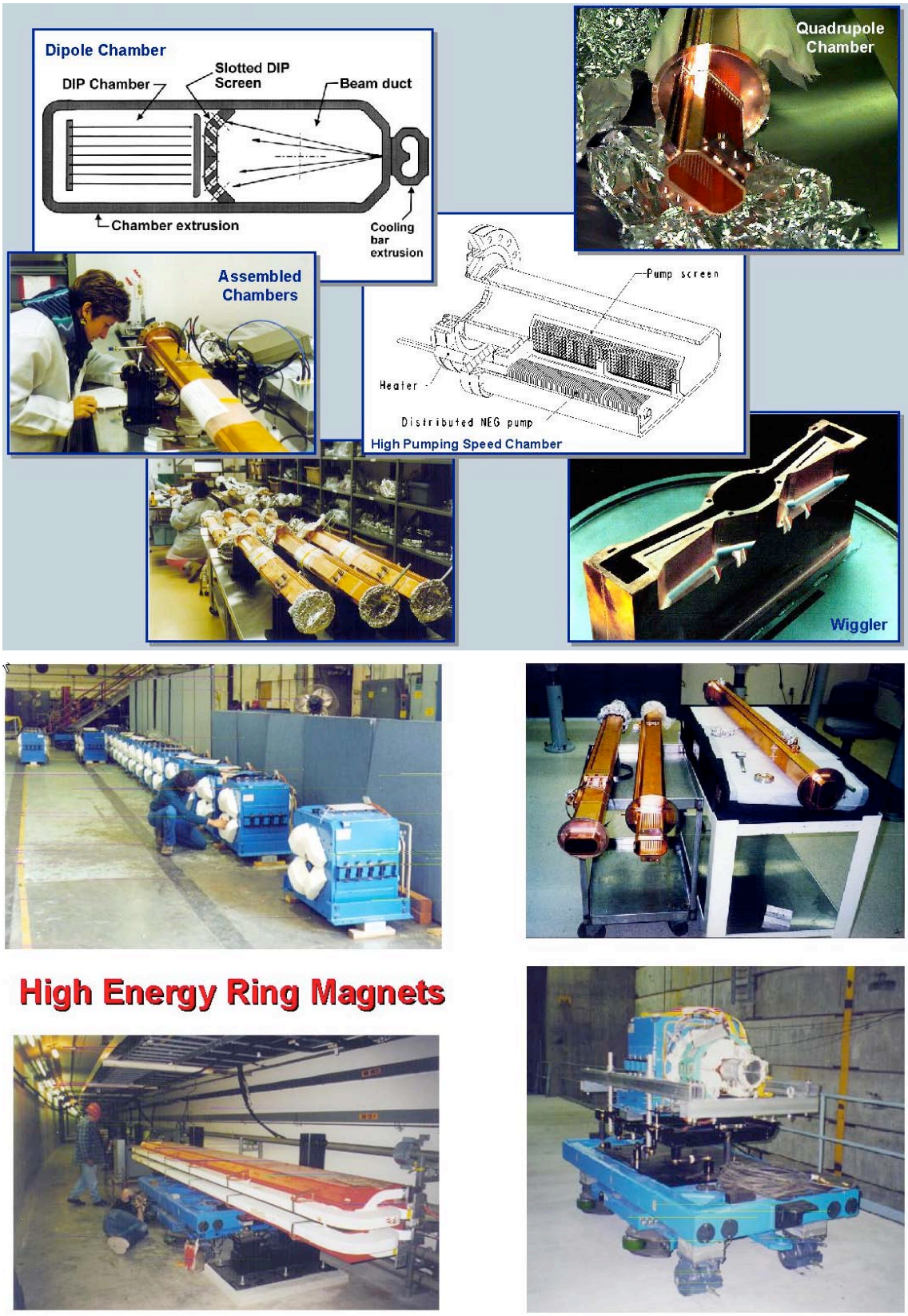


**Figure 3:** PEP-II HER magnet and vacuum chamber hardware.

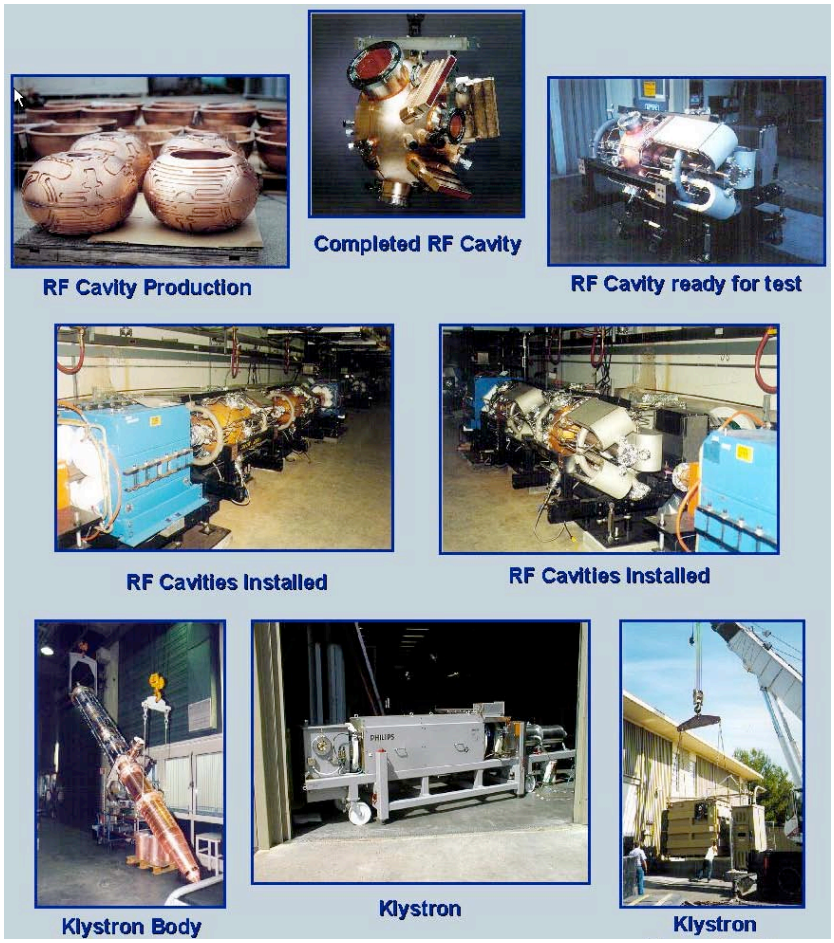


**Figure 4:** PEP-II RF klystrons and cavity hardware.

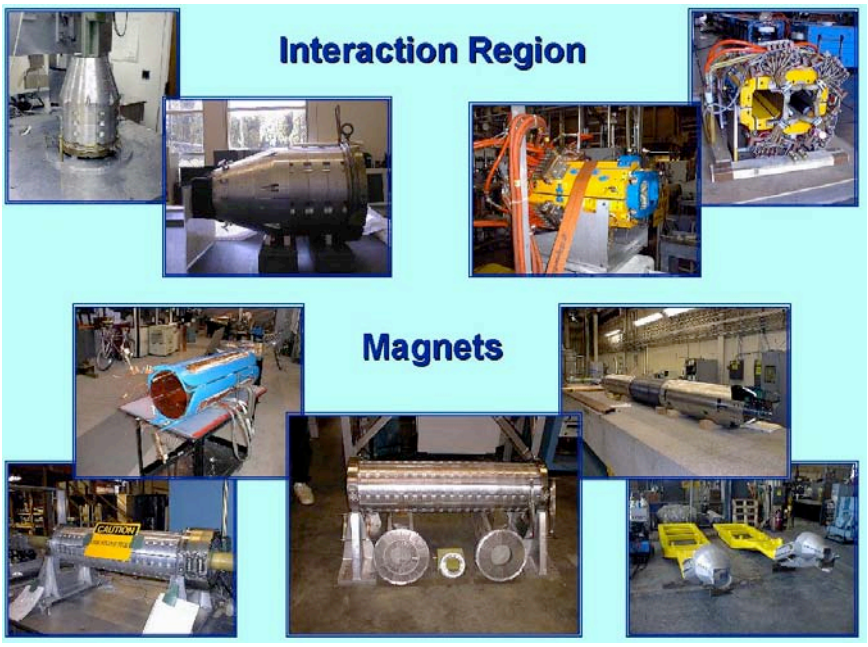


**Figure 5:** PEP-II Interaction region permanent magnets and electromagnets.

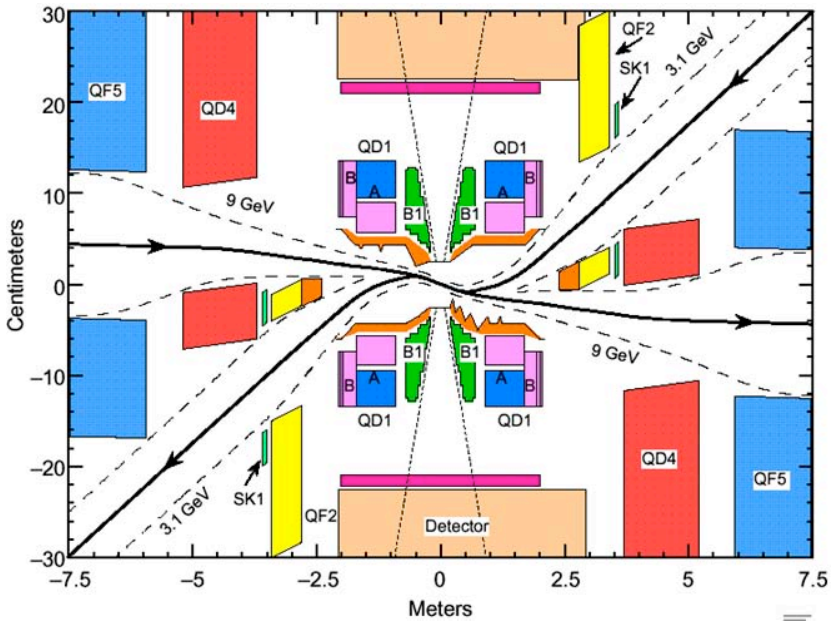


**Figure 6:** PEP-II Interaction Region (IR) with head-on collisions. There are four permanent magnets within the BaBar 1.5 T solenoidal field covering +/- 2.5 m.


**Figure 7:** IR double-walled Be collision chamber with nearby water cooling and permanent magnet dipoles.

### 3.7.4 High Current Operation

The high beam currents are supported by large RF systems consisting of 1.2 MW klystrons at 476 MHz and high power cavities with HOM absorbing loads. Each cavity has three HOM loads each with the capability of 10 kW. A cavity is shown in Figure 8. At peak currents a HER cavity receives on average 285 kW and the LER cavities

372 kW. The average klystron power was 1.01 MW. An overhead of about 20% in power was needed to allow the RF feedback systems to be stable. At high currents there were about 3 RF trips each day. The longitudinal bunch-by-bunch (4 nsec) feedback system is shown in Figure 9. The bunch-by-bunch (4 nsec) transverse feedback system is shown in Figure 10. Once tuned, these systems were quite robust. These systems were used to measure and feedback on beam instabilities (Figure 11). The coupled bunch instabilities were damped up to the highest current with some head room but the HER growth rates were somewhat anomalous being stronger than predicted.

The vacuum systems were extruded copper in the HER arcs and extruded aluminium with antechambers and photon-stops in the LER arcs. Both rings had stainless steel double walled chambers in the straight sections. The chambers were water cooled continuously over their 2.2 km lengths due to beam heating. From beam-off to beam-on the vacuum chambers expanded and high power expansion bellows were needed (Figure 12).

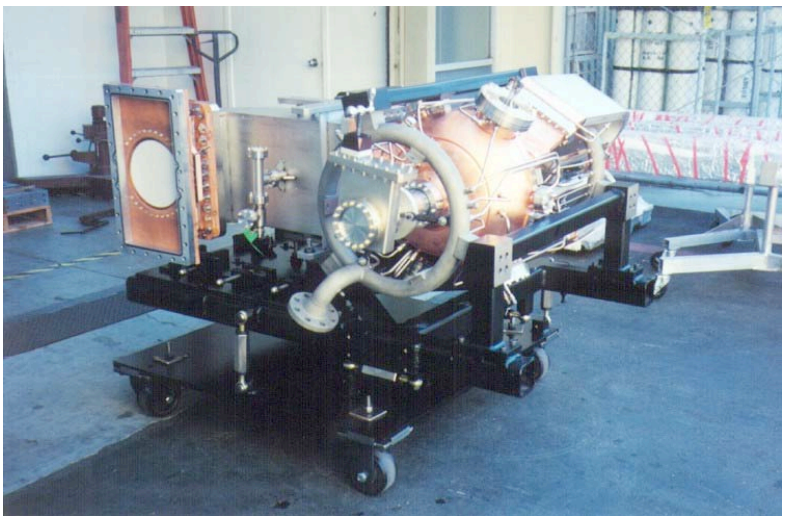

**Figure 8:** PEP-II high power copper RF cavity, water cooled with a 500 kW ceramic window and 3 HOM loads.

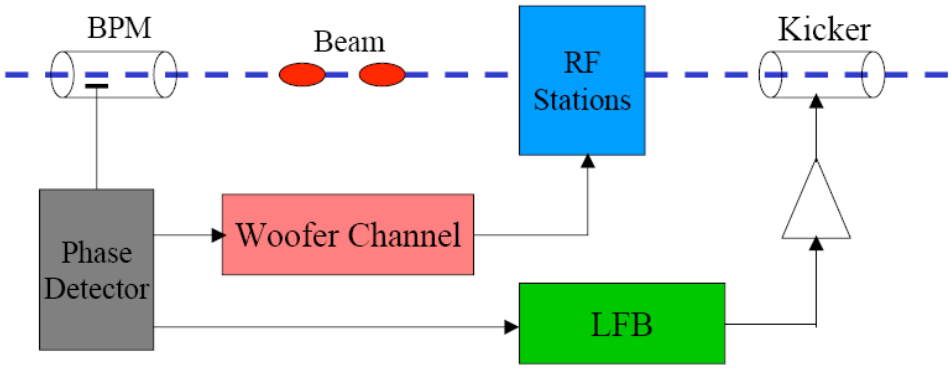


**Figure 9:** Bunch-by-bunch longitudinal feedback system with an added low level (woofer) channel.

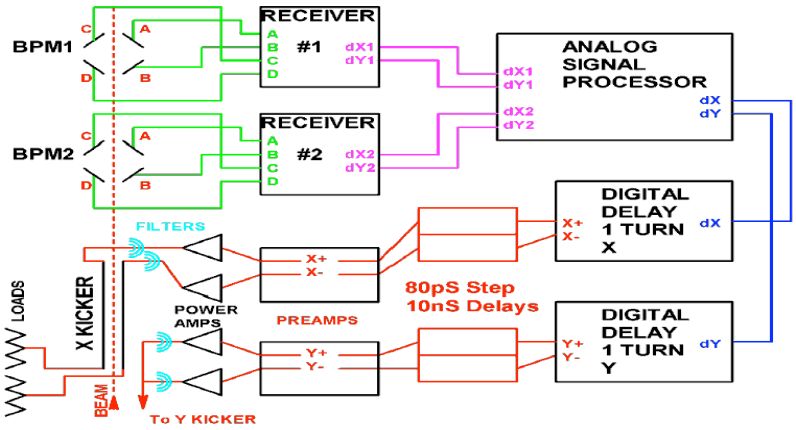


**Figure 10:** Bunch-by-bunch transverse feedback system.

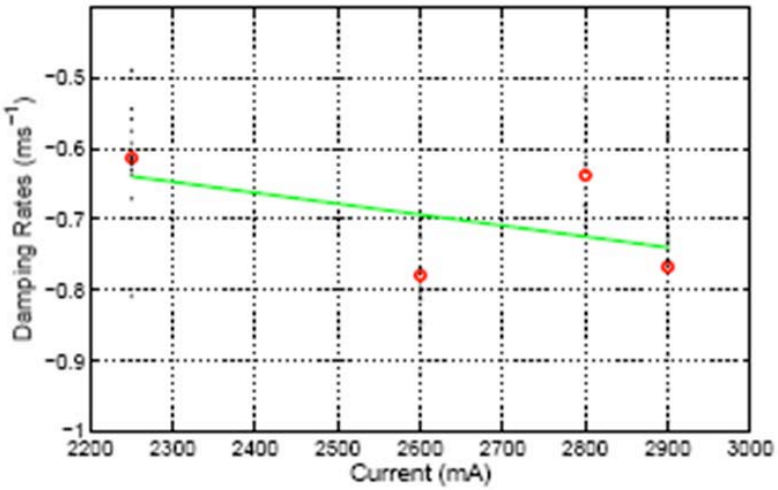


**Figure 11:** LER longitudinal feedback damping rates with total positron current.

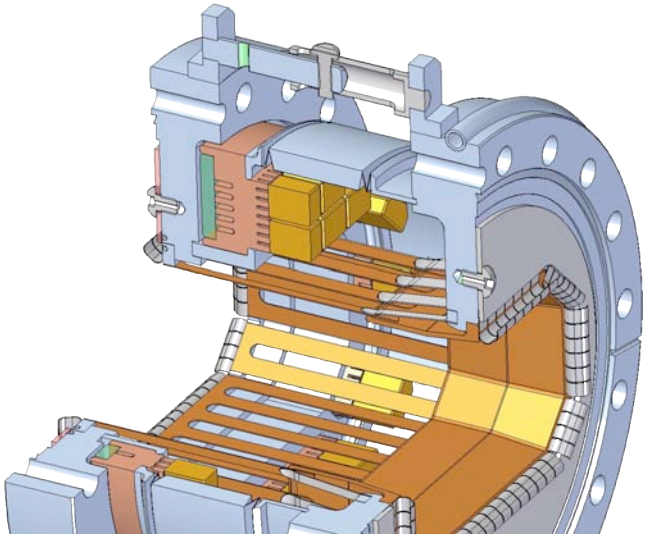

**Figure 12:** Ultimate design of the PEP-II high power expansion bellows module with sliding fingers, compression (hold down) fingers, beam RF seals at the ends, and water cooled HOM absorbing tiles.

### 3.7.5 Beam-Beam and Luminosity

The best location in the tune plane was chosen by the best beam-beam performance. The best location was obtained with the horizontal tune just above the half integer ~0.508 and the vertical tune around 0.574. In Figure 13 are shown simulation luminosity contours on the x-y tune plane indicating optimal performance near the observed best location. Considerable but successful work was needed to correct horizontal beta beat errors at these horizontal tunes.

The measured luminosity versus the product of the bunch currents is shown in Figure 14 and the specific luminosity in Figure 15. The resulting maximum vertical beam-beam parameters in the two rings were 0.05 to 0.065. At the highest currents with collisions, the HER current was limited by the LER lifetime and the LER current by HER generated IR backgrounds in the detector. At the highest luminosities, the HER lifetime was about 2 hours and the LER about 1 hour. Continuous injection, of course, made up for these losses and kept the currents constant. In collision an increase in the LER current also increased its own horizontal beam size, which is still not understood.

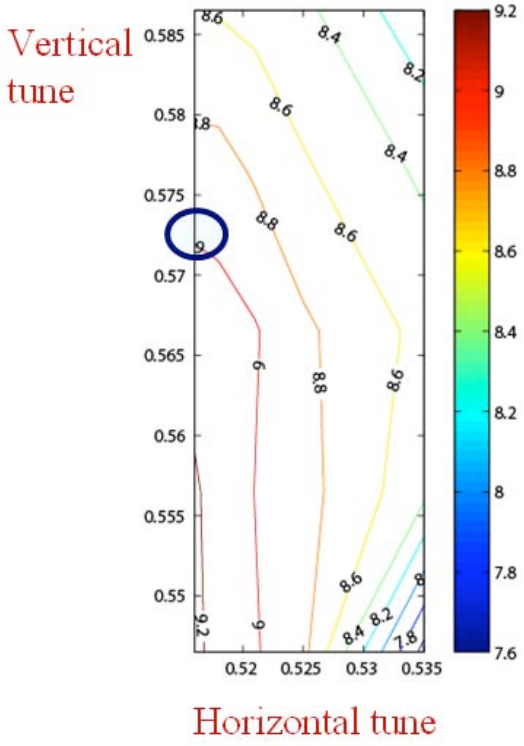


**Figure 13:** Contours of simulated luminosity in the tune plan. The best fractional tunes were 0.508 horizontally and 0.574 vertically, generally agreeing with experiment.

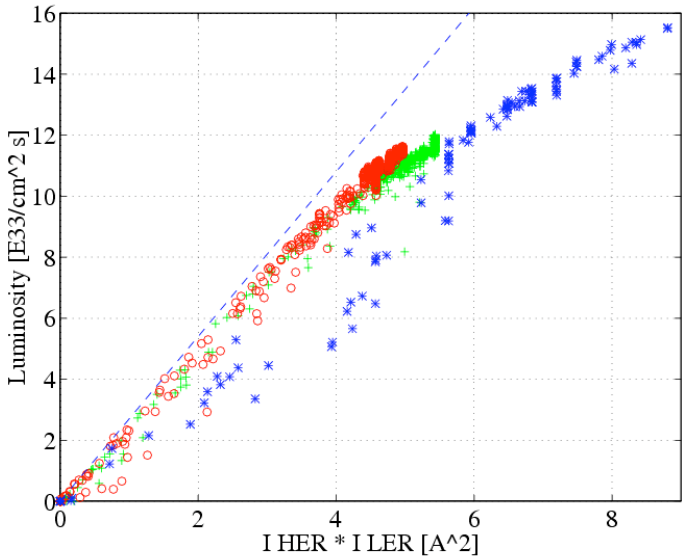


**Figure 14:** Luminosity versus the product of the bunch currents. The red and green curves show luminosity in the By-2 pattern (4 nsec) bunch spacing during routine operation achieving a luminosity of 1.2 x $10^{34}$. The blue curve shows the By-4 bunch pattern (8 nsec) scaled to a By-2 bunch pattern, indicating an increased luminosity may have been possible in PEP-II with the By-2 pattern.

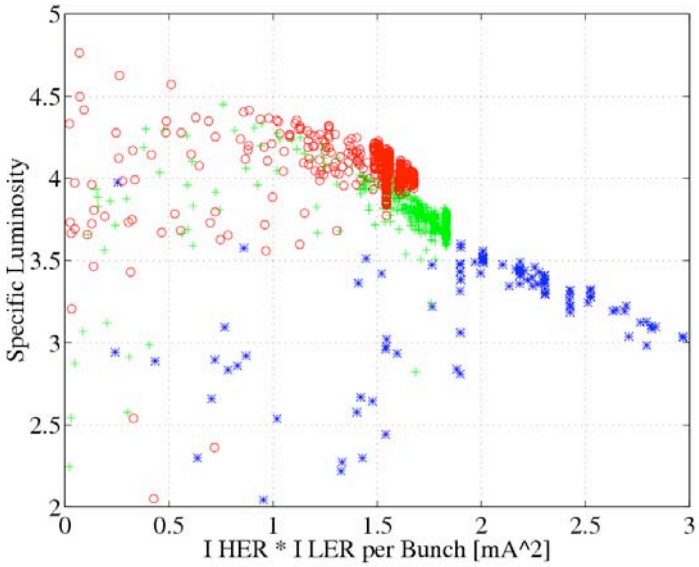


**Figure 15:** Specific luminosity versus the product of the bunch currents. The specific initially rises because of dynamic beta effects and then falls due to beam-beam interaction from both primary and parasitic collisions. The parasitic beam-beam effect was only a few percent. The blue points are By-4 pattern scaled to the By-2 pattern.

Continuous (trickle charge) injection was planned for from the initial design phase of PEP-II. The LER was accomplished first in November 2003 with BaBar taking data. The HER continuous injection occurred six months later. See Figure 16 before and Figure 17 after. A 40% increase in average integrated luminosity was achieved.

### 3.7.6 Overall Beam Performance

PEP-II was operated on five upsilon resonances with the majority of data on the Y4S as shown in Table 2. Figure 18 shows the total integrated luminosity of PEP-II achieving 557.4 $fb^{-1}$. The flat regions are maintenance and installation periods. In Figure 19 shows the monthly integrated luminosity delivered to BaBar by PEP-II. The period of the last few months was for running on the Y2S, Y3S, and the energy scan above the Y4S. In Figure 20 is shown the highest luminosity in each month over the life of PEP-II. The design luminosity was achieved just over a year into operations. The luminosity record of PEP-II of 1.2 x $10^{34}/cm^2/s$ was achieved in August 2006. A summary of the performance achievements of PEP-II are shown in Table 3. The PEP-II staff members on April 7, 2008, are shown in Figure 21.

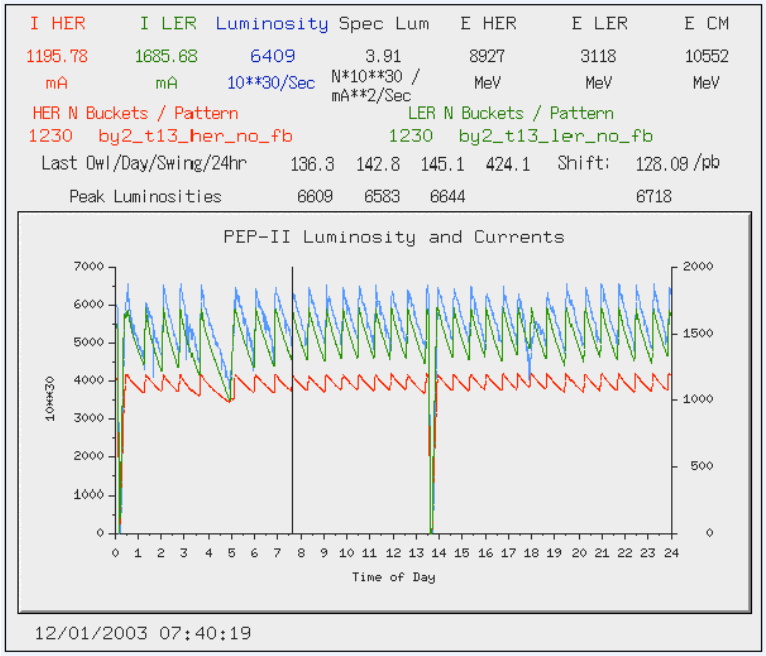


**Figure 16:** Luminosity and beam currents for 24 hours showing the fill-coast mode of PEP-II in early years.

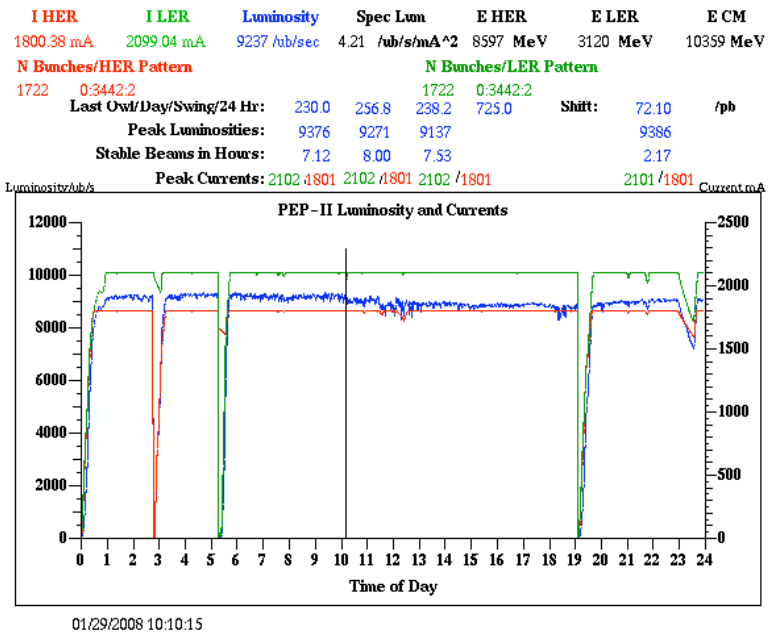


**Figure 17:** Continuous injection of both PEP-II beams.

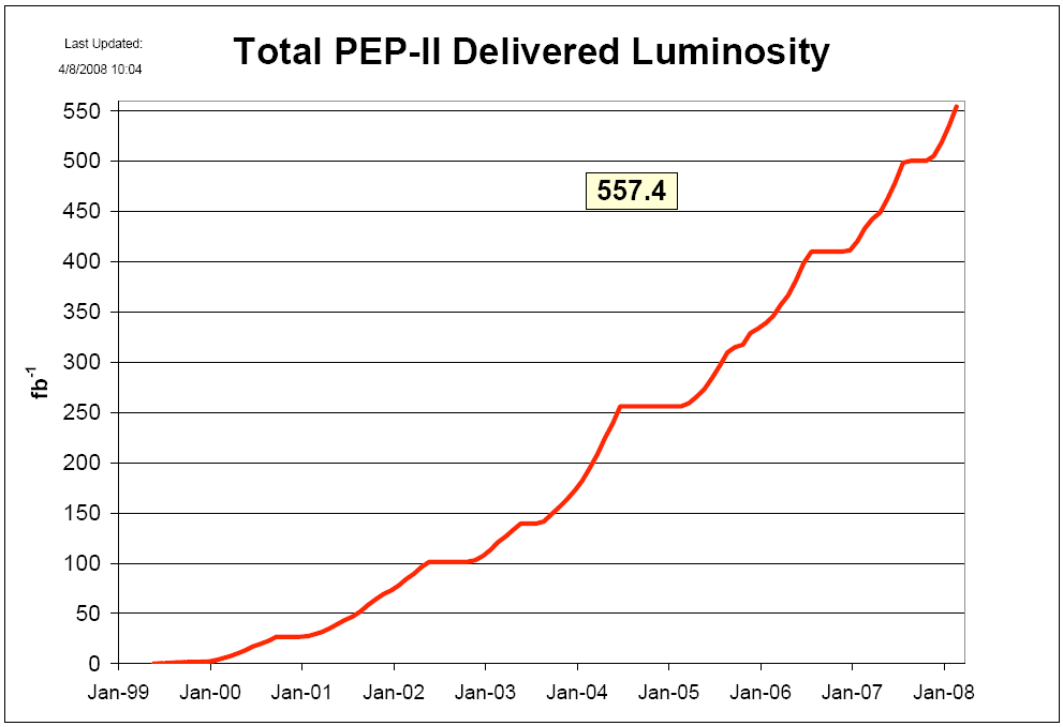


**Figure 18:** Total integrated luminosity from 1999 to 2008.

**Table 2:** Operation of PEP-II on different Upsilon resonances. The remainder of the total integrated luminosity of the 557.4 $fb^{-1}$ was taken as "off resonance" data near the resonances, together totalling about 78 $fb^{-1}$. Due to the permanent magnet IR quadrupoles, the LER energy was not changed.

| *Resonance* | *Data* | *HER Energy* |
|---|---|---|
| Y2S | 14.5 $fb^{-1}$ | 8.1 GeV |
| Y3S | 30 $fb^{-1}$ | 8.4 GeV |
| Y4S | 433 $fb^{-1}$ | 8.97 GeV |
| Y5S | 0.9 $fb^{-1}$ | 9.47 GeV |
| Y6S | 0.8 $fb^{-1}$ | 9.73 GeV |
| Off Resonance | 78 $fb^{-1}$ | Various |

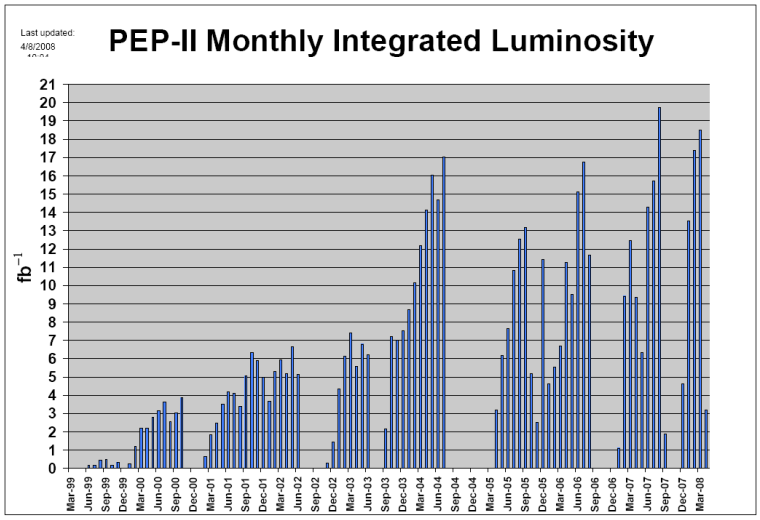


**Figure 19:** Monthly integrated luminosity from 1999 to 2008. The best month was August 2007 with 19.7 $fb^{-1}$.

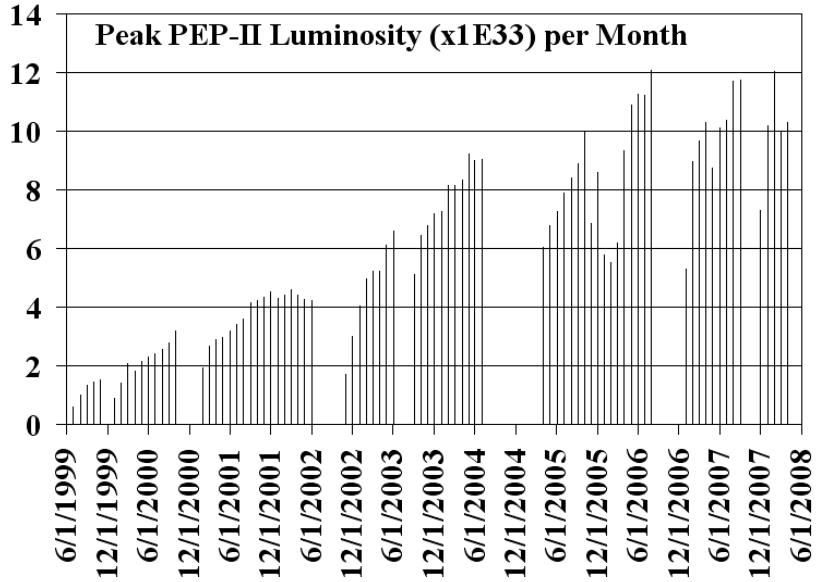


**Figure 20:** Peak luminosity in a given month from 1999 to 2008. A peak luminosity of $1.21 \times 10^{34}/cm^2/s$ was achieved.

### 3.7.7 PEP-II Innovations to Extend the Peak Luminosity

All PEP-II components, as designed, worked well enough to get above the design luminosity parameters (magnets, RF system, vacuum system, interaction region, background mitigation, beam instabilities, bunch-by-bunch feedbacks, injection, and controls). However, to get far above the design up to x 4 design luminosity and x 7 integrated luminosity per day, several major upgrades were done [2-14].

A) The electron cloud instability (ECI) in the LER for $e^+$ needed ~30 gauss solenoids on the straight section stainless steel vacuum chambers. About 1.8 km of solenoid was wound. This proved very successful. The LER Arc chambers with ante-chambers, photon stops and TiN coatings worked well against ECI as designed. In the end, ECI did not degrade the peak luminosity.
B) The small (10 cm O.D.) expansion bellows on each end of the IP Be chamber had to have extra air and water cooling installed to survive the higher combined beam currents of over 5 A.
C) The synchrotron and lost particle masking near the detector was improved as the currents were raised.
D) Seven RF stations were added for a total of 15 stations to handle the highest beam currents in the two rings (3.2 A x 2.1 A).
E) The feedback kickers were upgraded for both the longitudinal and transverse systems. The new cavity style (Frascati) longitudinal kickers worked very well.
F) As the beam currents were increased, the RF controls were refined with modest upgrades and careful tune up procedures.
G) Higher power vacuum expansion bellows went through several designs being able to handle ever increasing HOM powers. See Figure 12 for the best design.
H) Continuous injection needed a lot of careful work to make it acceptable to BaBar data taking. Both the accelerator and detector people worked together on masking, injection control, and diagnostics.
I) The abort gap was reduced from 5% of the circumference to about 1.6% with an improved abort kicker pulser.
J) Nearly continuous improvements to the quadrupole lattices were made. Tuning of the interaction region made for better beta and dispersion control, detector solenoid coupling correction, and minimizing vertical emittance.
K) Improved x-y coupling control was needed in the LER to maximize the luminosity. Permanent magnet skew quadrupoles were built and installed in very tight locations near the interaction region.
L) Vertical and horizontal beta-beats in the arcs near the IR were carefully worked to maximize the luminosity.
M) Simulation codes in 3-D were developed to understand all the aspects of the beam-beam interaction and tune shift limits. Good agreement with experiments was reached in most cases.
N) Every beam abort was studied, categorized, and analyzed offline. There were on average about 8 beam aborts per day with about three from the RF system, three from unstable beams, and two from detector backgrounds.

**Table 3:** PEP-II overall operational performance records.

## PEP-II Records

Last update: April 8, 2008

### Peak Luminosity

$12.069 \times 10^{33}$ $cm^{-2}sec^{-1}$ — August 16, 2006

1722 bunches 2900 mA LER 1875 mA HER

### Integration records of delivered luminosity

| | | |
|---|---|---|
| Best shift (8 hrs, 0:00, 08:00, 16:00) | 339.0 $pb^{-1}$ | Aug 16, 2006 |
| Best 3 shifts in a row | 910.7 $pb^{-1}$ | Jul 2-3, 2006 |
| Best day | 858.4 $pb^{-1}$ | Aug 19, 2007 |
| Best 7 days (0:00 to 24:00) | 5.411 $fb^{-1}$ | Aug 14-Aug 20, 2007 |
| Best week (Sun 0:00 to Sat 24:00) | 5.137 $fb^{-1}$ | Aug 12-Aug 18, 2007 |
| Peak HER current | 2069 mA | Feb 29, 2008 |
| Peak LER current | 3213 mA | Apr 7, 2008 |
| Best 30 days | 19.776 $fb^{-1}$ | Aug 5 – Sep 3, 2007 |
| Best month | 19.732 $fb^{-1}$ | August 2007 |
| Total delivered | 557 $fb^{-1}$ | |

PEP-II turned off April 7, 2008

**Figure 21:** The PEP-II Staff April 7, 2008.

### 3.7.8 Acknowledgments

This work was supported by US DOE contract DE-AC02-76SF00515. The authors and all the PEP-II team wish to thank the operations staff, the maintenance crews, the safety teams, and all other supporting staff at SLAC for their hard work and efforts. Many thanks go to the US DOE Office of High Energy Physics for support. The two PEP-II Machine Advisory Committees helped the project in many ways. Our colleagues at LBNL, LLNL and Frascati made many contributions.

### 3.7.9 References

1. "PEP-II an Asymmetric B Factory", Conceptual Design Report, CALT-68-1869, LBL-PUB-5379, SLAC-418, UCRL-ID-114055, UC-IIRPA-93-01, June 1993.
2. J. Seeman, "The Last Year of PEP-II," EPAC, June 2008.
3. J. Seeman, et. al., "PEP-II at $1.2 \times 10^{34}/cm^2/s$ Luminosity", PAC 2007, pg. 37.
4. M. Sullivan, et. al., "Results from a Prototype Permanent Magnet Dipole-Quadrupole Hybrid for the PEP-II B-Factory", PAC 1997, pg. 3330.
5. J. L. Turner, et. al., "Trickle-charge: a New Operational Mode for PEP-II", EPAC 2004, pg. 881.
6. U. Wienands, et. al., "High-temperature Kicker Electrodes for High-beam-current Operation of PEP-II", EPAC 2004, pg. 2843.
7. J. D. Fox, et. al., "Development and Testing of a Low Group-delay Woofer Channel for PEP-II", Proceedings of EPAC 2004, pg. 2822.
8. P. A. McIntosh, et. al., "An Over-damped Cavity Longitudinal Kicker for the PEP-II LER", PAC 2003, pg. 1341.
9. P. A. McIntosh, et. al., "PEP-II RF System Operation and Performance", EPAC 2004, pg. 1087.
10. U. Wienands, "Vacuum Performance and Beam Lifetime in the PEP-II Storage Rings", PAC 2001, pg. 597.
11. U. Wienands, et. al., "Tracking Down a Fast Instability in the PEP-II LER", EPAC 2006, pg. 658.
12. M. Sullivan, et. al., "Anomalous High Radiation Beam Aborts in the PEP-II B-factory", EPAC 2006, pg. 652.
13. A. Novokhatski, et. al., "Modeling of the Sparks in Q2-bellows of the PEP-II SLAC B-factory", PAC07, 2007, pg. 658.
14. A. Novokhatski, et. al., "Damping the High Order Modes in the Pumping Chamber of the PEP-II Low Energy.

## 3.8 The Interaction Region of PEP-II

Michael K. Sullivan, S. DeBarger, S. Ecklund, K. Fant, N. Kurita, M. Nordby,
A. Ringwall, K. Skarpaas
SLAC National Accelerator Laboratory, 2575 Sand Hill Rd. Menlo Park,
CA 94025 USA
Mail to: sullivan@slac.stanford.edu

### 3.8.1 Introduction

The PEP-II e+e- collider turned off last year after a very successful 9 years of running. The accelerator achieved a peak luminosity of $12\times10^{33}cm^{-2}s^{-1}$, 4 times over the design of $3\times10^{33}cm^{-2}s^{-1}$ [1]. The peak beam currents were quite high; over 3 A for the positron beam and over 2 A for the electron beam [2]. The beams were stored in separate storage rings. The PEP-II design called for a head-on collision at the interaction point (IP). This was possible because of the asymmetric beam energies (9 on 3.1 GeV) and was achieved using permanent magnet (PM) dipoles. I describe the actual interaction region (IR) layout including some of the design constraints that led to the final design and discuss operation issues related to the IR design.

### 3.8.2 IR Layout and Design

#### *3.8.2.1 Design Constraints*

As mentioned above, one of the first design constraints was a head-on collision. This immediately raises the question of how to get the beams into and out of collision. Vertical separation was initially considered but deemed more risky than a horizontal separation based on the unfavorable experience of collisions using a vertical crossing angle from DESY (meaning that the vertical plane is more sensitive to small crossing angles) and because beam injection was in the vertical plane. We decided to separate horizontally so we brought the beams into and out of collision through the use of strong PM horizontal dipoles (called B1) located as close as possible to the IP. The detector acceptance for physics events was set at 300 mrad from the detector axis which means that all of the accelerator components have to be below this angle. The B1 dipoles started 21 cm from the IP and were 0.5 m long. They gradually gained in magnetic field strength reaching a peak value of 8.25 kG as we were able to increase the amount of magnetic material and stay below the 300 mrad line. The main reason these dipoles were so close to the IP is that the beams must be separated enough at the first parasitic crossing (0.63 m from the IP) to minimize any beam-beam effects from this near-miss collision. Simulations showed that the separation had to be at least 7σ of the largest of the 4 sigmas at the parasitic crossing. The PEP-II design has a separation of 3.21 mm which equals 9σ.

The next accelerator component is a vertically focusing quadrupole (QD1) [3]. Both beams must go through this quadrupole as they have not been separated enough to go through individual magnets. This shared quadrupole was consequently aligned with the high-energy beam (HEB) orbit making the horizontal low-energy beam (LEB) orbit way off-axis in this quad. The strength of QD1 was set by the needs of the LEB. Since

QD1 is defocusing in x the LEB orbit was further bent away from the HEB orbit. This enabled us to make the next magnetic element (QF2) a septum magnet that is seen by only the LEB[4]. QF2 then completes the final focus doublet for the LEB. It was important to ensure that QF2 is not a shared quadrupole otherwise the beams would have been horizontally focused back together. QF2 had to be as close as possible to the IP because right behind this magnet is the rest of the final focusing doublet for the HEB QD4 and QF5. QD1 did not have enough strength to be the entire vertically focusing component for the HEB so an additional vertically focusing magnet, QD4 was added to complete the HEB vertical focusing and QF5, the first focusing element of the HEB, finishes the final focus "doublet" for the HEB. Figure 1 shows this layout using an expanded vertical scale (which is the horizontal plane of the design). The B1 dipoles and the QD1 magnets are all PM while the remaining six outboard magnets are all normal conducting Fe-Cu magnets.

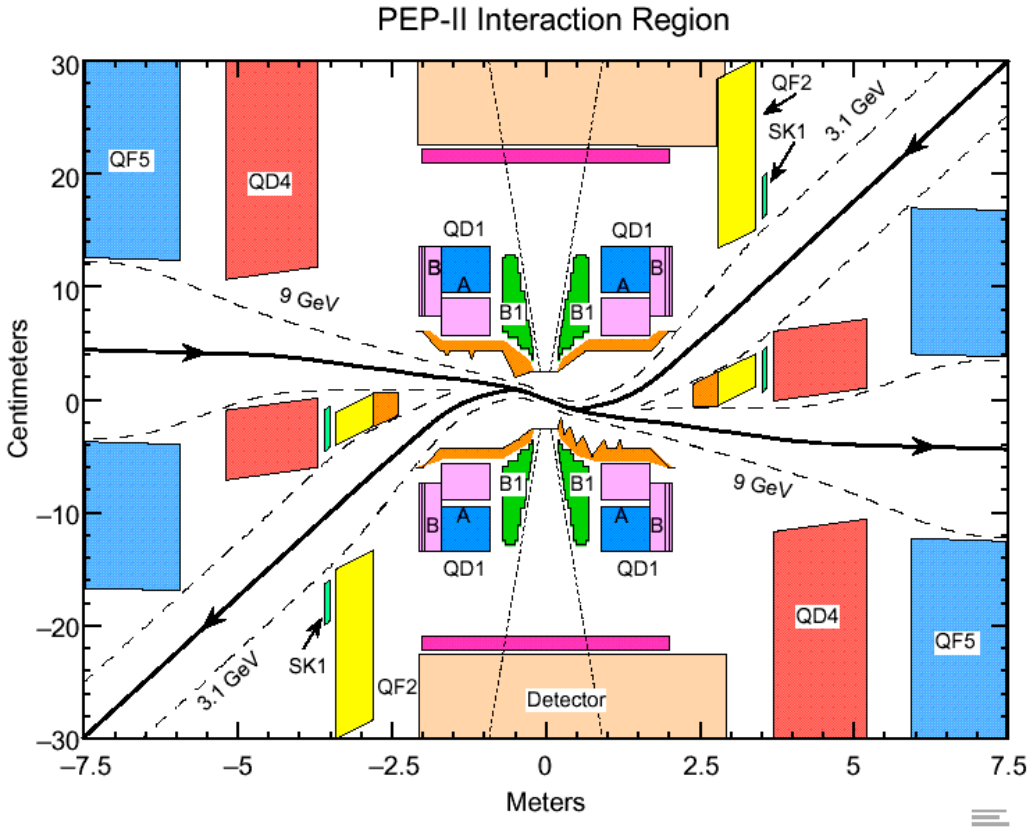


**Figure 1:** Layout of the interaction region of PEP-II. Note the anamorphic scale. The permanent magnets, B1 and QD1 are inside the detector magnetic field; a 1.5 T solenoid.

### *3.8.2.2 Synchrotron Radiation*

As one can see from Fig. 1 there is a significant amount of beam bending in the IR. The primary bending magnet for the HEB is B1. The peak field of these magnets is more than 4 times the field strength of the arc dipoles in the HEB. These two magnets together generate 50 kW of synchrotron power for a 1 A HEB. This became 90kW as the beam current rose up to the typical final running value of 1.8 A and reached nearly 120 kW at the very end when we were raising the HEB energy (more on this later). These overlapping fans of intense radiation must escape from the local interaction

region and ended up striking, at a very oblique angle, a long water-cooled copper chamber located between 10 m and 20 m from the IP. These very high power fans limited the range of x angle adjustment at the IP to about ±2-3 mrad and about ±5 mrad for the y angle for the HEB.

The LEB was also bent by the B1 magnets and in addition suffered an even larger bend from the QD1 magnets. The large overall bending angle of over 3.8 deg (65 mrad). on either side of the IP meant that this radiation did not escape from the local IR area and indeed struck many beam pipe surfaces both upstream and downstream of the IP. The power of these fans of radiation totaled nearly 27 kW at a beam current of 2.9 A. The local beam pipe cooling had to be carefully designed as well as the masking required to protect the detector beam pipe from this radiation. On the other hand, this also meant that the radiation power on various surfaces is somewhat independent of the x angle at the IP giving us an effectively larger range of flexibility. We found we could move the LEB IP angle about ±5 mrad in x and ±8 mrad in y. During actual running, we were held to a range of less than ±1 mrad in x and less than ±2 mrad in y in order to be within the acceptance of the luminosity detector which used the collision-axis collinear radiative bhabha photons generated by the LEB. Figure 2 shows the synchrotron radiation fans for the LEB and the HEB.

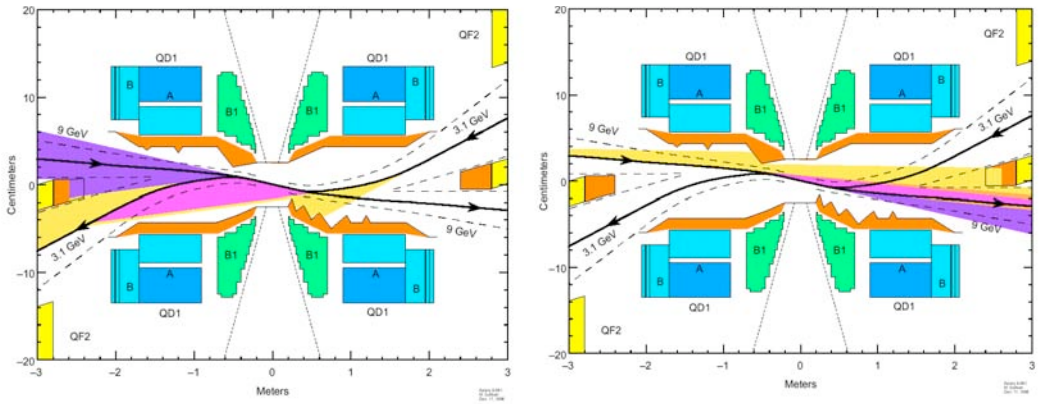


**Figure 2:** LEB and HEB synchrotron radiation fans in the interaction region. The fan intensity is depicted by a darkening of the fan color. The darker the color, the more intense the radiation.

### 3.8.3 Changing Beam Energies

The BaBar detector collaboration wanted about 10% of the collected data to be off the 4S resonance. This meant that we had to adjust the center-of-mass energy ($E_{cm}$) from the mass of the 4S (10.580 GeV) down by 40 MeV. Adjusting the energy of the LEB was much more difficult since QD1 was a permanent magnet. We did have a 2% strength air core quadrupole on the outside of QD1, however, because the HEB also goes through QD1 we would have to adjust at least QD4 as well. Adjusting the HEB is quite a bit easier, especially if we do not change the shared QD1 strength but adjust the QD4 coefficient to compensate for an unchanging QD1. We ended up lowering the HEB 68 MeV to get the 40 MeV change in the $E_{cm}$. For reference, $E_{cm}^2 = 4E_{HEB}E_{LEB}$.

During the last run of PEP-II the detector collaboration decided they wanted to run on the 3S and 2S resonances as well as perform an energy scan above the 4S resonance

to above 11 GeV $E_{cm}$. We had only once before tried to find the 3S resonance during a machine scrubbing startup time in the fall of 2002. We did manage to find and quickly scan the resonance at that time. Other than that one excursion the PEP-II energies were kept very close to the design values. In order to get down to the 3S resonance we lowered the HEB energy 376 MeV which lowered the $E_{cm}$ down to 10.355 GeV. This clearly changes the HEB orbit as it goes through the IR and in fact increases the bending from the B1 magnets. As one can see in Fig. 1, the HEB orbit will move closer to the LEB orbit and therefore reduce the distance between the beams at the first parasitic crossing. This was corrected by introducing an x angle at the IP in the HEB to restore the parasitic crossing distance. During the 3S running we only needed to adjust the x angle about 200 μrad and this change (along with regular luminosity optimization) was sufficient to restore the machine performance to better than that of the optimized 4S running. Another factor was that we ran for 2 months at the 3S and it was in the second month that machine performance was best.

The next step was to run at the 2S resonance which had never been tried before. We succeeded in lowering the HEB energy down to 8.016 GeV, 915 MeV (10%) from nominal 4S running of 8.932 GeV, making the Ecm 10.023 GeV. However, at this low beam energy the HEB ended up being too close to the LEB at the first parasitic crossing and consequently machine performance suffered. Even though we should have been able to further increase the IP x angle, the HEB trajectory required to increase this angle started to get too close to beam pipe walls generating beam lifetime and detector background issues. Luminosity was degraded for the same beam currents we had at the 3S and detector backgrounds significantly increased. We were never able to restore the machine performance to what we had at the 4S or the 3S. We did manage to restore performance to about 90% of the optimized value but detector backgrounds were very problematic throughout the approximately 30 days we ran on the 2S. There was also a brief off resonance run just below the 2S to complete the data set.

The last few days of Run 7, the last run of PEP-II, were used to scan the $E_{cm}$ from the 4S up to over 11 GeV in 5 MeV steps for a total of about 125 steps. This required changing the HEB beam energy upward about 8 MeV on each step. The detector collected data for about 1 hr at each step. As one can see from Fig. 1 the trajectory of the HEB will get straighter and straighter as the beam energy is increased. This will naturally introduce a crossing angle in the x plane at the IP and unless this angle is corrected will also tend to move the beams closer together at the first parasitic crossing. Correcting the IP crossing angle should increase the parasitic crossing distance and improve machine performance. We were able to change the HEB x angle by as much as 1200 μrad, but at the top end of the scan we started to run into background problems in the detector. Efforts to adjust the LEB x angle had limited success. Nevertheless, PEP-II performed very well during this 7 day scan. Energy changes for each step change were implemented using a button macro that changed the entire HEB ring magnets and injection beam line magnets without loosing the stored beam. Each energy change step took about 30 sec. Only near the top of the scan did we start to run onto problems with the increased synchrotron power around the entire ring. The IP beam pipes and masking worked without any problems throughout the entire scan.

### 3.8.4 Summary

PEP-II was a unique machine; the only two ring colliding beam accelerator with a head-on collision. The head-on requirement along with the need for a rapid beam separation led to high-field compact dipole magnets positioned as close to the collision point as possible. The intense synchrotron radiation fans generated from the HEB by these dipoles demanded that these fans strike no nearby beam pipes and be absorbed by obliquely striking the wall of a long copper chamber located 10-20 m from the IP. The next accelerator component outboard of the IP was a shared vertically focusing quadrupole aligned so that the HEB travels essentially along the axis of this magnet. This means the LEB travels far off-axis in this horizontally defocusing magnet further increasing the beam separation and permitting separate beam pipes and separated magnets for the rest of the final focus system for both beams. The separation dipoles and shared quadrupoles were all made from permanent magnet material.

Although designed and optimized for running at the upsilon 4S resonance, the PEP-II interaction region was able to accommodate fairly large HEB energy changes. We were able to run at the 2S resonance (albeit with some difficulty) by adjusting the HEB energy down nearly 0.9 GeV from the nominal 8.9 GeV and we were able to scan the center-of-mass energy from the 4S resonance up to 11.2 GeV a change in the HEB beam energy of about 0.8 GeV. In both cases the permanent magnet quadrupole strengths were left unchanged. The separation dipoles had no tunability. In spite of these limitations, PEP-II performance in terms of delivered luminosity varied by no more than about 10% until the last 1.5 days of the 7 day energy scan where limitations in deliverable RF power and in synchrotron radiation power heating (though not in the interaction region) limited beam currents and therefore reduced the peak luminosity.

### 3.8.5 References

1. “PEP-II an Asymmetric *B* Factory”, Conceptual Design Report, CALT-68-1869, LBL-PUB-5379, SLAC-418, UCRL-ID-114055, UC-IIRPA-93-01, June 1993.
2. J. Seeman, "Last Year of PEP-II B-Factory Operation", proceedings of the 2008 European Particle Accelerator Conference (EPAC08), Genoa, Italy (2008) TUXG01, pg 946.
3. M. Sullivan, *et. al*., “Results from a Prototype Permanent Magnet Dipole-Quadrupole Hybrid for the PEP-II B-Factory”, proceedings of the Particle Accelerator Conference (PAC97), Vancouver, B.C., Canada (1997), pg. 3330.
4. J. Osborn, *et. al*., “Design of the PEP-II Interaction Region Septum Quadrupole”, proceedings of the Particle Accelerator Conference (PAC97), Vancouver, B.C., Canada (1997), pg. 3321.

# 3.9 High-Current Effects in the PEP-II Storage Rings

U. Wienands, R. Akre, K. Bertsche, S. Curry, S. DeBarger, F.-J. Decker, S. Ecklund, A.S. Fisher, J. Fox, S. Heifets, R. Iverson, A. Krasnykh, A. Kulikov, N. Kurita, S. Novokhatski, N. Reek, J. Seeman, M. Sullivan, D. Teytelman, J. Turner, D. van Winkle, G. Yocky, A. Young
SLAC, Menlo Park, CA 94025, USA
Mail to: uli@slac.stanford.edu

## 3.9.1 Introduction

The PEP-II B-Factory operated at peak and integrated luminosity several times the original design values. Its storage rings operated at world-record beam currents with bunch lengths of about 10 mm. Correspondingly significant heat load was imposed on the vacuum system, both due to synchrotron radiation and by energy loss into higher-order modes. The latter in turn would lead to local heating or discharges wherever such energy got absorbed. Over the course of PEP-II running we experienced numerous such effects, which lead to upgrade programs of significant scope. In the following we will describe the most significant of such effects and their mitigation:

- Upgrades and repairs of RF seals and shields in both rings
- Redesign of overheating stripline kicker electrodes to withstand higher powers
- Redesign and replacement of BPM buttons following failure

## 3.9.2 Discharges in the Vacuum System

### *3.9.2.1 Fast LER Instability Observations*

During Run 5, the beam in the PEP-II Low Energy Ring (LER) became affected by a predominantly vertical instability with very fast growth rate of 10...60/ms and varying threshold. The coherent amplitude of the oscillation was limited to approximately 1 mm peak and would damp down over a few tens of turns, however, beam loss set in even as the amplitude signal damped, causing a beam abort. This led to the conclusion that the bunches were actually blowing up. The appearance of a $2\nu_s$ line in the spectrum suggested a possible head-tail nature of the instability, although chromaticity was not effective in changing the threshold. The crucial hints in tracking down the cause turned out to be vacuum activity near the RF cavities and observance of signals on the cavity probes of certain RF cavities.

Figure 1 shows the signature in the vertical plane of the observed transverse instability in the PEP-II LER [1]. The growth rate of the initial transient was evaluated to be between 10 and 60 $ms^{-1}$, much faster than any previously known instability in the LER. The maximum coherent amplitude was limited, typically no more than ±1 mm peak. Damping of the coherent motion occurred on a similar time scale, although residual coherent motion remained detectable until the beam was lost due to loss of charge triggering a beam-loss-rate interlock. When plotted together with the measured

bunch charge a striking observation was that the loss of charge occurs *after* the coherent signal was already significantly reduced, indicating growth of the bunches rather than coherent oscillation.

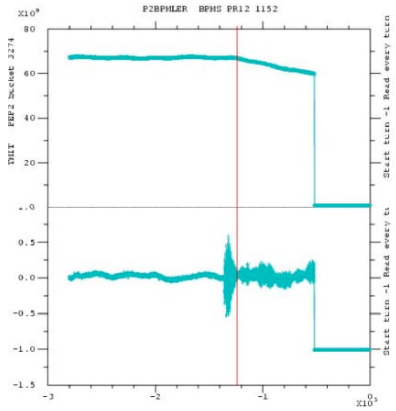

**Figure 1:** Loss of bunch charge (top). Fast LER coherent instability (bottom).

The motion observed involved the whole beam, as indicated in Figure 2. A modal spectrum showed only low-lying modes (see Figure 3).

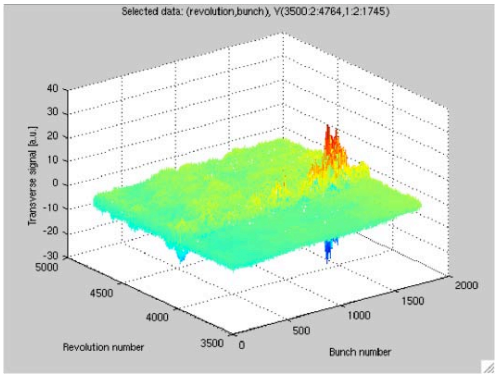


**Figure 2:** Bunch-by-bunch vertical position of the beam.

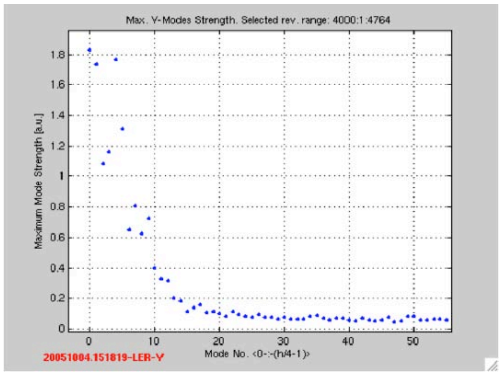


**Figure 3:** Modal spectrum of the motion during instability.

The transverse profile of a typical bunch in the ring was imaged on every 80$^{th}$ turn (0.6 ms spacing) by a synchrotron-light diagnostic using a rotating mirror [2]. Light

from each turn is narrowed in x and stretched in y to separate the images while showing the change in vertical size. A small centroid motion is visible in one image just before the onset of a rapid blow-up, which was seen in both x and y projections, followed by the abort (see Figure 4).

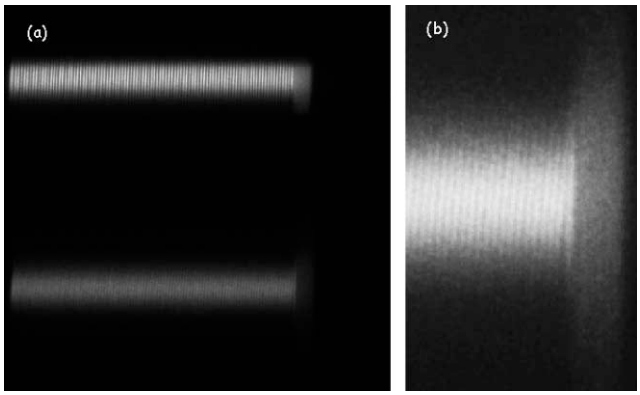


**Figure 4:** Sudden beam-blow-up in the LER, followed by an abort. (a) 125 images of one bunch, taken on every 80th turn (73 ms total). (b) A magnified view of the lower trace of (a), starting just before the instability. Centroid motion is visible in one image before the blow-up begins.

A further signature specific to this instability were spectral lines at $2\nu_s$ which are not normally seen in the LER. Figure 5 shows a "spectrogram" (frequency *vs* turn number) for about 4800 turns, at the end the beam aborted. Onset of the instability is clearly seen as is the onset of the $2\nu_s$ line. This hinted at a possible head-tail nature of the instability.

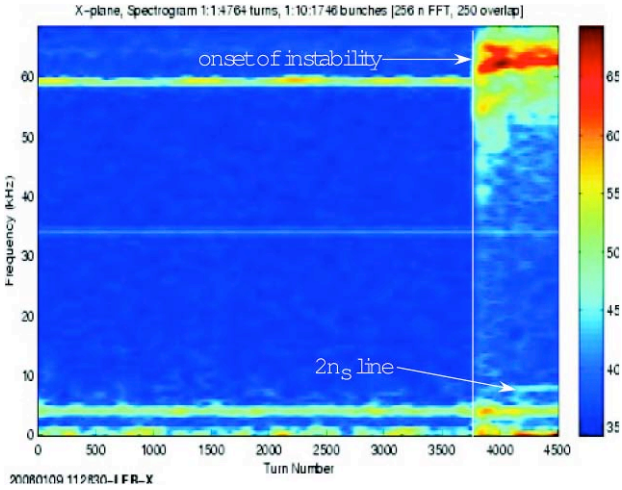


**Figure 5:** Vertical frequency spectrum *vs* turn.

To further analyze and determine the nature of the instability a series of experiments was undertaken:

- Threshold vs tune chromaticity
- Threshold vs bunch current
- Threshold vs RF voltage (bunch length)
- Running with TFB system off

However, no significant effect on the instability threshold could be produced, there was a signal detected on the field probes of the RF cavities in RF station 4-2 of the LER. Figure 6 shows a representative plot of the observed signals, such signals were not seen for the other RF cavities in the same region. Close inspection of the RF data also revealed an apparent additional energy loss of about 140 keV/turn during the phase of beam loss, evidenced by a shift in the synchronous phase. Given abort thresholds of 2...2.5 Amps beam current and a duration of the whole event of a few hundred turns, this corresponds to roughly 1 kJ of energy dissipated at the location of the event.

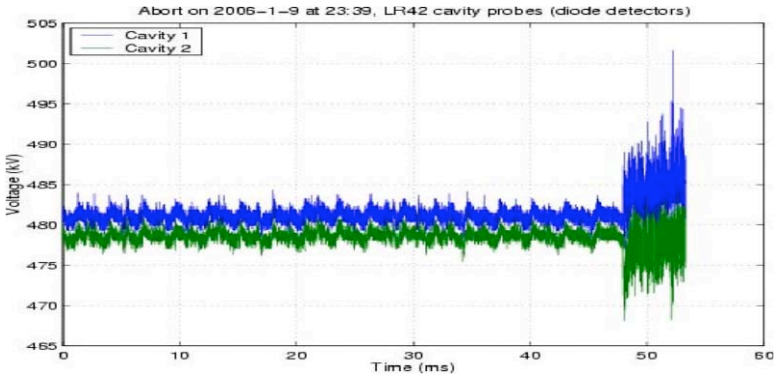


**Figure 6:** Signal of LER RF 4-2 cavity probes during instability.

A coincident spike in vacuum pressure observed in and near the RF cavities of the first RF station in Region 4 allowed localization of the events. A pump in between the cavities showed an even stronger signal. Borescoping the area indicated by the vacuum spikes revealed an RF seal ("gap ring") that was misplaced, apparently during installation of this pair of RF cavities. The misplaced ring is visible in Figure 7. On removal the ring showed discoloration and evidence of discharge. Moreover, copper could be seen having coated the vacuum chamber near the gap ring, indicating significant sputtering. The fields from the discharge apparently were broadband enough to be detectable by the cavity probe even though cutoff of the vacuum pipe is around 2.5 GHz, compared to 476 MHz RF frequency.

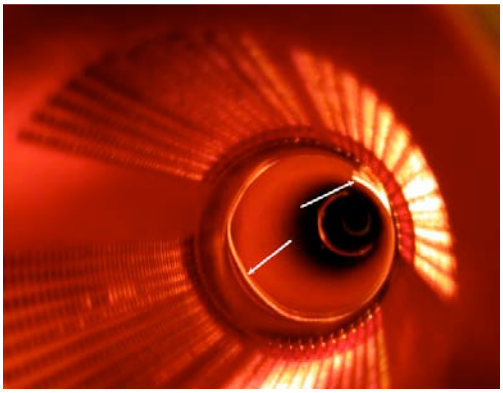

**Figure 7:** Dislocated RF seal in the LER vacuum chamber.

### *3.9.2.2 HER Discharge-Induced Instabilities*

#### 3.9.2.2.1 Characteristics of Instability

Two different signatures emerged in the HER ring, termed "Tiny Y" and "Ridge" according to the visual signature seen on a 3-d plot of beam position *vs* turn# and bunch#. Figure 8 shows an example of each. The data were acquired upon a beam abort with a fast digitizing system using signals from the transverse feedback systems [3]. Vacuum activity was seen coincident with many (though not every) occurrences of either instability.

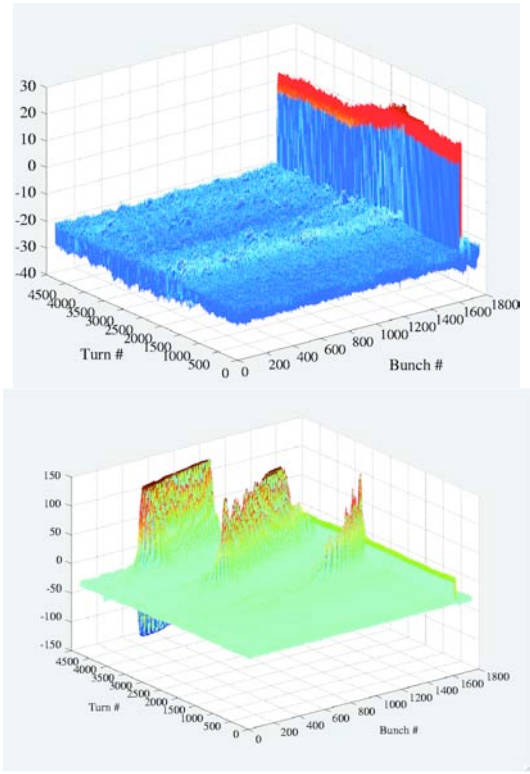


**Figure 8:** Transverse motion of "Tiny Y" instability (top, the abort gap is at high bunch numbers; "tiny-Y" motion starts at about turn 1500) and "Ridge" instability (bottom).

#### 3.9.2.2.2 "Tiny Y" Instability

This instability was characterized by quite small coherent amplitude, setting in along the whole bunch train at once. The spectrogram (tune $\nu_s$ time, see Figure 9) was rather noisy although it was clearly dominated by the vertical betatron frequency. Occasionally the horizontal betatron tune was also seen with significant or even dominant amplitude. The similarity to the "fast vertical" instability in the LER mentioned above is rather striking even though in case of the HER there was no observable effect in the longitudinal plane. The modal spectrum is shown in Figure 10 for the first 20 modes. There appears to be rapid initial growth of the 0 mode whereas a cluster around modes 8...10 is seen to grow at a slower rate, when the 0 mode is actually damping.

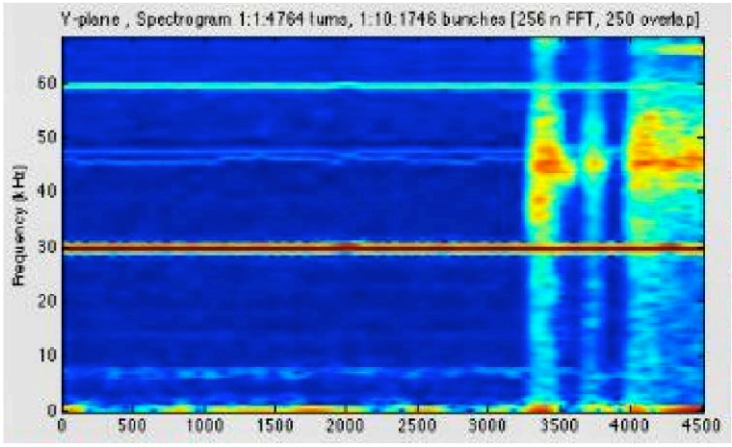


**Figure 9:** Spectrogram of "tiny-Y" instability.

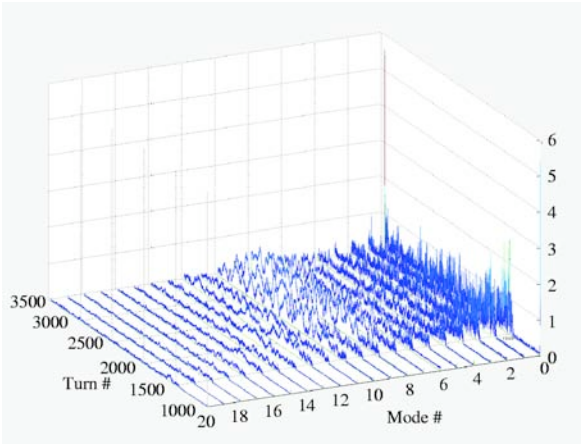


**Figure 10:** Modal spectrum *vs* turn # of "tiny-Y" instability.

The instability led to beam abort due to increased background in the detector, often within 10...20 ms of instability onset. In many cases a coincident pressure spike was observed. Analysis of a number of such events allowed us to identify a few locations in the HER where vacuum components were possibly failing. This evidence was sometimes corroborated by thermal activity.

3.9.2.2.3 "Ridge" Instability

As time progressed a wave of motion was moving from the head towards the tail of the beam, see Figure 11, bottom part, where the modal decomposition of the motion is shown. At the kicker gap, the process appeared to be interrupted, bunches at the head of the train tend to have rather smaller amplitudes of oscillation. A cluster of modes around 5...10 was growing to dominance. Overall amplitude of the oscillation was much larger than in the "Tiny Y" case, somewhat obscuring the amplitude of the 0 mode which was comparable to the one seen in the "Tiny Y" instability. Growth rates were on the order of 1 /ms, much slower than for the "Tiny-Y" signature but still quite fast. Again, "Ridge"-type instability was often accompanied by vacuum activity. In addition, the apparent interruption of coupling between bunches suggested that trapped ions could be the origin of this instability; the species being light enough to be swept out by the gap.

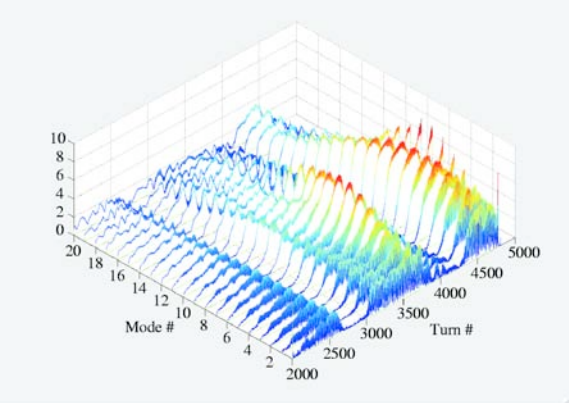


**Figure 11:** Modal spectrum *vs* turn # of "Ridge" instability.

#### *3.9.2.3 Vacuum System Symptoms*

Given the vacuum activity seen and the corroborating evidence obtained from thermal monitoring, suspect vacuum joints were opened and the adjacent components inspected. The first find was a shielded bellows unit with its shield fingers severely damaged and with clear signs of heat and sputtering or evaporation of the Ag coating, Figure 12.

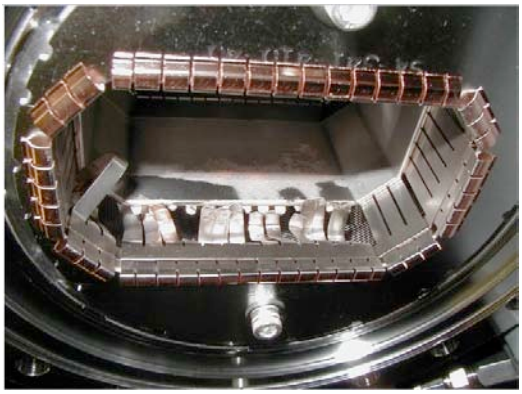

**Figure 12:** Damaged rf shield of a bellows unit.

Replacement of three units damaged in this way immediately brought relief in the rate of beam aborts although it did not reduce the vacuum-induced aborts to zero. In further inspections no more damaged bellows were found but a number of rf seals across flange joints were showing evidence of heat and melting (see Figure 13). All of these problems arose at joints involving "flex flanges"[4], at which the two chamber ends can move (flex) against each other with the rf seal fingers supposedly following such movement. For the last run, all such seals in the machine were replaced with seals of a new design using Inconel for the fingers and thermal monitoring was installed at the Flex Flanges.

**Figure 13:** Damaged rf seal from a flex-flange connection.

#### *3.9.2.4 Analysis*

The "Ridge" type instability suggests a mechanism coupling the bunches together. A disturbance that originates at a certain point in time and via bunch-to-bunch coupling travels along the train until it reaches the gap, which appears to a certain extent stopping the disturbance. After that it may start again. The dominance of modes 5...10 arises from a fine-structure visible within the ridges as shown in the magnified view in Figure 14. The period of the fine structure is 60...100 turns depending on the amplitude, or a frequency of about 1 to a few MHz. This is consistent with typical ion-oscillation frequency in the HER, seen e.g. when vacuum conditions were poor [5]. We therefore may conclude that the observed instability indeed is consistent with being induced by ions.

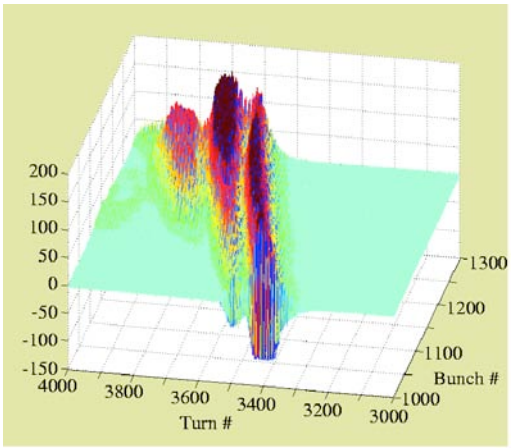


**Figure 14:** Fine structure of beam motion within a ridge.

The "Tiny-Y" signature is different and has defied an easy explanation. The small observed amplitude is inconsistent with the radiation it caused in the BaBar detector. However, there is evidence of bunch growth from fast synchrotron light monitoring, Figure 15, hinting at a single-bunch effect or at scattering of particles off material. The rather similar "fast vertical instability" seen in the LER [6] was most likely caused by metal vapor injected into the beam. These potentially fairly heavy and ionized objects

may not move appreciably on the time scale of the observation (35 ms); on the other hand, if quantity and state of ionization are sufficiently high they may affect the beam motion, leading to the small observed coherent signal.

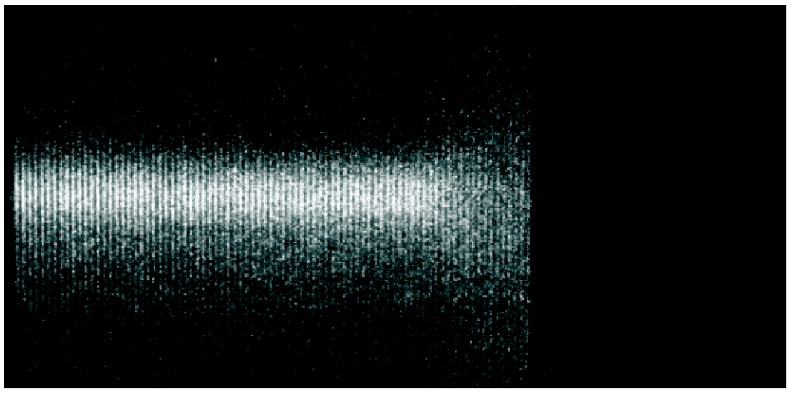

**Figure 15:** Vertical bunch size *vs* time, 80 turns increment.

Modes in the bellows structure were analyzed [7] up to 4 GHz; the lowest mode would be about 100. However, estimating the exact frequency spectrum of an actual bellows was very difficult due to the uncertainty in the exact compression of the unit, therefore, the estimate cannot be conclusive.

#### *3.9.2.5 Q2 Bellows*

A particularly difficult discharge issue arose in one of two bellows named "Q2 Bellows" in the common beam pipe near the detector. This bellow has ceramics tiles exposed to the beam, serving as an absorber for HOMs emanating from the irregular geometry in the interaction region (IR). The symptoms observed were vacuum bursts as well as instability of in particular the HER electron beam. The instability was readily identified as an ion-induced instability, but the source of the gas bursts remained elusive. RGA spectra proved inconclusive as did inspection with a borescope and even attempts to find lose tiles on the bellows by mechanical methods. The bellow itself was difficult to reach, being mostly buried within the detector, so de-installation was delayed until a spare could be ready. Once removed from the beam pipe, the issue was identified as discharges at one location involving a few of the ceramics tiles, see Figure 16. The traces of the discharge were not detectable from the inside of the beam pipe. The root cause of the discharge was identified as a small gap where the rf seal touched a tile rather than the metal of the flange, i.e. not making proper contact [8].

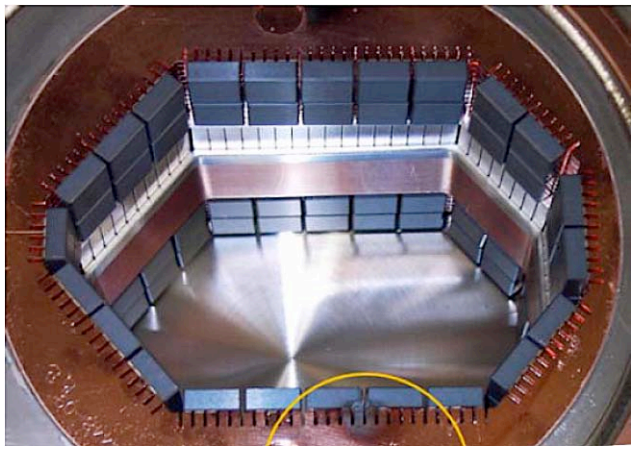

**Figure 16:** Q2 bellow showing traces of discharge near the ferrite.

### 3.9.3 BPM Button Heating

A serious issue was uncovered in the LER when its bunch length was reduced in order to mitigate the hourglass reduction of luminosity. A number of top BPM button electrodes fell off their feedthrough and, in one case, ended up lodged on a button at the bottom in such a way as to greatly increase the power induced into the bottom button, causing excessive heating and failure of the bottom feedthrough. The issue was traced to a loosening of the pressfit joint between the stainless steel button electrodes. As it heats up, the stainless steel expands faster than the molybdenum used for the feedthrough and the fit ultimately becomes too loose. Figure 17 shows a button fallen off the top feedthrough and resting on the bottom of the LER vacuum chamber.

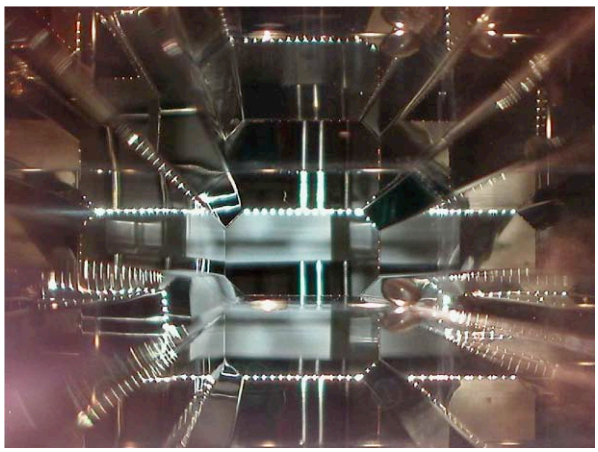

**Figure 17:** Photograph of a BPM button fallen off and resting on the bottom of the vacuum chamber.

The power in the button was thought to be primarily absorbed in a circumferential resonance at about 7 GHz for the 1.5 cm diameter buttons. According to this hypothesis, the absorbed power would scale with bunch length to a power of roughly 2, reflecting the increase in higher frequency content of the shorter bunches. A numerical estimate of the relative scaling with bunch current for different RF voltage in the LER -taking into account bunch lengthening - is shown in Figure 18.

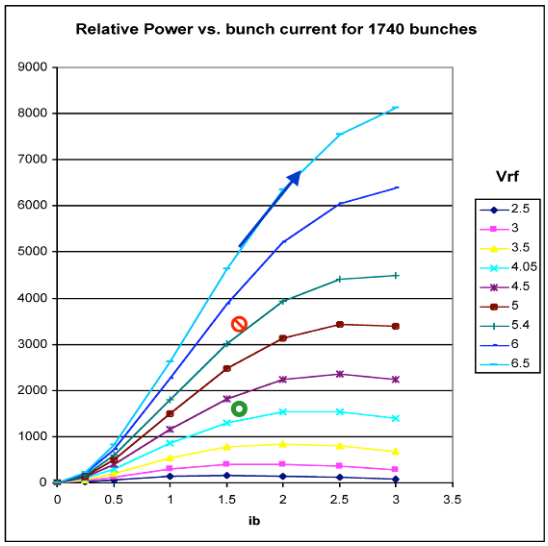


**Figure 18:** Relative BPM power dissipation *vs* bunch current for different RF voltages.

The issue presented a serious limit to the LER performance and the luminosity potential for PEP-II. The only practical way to reduce the power induced in the buttons was to reduce their size: a 7-mm button would absorb roughly a quarter of the power (potentially even less since the frequency of the resonance also increases significantly, so less power is available for any given bunch length). In the LER arc regions, the BPM feedthroughs are flanged so whole-sale replacement was conceivable and in fact was done. The new design employed 7-mm buttons and - as an added measure - the new buttons were made of molybdenum and an integral part of the inner conductor of the feedthrough so even excessive heat could not make the come off. The situation was more difficult in the interaction region, where most of the difficulties seemed to be located. There the BPMs are welded into the copper chambers, and replacement was not practical. Instead, it was decided to pull the buttons off and use only the feedthrough pins to detect the beam. With the high beam currents signals would be quite reasonable. This was achieved using a "collet", a manually operated device with a circular clamp closing around the button and then vertically pulling it off. In this way almost 100 buttons were pulled successfully with only one or two failures (where a leak developed in the feedthrough and had to be sealed).

### 3.9.4 Upgrades of Feedback Kickers for Higher Beam Current

#### *3.9.4.1 Stripline Kicker Electrodes*

Once the PEP-II storage rings reached beam-currents above 1 A, significant heating of the electrodes was observed using optical pyrometers. Since the temperatures observed appeared unreasonably high, the pyrometers were recalibrated using a spare pyrometer and a prototype of the longitudinal feedback kicker. This prototype had a geometry similar to the kickers considered here and an identical fused-silica window. The recalibration somewhat lowered the measured temperatures but they continued to be high, see Figure 19. A calorimetric method was therefore used to estimate the power dissipation in the kickers as the pyrometer calibration was deemed not reliable. This measurement essentially confirmed the pyrometer readings. Details are given in [9].

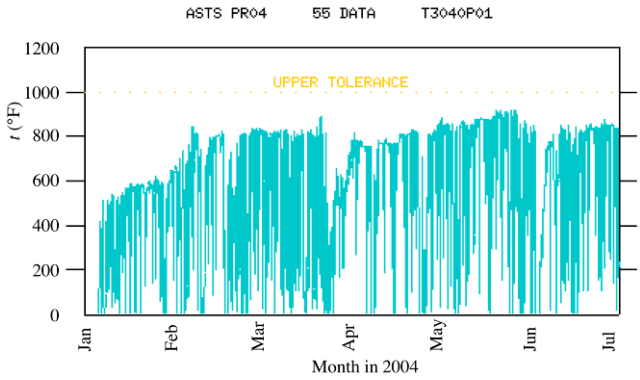


**Figure 19:** History of pyrometer reading.

### *3.9.4.2 High-Temperature Electrodes*

To allow for running at elevated temperatures, the electrodes were redesigned using molybdenum. Molybdenum turned out to be the material of choice for various reasons. It can withstand high temperatures, and it has a coefficient of thermal expansion three times lower than that of aluminum. Its electrical conductivity is about half that of aluminum, however, because of skin effect this translates into only 40% increased power dissipation which then causes only small additional temperature rise. In the 1950s, experiments with oxidation of various metallic surfaces showed that Mo will produce a stable oxide layer with high emissivity in the interesting IR range when baked in air at or below 530°C (1000°F)[10]. A series of tests was performed using Mo coupons and full-size samples, baking them and then measuring the emissivity. Figure 20 shows that an oxidized molybdenum coupon has emissivity in excess of 0.6 while a full-length electrode still had about 0.5. In comparison, one of our spare CuO coated electrodes measured less than 0.5, significantly below the nominal value of ε=0.8.

HFSS simulations and TDR measurements taken using a prototype of the kicker were used to design a modified geometry at the ends in order to improve the match of the kicker to the drive.

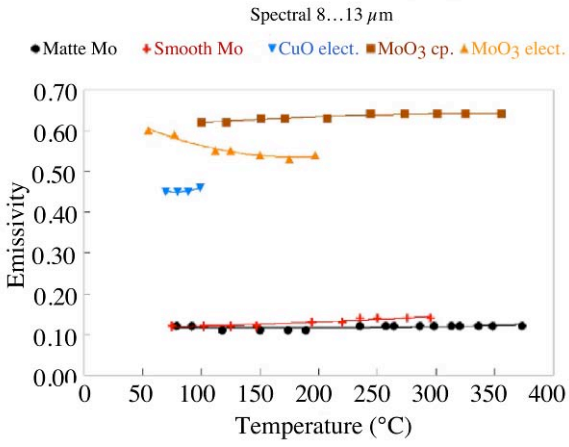


**Figure 20:** Emissivity of various surfaces.

The LER kickers with Mo electrodes was assembled and installed. The kicker performed very well. A difficulty arose when it was found that the electrodes of the horizontal kicker sagged due to their considerable weight. Supporting pins made from Macor were added to the ends to prevent this from becoming an issue, however, these pins led to discharge and failure. The spare kicker with molybdenum electrodes performed flawlessly until the end of PEP-II operation.

### 3.9.5 References


1. M. Zisman *et al.*, Proc. 1999 Part. Accel. Conf., New York, NY, p. 293.
2. A. Fisher, Proc. Beam Instrumentation Workshop 2006, FNAL, Batavia, US, 2006, and SLAC-PUB-11851, May 2006.
3. R. Akre et al., Proc. European Particle Accelerators Conference, EPAC06, Edinburgh, UK, June 2006, p. 3028.
4. M. Nordby et al., "A Zero-Length Bellows for the PEP-II High Energy Ring", Proc. Particle Accelerators Conference, Dallas, US, 1995, p. 2051.
5. D.Teytelman, 2006, unpublished.
6. U. Wienands et al., Proc. European Particle Accelerators Conference, EPAC06, Edinburgh, GB, June 2006, p. 658.
7. A. Novokhatski, 2006, unpublished.
8. A. Novokhatski et al, Proc. PAC07, Albuquerque, NM, p. 4213.
9. U. Wienands et al., Proc. EPAC 2004, Lucerne, CH, p. 2843.
10. W.R. Wade, NACA TN 4206, Langley Aeronautical Laboratory, Langley Field, Va, March 1958.


## 3.10 Experiments on Electron Cloud Mitigation at PEP-II


Johnny S. T. Ng and Mauro T. F. Pivi
SLAC, Menlo Park, California 94025, USA
Mail to: jng@SLAC.Stanford.Edu


### 3.10.1 Introduction

The electron cloud effect has been observed at many accelerator facilities. It has been the subject of many workshops and reviews [1, 2]. An electron cloud is formed when low energy photoelectrons released from the vacuum chamber surfaces and ionized residual gas molecules, driven by the beam fields of passing positively charged bunches, impinge on the chamber walls and create secondary emission. It is an important issue for many currently operating facilities and the damping rings of the proposed International Linear Collider (ILC) because beam-cloud interaction can severely impact the machines' performance.

Systematic studies on the electron cloud effect, and its possible remedies, have been carried out in many laboratories. At SLAC, the effort has been concentrated on theoretical understanding with the aid of computer simulations, and experimental measurements with high intensity positron beams at PEP-II. Computer simulation results have been presented at ECLOUD07 [1] and in an earlier article in this journal

[3]. In this article, we present recent results from electron cloud experiments at the positron storage ring of PEP-II. In particular, we discuss the performance of various mitigation techniques.

### 3.10.2 Remedies for Electron Cloud Build-up

The primary reason for the build-up of an electron cloud is that the number of secondary electrons emitted per incident primary electron is greater than one. The multipacting process responsible for this has been reviewed elsewhere [4]. The main goal of various proposed remedies is to mitigate multipacting by reducing the secondary electron yield (SEY). The SEY is a characteristic of the chamber wall material, and it depends on the primary electron's incident angle and energy. At a given angle, the SEY rises rapidly with the primary's energy, reaching a peak value, and then decreases slowly at higher energy. Its dependence on incident angle (with respect to normal to the wall) is approximately $1/\cos\theta$. The typical peak SEY values ($\delta_{\max}$) for as-received chamber material range from 1.5 to 2.2, and can be higher for aluminum. For the ILC damping ring, the single bunch instability threshold requires that $\delta_{\max} < 1.2$.

At PEP-II and KEKB, solenoid windings operating at low fields have successfully suppressed electron clouds by trapping secondary electrons close to the wall, thus reducing beam-electron interaction. It is, however, only feasible to install windings in sections of the beam line free of magnets. Future high-performance machines also require much stronger suppression of the electron cloud. The goals of the experimental program at PEP-II were to systematically investigate a) the effect of beam exposure and coating on SEY, b) the effectiveness of grooves in field-free regions, and c) mitigations in a magnetic dipole field. (The clearing electrode method for a positron storage ring has been demonstrated recently at the KEKB facility [5]; it will be not discussed further here.)

### 3.10.3 The Effect of Beam Conditioning and Coating on SEY

In this experiment [6], the secondary emission yield of samples of selected chamber materials were measured before and after exposure in high-intensity beam environment, a process called beam conditioning where the sample surface was bombarded by electrons and photons, thus "scrubbing" off undesirable contaminants. A dedicated stainless steel chamber was used. Several test samples were mounted in pairs on the chamber wall, one exposed to direct synchrotron radiation at $0^o$, while the other was positioned outside the radiation fan at $45^o$. When sufficient beam exposure had been accumulated, the samples were retrieved from the beam chamber, and transferred under ultra-high vacuum to a laboratory for detailed surface analysis.

One approach to reduce surface SEY is to coat it with a material, such as TiN, with low secondary electron yield. TiN is known as an effective coating material for reducing multipacting in RF couplers. Its effectiveness was studied using an aluminum substrate, where a 100 nm thin-film was deposited by reactive sputtering of Ti in an Ar/10%$N_2$ atmosphere. The results are shown in Figure 1 for the two samples (one inside and one outside the synchrotron radiation fan), before and after two months of beam conditioning with a dose of approximately 40 mC/mm$^2$ [6]. For TiN coated aluminum, $\delta_{\max}$ was measured to be 1.7-1.8 before beam conditioning; it decreased to

~0.95 afterwards. Note that the results are similar for the two samples. Spectroscopic analysis indicated that beam "scrubbing" had significantly reduced the carbon and oxygen content on the sample surface. The effect of recontamination was also studied. The sample was exposed to $H_2$ and CO atmosphere at $10^{-9}$ Torr, typical for accelerator vacuum, for ~1000 hours. The TiN coating was found to be stable, and $\delta_{max}$ remained below 1.0. The main concern regarding TiN is its long term structural stability. This will be investigated with sections of TiN coated vacuum chamber which had been exposed to beam throughout PEP-II's operating lifetime. The as-received aluminum used in this experiment had a $\delta_{max}$ of 3.5, which was reduced to 2.4 after beam conditioning.

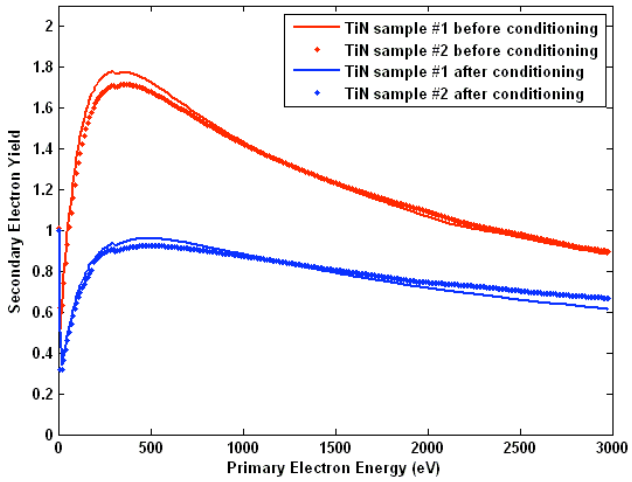


**Figure 1:** Secondary electron yield as a function of incident electron energy for TiN coated aluminum chamber, before and after exposure to high-intensity beam.

The TiZrV non-evaporative getter (NEG) material developed at CERN is believed to have superior long-term structural stability [4, 7]. This material was also investigated. The as-received maximum SEY of TiZrV coated samples was measured to be ~1.6, and it decreased to ~1.3 after heat activation at 200 $^{o}$C for more than 2 hours. It was further reduced to ~1.05 after several weeks of beam conditioning.

### 3.10.4 Performance of Grooved Chamber

Simulation studies indicated that incorporating grooves on the chamber walls may suppress multipacting by reducing the escape probability of secondary electrons near the surface [8]. Two aluminum test chambers were fabricated to evaluate this mitigation technique. One chamber had rectangular grooves extruded on its inner surface along the length of the chamber, while the other chamber was fabricated with a smooth surface as a reference. Both were coated with TiN. A photograph of the grooved chamber is shown in Figure 2. Two such pairs of chambers were installed in a magnetic-field free straight section of the PEP-II low energy ring (LER). Care was taken to properly align the chambers. A horizontal misalignment would result in the upstream chamber masking the synchrotron radiation. This would cause an artificially lower photoelectron generation in the downstream chamber.

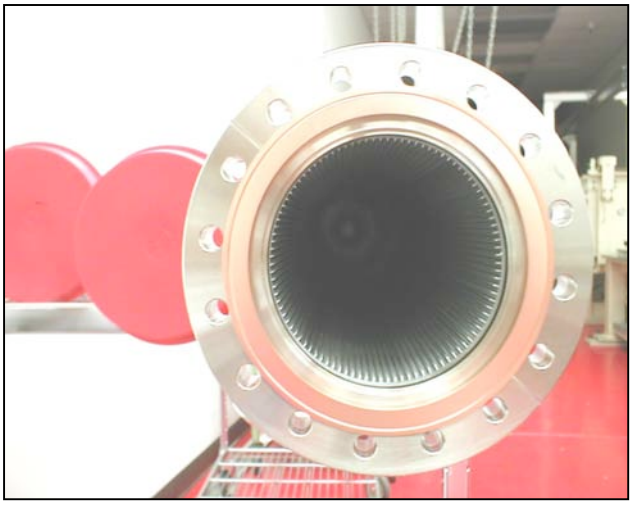

**Figure 2:** End-view of the grooved chamber.

The electron flux at the chamber wall was measured using a pickup electrode. The grooves were found to be effective in suppressing electron clouds, since the signal in the grooved chamber was approximately a factor of 20 smaller compared to the reference chamber, at a beam current of 2500 mA. The corresponding SEY could be extracted from the beam current dependence of the measured flux. But a large set of simulations with various photoelectron yield and SEY, with detailed description of the grooved profile in the code, would be required.

### 3.10.5 Electron Clouds in Dipole Magnetic Field

The two experiments described so far took place in magnetic-field free regions where there was easy access to the beam vacuum chamber. Magnetic elements, however, are critical components of any machine. Properties of the electron cloud there need to be understood to be able to properly model its impact, and appropriate mitigation techniques must be developed. In this section we discuss the chicane experiment at PEP-II where detailed investigation of the electron cloud and studies of possible mitigations in a dipole magnetic field were carried out [9].

The chicane was installed in a dedicated straight section of the PEP-II LER, downstream of the two experiments described earlier. The vacuum chamber sections in the first three dipoles were instrumented with electron detectors. The first chamber section was uncoated aluminum, while the other two were coated with TiN. Each detector consisted of a transversely segmented retarding field analyzer (RFA), housed in an aluminum box welled on top of the vacuum chamber. An array of holes in the chamber wall allowed cloud electrons to be detected with minimal disturbance. The RFA was capable of measuring the flux at the chamber wall, the (vertical) energy spectrum, and the lateral distribution of the cloud electrons. A photograph of the apparatus in the first dipole is shown in Figure 3.

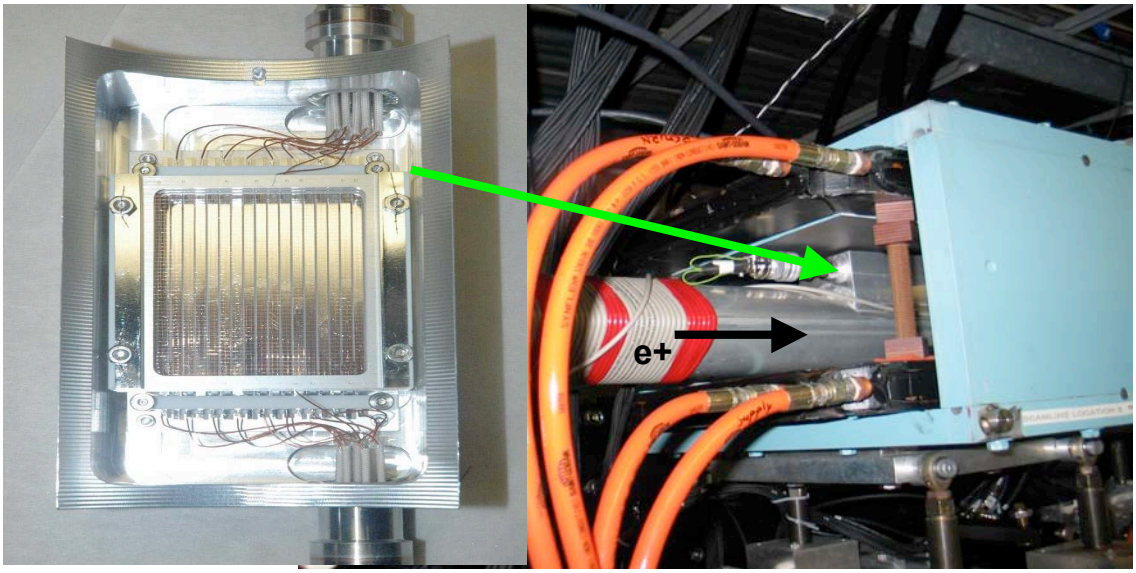


**Figure 3:** Photograph of the apparatus in the first dipole. On the left is a picture of the exposed RFA where the transversely segmented collector stripes are visible. On the right is a picture of the dipole showing the location of the RFA with respect to the beam line and the dipole field region.

The chicane configuration allowed the experiment to operate parasitically, with PEP-II delivering full luminosity for the B-factory. The electron cloud signal was measured as the positron beam current ramped up. The results are shown in Figure 4 for uncoated as well as TiN coated aluminum at fixed dipole field strength of ~861 G.

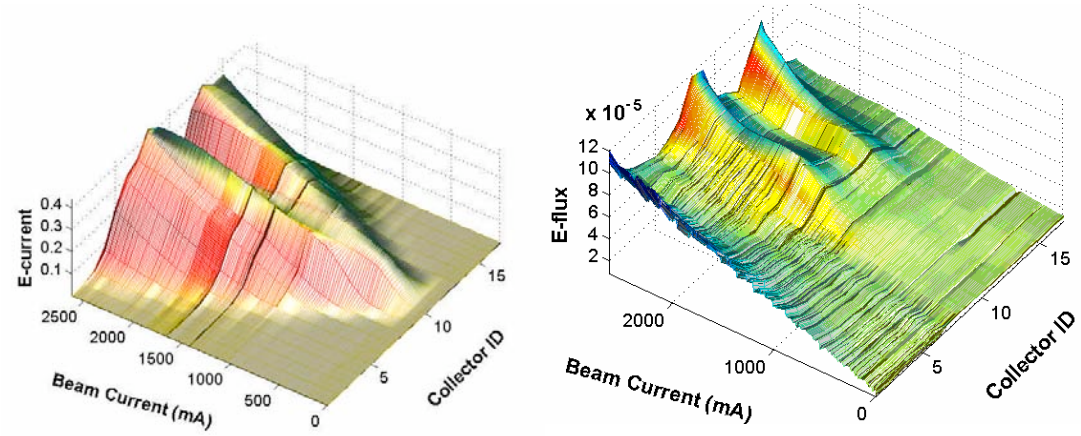


**Figure 4:** Electron cloud signal as a function of beam current for all RFA collectors, for uncoated aluminum (left) and TiN-coated aluminum (right) chambers. The dipole field was at 861 G.

Note that signal for TiN coated aluminum is 3 orders of magnitude smaller. As the beam current increases, the momentum imparted by the beam field to the cloud electrons increases as well. In particular, for an electron in close proximity to the beam

transversely, the vertical energy gain can be large enough so that it is above the energy of the SEY peak, and its secondary electron production rate decreases. For aluminum, this can be seen to occur at a beam current of ~800 mA, above which the signal detected in the central collector stripes decreases, resulting in a double-peaked lateral profile. This is characteristic of cloud electron distribution in a dipole field [10].

Motivated by recent simulation studies [11], the dependence of electron cloud dynamics on dipole field strength was also investigated. As the field strength varied, the relative phase of the electron's gyration motion with respect to beam arrival time also varied. On average, the simulation (using ILC parameters) indicated that in-phase electrons would gain more energy than out-of-phase electrons. And because the electrons initially have low energy, the in-phase electrons would also produce more secondary electrons. Thus, the electron flux is expected to modulate as the dipole field strength is varied. The result for aluminum chamber is shown in Figure 5 at beam current of 2500 mA, where the dipole field strength is given by the ratio $n$ of bunch spacing to electron cyclotron period ($\hat{o}_c = 2\pi \cdot m_e/eB$), representing the number of gyrations executed by an electron between consecutive bunch crossings. Note the peaks and valleys separated by integer values of $n$. The electron cloud flux, and presumably the density, modulated by a factor of 3 peak-to-valleys. This effect could be exploited as mitigation for future colliders by adjusting the dipole field strengths by a few tens of gausses to operate in the minimum flux regime. As can be seen from Figure 5, the data show complex features, especially as a function of transverse distance from the beam, suggesting intricate electron cloud dynamics caused by a highly non-uniform space charge force. Simulation studies have started to better understand this effect, and gain more insight into the electron cloud properties in a magnetic dipole field.

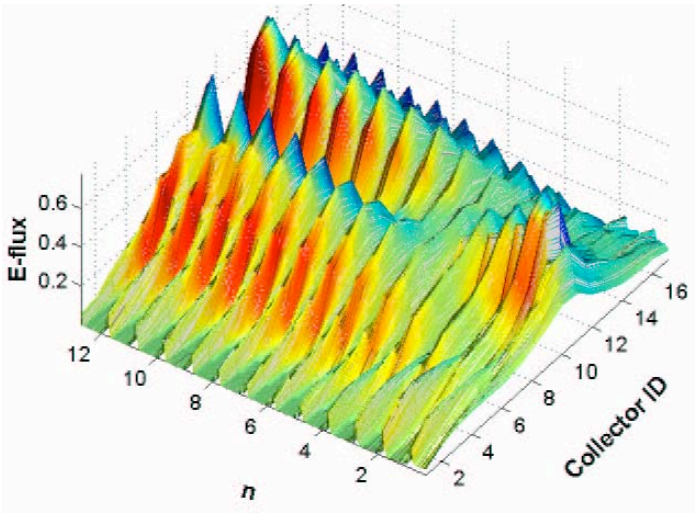


**Figure 5:** Electron cloud signal as a function of dipole field strength for all RFA collectors. Note the resonance peaks separated by integer values of the parameter $n$, the ratio of bunch spacing to electron cyclotron period. Beam current was 2500 mA.

### 3.10.6 Outlook and Summary

Even though experimental electron cloud work has been completed with the decommissioning of PEP-II, SLAC continues to be a key collaborator in experiments at

other laboratories. The experimental apparatus described here have been dismounted from PEP-II, and re-deployed at the CesrTA facility [12]. In addition, a new grooved chamber, with triangular profile optimized for mitigation in a dipole, is being fabricated and will be installed at CesrTA for further studies.

In summary, electron clouds and possible mitigation techniques have been investigated in detail in experiments at PEP-II's positron storage ring. TiN coating was found to be particularly effective in suppressing secondary emission. Its maximum SEY was measured to be below 1, sufficient for the single bunch stability requirement at the ILC damping ring. The remaining issue of long term structural stability will be studied. Complementary approaches were also studied. The grooved chamber was effective in experiments in magnetic-field free regions, and a version for use in a dipole will soon be tested. An experiment in a chicane indicated that TiN coating reduced the electron cloud flux by three orders magnitude. Furthermore, novel magnetic resonance effect was observed experimentally for the first time. This set of detailed data provides stringent constraints on simulation codes, allowing quantitative and reliable model predictions for the electron cloud effect in future machines.

### 3.10.7 Acknowledgments

We thank the SLAC support staff and the PEP-II operations team for their contributions that made these experiments possible. We are grateful to our colleagues for many helpful discussions, especially to F. Cooper, R. Kirby, F. King, D. Kharakh, C. M. Spencer, T. O. Raubenheimer, L. Wang, C. Celata, and M. Furman. We also thank F. J. Decker, S. DeBarger, J. Seeman, M. Sullivan, U. Wienands, and W. Wittmer for their support during commissioning of the experiment. Work supported by the U.S. Department of Energy under contract number DE-AC02-76SF00515.

### 3.10.8 References

1. Proc. Int. Workshop on Electron-Cloud Effects, edited by H. Fukuma et al. (Daegu, Korea, 2007), and references therein.
2. ICFA Beam Dynamics Newsletter No. 33, edited by K. Ohmi and M. Furman (2004).
3. M. Pivi and T. Raubenheimer, "Electron Cloud Effect in the Linear Colliders", in [2], p. 64.
4. F. Zimmermann, "Electron Cloud Build Up in Machines with Short Bunches", in [2]. P. 14.
5. Y. Suetsugu et al., "Demonstration of electron clearing by means of a clearing electrode in high-intensity positron ring", Nucl. Instr. Meth. A 598 (2009) 372.
6. M. Pivi et al., in Proc. 11th Euro. Part. Acc. Conf. (Genoa, Italy, 2008) MOPP064.
7. C. Benvenuti et al., Vacuum 60, (2001) 57.
8. L. Wang et al., "Suppression of secondary emission in a magnetic field using triangular and rectangular surfaces", Nucl. Instr. Meth. A 571 (2007) 588.
9. M. T. F. Pivi and J. S. T. Ng et al., preprint SLAC-PUB-13555, March 2008; also see Proc. 11th Euro. Part. Acc. Conf. (Genoa, Italy, 2008) MOPP063.
10. J. M. Jimenez et al., LHC Project Report 632 (2003).
11. C. Celata et al., Phys. Rev. ST Accel. Beams 11, 091002 (2008).
12. M. A. Palmer et al., in Proc. Part. Acc. Conf. (Albuquerque, NM, 2007), p.42.

## 3.11 Electron Cloud Instability in KEKB and SuperKEKB

Hitoshi Fukuma
High Energy Accelerator Research Organization (KEK)
Oho 1-1, Tsukuba, Ibaraki 305-0801, Japan
Mail to: hitoshi.fukuma@kek.jp

### 3.11.1 Introduction

A large number of electrons called "electron cloud (EC)" can be formed in positron or proton rings. Main sources of the EC in positron storage rings are photoelectrons generated by the synchrotron radiation and secondary electrons. The photoelectrons are attracted by a positive beam toward the center of a beam chamber and hit the opposite wall where the secondary electrons are generated. Under some operational conditions of machines rapid growth of the electrons known as a beam induced multipacting can occur to form the EC. The EC causes various effects on the beam. In KEKB low energy positron ring (LER) the EC effects are observed as a vertical beam blow-up, a tune shift along a bunch train and a coupled bunch instability. Among them the most serious effect was the vertical beam blow-up which severely limited the luminosity. The beam size as a function of the beam current started to increase at a threshold beam current and was almost doubled at 300 mA in early operation period. Now the blow-up is explained as the head-tail instability due to the EC [1, 2]. The instability occurs only in multi-bunch operation since the EC is built-up by successive passage of the bunches.

A measure taken to mitigate the EC effects in KEKB LER was installation of solenoid magnets in order to confine the EC near a chamber wall [3]. The solenoids were installed first in September 2000. The effect of the solenoids on the blow-up was confirmed immediately by measurements of the vertical beam size and the luminosity [4].

Measures against the EC instability (ECI) in SuperKEKB which is an upgrade plan of KEKB are being discussed based on research and development works by the KEKB vacuum group and also simulations of the EC build-up and the instability related to the EC.

This article briefly summarizes experimental study and cures of the ECI in KEKB and simulation study of the ECI in SuperKEKB.

### 3.11.2 Experimental Study of the Electron Cloud Instability in KEKB

The experimental study of the EC effects in KEKB LER consists of the measurement of the EC by electron monitors, the measurement of the tune shift of each bunch, the observation of the vertical beam blow-up and the observation of the transverse coupled bunch instability. So far no evidence is found for a longitudinal instability caused by the EC.

#### *3.11.2.1 Measurement of Electron Cloud*

An amount of the EC has been measured by a retarded field analyzer. Particularly the density of the EC near the beam was estimated by selecting a high energy

component of the electron current applying a high retarded voltage of -500V to a retarding grid [5]. The measurement showed that the electron density near the beam was 7.5 x $10^{-11}$ $m^{-3}$ in a field free arc-section at the beam current of 1500mA in 3.5 RF bucket spacing between adjacent bunches. The estimated electron density was consistent with simulations. The measurement of the electron density near the beam in a solenoid and a quadrupole magnet is in progress using specially designed electron monitors [6]. In the solenoid field of 50 Gauss the electron density decreased to 1/100 or less. In the quadrupole magnet the electron density was 4.0 x $10^{-10}$ $m^{-3}$ at the beam current of 1230 mA in 3.06 RF bucket spacing. The result was close to a simulation.

#### *3.11.2.2 Measurement of Tune Shift*

Gradient of the electric field generated by the EC causes the tune shift along a bunch train. The tune shift can be a good measure of the electron density [7]. The tune of each bunch has been measured by a gated tune meter [8]. The tune increased along a train then saturated [9], which showed the build-up of the EC along the train. The saturated tune shift in the vertical plane was consistent with the result of a simulation [10]. Build-up time of the tune shift along the train in 4 RF bucket spacing was about 20 bunches which was also consistent with the simulation. The saturated horizontal and vertical tune shifts were almost same [11]. When applying the solenoid field the horizontal tune shift was almost disappeared while the vertical tune shift decreased only to about 60% [11]. The reason why the solenoids have a different effect on the horizontal and vertical tune shift is not understood yet.

The measurement of a decay time gives information on quantity of the low energy electrons in the EC and a trapping of the electrons inside magnets. A test bunch was injected at the end of a train, then the tune shift was measured by changing the distance between the train and the test bunch. The measured decay time was about 30ns. In another experiment, the vertical beam size of each bunch was measured by a fast-gated camera when two trains separated by 64ns were injected in the ring [9]. While the blow-up started at about 7th bunch in the first train, second bunch already blew-up in the second train, which showed that the effect of the EC would sustain in long time interval.

Injecting a test bunch behind a bunch train also enables a measurement of the transverse dipole kick due to the EC for various cloud densities [11, 12]. The tune shift per bunch current $Dn/DI_b$ and the width of the tune spectrum DW by a swept frequency measurement were obtained under a constant train current by changing the bucket position of the test bunch [11, 12]. The horizontal $Dn/DI_b$ and DW as a function of the bucket position did not change much. On the other hand, the vertical $Dn/DI_b$ and DW showed strong dependence on the bucket position when the test bunch approached the train, which indicated strong effect of the EC on the vertical plane.

#### *3.11.2.3 Beam Size Blow-up or Single Bunch Instability*

The vertical beam size blow-up was observed at the beginning of KEKB operation by an interferometer as described before. Since then a large amount of data was collected by the interferometer, the fast-gated camera, a streak camera and so on. The results are summarized as follows.

- The single bunch nature of the blow-up was examined by injecting a test bunch immediately behind a train. The beam size of the test bunch was measured at

several bunch currents. The beam size increased as the current of the test bunch increased, which demonstrated that the blow-up is a single bunch effect [9].

- The measurement by the fast-gated camera showed that the vertical beam size increased along a bunch train. It was also shown that the chromaticity had an effect on the blow-up. The blow-up along the train became weaker when the chromaticity was increased [9, 13].
- Two-dimensional longitudinal and vertical distribution of bunches was measured by a streak camera in order to detect the head-tail motion of the bunches [14]. The vertical beam size started to increase at the third or fourth bunch when the solenoids were powered off. A vertical tilt within a bunch was not clearly observed even in the tail part of the train where a large cloud density was expected.
- A vertical sideband near the betatron frequency was found [15]. Appearance of the sideband depended on the strength of the solenoids and was also associated with loss of the luminosity during collision [16]. The threshold where the sideband appeared coincided with that of the beam blow-up. The sideband appears to be a signature of the strong head-tail instability due to the EC. The dependence of the strength of the sideband on the chromaticity, the synchrotron tune and the initial beam size was measured [17]. The results supported the strong head-tail instability as the model of the blow-up. The sideband is seen on the upper side of the betatron peak, which suggests that the effective wake function is a focusing wake generated by the EC. Simulations by HEADTAIL and PEHTS succeeded in reproducing the sideband when the size of the EC was 20 times larger than that of the beam [18]. For the bunches in the EC with high electron density the bunch luminosity of even low current bunches was suppressed. The sidebands were not detectable at those low currents [19]. This phenomenon might be an indication of incoherent effects below head-tail instability threshold though possibility of other luminosity reduction mechanism is not excluded.

#### *3.11.2.4 Transverse Coupled Bunch Instability*

The coupled bunch instability caused by the EC has been observed in LER [20]. The time evolution of the instability just after turning-off the transverse bunch-by-bunch feedback [21] was recorded with several weak solenoid field conditions. Mode spectra of the instability were totally different with and without solenoid field, which strongly suggested that the instability was caused by the EC because usual wake fields are not affected by the weak DC solenoid field. Two groups of wide unstable modes appeared both for the horizontal and vertical planes when the solenoids were turned off. The mode numbers at the peaks of the distribution were about 180 and 850. The group centered at 850 had the major contribution in both planes. The mode spectrum supports the simulation where the electrons are almost uniformly emitted from the chamber wall [22]. The observed mode spectra without the solenoid field and the growth rate with changing the solenoid field suggest rather low secondary electron yield of about 1.0 on the chamber surface [20]. The mode spectra with the solenoid field showed higher frequency peaks than those given by a simulation. The difference suggests that the

effective field strength is weaker than an expectation or the electrons may stay nearer to the beam position apart from the chamber surface [20].

#### *3.11.2.5 Cures*

The ECI in KEKB is mitigated by solenoid magnets which confine the EC near the chamber wall. The solenoids were installed several times in LER since September 2000. The maximum longitudinal magnetic field at the centre of a solenoid is about 45 Gauss [3]. The polarity of the solenoids was arranged such that the integrated longitudinal field vanished between adjacent quadrupole magnets in order to suppress the x-y coupling due to the solenoids.

The effect of the solenoids on the blow-up was confirmed by the measurement of the vertical beam size with the interferometer after first installation of the solenoids where about 800 m was covered by the solenoids [4]. The threshold current of the blow-up increased by 80% after turning on the solenoids. The beam size of each bunch along the train was measured by the gated camera [4]. The blow-up started at 7th bunch without the solenoids while it started at 30th bunch with the solenoids. The effect of the solenoids was also confirmed by the luminosity measurement [4]. The specific luminosity decreased when all solenoids were turned off.

After the confirmation of the effect of the solenoids on the luminosity, the solenoids were additionally installed in each shut down period. In February 2002 about 10000 solenoids covered 78 % of the circumference of the ring. Then the instability was mitigated to the extent that the blow-up was not observed up to the beam current of 1600mA in 4 RF buckets spacing.

A large-scale installation of the solenoids is not done after 2002. Suspecting that the electrons might be accumulated in regions where the polarity of the solenoids are changed or in regions near the beam axis in quadrupole magnets where the magnetic field vanishes, the change of the polarity of the solenoids and winding of the solenoids in the quadrupole magnets were tried [23, 24]. But the effect on the blow-up was not seen in either case.

The blow-up is still observed as the reduction of the bunch luminosity and appearance of the sideband if the bucket separation is reduced to 2 RF buckets.

The solenoids mitigate the coupled bunch instability as well as the blow-up of the beam size. The growth rate of the coupled bunch instability was reduced by applying the solenoid field. Remaining dipole oscillation of the bunches after installing the solenoids is damped by the bunch-by-bunch feedback system [21].

### 3.11.3 Electron Cloud Instability in SuperKEKB

The EC build-up in SuperKEKB was simulated by a code CLOUDLAND [25, 26]. A positron beam was assumed to be stored in HER taking consideration of so called charge switch [27]. Ante-chambers were also assumed in the simulation. The ante-chambers are effective to reduce the number of primary photoelectrons. In the simulation the primary electrons were generated uniformly around a chamber wall assuming that the ante-chambers work well to absorb the photons. The number of the primary electrons was provisionally assumed to be 1% of the number of photons emitted by the synchrotron radiation. The maximum secondary electron yield of 1.5, that is no coating on a wall was assumed. The solenoid field of 60 G was applied in the drift space. The simulation results showed that 1) the integrated electron density near

the beam along the ring circumference is 0.6 x $10^{15}m^{-2}$, 2) solenoid field of 60G is very effective to reduce the electron density at the center of the chamber. The threshold electron density of the strong head-tail instability was estimated by a simple model [1]. The result showed that the electron density estimated by the simulation is well below the threshold density of the instability. A betatron tune shift by the EC was estimated to be as small as 0.0005. The simulation showed that some electrons are trapped in a quadrupole magnet [28] and in a solenoid. In a dipole magnet strong multipacting of the electrons produces two strips of the electrons. Though these electrons will not contribute to the blow-up because of low electron density near the beam, they may cause the coupled bunch instability [29]. The estimation of the strength of the coupled bunch instability will be studied later.

Recently the EC build-up was calculated in case of positron storage in LER. The method of the simulation was similar to that in case of positron storage in HER. This time, secondary emission yield of 1.0 was used assuming that TiN coating is applied on the chamber wall. The integrated electron density along the ring circumference near the beam was 0.086 x $10^{15}$ $m^{-2}$ which is well below the threshold electron density of the strong head-tail instability. The trapping of the electrons in the quadlupole magnet was appeared as well as in positron storage in HER.

Measures against the ECI that will be taken in SuperKEKB are under discussion. They will be determined taking into account of recent research and development works conducted by the KEKB vacuum group and results of simulations of the EC build-up and the ECI. Please see an article by Y. Suetsugu et al. in this special issue about the research and development works for EC mitigation techniques by the KEKB vacuum group.

### 3.11.4 Discussion

Even though extensive studies about the EC effects have been done in KEKB, several open questions remain as follows.

- The blow-up is still observed even after a large number of the solenoids were installed. Questions are where the electrons are and how they can be removed.
- The horizontal tune shift along the train almost disappeared after 95% of the drift space was covered by the solenoids, while the vertical tune shift decreased only to about 60%. The effect of the solenoids on the tune shifts is not fully understood yet.
- A measurement showed that the luminosity loss was observed for low current bunches where the sidebands were not detectable. The phenomena might be related to the incoherent effects below the threshold of the strong head-tail instability.

### 3.11.5 References

1. K. Ohmi and F. Zimmermann, "Head-Tail Instability Caused by Electron Clouds in Positron Storage Rings", Phys.Rev.Lett., 85, 3821(2000).
2. K. Ohmi, F. Zimmermann and E. Perevedentsev, "Wake-field and fast head tail instability caused by an electron cloud", Phy. Rev. E, 65, 016502(2001).
3. H. Fukuma et al., "Status of Solenoid System to Suppress the Electron Cloud Effects at the KEKB", Proceedings of the 20th ICFA Advanced Beam Dynamics Workshop on

High Intensity and High Brightness Hadron Beams", FNAL, Batavia, Illinois, 2002 (AIP Conference Proceedings 642), p.357.
4. H. Fukuma et al., “Study of Vertical Beam Blowup in Kekb Low Energy Ring”, Proceedings of HEAC2001, Tsukuba, 2001.
5. K. Kanazawa et al., "Measurement of the Electron Cloud Density Around the Beam", Proceedings of PAC20005, Knoxville, Tennessee, 2005, p.1054.
6. K. Kanazawa et al., private communications.
7. K. Ohmi, S. Heifets and F. Zimmermann, "Study of Coherent Tune Shift Caused by Electron Cloud in Positron Storage Rings", Proceedings of Second Asian Particle Accelerator Conference (APAC'01), Beijing, 2001, p.445.
8. T. Ieiri et al., "Bunch-by-bunch measurements of the betatron tune and the synchronous phase and their applications to beam dynamics at KEKB", Phys. Rev. ST Accel. Beams 5, 094402 (2002).
9. H. Fukuma et al., "Observation of Vertical Beam Blow-Up in KEKB Low Energy Ring", Proceedings of EPAC2000, Vienna, June 2000, p.1122.
10. F. Zimmermann, “Electron-Cloud Studies for the Low Energy Ring of KEKB”, CERN SL-Note-2000-004 AP (2000).
11. T. Ieiri et al., "Measurement of Wake Effects by Means of Tune Shift in the KEKB Low-Energy Ring", Proceedings of EPAC2006, Edinburgh, Scotland, 2006, p.2102.
12. T. Ieiri et al., "Variations of Betatron Tune Spectrum Due to Electron Cloud Observed in KEKB", Proceedings of PAC07, Albuquerque, New Mexico, 2007, p.825.
13. J. Flanagan et al., “High-Speed Gated Camera Observations of Transverse Beam Size Along Bunch Train at the KEKB LER”, Proceedings of EPAC2000, Vienna, 2000, p.1119.
14. H. Fukuma et al., " Recent Observations of Collective Effects at KEKB ", to be appeared in Proceedings of 30th Advanced ICFA Beam Dynamics Workshop on High Luminosity e+e- Collisions, Stanford, California, 2003,
15. J. W. Flanagan et al., "Observation of Vertical Betatron Sideband due to Electron Clouds in the KEKB Low Energy Ring", Phys. Rev. Lett., 94, 054801(2005).
16. J. W. Flanagan et al., "Betatron Sidebands Due to Electron Clouds Under Colliding Beam Conditions", Proceedings of PAC2005, Knoxville, Tennessee, 2005, p.681.
17. J. W. Flanagan et al., "Further Studies on Betatron Sidebands Due to Electron Clouds", Proceedings of EPAC2006, Edinburgh, Scotland, 2006, p.2898.
18. E. Benedetto et al., "Simulation of the Synchro-Betatron Sideband Instability Caused by Electron Clouds at KEKB", Proceedings of PAC07, 2007, Albuquerque, New Mexico, p.4033.
19. J. W. Flanagan et al., "Electron Clouds and Specific Luminosity Measurements at KEKB", KEK Proceedings 2007-10 (Proceedings of ECLOUD'07), Daegu, Korea, 2007, p.15.
20. M. Tobiyama et al., "Coupled bunch instability caused by an electron cloud", Phys. Rev. ST Accel. Beams, 9, 012801 (2006).
21. M. Tobiyama and E. Kikutani, "Development of a high-speed digital signal process system for bunch-by-bunch feedback systems", Phys. Rev. ST Accel. Beams, 3, 012801 (2000).
22. S. S. Win et al., "Numerical study of coupled-bunch instability caused by an electron cloud", Phys. Rev. ST Accel. Beams, 8, 094401 (2005).
23. H. Fukuma et al., "The Effect of the Solenoid Field in Quadrupole Magnets on the Electron Cloud Instability in the KEKB LER", Proceedings of EPAC 2006, Edinburgh, Scotland, 2006, p.2901.
24. H. Fukuma et al., "Electron Cloud Effects in KEKB", CERN-2005-001 (Proceedings of ECLOUD'04), 2005, p.15.

25. L. F. Wang et al., "Numerical study of the photoelectron cloud in KEKB Low Energy Ring with a three-dimensional particle in cell method", Phys. Rev. ST Accel. Beams, 5, 124402 (2002).
26. H. Fukuma and L. F. Wang, "Simulation Study of the Electron Cloud Instability in Superkekb", Proceedings of PAC2005, Knoxville, Tennessee, 2005, p.868.
27. K. Abe et al., "Letter of Intent for KEK Super B Factory", KEK Report 2004-4.
28. L. F. Wang et al., "Photoelectron trapping in quadrupole and sextupole magnetic fields ", Phys. Rev. E 66, 036502 (2002).
29. S. S. Win et al., "Simulation Study of Coupled-Bunch Instability Due to Electron Cloud in Super KEKB", Proceedings of APAC2004, Gyeongju, Korea, 2004, p.204.

## 3.12 Vacuum System for High-Current $e^-/e^+$ Accelerators

Yusuke Suetsugu, Ken-ichi Kanazawa, Kyo Shibata, Hiromi Hisamatsu,
Mitsuru Shirai
High Energy Accelerator Research Organization (KEK),
1-1 Oho, Tsukuba, 305-0801, Japan
Mail to: yusuke.suetsugu@kek.jp

### 3.12.1 Introduction

In future high-current $e^-/e^+$ colliders, such as Super B-factories, a stored beam current of several amperes, a short bunch length of a few millimeters and/or a low beam emittance the order of nano-meters are required to achieve a luminosity of the order of $1 \times 10^{36}$ $cm^{-2}s^{-1}$ [1–3]. These parameters impose very severe challenges to a vacuum system [4]. The beam pipe has to manage a synchrotron radiation (SR) power density of up to several tens of watts per square millimeters. The vacuum components should have a low beam impedance in order to store the beam in a stable manner and to be able to stand up against the intense higher-order modes (HOMs) at the same time. Suppression of the electron cloud effect (ECE) is also a serious problem in a positron ring [5]. These are common key issues relating to not only a high-current factory machine but also the dumping ring (DR) of the international linear collider (ILC) and the next generation of SR sources, such as an energy recovery linac (ERL) [6, 7].

R&D on various vacuum components to meet these demands is in progress at KEK [8–16]. Copper beam pipes with antechambers have been proposed to deal with the intense SR power [9]. A special connection flange has been designed; this flange realizes a small step or gap inside even in the case of a beam pipe with antechambers [10]. A distributed pumping system applicable to the antechamber space has also been developed [11]. The antechamber structure can also simultaneously suppress photoelectrons; this is effective in mitigating the ECE [9]. Various techniques to mitigate the ECE in a high-current region, such as a surface with a low secondary electron yield (SEY), have been studied in parallel [12, 13]. Bellows chambers and gate valves with a comb-type RF-shield have also been developed [14, 15]. A movable collimator (mask) with low impedance has been proposed and is under development [16].

These beam pipes and components have been installed for testing at the KEKB B-factory [17]. KEKB is an $e^+e^-$ collider with asymmetric energies and consists of two rings, an 8.0 GeV $e^-$ ring and a 3.5 GeV $e^+$ ring. The maximum stored beam currents for

the $e^-$ and $e^+$ rings are 1.4 A and 1.7 A with 1389–1585 bunches, respectively. At present, KEKB is the most suitable machine for R&D about future accelerators with high intensities. Herein, we present the design study for a vacuum system for future high-intensity storage rings, suitable for applications such as the Super KEKB [1].

### 3.12.2 Beam Pipe

The typical structure of a copper beam pipe developed in this study is presented in Fig. 1 (the connection flange is omitted). The beam pipe consists of two sections: a beam channel where an electron or positron beam circulates and the antechambers on the sides of the beam channel. The SR passes through these antechambers. The beam pipe in this figure is that for an arc section of a ring, so a pump channel is located inside one of the antechambers (see Sec. 1.1.4). Cooling channels are provided outside the antechambers in order to absorb the heat deposited by SR.

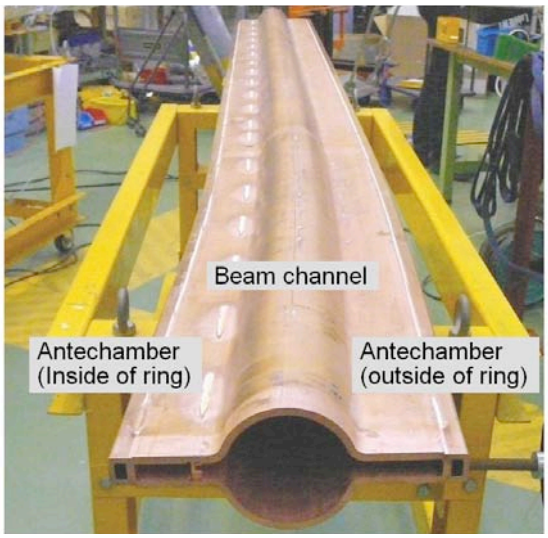


**Figure 1:** Copper beam pipe with antechambers.

One of the main purposes of the antechambers is to decrease the SR power density on the side wall. Since the hitting point of the SR is far from the emitting point on the beam orbit, the incident SR power density can be diluted several times by the vertical and/or horizontal spread of the SR. The aperture of beam pipes in accelerators is usually limited by the cores of magnets such as quadrupole magnets. Therefore, the cross-section of beam pipes that have a wide width resembles the shape shown in this figure.

The electric field accompanied by a bunch is smaller by several orders of magnitude in the antechamber than that in the beam channel because of the narrow height of the antechamber. Therefore, the pumping ports and photon masks in an antechamber have little effect on the beam. Thus, the cross section has an advantage from the view point of beam dynamics as well. Furthermore, the electron cloud is initially created by photoelectrons emitted from the surface upon SR irradiation. The antechamber structure helps to minimize the effects of the photoelectrons because the emission points of the photoelectrons are far from the beam orbit.

Because of its high thermal strength, high electrical conductivity, good welding property, and relatively low photoelectron yield, oxygen-free copper (OFC) is the most

suitable material for our beam pipe [18]. We used the electron beam welding method for making the proposed beam pipe in order to avoid the annealing of copper. However, this is the first time ever that copper beam pipes with antechambers were manufactured. Two manufacturing methods, the pressing method and the cold-drawn method, were tried. In the pressing method, a copper plate was pressed by a special die. Then, two formed plates were welded together by an electron beam together with two cooling channels at both ends. In contrast, in the cold-drawn method, the manufacturing process began with a circular copper pipe. The pipe was drawn through several molds in a step-by-step process at room temperature. Finally, two cooling channels were welded on both sides. From the viewpoints of reliability and applicability to large-scale production, the cold-drawn method is preferable to the pressing method.

The beam position monitor (BPM) section was machined from a copper block and reinforced by using two stainless-steel ribs. The pickup electrodes were attached to the pipe by a UHV flange (ICF034). The final detailed calibration of the BPM will be performed using a circulating beam (i.e., the beam-based alignment).

Several beam pipes with ante-chambers for tests were installed into KEKB. The temperatures and vacuum pressures around the beam pipes were monitored during beam operation of up to a beam current of 1.7 A (1389 bunches). Although arcing was observed at a welding part of one model at the beginning of commissioning [9], no problem was found after modifying the welding structure. The temperature of the pipe was slightly higher, but almost in agreement with the expected value.

In order to estimate the effect of antechamber on the ECE, the number of electrons around the beam was measured [9]. A reduction by one or two orders of magnitude in the number of photoelectrons in the beam pipe as compared to a simple circular pipe was confirmed in a low-current region ($\leq$0.1 A) where the photoelectrons were dominant. The number of electrons in a high-current region such as 1.5 A was also smaller, but the reduction rate was much lower than that in a low-current region. This was so because the main component of the electron cloud in the beam current region was the secondary electrons, which were generated in a multiplication process by successive bunches. The mitigation in the high-current region is discussed in Sec. 1.1.5.

### 3.12.3 Connection Flange

The large number of connection flanges of beam pipes can lead to the flanges becoming a source for considerable impedance. Helicoflex sealing would be no longer sufficient even if the depth of a gap was a few millimeters [18]. The Helicoflex sealing cannot follow the complicated aperture such as that of a beam pipe with antechambers. The conventional finger-type RF-bridge may be able to follow the complicated aperture, but a uniform electric contact can hardly be guaranteed.

The MO-type (Matsumoto-Ohtsuka-type) flange seals a vacuum at only the inner surface by using a copper gasket [10]. The copper gasket also works as a secure RF-bridge; this bridge has no gap and little step at the inner surface. The thermal strength of the copper gasket is considerably higher than that of thin metal fingers or O-rings.

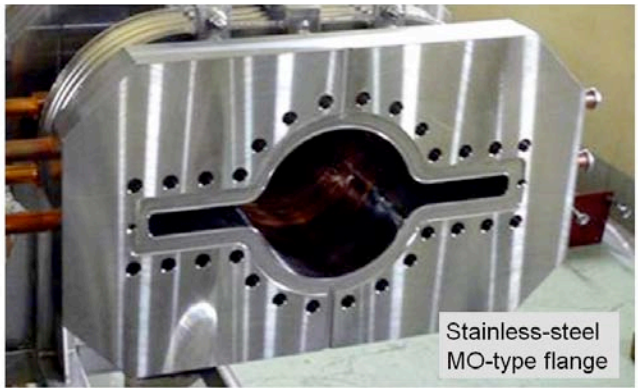


**Figure 2:** Specially designed MO-type flange.

The specially designed MO-type flange was adopted for the beam pipe with antechambers, as presented in Fig. 2. The material used was stainless-steel 316. A vacuum seal was achieved with a fastening torque of 16–18 Nm, which was almost the same as in the case of a standard circular conflat flange with a similar diameter. Further, there was no air leak observed even when the beam pipe was baked at temperatures up to 200°Cseveral times.

In the beam test, no serious problem was found up to a beam current of 1.7 A (1389 bunches). One problem discovered during the beam test was the heating up of the stainless-steel flanges. The temperature rose up to approximately 45°C ($\Delta T = 20°C$) at a beam current of 1.7 A. This problem could be attributed to the heating of the surface of stainless-steel flange due to the Joule loss for the wall current and/or due to the SR irradiation with a vertical fan. A promising solution to this problem is to use a copper-alloy flange. The MO-type flange made of a chrome-zirconium-copper alloy is under investigation and will be applied to the next trial models of the beam pipe.

### 3.12.4 Main Pump

In the case of particle accelerators, a distributed pumping system is usually adopted because of the limited conductance of the beam pipe. However, according to beam dynamics, many pump ports along the beam channel become a source of considerable impedance. In the case of a beam pipe with antechambers, the pump port can be placed in the antechambers on either side. For arc sections, especially, the antechamber at the inside of the ring can be used as a pump channel. A screen to shield the pump from the beam will be set in the antechamber between the pump and the beam (see Fig. 1).

A distributed pumping system using multi layered NEG strips for the narrow pumping space was designed, as shown in Fig. 3 [11]. The strip-type NEG can be used anywhere, irrespective of the presence of magnetic fields, unlike the distributed sputter ion pumps (DIP). The number of layers of NEG strips was optimized by calculating the pressure distribution inside the pump channel; in the end, three strips were used. Indirect heating with sheath heaters was considered instead of direct Joule heating in order to safely and surely activate the NEG strips in the narrow space. Sputter ion pumps will be used as auxiliary pumps to evacuate inner gases and will be located at intervals of approximately 10 m along the ring.

The trial models shown in this figure consisted of four or six modules of NEG strips (length; approximately 300 mm). The modules easily followed the curvature of the bent

beam pipe. The pumping speed of the trial model was measured for nitrogen, and a reasonable pumping speed was obtained. The pump system will be integrated with the antechamber and tested with beams at KEKB soon.

Note that NEG-coated beam pipes, which provide the pumping action to the inner surface, have recently been used in some accelerators [19]. These are ideal beam pipes from the viewpoint of pumping. It has also been reported that the NEG-coated chamber has a low photo-desorption rate and a low SEY. However, the small capacitance of the coating may be a problem for relatively high gas-loaded machines [20]. Furthermore, the heating of the beam pipe to around 180°C for activating the NEG coating should be avoided in some practical cases.

**Figure 3:** Three-layered NEG strip pump for antechamber.

### 3.12.5 Electron Cloud Issue

As described above, secondary electrons play a significant role in the formation of an electron cloud in a high-current region. Therefore, one promising way to suppress the ECE is to apply a surface with a low SEY to the inner surface of a beam pipe. In the case of the drift space, a solenoid magnetic field from outside of the beam pipe was effective in reducing the secondary emission [21]. However, in the case of magnets such as bending and quadrupole magnets, any surface with a low SEY is indispensable since the solenoid magnetic field cannot be sufficiently applied there. Mitigation techniques analyzed in this study were those using coatings, clearing electrodes and groove surfaces.

The candidate materials for the coatings considered here were NEG material and TiN since the procedure to make a thin film of these materials is well established [12]. Circular copper test chambers for tests with NEG or TiN coatings were installed in arc and straight sections. The number of electrons around the beams was measured up to a beam current of approximately 1.7 A in each case and compared with the values obtained for the other cases. The number of electrons for the case of the TiN coating and the NEG coating was approximately 1/3 and 2/3 of that in the case of a copper chamber without a coating in the straight sections. The estimated maximum SEY ($\delta_{max}$) for the TiN coating, the NEG coating, and the uncoated copper were 0.8-0.9, 1.0-1.1, and 1.2-1.3, respectively. The TiN coating also had a lower photoelectron yield than the others.

Another direct and efficient mitigation technique is the installation of a clearing electrode into a beam pipe. This electrode is used to attract or repel electrons through a static electric field [22]. A strip-line clearing electrode applicable to high-intensity beams was developed and tested using the KEKB $e^+$ ring [13]. The electrode is composed of a thin tungsten layer (thickness; 0.1 mm) formed on a thin alumina ceramic layer (thickness; 0.2 mm). The narrow alumina gap between the electrode and the beam pipe decreases the beam impedance and enhances the heat transfer from the electrode to the beam pipe. The electrode installed in a test chamber is shown in Fig. 4. The test chamber was installed into a wiggler magnet (0.77 T). In the case of the positive electrode voltage ($V_{elec}$), the measured electron current decreased monotonically with an increase in $|V_{elec}|$. The reduction ratios of electrons at the beam position were approximately 1/100 for $V_{elec}$ = +300 V as compared to the case of $V_{elec}$ = 0 V. The electron density was roughly estimated to be approximately $1 \times 10^9$ electrons $m^{-3}$ for bunch spacings of 6 ns. Similar results were obtained for other bunch fill patterns with bunch spacings of 4, 8, and 16 ns. The results experimentally demonstrated the feasibility of a clearing electrode in a strong magnetic field.

**Figure 4:** Test model of clearing electrode.

Another promising mitigation technique is the application of a groove surface in a beam pipe [23]. This technique can be also applied inside magnets and requires no electric power supplies unlike the clearing electrode. A groove surface, shown in Fig. 5, was installed into a wiggler magnet as in the case of the clearing electrode. The results clearly demonstrated the effectiveness of the groove surface in reducing the electron density near the beam. The number of electrons near the beam orbit was reduced by several factors, almost close to by one order of magnitude, compared to the case of a smooth surface for various bunch filling patterns. The result provided an effective technique to mitigate the ECE in a magnetic field as well as the clearing electrode.

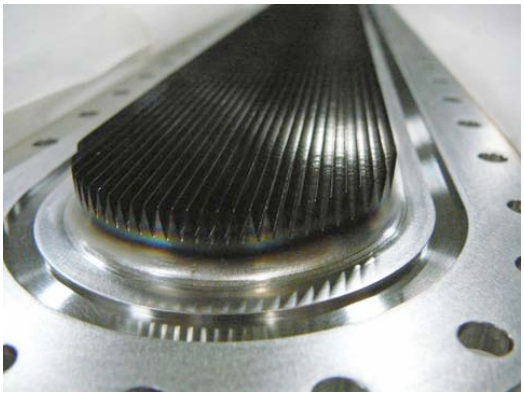

**Figure 5:** Test model of groove surface.

### 3.12.6 Bellows Chambers and Gate Valves

Bellows chambers and gate valves with an RF-shield structure are indispensable while connecting beam pipes with one another. The cross section of the RF-shield has to fit into that of the beam pipes. The RF-shield should have a uniform inner surface in order to decrease the impedance, a reliable electric contact in order to ensure a smooth flow of the beam-induced wall current, and a high thermal strength.

Bellows chambers and gate valves with a comb-type RF-shield have been developed [14, 15, 24]. The comb-type RF-shield consists of nested comb teeth and not thin fingers. The RF-shield was able to follow the complicated apertures of beam pipes. On the basis of simulations, we concluded that the comb-type RF-shield had a lower beam impedance than the conventional finger-type one. However, the transverse offset was limited compared to that in the finger-type RF-shield.

An inside view of a gate valve is presented in Fig. 6, for example. A key problem of the RF-shield for gate valves was the generation of dust due to abrasion during open/close motions. The comb-type RF-shield could provide a slide-less contact. The base design of the valve, such as the vacuum sealing mechanism, was the same as the standard design. The teeth of the RF-shield were made from pure copper, while the other parts were made of stainless steel. Bellows chambers customized to fit the proposed beam pipe were also manufactured for the test [24].

Various types of bellows chambers and gate valves with the comb-type RF-shield were installed into the KEKB $e^-/e^+$ rings and tested with real beams. No serious problem was found except in one model, where the structure of the RF-shield had been modified improperly. The temperatures of bellows with the comb-type RF-shield were almost always several times lower than the case of bellows with an old finger-type RF-shield. It was also interesting to note that the temperature of a bellows chamber connected to the gate valve also decreased after exchanging the gate valve to new-type one with the comb-type RF-shield. This is an indication that the excited HOM decreased upon using the comb-type RF-shield.

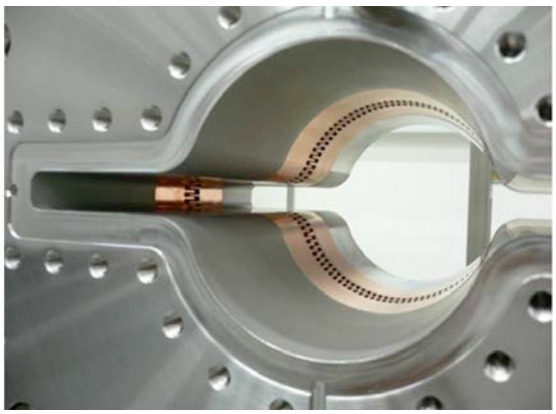

**Figure 6:** Gate valve with comb-type RF-shield.

### 3.12.7 Collimators

A movable collimator (mask) is a special vacuum component used to cut off spent particles around a nominal beam orbit and then to decrease the background noise of the particle detector. It has a head (a block of metal with several radiation lengths) near the beam orbit. The movable collimator, therefore, inherently has high beam impedance [25]. Another problem of the collimator is the damage to the head due to the direct hitting of the beam, where the head has been made of copper or titanium.

A new structure of a movable collimator with low beam impedance was proposed [16]. The head was supported by a dielectric rod, which could reduce the interference between the collimator head and the beam and thus reduce the impedance. The head was made of graphite, which has a higher thermal strength compared to the metals used thus far. The new type of collimator head is presented in Fig. 7.

Several test models were manufactured and installed into the KEKB. The principle of the new structure was demonstrated in a low current region (< 1 A), that is, the temperature of bellows just near the test models decreased after the installation [26]. However, it was also found that further improvement is necessary in order to use this new structure at higher beam currents. The structural and material modifications are now underway.

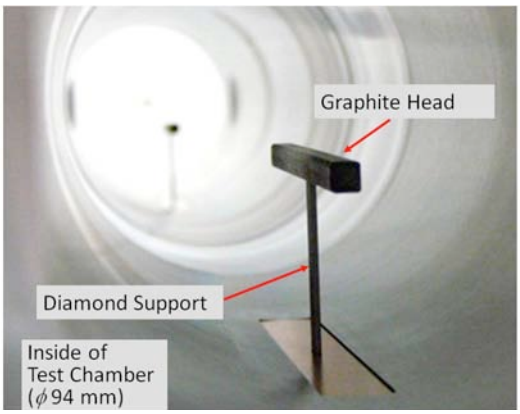


**Figure 7:** Head of new type of movable collimator.

### 3.12.8 Summary

The vacuum system for future high-intensity colliders have been systematically developed on the basis of a copper beam pipe with antechambers. A fabrication technique for copper pipes with complicated apertures was established by using a cold-drawn method and adopting electron beam welding for connections. The distributed pump utilizing multi layered NEG strips showed promise. The beam pipes and the associated vacuum components such as the gate valves, the bellows chambers, and movable collimators were tested using the intense $e^-/e^+$ beams at KEKB. The beam pipes and components showed no serious problems. The reduction in the number of electrons near the beam orbit in using the antechamber scheme was observed in the $e^+$ ring in a low-current region. The TiN coating, the clearing electrode, and the groove surface were found to be effective in reducing the electron cloud in a high-current region, even in a strong magnetic field.

### 3.12.9 Acknowledgement

We would like to express our sincere gratitude to Professor K. Oide for his continuous encouragement for this study. We would also like to thank the staff of KEK B-factory for the technical support they provided for our experiments.

### 3.12.10 References

1. SuperKEKB Task Force, “Letter of Intent for KEK Super B Factory”, KEK Report 2004–4 (2004)
2. P. Raimondi, “New Developments in Super B-Factories”, Proceedings of the 2007 Particle Accelerator Conference, Albuquerque, New Mexico (2007).
3. J. Seeman, et al., “PEP–II Status and Future Plans”, Proceedings of the 2002 European Particle Accelerator Conference, Paris (2002).
4. Y. Suetsugu, “Vacuum System for High Power Lepton Rings”, Proceedings of the 2003 Particle Accelerator Conference, Portland, Oregon (2003).
5. K. Ohmi, and F. Zimmermann, “Head-Tail Instability Caused by Electron Clouds in Positron Storage Rings”, Physical Review Letters, **85** (2000) 3821.
6. Reports presented in the ILC Damping Rings R&D Workshop, ILCDR06, Cornell University (2006), and ILCDR08, Cornell University (2008).
7. T. Kasuga, et al., “Status of R&D Efforts Toward the ERL-based Future Light Source in Japan”, Proceedings of the 2007 Particle Accelerator Conference, Albuquerque, New Mexico (2007).
8. Y. Suetsugu, K. Shibata, H. Hisamatsu, M. Shimamoto, M. Shirai, and K. Kanazawa, “R&D on Copper Beam Ducts with Antechambers and Related Vacuum Components”, proceedings of the 2006 European Particle Accelerator Conference, Edinburgh (2006).
9. Y. Suetsugu, K. Kanazawa, K. Shibata, H. Hisamatsu, K. Oide, F. Takasaki, A.E. Bondar, V. Kuzminykh, A. Gorbovsky, R. Dostovalov, K. Sennyu, and H. Hara, “R&D of Copper Beam Duct with Antechamber Scheme for High Current Accelerators”, Nuclear Instruments and Methods in Physics Research A, **538** (2005) 206.
10. Y. Suetsugu, M. Shirai, and M. Ohtsuka, “Application of MO-type Vacuum Flange to Beam Duct for High-Current Accelerators”, Journal of Vacuum Science & Technology A, **23** (2005) 1721.
11. Y. Suetsugu, K. Shibata, and M. Shirai, “Design Study of Distributed Pumping System

Using Multilayer NEG Strips for Particle Accelerators", Nuclear Instruments and Methods in Physics Research A, **597** (2008) 153.
12. Y. Suetsugu, K. Kanazawa, K. Shibata, and H. Hisamatsu, "Continuing Study on the Photoelectron and Secondary Electron Yield of TiN Coating and NEG (Ti-Zr-V) Coating under Intense Photon Irradiation at The KEKB Positron Ring", Nuclear Instruments and Methods in Physics Research A, **556** (2005) 399.
13. Y. Suetsugu, H. Fukuma, L. Wang, M. T. F. Pivi, A. Morishige, Y. Suzuki, and M. Tsukamoto, "Demonstration of Electron Clearing Effects of Clearing Electrode in High-Intensify Positron Ring", Nuclear Instruments and Methods in Physics Research A, **598** (2005) 372.
14. Y. Suetsugu, M. Shirai, and K. Shibata, "Possibility of Comb-type RF Shield Structure for High-Current Accelerators", Physical Review Special Topics – Accelerators and Beams, **6** (2003) 103201.
15. Y. Suetsugu, M. Shirai, K.Shibata, K. Murata, M. Kaneko, K. Sakamoto, K. Sugisaki, and M. Kawahara, "Development of a Bellows Assembly with Comb-Type RF Shield for High Current Accelerators", Nuclear Instruments and Methods in Physics Research A, **531** (2004) 367.
16. Y. Suetsugu, K. Shibata, A. Morishige, Y. Suzuki, and M. Tsuchiya, "Design Study of a Movable Mask with Low Beam Impedance", Physical Review Special Topics – Accelerators and Beams, **9** (2006) 103501.
17. K. Akai, et al., "Commissioning of KEKB", Nuclear Instruments and Methods in Physics Research A, **499** (2003) 191.
18. K. Kanazawa, S. Kato, Y. Suetsugu, H. Hisamatsu, M. Shimamoto, and M. Shirai, "The Vacuum System of KEKB", Nuclear Instruments and Methods in Physics Research A, **499** (2003) 66.
19. C. Benvenuti, P. Chiggiato, F. Cicoira, and Y. L'Aminot, "Nonevaporable Getter Films for Ultrahigh Vacuum Applications", Journal of Vacuum Science & Technology A, **16** (1998) 148.
20. C. Benvenuti, P. Chiggiato, P. Costa Pinto, A. Escudeiro Santana, T. Hedley, A. Mongelluzzo, V. Ruzinov, and I. Wevers, "Vacuum Properties of TiZrV Non-evaporable Getter Films", Vacuum, **60** (2001) 57.
21. H. Koiso, et al., "Present Status of the KEKB B-Factory", Pproceedings of the 2002 European Particle Accelerator Conference, Paris (2002).
22. L. F. Wang, D. Raparia, J. Wei, and S. Y. Zhang, "Mechanism of Electron Cloud Clearing in the Accumulator Ring of the Spallation Neutron Source", Physical Review Special Topics – Accelerators and Beams, **7** (2004) 034401.
23. L. Wang, T. O. Raubenheimer, and G. Stupakov, "Suppression of Secondary Emission in a Magnetic Field Using Triangular and Rectangular Surfaces", Nuclear Instruments and Methods in Physics Research A, **571** (2007) 588.
24. Y. Suetsugu, K. Kanazawa, N. Ohuchi, K. Shibata, and M. Shirai, "Application of Comb-Type RF Shield to Bellows Chambers and Gate Valves", Proceedings of the 2005 Particle Accelerator Conference, Knoxville, Tennessee (2005).
25. Y. Suetsugu, K. Shibata, T. Sanami, T. Kageyama, and Y. Takeuchi, "Development of Movable Mask System to Cope with High Beam Current", Review of Scientific Instruments,**74** (2003) 3297.
26. Y. Suetsugu, K. Shibata, A. Morishige, Y. Suzuki, and M. Tsuchiya, "Beam Test of a Movable Collimator (Mask) with Low Beam Impedance", Proceedings of the 2008 European Particle Accelerator Conference, Genoa (2008).

## 3.13 KEKB RF System and Crab Cavity

T. Abe, K. Akai, K. Ebihara, E. Ezura, T. Furuya, K. Hara, T. Honma,
K. Hosoyama, S. Isagawa, A. Kabe, T. Kageyama, Y. Kojima, K. Marutsuka,
S. Mitsunobu, Y. Morita, H. Nakai, H. Nakanishi, K. Nakanishi, S. Ninomiya, M. Ono,
H. Sakai, M. Suetake, S. Takano, Y. Takeuchi, Y. Yamamoto, M. Yoshida,
S. Yoshimoto and K. Yoshino
KEK, Tsukuba, Japan
Mail to: kazunori.akai@kek.jp

### 3.13.1 Introduction

KEKB RF system has been designed to store an electron beam of 1.1 A in the High Energy Ring (HER) and a positron beam of 2.6 A in the Low Energy Ring (LER). One of the issues arising from the high-current beams is fast growing longitudinal coupled-bunch instabilities driven by the accelerating mode at the coupled-bunch modes of -1, -2, etc. In a large circumference ring with a high-current stored beam the detuning frequency of the cavities to compensate for the reactive component of beam loading can become so large with respect to the revolution frequency that the instability can be excited. In order to avoid this problem, two types of cavities, the Accelerator Resonantly-coupled with Energy Storage (ARES) normal-conducting cavities [1] and single-cell superconducting cavities (SC) [2], were developed at KEK. The high stored energy in these cavities reduces the detuning frequency by an order of magnitude, and the instability is suppressed. Another issue is coupled-bunch instabilities due to higher-order modes (HOM) of cavities. The HOM impedances of the ARES and SC cavities are sufficiently lowered by adopting HOM-damped structures. Furthermore, a large amount of power needs to be provided to the beam, while the required RF voltage is relatively low. Consequently, the RF stations need to be operated at high power of close to 1 MW. Each RF station includes a 1.2 MW CW klystron, its power supply, a 1 MW circulator, a 1.2 MW water load, WR-1500 waveguide components, etc. The low-level RF system was designed to accurately control the cavities and klystrons under the heavy beam loading [3].

Commissioning of KEKB started in December 1998 with about half of the total RF stations, and the other half stations were added year by year until all stations were completed in 2003. Table 1 shows RF-related parameters achieved during the operation. Although the LER beam current was successfully raised up to 2.0 A in a machine study, it has been operated at around 1.8 A for the physics run due to the electron-cloud instability. On the other hand, the HER beam current was increased more than the design value up to 1.4 A to increase the luminosity more. The beam current and the power delivered to the beam per a cavity are the world-highest values for superconducting cavities.

Two superconducting crab cavities had been developed, and installed in the KEKB tunnel in January 2007, one for each ring [4]. The crab crossing operation started in February 2007, and has continued until now [5]. The crab cavity system has been successfully working with high-current beams to conduct the crab crossing operation for high-luminosity physics run.

Upgrading KEKB to a next generation high luminosity collider, SuperKEKB, is being planned. The current design of SuperKEKB is based on four times higher beam

current of 9.4 A in the LER and 4.1 A in the HER with a shorter bunch length of 3 mm than KEKB [6]. This requires further improvements for the RF system, and the R&D is going on at KEK.

In the following sections the commissioning, the operating status and experiences with the ARES, SC and crab cavities as well as future plans are described.

**Table 1:** RF-related parameters achieved during the operation.

| Parameter | LER | HER | |
|---|---|---|---|
| Beam energy (GeV) | 3.5 | 8.0 | |
| Maximum stored beam current (A) | 2.0 | 1.4 | |
| Operating RF voltage (MV) | 8.0 | 13 - 15 | |
| Cavity type | ARES | ARES | SC |
| Number of cavities | 20 | 12 | 8 |
| Number of klystrons | 10 | 7 | 8 |
| Operating voltage / cavity (MV) | 0.4 | 0.31 | 1.24 |
| Maximum voltage / cavity (MV) | 0.55 | 0.475 | > 2.2 |
| Total beam power (MW) | 3.3 | 5.0 | |
| Beam power / cavity (kW) | 170 | 170 | 380 |
| HOM power / cavity (kW) | 6 | | 15 |

## 3.13.2 ARES Cavity

### *3.13.2.1 RF Schematic*

The ARES cavity is a three-cavity system operated in the π/2 mode, in which an accelerating cavity is resonantly coupled with an energy storage cavity via a coupling cavity between [1]. The name of ARES stands for Accelerator Resonantly coupled with Energy Storage, which just represents its RF schematic. Figure 1 shows an equivalent kinematic model of three coupled pendulums. The energy storage cavity, which corresponds to the left-side pendulum with a relatively huge mass, functions as a kind of electromagnetic flywheel to stabilize the π/2 accelerating mode against heavy beam loading onto the accelerating cavity which corresponds to the right-side pendulum. The coupling cavity, corresponding to the central pendulum, is equipped with a parasitic mode damper against the 0 and π modes. The resonant coupling scheme with the π/2-mode operation enables the following key design features of the ARES cavity system:

- The π/2 mode is most stable against tuning errors and heavy beam-loading conditions.
- The stored energy ratio, Ua : Us, where Ua is the stored energy in the accelerating cavity and Us in the storage cavity, can be easily adjusted by changing the coupling factor ratio, ka : ks, where ka is the coupling factor between the accelerating and coupling cavities and ks is that between the storage and coupling cavities.

- The parasitic 0 and π modes can be selectively damped with an antenna-type coupler installed into the coupling cavity. Furthermore, the damped 0 and π modes are located nearly symmetrically with respect to the π/2 mode. Therefore, those impedance contributions to beam instabilities can be adjusted so as to cancel out each other.

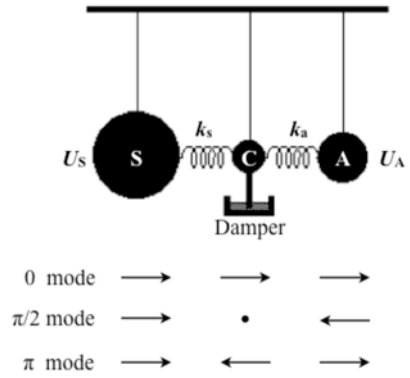


**Figure 1:** A coupled pendulum system showing the ARES cavity scheme.

### *3.13.2.2 RF Structure, HOM Damping, and Coupler Devices*

Figure 2 shows a 3D schematic view of the ARES cavity system. The design is based on a conceptual demonstrator named ARES96 [7] with an energy storage cavity operated in the $TE_{013}$ mode. The stored energy ratio $U_s$ / $U_a$ is set at 9, and the design cavity voltage of 0.5 MV is generated with a wall dissipation of 150 kW in total, 60 and 90 kW inside the accelerating and storage cavities, respectively.

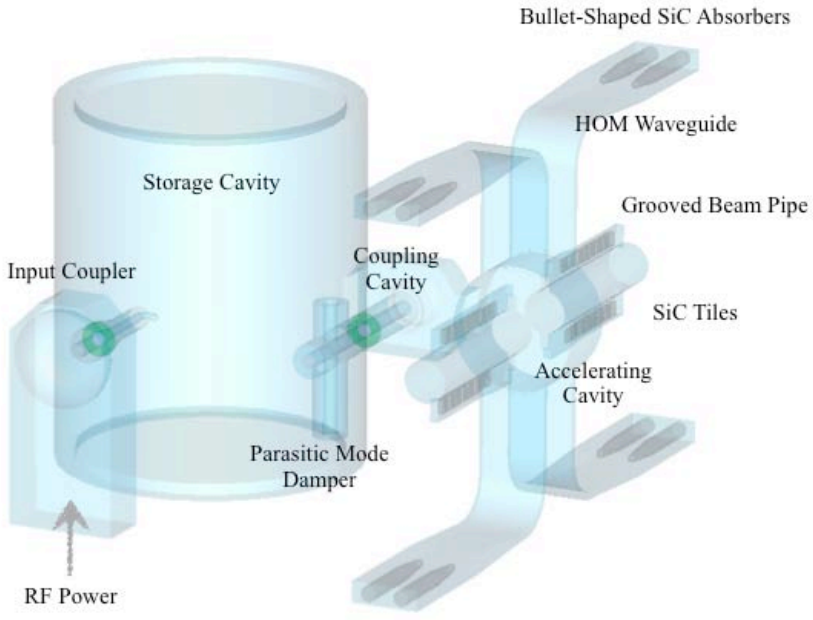


**Figure 2:** A 3D schematic view of the ARES cavity system.

The accelerating cavity, itself, is a HOM-damped structure, which mainly consists of Oxygen Free Copper (OFC) parts brazed stepwise in a vacuum furnace. We have carefully designed the HOM-damped structure to be smoothly embedded into the whole ARES scheme without any structural or electromagnetic incompatibilities. Four rectangular waveguides are directly brazed to the upper and lower sides of the accelerating cavity in order to damp monopole HOM's and dipole ones deflecting the beam in the vertical direction. Extracted HOM power is guided through an E-bend waveguide in the horizontal direction, and finally dissipated in two bullet-shaped SiC ceramic absorbers inserted at the end of each waveguide. Each SiC absorber is directly cooled by water flowing in the channel bored inside. On the other hand, in order to damp the dipole modes defecting the beam in the horizontal direction, grooved beam pipes [8] are attached to both endplates of the accelerating cavity. The grooved beam pipe with an inside diameter of 150 mm is twofold with two grooves at its upper and lower sides. Inside each groove, there are eight SiC tiles arranged in line and brazed to a water-cooled copper plate. Details of the HOM loads are reported in [9].

The coupling cavity made of OFC parts is brazed to one side of the accelerating cavity in the horizontal direction. As shown in Figure 2, the coupling cavity is equipped with a coupler in order to damp the parasitic 0 and $\pi$ modes. The parasitic mode coupler [10] is a coaxial line complex, which consists of an antenna-type coupler inserted right into the middle of the coupling cavity, a disk-type ceramic window, and a cross stub support. Extracted RF power is guided downward through a tapered coaxial line toward a water-cooled dummy load.

The energy storage cavity operated in the $TE_{013}$ mode is a large cylindrical steel structure with dimensions of 1070 mm in diameter and 1190 mm in axial length, whose inner surfaces are copper plated. The Q value of the $TE_{013}$ mode is $1.65 \times 10^5$, which is 85% of the theoretical value assuming a copper electrical conductivity of $5.81 \times 10^7$ S/m. The storage and coupling cavities are coupled through a rectangular aperture of 120 mm x 180 mm, and mechanically connected with rectangular flanges. The flange connection is vacuum-sealed by welding thin stainless-steel lips together around the perimeter.

RF power is fed through an input coupler attached to a drive port of the storage cavity. RF power is transmitted from the rectangular waveguide input, via a doorknob transition with a capacitive iris, to the coaxial line with a disk-type ceramic window. The coaxial line is tapered down and ends with a magnetic coupling loop. The input coupler developed for the ARES cavity system has a power capability of up to 950 kW [11], far above the design power capability of 400 kW for KEKB.

#### *3.13.2.3 Operations through KEKB's Exploration and Beyond*

Through KEKB's exploration, especially in its early phases, we encountered many problems with the ARES cavities. Those problems can be roughly categorized into two groups: infancy problems, especially with accessory devices, emerging in a long-term operation with the beam currents being increased stepwise, and cavity problems attributed to quality-control issues, usually incompatible with stringent cost goals in the cavity production phase. Fortunately, none of the problems have been fatal to limit the

KEKB machine performance so far. Recently, the trip rate for all the 32 ARES cavities, 20 for LER and 12 for HER, has greatly decreased down to a level of a couple of trips in total per week. With our experience accumulated through those machine operations so far, we are confident of the performance of the ARES cavity system and its growth potential toward the SuperKEKB collider under consideration.

Extensive R&D studies have been ongoing in order to develop a next generation of the ARES cavity system, which should be capable of stable beam acceleration up to the design current of 9.4 A for the LER of the SuperKEKB collider. Three major items of the upgrading menu are as follows. First, the stored energy ratio $U_s$ / $U_a$ is to be increased from 9 to 15 by simply changing the coupling factor ratio, $k_a$ : $k_s$ [12]. Second, the grooved beam pipe is to be replaced with a winged chamber having a bullet-shaped SiC absorber directly water-cooled in each wing [13]. The third one is to upgrade the power capabilities of HOM absorbers, on which extensive R&D studies have been ongoing at a newly built test stand with an L-band klystron [14]. Fortunately, for the SuperKEKB HER, the ARES cavities presently operated for KEKB can be reused without any modifications up to the design beam current of 4.1 A. As for the input coupler, multipactoring inside the coaxial line has been systematically studied [15], and a counter measure with fine grooving on the surface of the outer conductor has been proposed [16], and currently being tested under actual operating conditions simulated at a test stand [17]. Furthermore, R&D on the application of high purity alumina to the RF window of the input coupler has been ongoing in order to upgrade its thermal structural properties to be capable of stably transmitting CW RF power of 1 MW [18].

### 3.13.3 KEKB Superconducting Accelerating Cavity

#### *3.13.3.1 Operating Parameters*

A cross sectional view of a KEKB SC accelerating cavity is shown in Figure 3. Four cavities were installed in 1998, and another four cavities were added in 2000. A hybrid RF system including the eight SC cavities and twelve ARES cavities provides the total RF voltage of 13 ~ 15 MV in the HER. Each SC cavity provides a voltage of 1.4 MV delivering an RF power of 350 ~ 400 kW to the electron beam of 1.4 A.

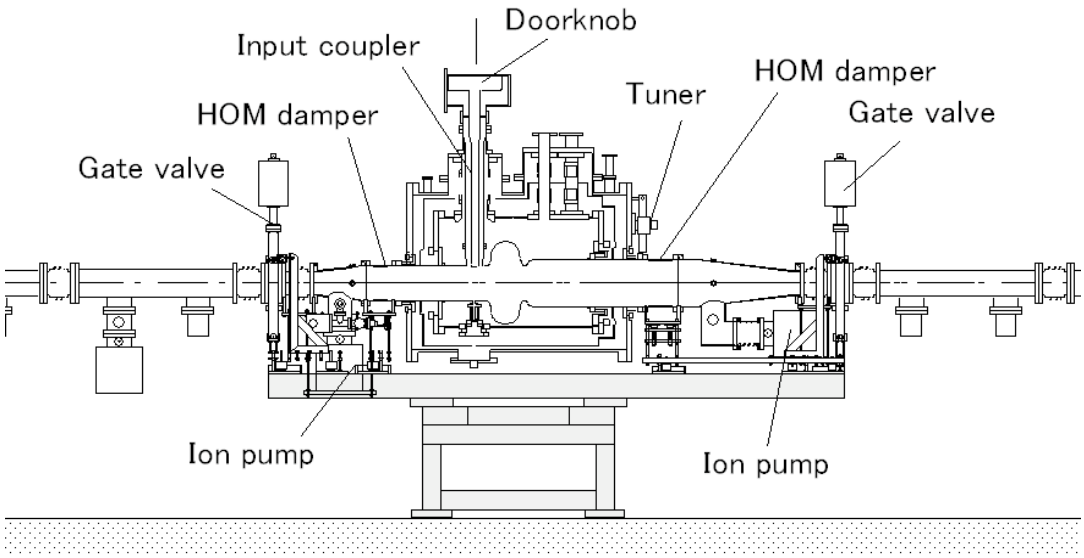


**Figure 3:** A cross sectional view of the KEKB superconducting accelerating cavity. A 509 MHz single cell cavity with a large iris diameter of 220 mm has ferrite HOM absorbers on both sides and a coaxial-type power coupler. The cryomodules of 3700 mm in length are connected to the beam ducts of 150 mm in diameter.

Typical forward and reflecting power of each cavity is shown in Figure 4. The original external Q-value of a coaxial power coupler had been chosen as $7 \times 10^4$ for the design voltage of 1.5 MV and the power of 250 kW at the design beam current of 1.1 A. In 2004, however, the external Q was lowered to $5 \times 10^4$ for upgrading the HER to store up to 2 A (Figure 5) [19]. Design and achieved performances are listed in Table 2.

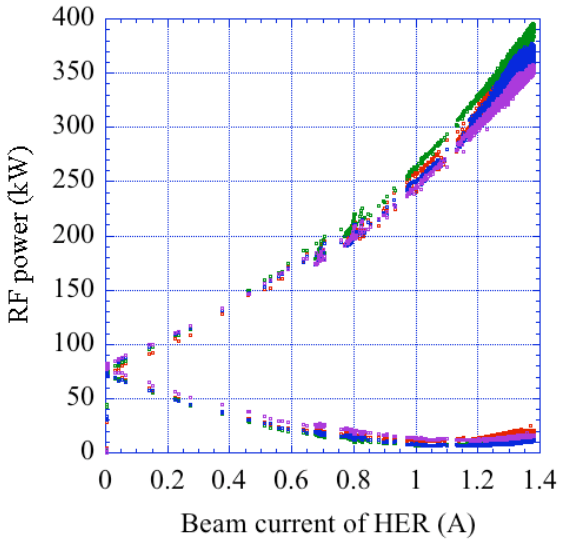


**Figure 4:** RF power of each SC cavity: Input and reflecting power for the external Q of $5 \times 10^4$ at 1.4 MV.

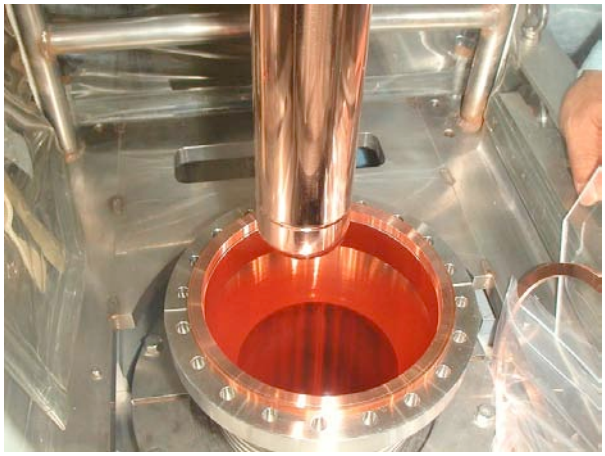

**Figure 5:** Coupling of the power coupler is variable by replacing a vacuum gasket to a thinner one changing the penetration of the inner conductor into the cavity.

**Table 2:** Achieved performance of the KEKB SC accelerating cavities.

| *Parameter* | *design* | *achieved* | *unit* |
|---|---|---|---|
| Number of SC cavities | 8 | 8 | |
| Maximum beam current | 1.1 | 1.4 | A |
| Bunch charge | 2 | 10 | nC/bunch |
| RF voltage | 1.5 | 1.2 - 2 | MV/cavity |
| Power delivered to beam | 250 | 350 - 400 | kW/cavity |
| HOM power | 5 | 16 | kW/cavity |

#### *3.13.3.2 RF Trip*

A high intensity beam of a short bunch length leaves a large amount of HOM power in the cavity. Furthermore, the operating number of bunches is about one-third that of the design value to avoid the electron-cloud instability in the LER. This results in three times higher HOM power compared to the design value; the HER beam of 1.4 A in 1400 bunches leaves the HOM power of 16 kW in each SC cavity. The HOM power heats up the ferrite dampers on the beam pipes at room temperature to about 90°C. Then the gas condensed on the cold cavity surface comes out, which may trigger a discharge in the cavity. Operational statistics of all beam trips and those caused by RF trips in the HER is summarized in Figure 6.

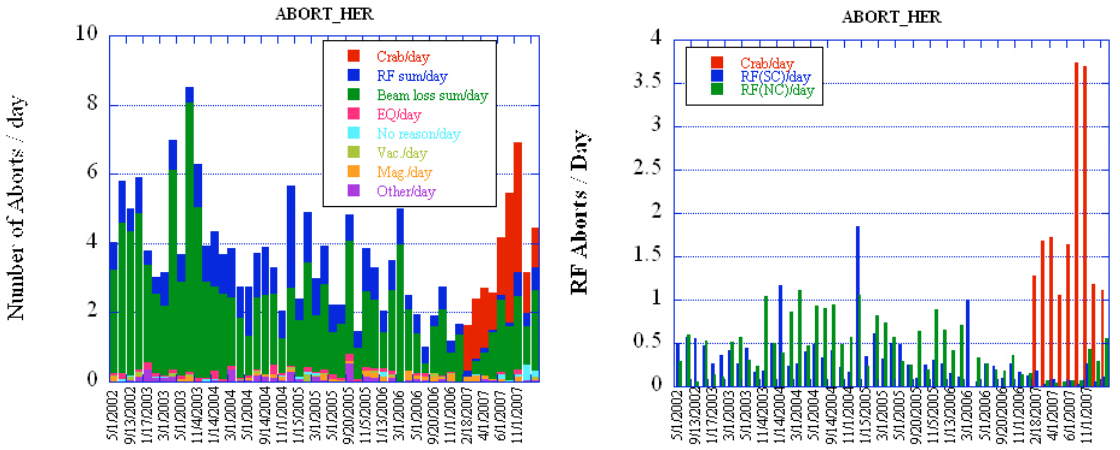


**Figure 6:** Statistics of beam aborts in the HER: (left) All beam trips have been classified by the causes; crab cavity, RF cavities, beam loss, earthquake (EQ), vacuum (VAC), magnets (Mag), others and unknown. (right) Beam aborts caused by the crab, SC and ARES cavities. Trip rate of the SC cavity is 0.5/day at 1.4 A and 0.1/day at 0.85 A, which corresponds to once per 80 days for one SC cavity in average.

The trip rate of the SC cavities reduced from 0.5/day to 0.1/day in 2007 when the beam current was lowered to 1 A by adopting the crab crossing. This trip rate corresponds to 80 days per trip for one SC cavity in average. A half of them are caused by discharge in the cavity or in the power coupler, and the other half are due to the system failure such as RF power sources, the cryogenic system and so on.

#### *3.13.3.3 RF Conditioning*

Regular conditioning of the power coupler and the cavity is effective to maintain stable long-term operation. Before every cool down of the cavities, the power couplers are conditioned at room temperature up to 300 kW under full reflection condition. A DC voltage of less than ±2 kV is applied between the inner and outer conductors of the coupler during the conditioning process to release the condensed gas on the surface by enhancing the multipacting. The cold cavity is conditioned with an RF power for about two hours on maintenance days once every two weeks. In this processing, so-called pulse conditioning is sometimes applied, where a small RF pulse is superimposed to the CW power of just below the cavity quench level. This conditioning can remove the condensed gas on the cavity surface accumulated during the operation.

#### *3.13.3.4 Improvements for SuperKEKB*

The most challenging issue for the SC cavities for upgrading to SuperKEKB is that the HOM power per a cavity is increased to 90 kW at a design beam current of 4.1 A and a bunch length of 3mm. This power may heat up the ferrite surface close to the Curie point and cause a large amount of out gas. The HOM power can be reduced to 60 kW by enlarging the diameter of the beam ducts from 150 mm to 220 mm, which reduces the loss factor of tapers on both sides. It is also effective to reduce the ferrite thickness from 4 mm to 3 mm to suppress the temperature rise. Fabrication and power test of a 3 mm thickness ferrite damper is undergoing (Figure 7) [20].

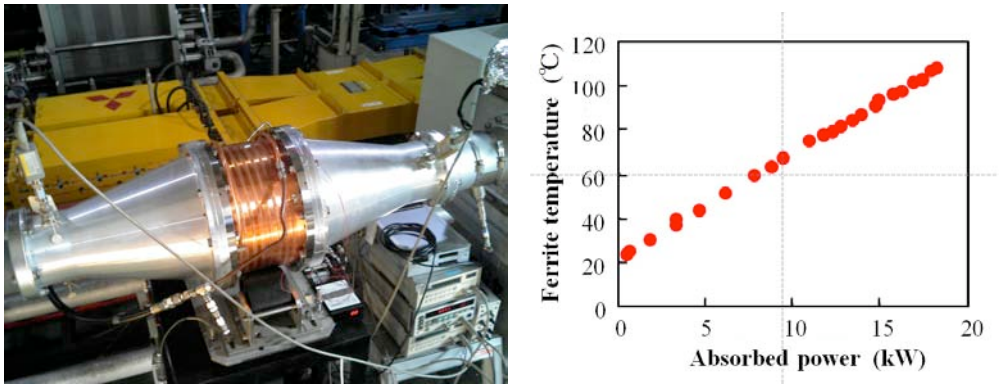


**Figure 7:** (left) Power test of a HOM damper. A cylindrical ferrite of 3mm in thickness is bonded inside a copper beam pipe by HIP, which is cooled from the outside by water. (right) The temperature of the ferrite surface is measured with an infrared thermometer.

### 3.13.4 Commissioning of KEKB Crab Cavities

#### *3.13.4.1 Superconducting Crab Cavity*

A schematic view of the KEKB superconducting crab cavity is shown in Figure 8. It has a squashed cell and a coaxial beam pipe with a notch filter to sufficiently damp any parasitic mode, not only HOMs but also the lower-frequency mode (LOM) corresponding to the accelerating mode, and the unwanted polarization of the crabbing mode [21]. Two crab cavities were installed in KEKB in January 2007, one for the LER and the other for the HER (Figure 9) [4]. After cool-down and conditioning of the cavities, system adjustment and machine tuning with the crab crossing started with low-current beams. Since October 2007 high-current crab crossing operation continued for more than one year. Achieved parameters of the crab cavities during the operation are listed in Table 3.

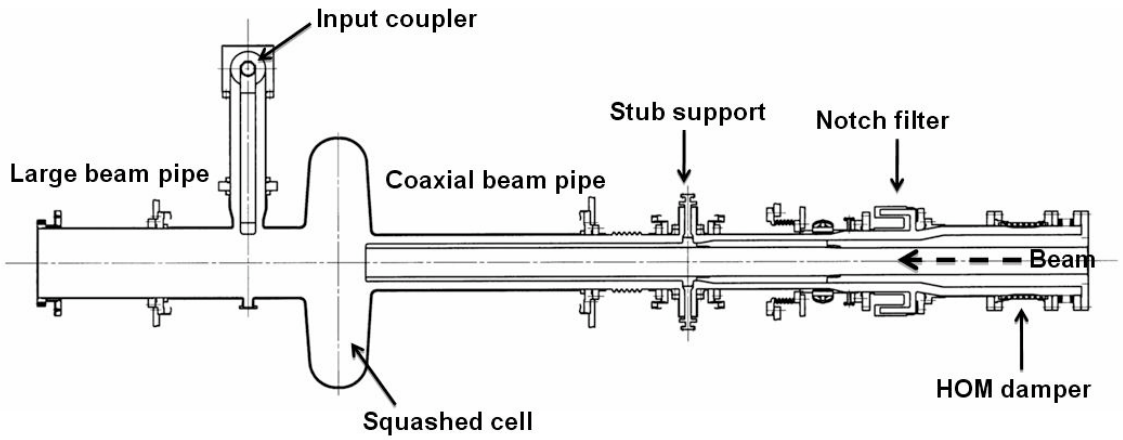


**Figure 8:** A schematic view of KEKB crab cavity.

**Figure 9:** KEKB superconducting crab cavities. (left) Crab cavity for the HER, and (right) crab cavity for the LER.

**Table 3:** Achieved parameters of KEKB crab cavities during the operation.

| | **LER** | **HER** | *Unit* |
|---|---|---|---|
| Beam current (Crab ON) | 1620 | 1043 | mA |
| Beam current (Crab detuned) | 1700 | 1350 | mA |
| Crab voltage (maximum) | 1.5→1.1→1.33 | >1.8 | MV |
| Crab voltage (typical operation) | 0.8~0.95 | 1.3~1.5 | MV |
| Maximum HOM power | 12+15(SiC) | 12 | kW/cavity |
| Tuner phase stability (w/piezo)<br>(w/o piezo) | ±13<br>±15 | ±1<br>±3 | degree<br>degree |
| Crab phase stability | ±0.1 | ±0.1 | degree |
| Average trip rate | 0.6 | 1.4 | times/day |

#### *3.13.4.2 Crabbing Voltage*

The HER crab cavity has maintained the required operating voltage of 1.3 to 1.48 MV. The voltage was even raised up to 1.8 MV for conditioning. On the other hand, the LER crab cavity degraded from 1.5 to 1.3 MV at the first processing in the tunnel. Furthermore, a heavy quench occurred on March 17, 2007, and the voltage degraded to 1.1 MV. Neither conditionings nor warm-up to room temperature could recover the performance. The cavity has been operated at a lower voltage between 0.8 and 0.95 MV, and the beta function at the crab cavity was increased from 40 to 80 m to obtain the necessary kick with the lower voltage. The cavities were regularly conditioned on the maintenance days every two or three weeks. Recently, it shows a sign of recovering the voltage up to 1.33 MV.

#### *3.13.4.3 Tuner Control System and Phase Stability*

The tuner system consists of a main tuner and two sub-tuners. The main tuner changes the insertion of the coaxial beam pipe into the cavity cell to tune the resonant frequency, while the sub-tuner adjusts the horizontal alignment of the coaxial beam pipe with respect to the cavity. The main tuner has a mechanical motor jack and a piezo actuator. The HER crab tuner system well stabilizes the tuning phase within ±1°. On the other hand, the LER tuner has a large fluctuation of ±13° due to a backlash behavior

caused by a mechanical problem [22]. Despite the large fluctuation of the tuning phase, the amplitude and phase of the crabbing field is sufficiently stabilized by the low level RF feedback loops. The phase fluctuation was estimated from the sideband peak heights of measured pickup spectrum. The phase fluctuation faster than 1 kHz is less than ±0.01° and slow fluctuation from ten to several hundreds of hertz is about ±0.1°. They are much less than the allowed phase error estimated by beam-beam simulations.

The piezo actuators broke several times in 2007. It is suspected that the breakdown is caused by pulling force acting on the piezo actuator, and a coil spring with pre-load of 49 N in a driver shaft was added in January 2008. The crab phase and amplitude fluctuation was still acceptable without the piezo control.

#### *3.13.4.4 Coherent Oscillation at High Current*

In the high current crab-crossing operation we observed a large amplitude coherent oscillation of beams and the crabbing field at about 540 Hz. The oscillation caused luminosity degradation and short beam lifetime. It occurred with high-current colliding beams; it never occurred in single beam operation, even at a high beam current. After several beam studies, we concluded that the oscillation is caused by the beam loading on the crab cavities together with the beam-beam force at the interaction point. We found that the oscillation can be avoided by properly setting the tuning offset angles and the crabbing phase [23].

#### *3.13.4.5 Trip Rate*

Figure 10 shows the history of number of trips per week of crab cavities. Most of the trips are caused by a discharge or multipacting in the cavity or at the input coupler. They are detected by interlock systems such as a quench detector, arc sensors, etc, then the RF power is switched off and the stored beam is aborted. The two-year crab-crossing operation is divided into four periods; the first period (Feb. to Jun. 2007) was mostly for low-current machine tuning, while the other three periods are dedicated for the physics run with high-current beams of typically 1.6 A in the LER and 1.0 A in the HER.

When the beam current was first raised above 200mA in the Period 1, the vacuum pressure of the LER crab cavity rose above 3 x $10^{-7}$ Pa, and the cavity frequently tripped. Then the cavity was warmed up to room temperature to remove condensed gases on the surface. After the warm-up, the trip rate was drastically reduced to about 1 times/day. The second high current trial at the end of this period was successfully conducted, and the LER current was raised up to 1.3 A. The average trip rate of the HER crab cavity during the Period 1 was 1.3 times/day.

At the beginning of the Period 2, the HER cavity had a higher trip rate of 3.5 times/day, and frequent conditioning was needed. After slightly decreasing the crab voltage from 1.48 to 1.36 MV, the trip rate was reduced to 1 times/day. In the Period 3 and 4 the HER cavity has kept stable operation with a trip rate of 1.3 times/day, even at a higher voltage of 1.5 MV. The average trip rate of the LER crab cavity during the Period 2 to 4 was 0.3 times /day.

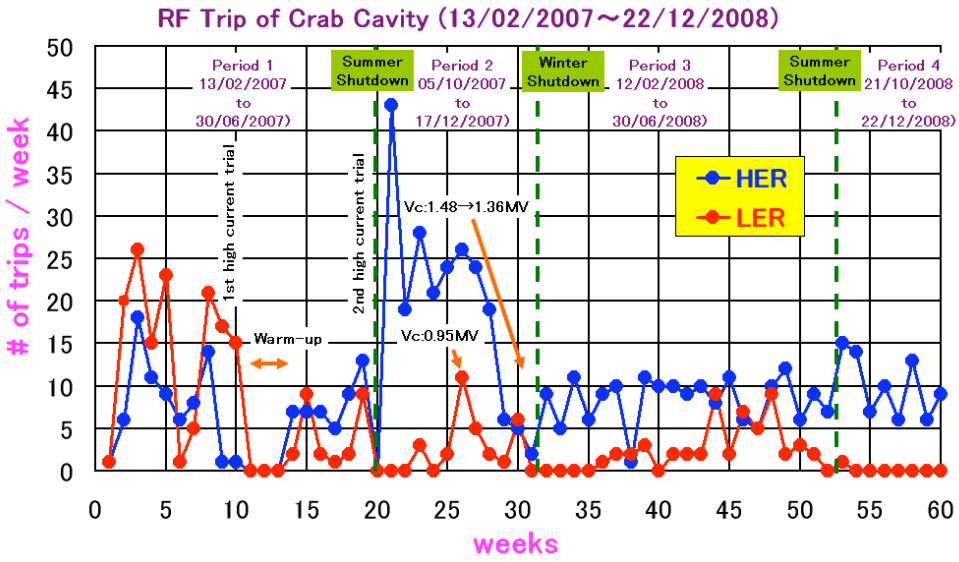


**Figure 10:** Numbers of trips per week of crab cavities.

### *3.13.4.6 HOM Damper*

The crab cavity has two HOM dampers made of ferrite RF absorbers HIPped (Hot Isostatic Press) on the copper beam pipes. One damper is located on the beam pipe of 240 mm in diameter, and the other is at the end of the coaxial beam pipe. The good damping property was confirmed by observing beam-induced RF spectrum. In particular, the most dangerous lower-frequency mode, LOM, is sufficiently damped by the coaxial damper. The frequency and the Q factor obtained from the spectrum were well in agreement with the design values, and also with the values measured at a bench test [24].

The maximum HOM power absorbed by the HER cavity dampers was 12 kW at the beam current of 1.35 A, which agrees with an estimation from a calculated loss factor. In the case of LER crab cavity, an additional damper made of SiC of 150 mm in diameter is located on the beam pipe downstream of a taper section connected to the 240 mm diameter ferrite damper. The maximum HOM power absorbed by the ferrite dampers was 12 kW and the SiC damper 15 kW at the beam current of 1.7 A. The total HOM power absorbed by these dampers agrees with the calculation.

### *3.13.4.7 Need for Higher Crabbing Voltage*

The horizontal beta function at the crab cavity is enlarged compared to other sections to obtain the required crab kick. But this might limit the beam lifetime at a high bunch current due to the physical aperture at the crab cavity. It is desired to reduce the beta function by increasing the crabbing voltage. One possible way is to reduce the operating temperature from 4.4 K with saturated liquid helium to a lower temperature to improve the cavity performance. A new pumping system in the helium transfer line (Figure 11) has been prepared for this purpose, and tested in December 2008. The cavities were cooled down to 3.7 K with a heater load of 100 W for several days. The cavities will be tested with an RF power at the lower temperature before the next KEKB operation starts in April 2009.

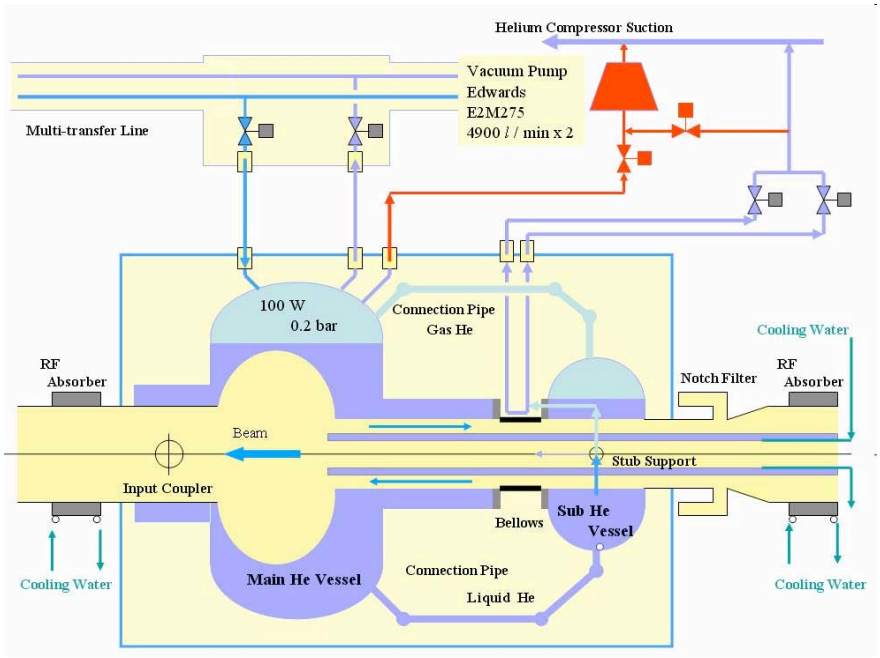


**Figure 11:** Improved cooling system with new pumping system.

### *3.13.4.8 New Crab Cavities for SuperKEKB*

Current design for the upgrading KEKB to SuperKEKB is based on higher beam currents of 9.4 A in the LER and 4.1 A in the HER and a shorter bunch length of 3 mm. Since the present crab cavity has different beam pipe radii in both sides of the cell, which increases the loss factor, especially for the short bunch length, the HOM power would be unacceptably increased. Two types of new crab cavity designs were proposed for SuperKEKB [25]. A schematic view of one of them is shown in Figure 12. To heavily damp the LOM and the HOMs, waveguides and coaxial couplers are directly attached to the cavity cell. The coaxial coupler damps the LOM, and its external Q factor is reduced to 50. The waveguides damp other monopole and dipole modes. This design has a larger physical aperture and a lower loss factor compared to the present crab cavity. The R&D for the SuperKEKB crab cavity is underway.

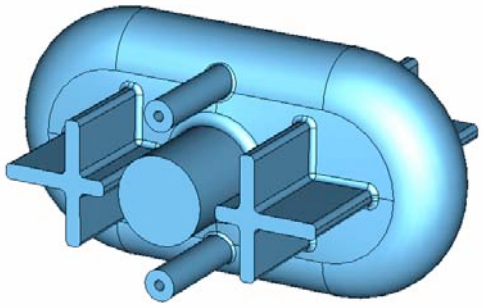

**Figure 12:** A design of new crab cavity for SuperKEKB.

### 3.13.5 Beam Instability-Related Issues

#### *3.13.5.1 The -1 Mode Instability and Damper*

Even with the ARES and SC cavities, at first the beam currents in both rings were limited at around 1 A due to the excitation of the -1 mode longitudinal instability. One reason for the excitation at a lower current than expected is a lower operating voltage than the design value. Another reason may be due to small differences in the operating conditions between the cavities. To solve this problem, the -1 mode damper feedback system was installed in both rings, which selectively reduces the impedance at the -1 mode driving frequency. Then the instability was suppressed, and the beam currents could be increased beyond 1 A [26].

#### *3.13.5.2 Transient Effects of RF Trips*

For a relatively low-current beam, even when one or two RF stations trip, the beam could be kept without any loss. Keeping the beam without aborted would save time for refilling. For a high-current beam, however, transient change of the beam energy and phase to an RF trip can be large due to the heavy beam loading. At the beginning of the operation when the beam current was first increased more than about 500 mA we encountered two problems caused by the RF trips; damages on movable mask heads and a large amount of radiation doze accumulated at the Belle detector. In order to avoid these problems the beam abort trigger system was improved by adding a beam phase detection system and loss monitors [27].

### 3.13.6 Conclusions

The KEKB RF system with the ARES and the SC cavities have been working very stably with high-current beams up to 2.0 A in the LER and 1.4 A in the HER during the long-term physics run for about ten years. The first crab cavity system has been successfully operated with the high-current beams providing the crab crossing operation. The requirements for the RF system for upgrading to SuperKEKB with the design beam currents of 9.4 A in the LER and 4.1 A in the HER have been identified. The R&D has been ongoing toward the challenging goals.

### 3.13.7 References

1. Y. Yamazaki and T. Kageyama, Particle Accelerators 44 (1994), p. 107.
2. T. Furuya et al., "Achievement of Superconducting Damped Cavities in KEKB Accelerator", Proc. of the 11th Workshop on RF Superconductivity SRF 2003, MoP21.
3. K. Akai et al., "RF Systems for the KEK B-Factory", Nuclear Instruments and Methods A 499 (2003) p. 45.
4. K. Hosoyama et al., "Development of the KEK-B Superconducting Crab Cavity", Proc. of the 11th European Particle Accelerator Conference, Genoa, 2008, p. 2927.
5. Y. Funakoshi et al., "Performance of KEKB with Crab Cavities", Proc. of the 11th European Particle Accelerator Conference, Genoa, 2008, p. 1893.
6. SuperKEKB Task Force, "Letter of Intent for KEK Super B Factory", KEK Report 2004-4 (2004).
7. T. Kageyama et al., Proc. of the Particle Accelerator Conference, Vancouver, Canada,

1997, p. 2902.
8. T. Kageyama, Proc. of the 15th Linear Accelerator Meeting in Japan, Sapporo, 1990, p. 79, and Proc. of the Eighth Symposium on Accelerator Science and Technology, Wako, Japan, 1991, p. 116.
9. Y. Takeuchi et al., Proc. of the Particle Accelerator Conference, Vancouver, Canada, 1997, p. 2986.
10. F. Naito et al., Proc. of the Particle Accelerator Conference, Vancouver, Canada, 1997, p. 2977.
11. F. Naito et al., Proc. of the Asian Particle Accelerator Conference, Tsukuba, Japan, 1998, p. 776.
12. T. Kageyama et al., Proc. of the 14th Symposium on Accelerator Science and Technology, 2003, p. 66.
13. T. Kageyama et al., Proc. of the Particle Accelerator Conference, Knoxville, TN, 2005, p. 1186.
14. Y. Takeuchi et al., Proc. of the 4th Annual Meeting of Particle Accelerator Society of Japan and the 32nd Linear Accelerator Meeting in Japan, 2007, p. 446.
15. T. Abe et al., Phys. Rev. Special Topics – Accel. and Beams 9, 062002, 2006.
16. T. Abe et al., Proc. of European Particle Accelerator Conference, Edinburgh, Scotland, 2006, p. 1310.
17. H. Sakai et al., Proc. of the Particle Accelerator Conference, Knoxville, TN, 2005, p. 1294.
18. K. Yoshino et al., Proc. of the 4th Annual Meeting of Particle Accelerator Society of Japan and the 32nd Linear Accelerator Meeting in Japan, 2007, p. 443.
19. S. Mitsunobu et al., "High Power Input Coupler for KEKB SC Cavity and New 1 MW Test Bench", Proc. of the 11th Workshop on RF Superconductivity SRF 2003, ThP33.
20. S. Mitsunobu et al., "Status of KEKB Superconducting Cavities", Proc. of the 13th Workshop on RF Superconductivity SRF 2007, TUP23.
21. K. Akai et al., "Crab Cavity for the B-factories", Proc. B-factories, SLAC 1992, SLAC-400 (1992) p. 181.
22. Y. Yamamoto et al., "Horizontal Tests for Crab Cavities in KEKB", Proc. of the 13th Workshop on RF Superconductivity SRF 2007, WEP27.
23. K. Akai et al., "Commissioning and Beam Operation of KEKB Crab RF System", Proc. of the 13th Workshop on RF Superconductivity SRF 2007, WEP57.
24. Y. Morita et al., "Beam-induced RF Modes and RF Power in the Crab Cavity for KEKB", Proc. of the 13th Workshop on RF Superconductivity SRF 2007, WEP55.
25. K. Akai and Y. Morita, "New Design of Crab Cavity for Super KEKB", Proc. of the Particle Accelerator Conference, Knoxville, 2005, p. 1129.
26. S. Yoshimoto et al., "The -1 Mode Damping System for KEKB", Proc. of the 14th Symposium on Accelerator Science and Technology, 2003; KEK Preprint 2003-72A.
27. K. Akai et al., "Protection of Hardware Components with High-current Beam against RF Trips in KEKB", Proc. of the 8th European Particle Accelerator Conference, Paris, 2002, p. 2112.

## 3.14 A Retrospective on LEP

Helmut Burkhardt and John M. Jowett
CERN, CH-1211 Geneva 23
Mail to: Helmut.Burkhardt@cern.ch, John.Jowett@cern.ch

### 3.14.1 Introduction

LEP was the highest energy electron-positron collider ever built. It was almost certainly the last in the lineage of $e^+e^-$ ring colliders, expanding in size and energy reach from ADA (through SPEAR and several other machines). Further steps in $e^+e^-$ energy are expected to occur only at linear colliders. Since LEP was shut down in the year 2000, a new generation of colliders, the *factories,* has broken new ground by revisiting lower energy scales at greatly increased luminosity (see other articles in this Newsletter). As we see it, two machines, CESR and LEP, paved the way for this transition in the late 1980s and 1990s. Both were originally conceived as energy frontier machines, and performed as such, but were also adapted through various upgrade schemes to become pioneers of the luminosity frontier.

The importance of this development may not be obvious to those who were not yet active in the early 1980s. Back then, it seemed to many that the principles of $e^+e^-$ ring design were cut and dried, that the technology had matured and had certain insuperable limits (a beam-beam limit $\xi \approx 0.03$, problems with crossing angles, limitations on the number of bunches in a ring, etc.). The historical article [10] gives an account of the achievements of the pioneers of the technology and confirms our recollection of the *zeitgeist*. To a large extent, this was an understandable conservative reaction to the unfulfilled luminosity projections of some earlier projects (those, in turn, were conceived when beam-beam and other limitations were not yet appreciated). So it is perhaps not surprising that ideas for factories with luminosities beyond about $10^{32}$ $cm^{-2}$ $s^{-1}$ seemed outlandish when they were put forward in the later 1980s. We believe that the luminosity upgrades of CESR and LEP did much to change this outlook, making it possible to approve the construction of high-luminosity factories like DAΦNE, PEP-II and KEKB in the 1990s.

Strangely enough, the conservative-optimist dilemma is once again relevant as we contemplate proposals for future Super B-Factories. This time round, the hopes for even higher luminosity are based on a deeper understanding of the limits, ingenious new ideas for overcoming them and the predictions of the most advanced simulation programs.

In this article we try to turn things around again and take a look back at LEP from the perspective of what is now known from the latest generation of colliders.

#### *3.14.1.1 Brief History and Description of LEP*

LEP produced its first collisions on 13 August 1989, less than six years after ground was broken on 13 September 1983. The construction of LEP was the largest civil engineering undertaking in Europe between 1983 and 1988.

The near-circular tunnel extends from the foothills of the Jura Mountains to Geneva airport and straddles the border between France and Switzerland.

The 26.66 km circumference was composed of eight 2.8 km long arcs and eight straight sections extending for 245 m on either side of the 8 collision points of which half were used for experiments. About 3300 dipole, 800 quadrupole, 500 sextupole and over 600 orbit corrector magnets were installed in the tunnel. The magnet lattice was of the FODO type with a period (cell) length of 79 m and 31 regular lattice periods per octant. Both beams circulated in the same beam pipe. Beams were injected at 22 GeV and then ramped to the physics energy. During injection, ramp and β-squeeze, beams were separated using electrostatic separators. After the ramp and squeeze, the beams were brought into collision in four interaction points.

Operation until 1995 was for Z-production at beam energies close to 45.6 GeV and this phase, powered by the original normal conducting RF system, is referred to as LEP1.

LEP1 was designed to operate at a maximum energy of 55 GeV. The knowledge that $\sqrt{s} = 92.4$ GeV was the interesting centre-of-mass energy came only later with the discovery of the W and Z bosons at the SPS collider.

The progressive installation of superconducting cavities in the following years allowed the energy to be increased through 65 GeV, a number of energies between 80 and 101 GeV, up to the final maximum of 104.5 GeV per beam, well beyond the W-pair production threshold. This phase is referred to as LEP2. LEP2 operation was stopped at the end of the year 2000.

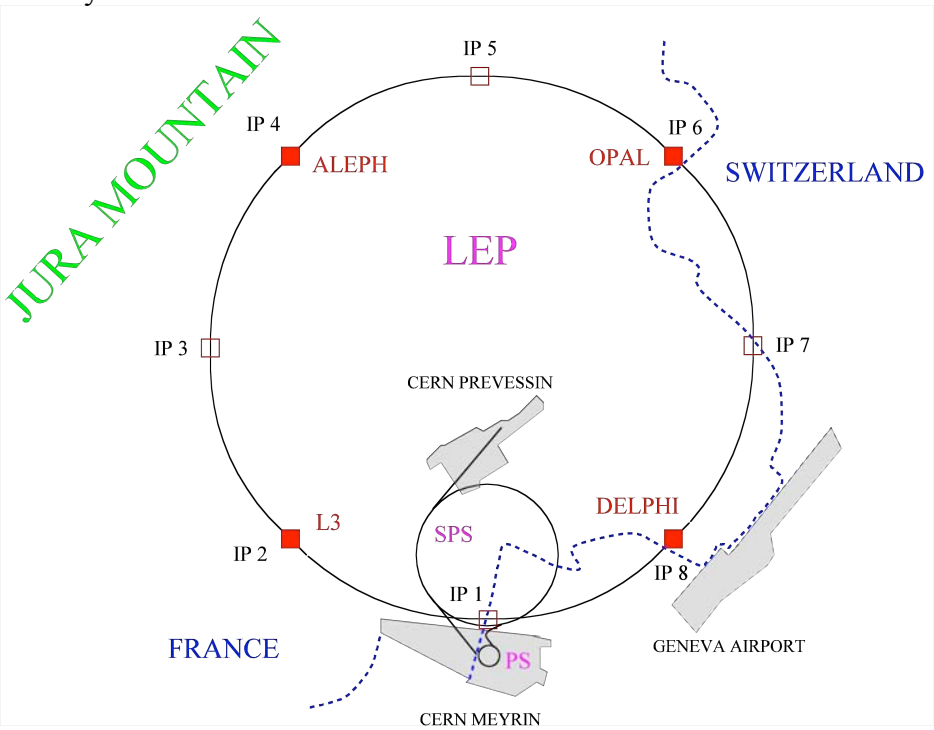


**Figure 1:** Layout of the LEP ring on the border of France and Switzerland. The 8 access points are denoted IP1 through IP8. The 4 LEP experiments L3, ALEPH, OPAL and DELPHI are installed at the even numbered access points. Positrons travel clockwise, electrons anti-clockwise from points 1 to 8. The locations of two LEP injectors, the SPS (Super Proton Synchrotron) and the PS (Protron Synchrotron), are also indicated.

As originally anticipated, the beam-beam interaction was a much more stringent limit at the lower and intermediate energies. The horizontal tune shift $\xi_x$ was generally

significantly lower than $\xi_y$. Table 1 lists beam parameters recorded in LEP at the times of maximum vertical beam-beam parameters. Table 2 is a brief summary of the performance (but omits many details, e.g., in years when multiple energies were visited).

**Table 1:** LEP beam parameters corresponding to the best performances at three different energies. The luminosities and beam-beam tune shifts are averaged over a time interval of 15 minutes. For each beam energy, the first line corresponds to the horizontal, the second line to the vertical plane.

| $E_b$ (GeV) | $N_b$ ($\times 10^{11}$) | $k_b$ | $\mathcal{L}$ ($\mathrm{cm}^{-1}\mathrm{s}^{-2}$) | $Q_s$ | $Q$ | $\beta^*$ (m) | $\epsilon$ (nm) | $\sigma$ ($\mu$m) | $\xi$ |
|---|---|---|---|---|---|---|---|---|---|
| 45.6 | 1.18 | 8 | $1.51 \times 10^{31}$ | 0.065 | 90.31 | 2.0 | 19.3 | 197 | 0.030 |
| | | | | | 76.17 | 0.05 | 0.23 | 3.4 | 0.044 |
| 65 | 2.20 | 4 | $2.11 \times 10^{31}$ | 0.076 | 90.26 | 2.5 | 24.3 | 247 | 0.029 |
| | | | | | 76.17 | 0.05 | 0.16 | 2.8 | 0.051 |
| 97.8 | 4.01 | 4 | $9.73 \times 10^{31}$ | 0.116 | 98.34 | 1.5 | 21.1 | 178 | 0.043 |
| | | | | | 96.18 | 0.05 | 0.22 | 3.3 | 0.079 |

**Table 2:** Overview of LEP (instantaneous) peak performance 1989-1999. $\int \mathcal{L}\, dt$ is the luminosity integrated per experiment over each year. The design luminosity at 45 GeV was $17 \times 10^{30}$ $\mathrm{cm}^{-2}\mathrm{s}^{-1}$.

| Year | $\int \mathcal{L} dt$ ($\mathrm{pb}^{-1}$) | $E_b$ ($\mathrm{GeV/c}^2$) | $k_b$ | $2k_bI_b$ (mA) | $\mathcal{L}$ ($10^{30}$ $\mathrm{cm}^{-2}$ $\mathrm{s}^{-1}$) | $\xi_y$ |
|---|---|---|---|---|---|---|
| 1989 | 1.74 | 45.6 | 4 | 2.6 | 4.3 | 0.017 |
| 1990 | 8.6 | 45.6 | 4 | 3.6 | 7 | 0.020 |
| 1991 | 18.9 | 45.6 | 4 | 3.7 | 10 | 0.27 |
| 1992 | 28.6 | 45.6 | 4/8 | 5.0 | 11.5 | 0.027 |
| 1993 | 40.0 | 45.6 | 8 | 5.5 | 19 | 0.040 |
| 1994 | 64.5 | 45.6 | 8 | 5.5 | 23.1 | 0.047 |
| 1995 | 46.1 | 45.6 | 8/12 | 8.4 | 34.1 | 0.030 |
| 1996 | 24.7 | 80.5 to 86 | 4 | 4.2 | 35.6 | 0.040 |
| 1997 | 73.4 | 90 to 92 | 4 | 5.2 | 47.0 | 0.055 |
| 1998 | 199.7 | 94.5 | 4 | 6.1 | 100 | 0.075 |
| 1999 | 253 | 98 to 101 | 4 | 6.2 | 100 | 0.083 |
| 2000 | 233.4 | 102 - 104 | 4 | 5.2 | 60 | 0.055 |

### 3.14.2 Some Interesting Features of LEP

LEP had many unique and important features. Some, like the huge superconducting RF system, the single-bunch collective instabilities and the systematic use of resonant depolarization for energy calibration are well-documented elsewhere and we shall not revisit them here. In the limited context of this article we would like to recall some

interesting beam physics and some of the features that gave LEP the flexibility to run with maximum luminosity over a large range of operating energies.

#### *3.14.2.1 Multiple Arc-Cell Phase Advances*

The initial design of LEP envisaged running LEP1 with phase advances $(\mu_x, \mu_y) = (60^\circ, 60^\circ)$ in the arc cells and changing to $(\mu_x, \mu_y) = (90^\circ, 90^\circ)$ to get a lower emittance for LEP2. This came from design procedures where the emittance was adjusted to achieve the predicted beam-beam parameter in both planes with the maximum current per bunch. In the construction phase, it was realized that a better strategy would be to start with a low-emittance lattice and the switch was made very soon after the start-up of the machine. This gave higher luminosity with lower bunch currents and the emittance wigglers (see below) were always available to increase the horizontal emittance when necessary.

We did not stop with $(\mu_x, \mu_y) = (90^\circ, 90^\circ)$ but went on to consider even higher horizontal phase advances and various vertical ones changing optics almost annually as the LEP2 RF was installed and the energy crept up. Two of the most successful optics were $(\mu_x, \mu_y) = (90^\circ, 60^\circ)$ and $(\mu_x, \mu_y) = (102^\circ, 90^\circ)$

#### *3.14.2.2 Wigglers*

LEP was initially equipped with two families of four 3-pole wiggler magnets. The "damping wigglers" were installed in dispersion-free locations to provide additional radiation damping at injection while the "emittance wigglers" were installed in dispersive locations to increase quantum excitation and horizontal emittance. As far as we know, LEP was the first machine in which the wigglers could be adjusted as transparent, tunable nonlinear knobs with built-in compensation of their vertical tune-shifts using nearby quadrupoles. So, for example, they could be gradually ramped down in the energy ramp without any effect on the tunes.

The emittance wigglers were useful at LEP1 to moderate the beam-beam effects (e.g., flip-flop, background spikes) caused by small horizontal beam size.

Later, an additional set of 12 stronger damping wigglers (the so-called "polarization wigglers") were added and also proved their worth in helping larger intensities to be injected. Since they were made quickly and cheaply they were not so well-behaved as the original wigglers and gave some trouble through their effects on the beam orbits.

#### *3.14.2.3 Damping Partition*

An additional control of both emittance and bunch length was the possibility to vary the damping partition by small changes of the RF frequency. This was used extensively at LEP2 to reduce the emittance when the energy was too high for the wigglers to have much effect beyond radiation damage.

#### *3.14.2.4 Extreme Synchrotron Radiation Effects*

LEP2 was the most extreme e+e- ring ever in terms of energy, radiation damping time and quantum fluctuations. The energy loss per turn reached 3 GeV. It truly entered the regime in which the large superconducting RF system really had to be considered as part of optics (systematic use of the 6D linear beam dynamics formalisms of Chao,

Mais-Ripken etc.). The energy sawtoothing between RF stations resulted in large (>1 cm) orbit separations in the arcs and very different optical functions of the two beams. Lattice imperfections could then lead to significant differences of global parameters (tune, chromaticity …) between beams, rather as happened earlier with the pretzel scheme.

The extremely rapid radiation damping (a few tens of turns) meant that LEP2 was probably the only machine where dynamic aperture could be calculated unambiguously in 50 turns of tracking so that 4-dimensional phase space scans of ensembles of imperfect machine models could be carried out in reasonable amounts of computer time. The physics limiting the dynamic aperture depended on radiation effects in quadrupoles and the linear optics with the traditional effects of multipole fields and high-order resonances almost invisible. However low-order resonances, with their phase-space portraits modified by the dissipative effects of radiation were important in certain optics.

#### *3.14.2.5 Beam Lifetime*

Beam lifetimes in LEP were generally rather long, of the order of 40–100 hours without collisions and 5–20 h with collisions, depending on the luminosity. In stable running conditions, beam lifetimes in LEP can be accounted for by three inelastic scattering process:

1) Compton scattering on black body photons with typically 60 h lifetime,
2) Beam-gas bremsstrahlung of the order of 100 h and
3) $e^+e^-$ collisions, dominated by very small angle radiative Bhabha scattering (beam-beam Bremsstrahlung).

It was only shortly before LEP went into operation that we learned from V. Telnov [6] that Compton scattering would become relevant in high energy electron machines. That this process would be the main single beam lifetime limitation and the dominant source of off-momentum background was only fully appreciated after some years of LEP operation. Fortunately the consequences were rather limited and lifetimes still dominated by the (wanted) $e^+e^-$ collisions. Initially, we were also surprised to find that the lifetimes in collisions were about 30% longer than anticipated [7]. The discrepancy can be explained by introducing a length cut-off in the cross section calculation on the level of some micrometres which corresponds to the mean distance of particles in the bunch at rest. Later we learned that this had previously been observed and explained as a beam-size effect at Novosibirsk [9]. For most of the LEP operation, we operated with a safe margin in RF voltage such that losses by quantum lifetime were negligible. In the last years of LEP2 operation instead, we operated very close to the quantum lifetime limit and found that the observed quantum lifetimes was a bit longer than anticipated. This can be explained by a more detailed calculation of the RF bucket which takes into account that particles have less energy and radiate less synchrotron radiation at the lower side of the RF bucket [8].

### 3.14.3 Paths to Higher Luminosity

As ever, high luminosity is reached by combination of many factors. Here we discuss only some schemes for increasing the number of bunches in LEP without

mention of many other important factors such as the maximization of injected beam current, working points, correction of orbit and optics, improvements of operational procedures, instrumentation, vacuum, etc.

#### *3.14.3.1 Vertical Separation*

From the beginning, the LEP designers favoured vertical separation over horizontal. The basic scheme for separation at the IPs during injection and ramp was based on local closed bumps created by vertical electrostatic separators. LEP always aimed for head-on collisions and never adopted horizontal crossing angles like the present factories.

Two bunches per beam provided collisions at the 4 experiments at the even-numbered IPs. To allow 4 bunches per beam, vertical separation bumps were also installed at the odd-numbered IPs. These were kept on to maintain separation at these points in collision conditions.

To follow this approach to 8 evenly-spaced bunches per beam would have meant installing separation bumps around the mid-points of each arc. While such schemes were designed in the early 1980s they would have required modifications of the basic arc cell structure and special hardware installations at the most inaccessible points in the whole ring. They were never adopted.

#### *3.14.3.2 High Luminosity LEP*

The main lines of the single-ring LEP design were set down in late 1970s and the Design Report was published in 1983 with construction starting soon afterwards. The highest energy colliders of the earlier generation were either operating (PEP, PETRA) or due to be commissioned in the next few years (TRISTAN). The first ideas for the present generation of double-ring e+e- factories only emerged in the late 1980s (earlier double-ring machines had not established the technology). With hindsight though, it is interesting to ask whether it would have been a good idea to build LEP as a two-ring machine like the more recent factories.

Obviously the extra ring and upgrades of the experiments would have cost more, perhaps a lot more for a larger tunnel cross-section (depending on the magnet design adopted). It would not have helped at LEP2 where the number of bunches was limited by installed RF power. Moreover, at LEP2 the operators could not have enjoyed the operational simplification of measuring and correcting the average orbit of the two beams which made the large orbit separation from the energy sawtooth invisible.

Another ring would have been a clean way to collide more bunches at LEP1 energy. With the installed RF power of LEP2, the number of bunches could have been increased to ~100, gaining at least one order of magnitude in luminosity over the 4-bunch case.

One year before LEP was due to be switched on, a suggestion was made [5] to increase the number of bunches by following the highly successful pretzel approach used at CESR. This would allow the RF power due to be installed for LEP2 to be exploited at LEP1 energy, potentially boosting the luminosity by an order of magnitude. This led to a study of “High Luminosity LEP” as a factory based on the pretzel scheme [11, 12] which showed a possibility of colliding up to 36 bunches. The experience at CESR was incorporated into the design.

The full realization of this scheme would have required new horizontal electrostatic separators and upgrades of a number of systems, not least the experiments. It could have been operated at various energy stages. A final phase of maximum luminosity at the Z

could presumably have been carried out after LEP2, probably implying some delay of the LHC.

#### *3.14.3.3 The Crash Pretzel*

In the end, only a limited, low-cost, version of the pretzel scheme (dubbed the "Crash Pretzel") was implemented using horizontal electrostatic separators recuperated from the separation scheme in the SPS collider. Because of the limited number of high-voltage supplies available, the 8 separators creating the 4 long-range pretzel bumps were connected in such a way that changing the voltage in any one of them had a domino effect on all the others (see Figure 2). Apart from the use of two additional "trim" separators, the only way to vary electric fields individually was to mechanically vary the gaps between the electrodes. Sparking of the separators was a concern so these manipulations were also limited. A few sextupoles were installed in straight sections to allow some adjustment of the tune-splits between beams and phase trombone schemes were implemented in the insertions. Apart from this limited set of knobs, we depended heavily on the global cancellation of differences (orbit, optics, damping partition,…) between the beams brought about by the anti-symmetry of the pretzel orbit around each IP. Operational optimization of differences between beams and collision conditions was always tricky because of the global effects of any local adjustment. We could only envy CESR's flexibility of individually powered quadrupoles and sextupoles.

The number of bunches per beam was limited to 8 by the energy-saving storage cavities attached to the normal-conducting RF system. Although this limitation would have been irrelevant later when more superconducting RF was installed, the experiments would have needed quite costly upgrades to accept a higher collision frequency.

It turned out that an unanticipated combination of the transverse mode-coupling instability and long-range beam-beam effects at the mid-arc encounters made it difficult to inject high bunch intensities without the use of negative chromaticity and transverse feedback.

Nevertheless, thanks to preparatory work in machine development sessions, the break-even in luminosity was achieved immediately when the scheme was put into operation for the last few weeks of the 1992 run. It allowed LEP1 to reach and exceed its design luminosity (with parameters quite different from the design) and produced LEP's major harvest of Z-events in 1993-94.

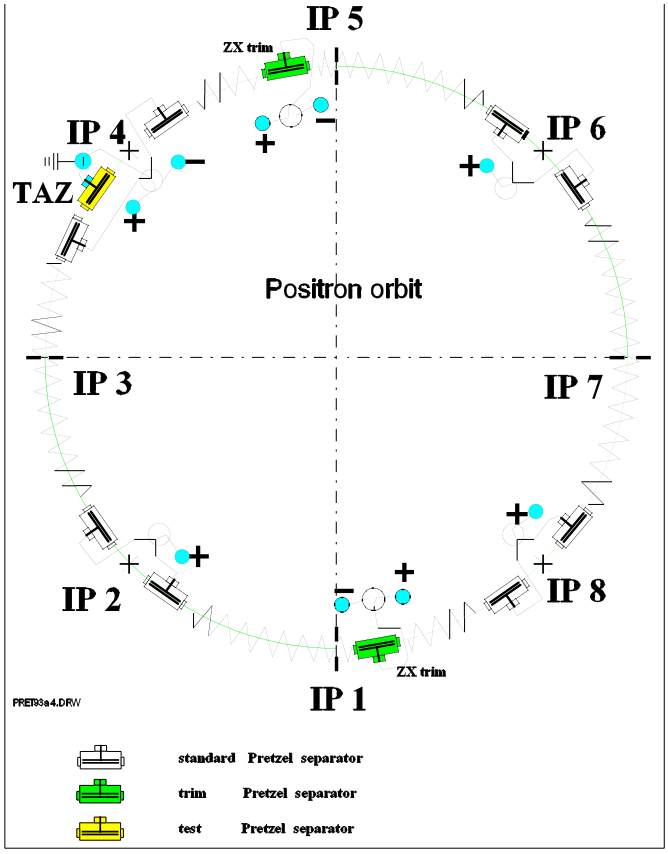


**Figure 2:** Schematic of the LEP Crash Pretzel scheme as operated in 1993-1994.

### *3.14.3.4 Bunch Train Scheme*

Another luminosity upgrade scheme was tried in 1995. This held out the hope that the number of bunches could be increased from 8 to 16, in 4 trains of 4, without the need for substantial upgrades of the experiments. Although superficially similar to the "bunch train" concept (involving a *horizontal* crossing angle) that had already been added on top of the pretzel scheme at CESR, the LEP scheme was really very different. It involved suppressing the pretzel scheme and installing additional *vertical* electrostatic separators around the IPs (Figure 3). While the original closed bumps spanned the IPs and were reduced to zero in collision, the new bumps transformed from a single closed bump with separation at the IP to two separate closed bumps on either side of the IP. The parasitic encounters of trains of bunches would occur inside these bumps.

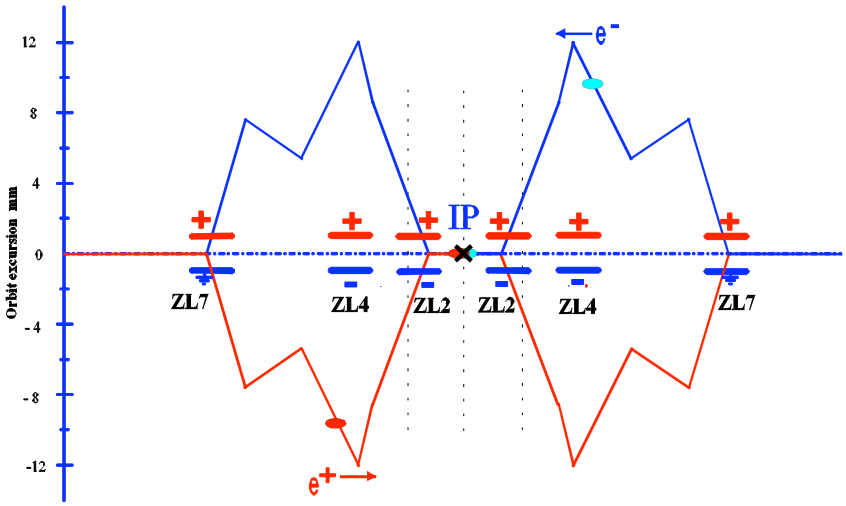


**Figure 3:** Schematic of the vertical separation around an IP in collision conditions of the LEP bunch train scheme.

This meant, however, that different bunches in each train would see a different sequence of parasitic encounters, resulting in different closed orbits and optical perturbations for each bunch. In particular, it was impossible to arrange for all bunch pairs to collide head-on at the IP and the combination of different vertical dispersion and closed-orbit for each bunch shifted the central collision energy between bunches and between experiments. The latter effect was important at LEP where the experiments needed to know the central energy with high precision. The number of bunches had to be reduced to 8 or, sometimes, 12.

### 3.14.4 Closing Remarks

For many years now, the main focus of CERN has been the construction and commissioning of the LHC. Nevertheless, much of the knowledge of building and operating such a large facility as LEP has also been fundamental for the LHC project. Some aspects of it remain relevant to the lower energy $e^+e^-$ factories of today. Should a sufficiently compelling physics case ever emerge, the combined experience of CESR, DAΦNE, PEP-II, KEKB and LEP could show the way towards building a very high luminosity Z-factory, still based on the $e^+e^-$ ring technology.

Originally, it was planned to leave LEP in place and to install the LHC in the same tunnel to allow the possibility of e-p collisions but this turned out to be impractical. LEP was stopped in 2000 and completely removed by 2002 to allow for the installation of the LHC, completed in 2007. With the end of HERA operation, there has been a renewed interest in a continuation of e-p physics and higher energies. Encouraged by ECFA, studies for the LHeC in which electrons would collide with the proton and ion beams in the LHC have recently begun. Two possibilities are being pursued, a ring-ring and a linac-option. In the ring-ring option it is foreseen to add a LEP-like electron ring on top of the proton ring in the LHC tunnel. Beam energies would be lower than for LEP2, in the range from 50 to 70 GeV to allow for many bunches and high luminosity [13].

### 3.14.5 Acknowledgement

So many people were involved in the design, construction, operation and upgrading of LEP from the late 1970s to 2000 that it would be impossible, and possibly invidious, to attempt to list them here. Many are well known to readers of this newsletter. Similarly, the following short reference list is just a sample, related to the rather personal perspective of this article.

### 3.14.6 References

1. D. Brandt, H. Burkhardt, M. Lamont, S. Myers, and J. Wenninger, "Accelerator Physics at LEP", Rept. Prog. Phys. **63** (2000) 939
2. R. Bailey et al., "The LEP Collider", Compt. Rend. Acad. Sci. (Paris) **9** (2002)
3. K. Hübner, "Designing and building LEP", Phys. Rept. **403-404** (2004) 177–188
4. A. Butterworth et al., "The LEP2 superconducting RF system", Nucl. Instrum. Meth. **A587** (2008) 151–177
5. C. Rubbia, "The 'Future' in High Energy Physics", Proc. European Particle Accelerator Conference, Rome, 1988, 290. http://accelconf.web.cern.ch/AccelConf/e88/PDF/EPAC1988_0290.PDF
6. V. I. Telnov, "Scattering of electrons on thermal radiation photons in electron-positron storage rings", Nucl. Instrum. Meth. **A260** (1987) 304.
7. H. Burkhardt and R. Kleiss, Beam Lifetimes in LEP, Proc. EPAC 1994.
8. H. Burkhardt, Beam Lifetimes and beam tails in LEP, Proc. e+e- Factories 99, CERN-SL-99-061-AP
9. G.L. Kotkin, V.G. Serbo; Phys.Rev.ST Accel.Beams 7:101001,2004 http://prst-ab.aps.org/abstract/PRSTAB/v7/i10/e101001
10. John R. Rees, "Colliding-Beam Storage Rings: a Brief History", SLAC Beam Line, Special Issue Number 9, March 1986. http://www-conf.slac.stanford.edu/40years/histories/BL-SI9-0386.pdf
11. J.M. Jowett, "More bunches in LEP", Proc. Particle Accelerator Conference, Washington, 1989, 1806 http://accelconf.web.cern.ch/AccelConf/p89/PDF/PAC1989_1806.PDF
12. Report of the Working Group on High Luminosities at LEP, CERN 91-02 (1991).
13. http://www.lhec.org.uk

## 3.15 Colliding Beams at the Cornell Electron Storage Ring CESR

David Rice, David Rubin
Laboratory for Elementary-Particle Physics, Cornell University, Ithaca, NY, USA
Mail to: David.Rice@cornell.edu

### 3.15.1 Introduction

The electron-positron collider CESR was constructed as an upgrade to the Cornell Electron Synchrotron in the late 1970's, originally designed to operate at 16 GeV center of mass with a maximum luminosity of $1x10^{32}$ $cm^{-2}$-$sec^{-1}$. [1] The parameter list specified a single 100 mA ($1.5x10^{12}$ e-) bunch in each beam and beam-beam parameters of 0.06 in each plane. The fortuitous discovery of the Upsilon family of resonances at

FNAL quickly focused activities at CESR in the 9.4-11 GeV c.m. regime. Eventually the excess design energy was traded for increased beam currents to push toward higher luminosity.

After a description of the beginnings of CESR we cover the main elements of change throughout its history as a collider. These include multi-bunch operation, optics development, and the transition to Charm physics, CESR-c. The development of several critical systems also plays a critical role in improvements and upgrades. These are covered in 1.1.5 Development of Accelerator Systems.

## 3.15.2 The Foundations of CESR

### *3.15.2.1 Initial CESR Configuration*

Constraints on the initial layout of CESR drove several design decisions that would prove central to later successes in luminosity achievements. In fact, throughout the development of CESR as a collider the hardware infrastructure has been an essential component to advances in performance.

The CESR collider was constructed as an upgrade to the existing "10 GeV Synchrotron" on the edge of the Cornell University campus. The ring had to share a 10 foot diameter tunnel with the synchrotron and provide space for two high energy physics (HEP) experiments. Since the synchrotron was close to circular, providing sufficient space for large experimental detectors required some significant manipulations to bending magnet configuration, inserting long drift sections (also to provide space for RF cavities) followed by small radius bends. Next, low field bends were required adjacent to the high energy physics detectors to control synchrotron radiation background. Furthermore, the RF sections of the synchrotron introduced interruptions to a uniform radius in the tunnel layout at several locations.

The two HEP detectors were located 180° apart in azimuth. A large detector (CLEO) with 1.5 T solenoid field, and optimized for particle detection was located in the larger interaction region in the main laboratory building. 15 m underground the CUSB (Columbia-Stony Brook) detector located at the symmetry point incorporated a lead-glass calorimeter for spectroscopy measurements. The CUSB detector was considerably smaller with no magnetic field at the beam line.

This geometry made the concept of a standard cell difficult to hold, and the need to manipulate optics functions to control the emittance generated in the high field bends caused the number of quadrupole families to grow week-by-week during the design stage. When the number of families reached 18 with pressure for more, the magnet power supply plan was reviewed and, with the introduction of a relatively inexpensive, high precision power supply concept [2] and high impedance coil configuration, the decision was made to power quadrupoles individually. It was natural to do the same for the sextupoles.

The concept of no quad families, and no standard cell led to alternate approaches in optics design. Rather than the conventional path of standard cells, matching sections, and inserts, global optimization algorithms had to be developed that could control optics functions at each quadrupole and the interaction points, including effects of the high field bends on beam emittance.

The former 10 GeV synchrotron was retained as part of the injector chain with a circumference of 60/61 times that of CESR. This feature permitted simultaneous

acceleration and injection into CESR of many bunches within each (60 Hz) acceleration cycle.

#### *3.15.2.2 Initial CESR Performance*

First beams were stored on April 2, 1979 with first measured luminosity on August 14 of that year. [1] For the reasons outlined below, beam-beam performance was initially mediocre, around $3x10^{30}$ $cm^{-2}$-$sec^{-1}$ with beam-beam parameters ~ 0.02. Low beta optics (10 cm $\beta^*_V$) for the CLEO IR were replaced with "mini-beta" optics (3 cm $\beta^*_V$) in 1981, resulting in luminosity increasing to $1.2x10^{31}$ $cm^{-2}$-$sec^{-1}$. In implementing the mini-beta optics, space for compensating solenoids (to cancel the effects of the 1.5 T experimental solenoid field) became occupied by quadrupoles, requiring alternative compensation schemes to be developed (see 1.1.4 Optics).

With the geometrical constraints described above, the optics were a compromise at best. The proximity of the RF cavities to high field bends prevented achieving zero dispersion in the cavities. It also proved impossible to have zero dispersion at both interaction points, resulting in a compromise, in hindsight with near worst case from a beam-beam dynamics viewpoint. Beam currents were limited by beam-beam effects with sudden losses when attempting to collide above the current limit (likely exacerbated by slow turn-off of electrostatic separators used for injection).

Reaching maximum current was a tenuous endeavor with the low current gun initially used. Multiple bunches were injected into the storage ring, then re-injected into the synchrotron where they "caught up" with an accreting bunch in the storage ring and were then again transferred to the storage ring. The 60/61 ratio of circumferences was chosen to facilitate this coalescing operation. In April, 1983 the low charge electron gun was replaced with a high charge gridded gun and new pre-acceleration optics and pre-bunchers, [3] providing sufficient charge to create and inject positrons into CESR without the need for coalescing.

Having struggled with what were at the time the conventional means for improving performance with only modest success, effort turned toward the less conventional directions, particularly those that could take advantage of CESR's special infrastructure.

### 3.15.3 Multibunch Operation

#### *3.15.3.1 CESR's Adaptability to Multiple Bunches*

While CESR was conceived as a single bunch per beam, two interaction region (IR) collider, a chance discussion between director B.D. McDaniel and his son during the December, 1981 holiday break turned thoughts toward additional circulating bunches. The difficult task of separating beams at parasitic collision points in the arcs was met by a "pretzel" orbit configuration cooked up by R. Littauer that winter. [4].

Higher currents resulting from multiple bunches could be handled by the vacuum system since the operating energy was well below the design energy of the storage ring, reducing synchrotron radiation power per unit current to 20% of an 8 GeV beam.

The Pretzel separation scheme employs closed orbit distortions propagating around the arcs with phase advance tailored to place the anti-nodes at parasitic crossing points. Four electrostatic separators created multiple wavelength closed orbits on each side of the diametrically opposed interaction points. With an integer horizontal tune of 9.39 it

was possible to separate 6 parasitic crossings on each half of the ring, accommodating up to 7 bunches in each beam, though initial operation used 3 bunches per beam with uniform spacing.

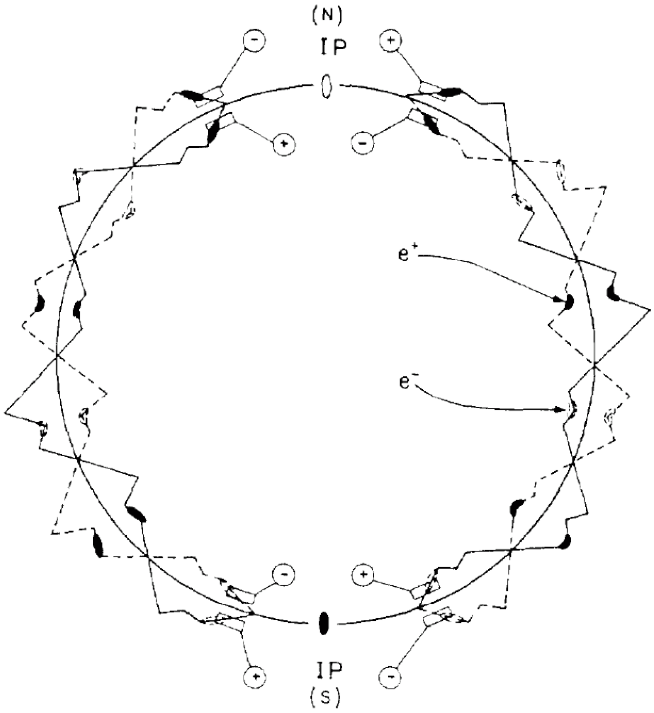


**Figure 1:** Early Pretzel orbits in CESR in anti-symmetric configuration.

Separation in the horizontal plane only was chosen to avoid complications from coupling introduced by vertical closed orbits in sextupoles. It was felt that dealing with the 1 dimensional optics distortions from the horizontal displacements in sextupoles was easier than fixing vertical coupling. Thus the electron beam and positron beam could have different optics functions, and even different coupling from skew-sextupole components. This and several other constraints on the optics (injection, interaction point, equal damping partition numbers etc.) leaned heavily on the flexibility of the individual quadrupole and sextupole powering scheme. A discussion of these constraints and solutions may be found in the next section.

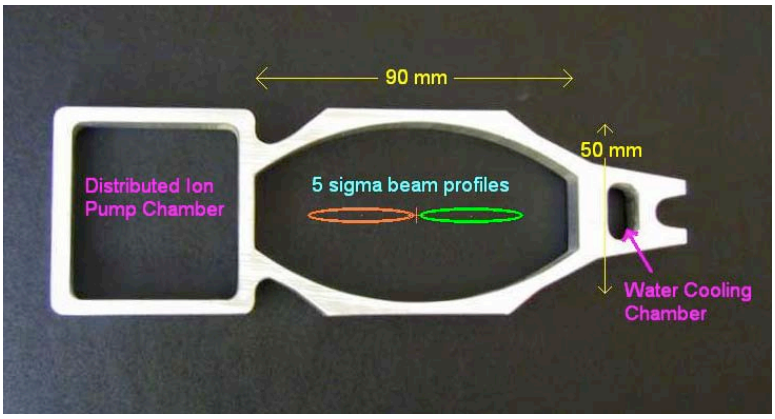


**Figure 2:** Separated beams in CESR vacuum chamber.

The injection process in CESR achieves stacking primarily in horizontal betatron phase space. The effective horizontal aperture is reduced by the electro-magnetic field of the counter-rotating bunches. This reduction is current dependent and ultimately imposes a current limit for two-beam operation. None the less, optics solutions and careful tuning have allowed injection to currents limited by beam-beam effects. Injection of multiple bunches (up to 45 in later configurations) is more effective than injecting a single bunch since the full energy synchrotron used in the injector chain is capable of accelerating 20 or more bunches on each injection cycle. When well tuned, filling rates of more than 150 mA/minute for electrons and 50 mA/minute for positrons are achievable.

#### *3.15.3.2 Initial Experience with Multi-bunch Operation*

Detailed design and engineering occupied the staff for most of 1982, leading to a test of a prototype electrostatic separator in early December, 1982. Four horizontal electrostatic separators were installed in CESR by mid-June, 1983. To make space for the two separators on the North half of the ring, a dipole magnet on each side had to be removed and the adjacent dipoles strengthened and moved to preserve geometry and orbit path length. (Repositioning the dipoles required carving into the tunnel wall in several places!) Three bunches per beam were used initially since only that number of bunches has perfectly uniform spacing as determined by the RF numerology. The first luminosity with three bunches per beam was measured on June 21. That Summer roughly half of scheduled operating time was devoted to machine studies to make multi-bunch operation work.

The optics effects from the separated trajectories were indeed substantial and a deep appreciation for control of optics parameters, particularly orbit control, vertical dispersion and coupling, developed during the following months. The pretzel scheme in fact embodied some of the most difficult effects of both single and two ring colliders. The electrons and positrons are in distinct rings as far as details of optics are concerned, yet the ability to correct them independently is limited. It was only in September that the luminosity with 3 bunches per beam passed that with a single bunch.

The first year's experience with pretzels is well documented in reference [4]. With the separate orbits for positrons and electrons, to be brought together at two interaction points (IP), there are many opportunities to introduce differential orbit perturbations causing misalignment at the IP's. Both symmetric and anti-symmetric pretzels were evaluated, finding the anti-symmetric pattern reduces tune differences (though independent control of tunes was later exploited for injection optimization) and lateral separation at the IP's. Isochronous pretzel orbits were also important for good performance, especially so because of the finite dispersion at the IP's.

With the finite horizontal aperture a good deal of optics optimization effort is put into "Pretzel efficiency" or the ratio between weighted minimum separation provided at parasitic crossing points to peak closed orbit excursion. As experience accumulated, more attention was turned to differential vertical orbit and differential coupling effects. In order to achieve these, and later other, conditions the ability to tailor the sextupole distribution without constraints of hard-wired families was extensively exploited.

As previously mentioned, several months of intensive studies passed before the break-even performance was reached with 3 bunches in each beam. High energy physics operation with three bunches started on October 21, 1983. After a year the 3-bunch luminosity reached $2.6 \times 10^{31}$ $cm^{-2}$-$sec^{-1}$, or 60% higher than that achieved with a

single bunch. Because of the ability to inject multiple bunches in each injection cycle, the daily integrated luminosity followed closely the gains in peak luminosity.

### *3.15.3.3 From 3 to 7 Bunches*

Since this pretzel configuration was designed to accommodate 7 bunches per beam, this was an obvious next step. During initial operation results were encouraging. However, after a few weeks of operation with increasing currents the RF cavity main power window failed. [5] (At this time a 14-cell copper RF cavity was in use.) After a second similar failure an intensive study was undertaken, resulting in modification of the cylindrical window structure to eliminate a trapped higher-order mode (HOM). A corona ring formed an effective edge-coupled waveguide around the circumference of the window. Fields from the HOM's initiated a discharge, then aggravated by the fundamental power fields to sputter metal onto the window. Removing the corona ring solved the problem.

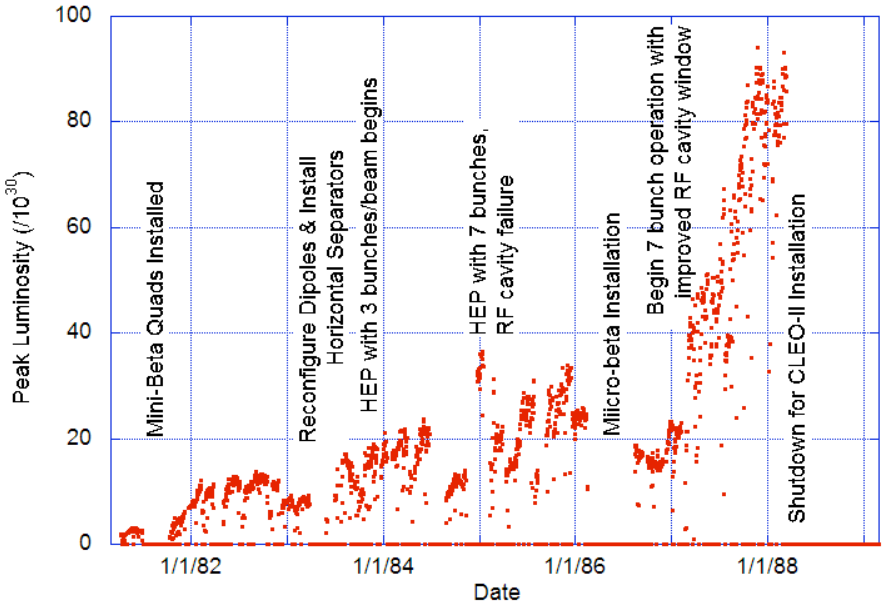


**Figure 3:** CESR Peak Luminosity 1981 to the CLEO-II installation shutdown in June, 1988. Most extended low luminosity periods reflect lower energy runs.

During the limited operation between window failures the peak luminosity reached $3.7 \times 10^{31}$ $cm^{-2}$-$sec^{-1}$, adding confidence that we were on the right track. Finally in December, 1986 a cavity with modified window was installed. Meanwhile in July, 1986 CESR started operation with a "micro-beta" IR optic employing permanent magnet quadrupole focusing beginning only 62 cm from the IP. Operation with three bunches did not yield an immediate luminosity increase, partly because of a run at lower energy on the Υ(3S) resonance. However, after 7 bunch operation was resumed in February, 1987 at 5.3 GeV and without the current limit imposed by the RF cavity windows, the luminosity increased rapidly, reaching $9 \times 10^{31}$ $cm^{-2}$-$sec^{-1}$ by December, 1987. This was achieved with 73 mA per beam distributed in 7 bunches. The vertical beam-beam parameter was saturated at 0.017, [6] the low value likely due to high dispersion in the interaction points. The value of $\beta^*_V$ was 2 cm, comparable to the bunch length. A scan

of performance vs. $\beta^*_V$ suggested that maximum luminosity (but not maximum beam-beam parameter) would be achieved when $\beta^*_V \sim$ bunch length. [7]

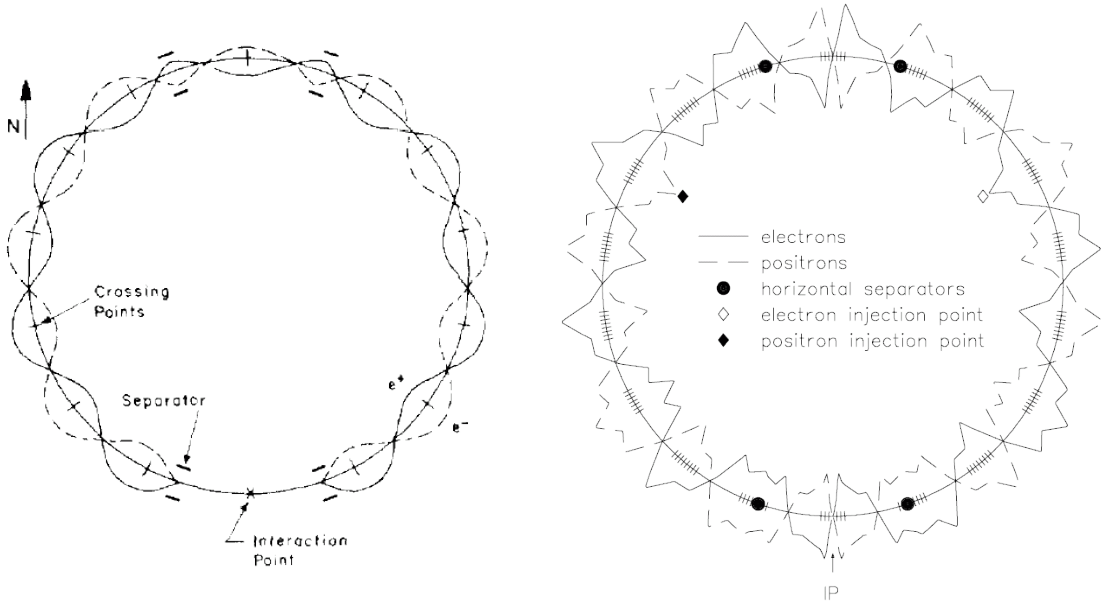


**Figure 4:** Single IR and Bunch Train / Crossing Angle Pretzel Orbits.

#### *3.15.3.4 Beyond 7*

Encouraged by the success with 7 bunches, thoughts turned to schemes to add more bunches. Placing separators very close to the (now single) IP was studied but the technical difficulties were extreme, so this option was side lined while others were examined. A "Delta-E" option was studied extensively – by creating anisochronous pretzels the two beams could be given different energies, possibly allowing magnetic separation, at least partially.[8] A well thought out proposal by R. Meller [9] to substitute trains of closely spaced bunches for the individual bunches, separating the resulting parasitic crossings near the IP by a small crossing angle won out in the end.

Nearly 2 years of studies followed before implementing a bunch train with crossing angle for HEP. Degradation of crossing angle luminosity for a single bunch was measured [10] and calculations of resonances performed [11]. There were also distractions such as the transition from two IP's to a single IP along with optics opportunities to improve beam-beam performance, transition from 14 cell to 5 cell CESR RF cavities, feedback kickers installed and feedback system commissioned, separators with lower HOM impedances installed, etc. All of these improvements likely contributed to a gradual climb in performance from 0.9 to $2.8 \times 10^{32}$ $cm^{-2}$-$sec^{-1}$, or 0.28/nb/sec in 7 bunches, single IP operation. By February, 1994 tests with crossing angle collisions had progressed sufficiently to start HEP operation with 9 bunches (1 bunch per "train") and a crossing angle at the IP. In November a second bunch was added in each train 28 ns behind the first. While 9 bunch luminosity didn't quite attain the best 7 bunch levels, with 18 bunches per beam the luminosity quickly climbed beyond , reaching 0.33/nb/sec just before a shutdown for CLEO upgrade work and modified IR optics beginning in April, 1995.

After the shutdown continual tuning and optimization of conditions resulted in a gradual increase in luminosity to 0.48/nb/s in March, 1998 (Figure 5) when a third

bunch was added to each of the 9 trains followed by a fourth in November. Over the holiday break, with uninterrupted running and tuning, the luminosity reached 0.75/nb/sec. Later conversion to S.C. RF cavities, addition of longitudinal feedback plus much tuning would lead to a peak luminosity of 1.3 /nb/sec, at that time a world record for colliders by a wide margin. Beam currents had increased to 380 mA per beam with 45 bunches, or 9 trains of 5 bunches each.

#### *3.15.3.5 Il Primo, Il Contorno, Il Dolce*

While multi-bunch with pretzel was the main dish during this period, the dinner could not have been completed without many other changes to the configuration of CESR and its injector. Upgrades to the RF system to handle the higher currents and lower parasitic mode impedances was essential – first from 14 cell copper to 5 cell copper, then to single cell super conducting cavities. Wide band feedback systems in all 3 dimensions were developed and commissioned over this period. The transition to single IR with zero dispersion and horizontal tunes above and close to the half-integer broke through the 0.025 beam-beam tune shift limit, eventually exceeding 0.06. Several upgrades to the IR improved the ability to compensate coupling and errors, and lowered the natural chromaticity.

While having the right hardware is the basis, persistent and focused tuning is just as essential to realize peak performance. This is evident from the slow yet steady increases in performance between major hardware changes.

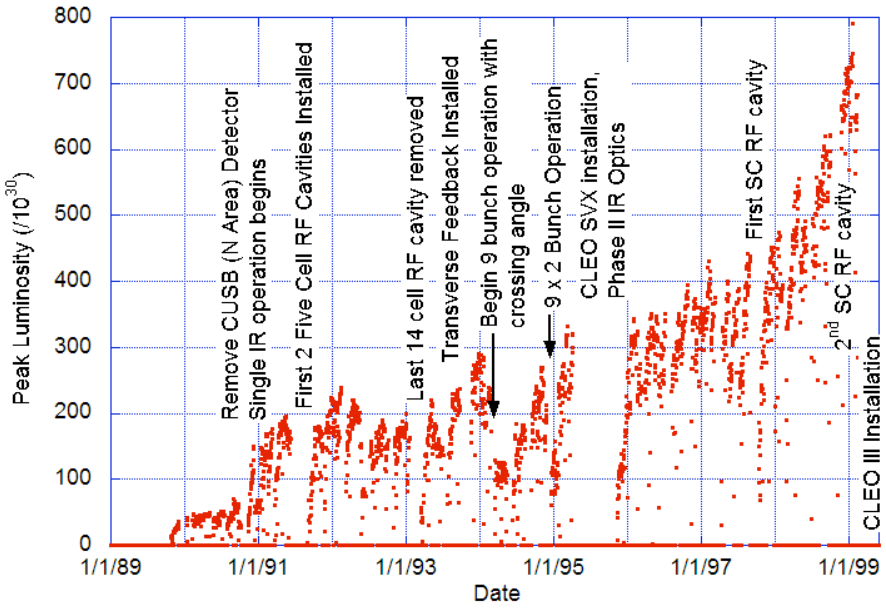


**Figure 5:** CESR peak luminosity from 1990 through 1998. The cyclic patterns, particularly evident in the later years, result from shutdown recovery or energy or equipment changes.

## 3.15.4 Optics

### *3.15.4.1 Two Interaction Regions*

With two interaction regions and pretzeled orbits designed to accommodate 7 bunches/beam, CESR operated with both horizontal and vertical tunes just below the half integer. The difference in fractional tunes (Qh-Qv) was less than 0.15, so that it was straightforward to tune onto the coupling resonance to diagnose global coupling. The integer part of the horizontal tune was 9 to satisfy the constraints imposed by the horizontal separation scheme, 3 full wavelengths in each arc between each separator pair, and then a bit more than 1.5 wavelengths from the east separator, through the IR to the west separator.

The separators in the east and west arcs were powered with anti symmetric voltages so that sextupole feed down would contribute symmetrically to pretzel dependence of tune shift and $\beta^*$. The two family sextupole distribution, while enough to adjust horizontal and vertical chromaticity, was extended to four families with a degree of freedom to correct differential phase advance through the arcs.

Multibunch operation began with 3 bunches/beam. The sophisticated control system software that allowed for automatic filling of multiple bunches had not yet been developed and the procedure depended on an alert operator and reliable hardware. Each bunch experienced a unique set of parasitic interactions during injection and once stored and so each was characterized by a different injection efficiency and lifetime. Luminosity depends on the total current that can be brought into collision with acceptable lifetime, and the acceptable lifetime decreases with filling time. A consequence of our determination to optimize performance, operation was by definition on the edge. Only after many months tuning and iterating optics and beam parameters were we finally able to exceed with three bunches per beam the luminosity that we had achieved with a single bunch.

### *3.15.4.2 Micro-Beta*

In the mid 80's the mini-beta interaction region was amended with the addition of a 1.2m long permanent magnet final focus quadrupole. The front end of the magnet was only 60cm from the interaction point. The outer radius of the quadrupole was a mere 15cm, so it fit neatly inside the CLEO drift chamber. With a focusing strength k=0.86/m2, it was a factor of two stronger than any other quadrupole in CESR and allowed us to achieve $\beta^*_V$ <15mm with corresponding peak vertical $\beta$ less than 100m. The lower limit on beta* was imposed not from optical concerns about aperture or chromaticity but rather by the finite bunch length.

In order to cover that CESR continue to be capable of running on all of the Upsilon resonances, from 4.7GeV/beam for the 1S to 5.6 GeV/beam for the 5S, an electromagnetic trim quad was located just beyond the end of the permanent magnet. A wide aperture horizontally focusing quadrupole completed the final focus.

### *3.15.4.3 7 Bunches / Beam*

We proceeded to 7-bunch operation with some trepidation in view of the higher power that would necessarily be transmitted through the cylindrical of our 14 cell RF cavities. Indeed within the first several weeks of 7 bunch operation, a ceramic window

gave way and until the two 14 cell cavities were replace by four 5 cell structures, beam current and luminosity was RF limited.

Meanwhile we had yet to significantly increase the specific luminosity, i.e., the luminosity per unit average beam current. The beta functions at the interaction point were typically 15 mm vertically and 100cm horizontally and horizontal dispersion was about 1m. Contribution of emittance and energy spread to the horizontal beam size were roughly equal. The synchro-betatron coupling due to the finite dispersion likely limited the achievable beam-beam tune shift. But the increased beam width allowed a corresponding increase in the beam-beam limiting current.

#### *3.15.4.4 Single IR – Head on Collisions*

With the conclusion of the CUSB experimental program in 1988, the CESR optics were reinvented. The low beta optics in the CUSP interaction region were normalized, and the horizontal separators were powered with east-west symmetric voltages, so that the closed horizontal orbit distortion extended from just east of the CLEO IR, through the east arc, north area, and west arc to the west of the CLEO IR. With 7 bunches in each beam, there would be horizontal separation at all of the 13 parasitic crossing points, including that point diametrically opposite the remaining IR where beams would collide head-on. The vertical separators just beyond the final focus of the single interaction point, and that had been used during injection were removed. We took advantage of the available space by lengthening the permanent magnet quadrupole from 120 to 150cm (having recovered 30cm from each of the magnets coming out of the CUSB IR) and rearranging the electromagnet trims. The phase advance between the horizontal separators to either side of the IR was very nearly 1.5 wavelengths. By turning them off, the pretzel extended around the entire circumference of CESR, providing separation at all 14 crossing points, a circumstance well suited to injection of electrons with a full load of positrons already stored.

In the single IP configuration with symmetric separation, the horizontal tune was reduced from 9.4 (just below the half integer) to 8.57, just above. The vertical tune was increased from 9.37 to 9.6. No longer constrained to maintain symmetry of optical parameters at two interaction points, we were able to zero the dispersion at the single IP. With $\beta^*_V$ = 18mm/1m, we were able to increase the limiting beam-beam vertical tune shift parameter to over 0.04, nearly twice what we had achieved in the two IP operation.

The east-west symmetric pretzel effectively separated the electron and positron bunches at all of the parasitic collision points, but the cancellation of sextupole nonlinearities that arose naturally with the antisymmetric pretzel no longer obtained. A considerably more sophisticated algorithm for designing the sextupole distribution was required. All of the 76 sextupoles are independently powered, affording an enormous phase space of possibilities. The distribution was chosen to minimize pretzel amplitude dependence of twiss parameters at the IP, and tunes. Chromaticity was constrained and the local chromatic function was minimized and the dynamic aperture was optimized by minimizing the amplitude dependence of the full turn Jacobian matrix. Knobs were designed to tune chromaticity and “tonality,” that is the electron – positron tune difference.

### *3.15.4.5 Crossing Angle – Bunch Trains*

As long as we insisted that the beams collide head-on, the bunches in each beam were necessarily approximately evenly spaced, and the total number N was limited to be less than C/2d, where C is the circumference and d the distance from the IP to the horizontal separator. But in 1990, R. Meller suggested that if we were prepared to tolerate a small horizontal crossing angle that we could store trains of closely spaced bunches. At the parasitic crossings in the interaction region, at a distance s from the IP, where s is less than the distance to the first focusing element, the beams would be horizontally separated by x=s×theta. Theta is the crossing angle. He argued that the required crossing angle was less than the width/length of the beam, and thus not likely to have a significant impact on beam-beam dynamics. We developed optics with an integer tune of 10 that could accommodate nine evenly spaced trains with as many as 5 bunches in each train. The bunch spacing within the trains was limited to multiples of 14ns, the smallest integral multiple of linac, synchrotron and storage ring RF periods. The IR quadrupoles would be modified for increased aperture for reliable HEP operation. J. Hylas discovered that by crossing the synchro-betatron line $2Q_H$-$Q_S$=n and operating very close to the half integer, (Qh=10.51) that it was possible to increase vertical beam-beam parameter to in excess of 0.06.

### *3.15.4.6 CESR-c Optics*

Outgunned by the B-factories at SLAC and KEK, CLEO physicists began to think about charm. Having replaced the permanent magnet final focus quadrupole with a superconducting-permanent magnet hybrid, the the charm threshold was well within the energy reach of the CESR guide field. The complication with operation at the lower energy (1.9 GeV vs. 5. 3 GeV) was that the radiation damping time would increase 20-fold to about ½ second. At high energy, we injected at 60Hz, allowing a damping time between each injection cycle. A 2 Hz injection rate would make filling times unacceptably long. Furthermore lepton colliders, CESR included, depend on radiation damping to tame instabilities, wash out the effects of beam-beam nonlinearities, and otherwise dissipate high Q resonances.

A. Mikhailichenko designed a superferric damping wiggler with peak field of 2.1T. Eventually a dozen of these 1.3m long wiggler magnets were installed in CESR. In total, the wiggler radiation at 1.9GeV beam energy was 10 times that of all the rest of the bending magnets combined, thus reducing the radiation damping time to a tolerable 50ms. The wigglers featured a wide pole in order to preserve field uniformity over the full width of the vacuum chamber, consistent with the aperture requirements of the pretzel configuration. The very long wiggler period of 40cm was chosen to minimize the inherent third order nonlinearities. Finally, the CESR optics were again modified, this time to exploit the wiggler field to generate a sufficiently high horizontal emittance, as well as separation at 89 parasitic crossing points.

The damping wigglers provided a means to reduce damping time and increase horizontal emittance at low energy. Evidenced by extensive tracking studies and machine experiments, wiggler non-linearity had no significant impact on dynamic aperture or beam-beam performance. But one unavoidable consequence of depending on very high and localized magnetic fields to generate radiation damping was an increased energy spread. In order to preserve a sufficiently short bunch, it was necessary

to operate at a high synchrotron tune ~0.1. The combination, further compromised by our solenoid compensation scheme, limited the achievable beam-beam tune shift.

#### *3.15.4.7 Solenoid Compensation*

The CLEO experimental solenoid operated at 1.5T with a length that corresponded to a rotation of about 6 degrees for a 5 GeV beam. Compensation with anti-solenoids was abandoned with the introduction of so-called mini-beta focusing so that the final focus quadrupoles could be placed closer to the IP. The IR quadrupoles were mounted so that they could be rotated about the beam axis. Three antisymmetric couplers are required to compensate the coupling of horizontal to vertical motion through a solenoid, the vertically focusing IR quads, the horizontally focusing IR quads, and then a pair of skew quads outside the IR. The skew quad was necessarily beyond the first bend and it generated some vertical dispersion at the IP. Additional arc skew quads were included in order to minimize the coupling of dispersion. The rotation angles of the IR quads were adjusted remotely by means of stepper motors. Tuning was tedious, mostly because the rotation mechanism did not provide for a reliable retreat. And colliding beam conditions were extraordinarily sensitive to residual coupling.

With the micro-β upgrade, in which the 1.5m long permanent magnet was installed as the final focus quadrupole, the permanent magnet quad as well as the vertical trim and the horizontal quads were rotatable, eliminating the need for additional skew quads to complete the compensation, and possibility of generating vertical dispersion.

Finally, in the IR with the superconducting/ permanent magnet hybrid final focus, the quadrupoles were all deployed at a fixed angle of rotation, and skew quad trim windings were used to adjust for energy and optical variations. A characteristic of this compensation scheme was a significant energy dependence, an effect exacerbated by the large energy spread associated with the damping wigglers. Superconducting anti-solenoids were added just beyond the final focus quads in an only partially successful attempt to ameliorate this effect. (As a retro-fit, there was no space closer to the IP.) In retrospect, the anti-solenoids would have been more effective superimposed directly over the superconducting quadrupoles, obviating the need for skew quad trim windings. Such an arrangement would have very significantly reduced the energy dependence of the compensation.

### 3.15.5 Development of Accelerator Systems

#### *3.15.5.1 CESR RF*

As mentioned above, the developments in the CESR RF system played an essential role in the performance increases. The original RF cavities were designed for high shunt impedance to efficiently provide the voltage necessary to sustain 8 GeV beams of 100 mA. Besides the afore-mentioned window problem, the 14 cell cavities were a poor match to the lower voltage operating conditions in CESR during the mid-1980's. While the beam currents were initially smaller than design (~60 mA/beam in early 7 bunch operation) the bunches were passing through the cavity closer together and the bunch length was much shorter than at 8 GeV, exciting more higher order modes in the cavities. In order to reduce both the fundamental and HOM RF power passing through

each window and provide a better match to high currents, the two 14-cell cavities were replaced by four 5-cell cavities between October 1991 and February 1993.

Meanwhile the development of super-conducting cavities, an activity at Cornell since the 1960's, had reached a stage of a practical cavity system for high current storage rings. The rational for super-conducting RF is not to save mains power (the cryogenic equipment running 24/7 uses most of the savings in RF transmitter power) but to reduce the shunt impedance of HOM's, significantly reducing the demands on feedback systems. Because of the very low wall losses, the cavity shape can be smoothed and the resulting lost of accelerating mode shunt impedance is not a serious penalty. Beam tests indicated that the copper RF cavities were a significant impedance contribution to a low longitudinal instability threshold. [12] Even as the last 5-cell copper cavities were being installed, construction was starting on the super-conducting replacement.

The first super-conducting cavity was installed in September, 1997, the first to be installed in a storage ring for long term use. After some initial problems such as multipacting in window and coupling waveguide, the cavity operated quite well. Lessons learned were applied to the succeeding cavities with resulting smoother installation and commissioning experiences. [13] As seen in Figure 5, the slope of luminosity changed markedly after just one half of the copper RF cavities were replaced. Today the SC RF cavities continue to perform well for both photon science (400 mA total, 5.3 GeV) and accelerator physics studies requiring high gradient at low currents.

#### *3.15.5.2 Injection*

The availability of a full energy, long pulse injector has been essential to maintaining an integrated luminosity increase close to the peak luminosity increase. The high current gridded gun installed in April, 1983 allowed direct acceleration and injection into the storage ring. Its flexible bunch pattern has been very useful in filling the bunch trains.

Until September, 1985, separate optics for injection and colliding beams were still being used. After modification of injection "beam bump" magnets to shorten their pulse length, and with careful tuning, top-up injection became practical, saving time consuming lattice changes and producing more stable conditions.

When the "micro-beta" IR was installed in 1986 the vertical separators in the IR used for injection had to be removed. By unbalancing the horizontal separators used for multi-bunch operation, sufficient separation could be created in the horizontal plane to allow efficient injection.

In late 1988 the electron transport line from linac to synchrotron was upgraded to handle the full 300 MeV from the linac, producing more stable and higher current beams captured by the synchrotron. Addition of electronic beam position monitors in the linac and new prebuncher cavities led to more stable and reproducible conditions.

With multi-bunch operation, the beam dynamics of injection became more complex. Capture efficiencies when the opposing beam was at full current were reduced to 20-30% even in the best conditions, and could be 5-10% in bad. This was especially true for the low energy operation in the CLEO/CESR-c era. Often the ability to inject would determine the beam current. Different bunch distributions in the trains were tried with varying success. Despite significant effort to find better conditions and compensate the

parasitic beam-beam effects [14], no good solution, other than empirical tuning skills, was found to effectively cure these limits.

#### *3.15.5.3 Instrumentation & Tuning*

Beam diagnostic instrumentation has played a critical role in commissioning optics and identifying sources of faults and beam losses. A good orbit measurement system is of course essential. Both horizontal and vertical measurement at every quadrupole, plus the ability to calibrate offsets using modulation of the local quadrupole have proven valuable. The technique of exciting an eigenmode of the betatron motion and recording phase and amplitude data on the position monitors to measure both phase advance and coupling has been extensively used to quickly measure and correct these parameters.

Fast signal recording to circular buffers to identify parameter variations causing beam loss has been essential to finding problems with electrostatic separators, RF control systems, and magnet power supplies.

Installation of a high rate radiative Bhabha luminosity monitor in 2004 aided tuning in the lower luminosity conditions of CESR-c operation. [15]

Finally, dedicated tuning has been responsible not only for the last 10-20% in performance, but also in identifying problems and finding new operating conditions. The source of an anomalous impedance affecting positron beams was associated with the sputter ion vacuum pumps by an extremely dedicated operator. This same operator found a much improved operating point near the half-integer resonance. First hand knowledge and feeling for a machine's response to parameter changes will always play an important role in the operation of these complex devices.

### 3.15.6 CESR-c

#### *3.15.6.1 Motivation and Some Basics*

As previously mentioned, while CESR had very productive years studying B meson decays with world-record luminosity, the arrival of the two asymmetric B factories at SLAC and KEK suggested that CESR's flexibility could better serve other areas of elementary particle physics. The ability to use a state-of-art detector, well characterized by years of observing B decays, along with record luminosities in the Charm regime has proven to be a very productive combination.

Producing Charm mesons requires operation of the storage ring at a fraction of the original 8 GeV design maximum energy. The need for enhanced damping to sustain the high currents and beam-beam space charge limits was quickly realized, and strong wiggler magnets, providing 90% of the synchrotron radiation power, were the primary accelerator upgrade task.

Twelve 2.1 T wigglers, each 1.3 m in length can reduce the transverse damping time at 1.9 GeV from over 500 to 50 ms and control the transverse emittance within a desirable range. The wigglers were designed considering pretzel orbits, i.e., with a wide good field region initially evaluated by particle tracking through 3-D wiggler fields. [16, 17]

Such strong magnets are not without undesirable effects of course. There is an uncontrollable increase in energy spread from the high magnetic fields. Wigglers have strong focusing, both linear and non-linear, in the vertical plane only, making it difficult

to simply compensate with adjacent quadrupoles. Depending on the field quality, there may be non-linear terms in both planes due to magnetic field changes at large displacements from the centerline.

Other challenges to low energy operation come from the change in beam rigidity and different operating range of magnets, separators, and kickers. One concern was the two windows and a length of Helium gas separating the storage ring vacuum from the synchrotron. The Coulomb scattering cross section increases as $(Z/E_0)^2$. The Titanium windows were replaced with Beryllium to reduce the emittance growth, which nevertheless increased from 0.12 (5.3 GeV) to 0.6 (1.9 GeV) $x10^{-6}$ m-rad.

With the planned 45 bunches per beam, there are 89 parasitic crossings for each bunch. These effects proved to be the major focus of efforts to improve CESR-c performance.

#### *3.15.6.2 Commissioning Experience & Performance*

CESR operated at low energy from August, 2003 until March, 2008. Once the first wigglers were installed in the ring, beam-based measurements were made to determine the level of non-linearities introduced by the wigglers. The principle technique used was to measure betatron tune as a function of beam position in the wigglers. Reasonable agreement with calculated values was found [18] and longitudinal damping rates and single-beam stability limits were both close to expected values.

One of the first issues found was that slow ion effects caused us to leave out one or two trains of bunches in order to destabilize the ions. This of course would be a factor in the achievable luminosity. Hints of this effect had been observed at 5.3 GeV in a vertical beam instability for a week or two following a vacuum intervention.

While single beam current limits were in excess of 150 mA, comparable to the 180 mA in the original parameter list, with counter-rotating beams the injection efficiency dropped quickly above approximately 80 mA per beam. In addition, the beam-beam parameter usually saturated around 0.026 with best achieved around 0.03. Maximum luminosity recorded was 0.075/nb/sec ($7.5x10^{31}$ $cm^{-2}$-$sec^{-1}$ in more conventional units) though constant tuning was required to maintain luminosity above 0.06/nb/sec. While well below target values, the delivered luminosity was well above that of previous machines at these energies. This, along with the capabilities and experience of the CLEO detector and collaboration, resulted in publication of more than 100 papers, with analysis and reporting continuing through 2009. Recently the CLEO collaboration submitted for publication their $500^{th}$ paper covering data taken since 1979.

In the final analysis the current limits during CESR-c operation were primarily caused by parasitic beam-beam interactions. Their effects had been inadequately assessed during the design stage, partly buoyed by the successful operation at higher beam energies. An important limit on specific luminosity likely comes from the very high synchrotron frequency required to control bunch length given the additional energy spread from the 1.9 to 2.1 T wigglers that accounted for 90% of the synchrotron radiation power. Other than this, no other detrimental effects from the damping wigglers has been identified.

Many of these conclusions have been supported by a detailed computer simulation providing particle tracking with both main and parasitic beam-beam interactions, local energy effects, high order field maps through the wigglers, as well as the usual nonlinear elements. [19] Software development was not sufficiently advanced at the design stage to utilize many of the detailed features used in later analyses.

The parasitic beam-beam interactions give each bunch its own optics functions dependent on the charges in counter-rotating bunches. These effects were strong enough that it was necessary to have two slightly different (empirically adjusted) optics for injecting from zero current and high current topping off injection. Differences in focusing effects caused bunches within a single train to have peak beta values varying up to 20%. Several attempts [14] were made to partially compensate these effects but were unable to produce measureable improvement in practice.

As described above, the beam energy spread from the wigglers aggravates the chromatic effects of the CLEO solenoid compensation. In January, 2006 compensating solenoids were installed in the IR, taking over most of the compensation from the skew quad components previously used. The following run showed a 25% increase in specific luminosity, but lower current limit due to poorer injection conditions. Tuning was easier and backgrounds lower (though backgrounds were not an operational issue during CESR/CLEO-c operations). This improvement was smaller in succeeding runs however.

The large (~0.1) synchrotron tune has been identified as an important factor limiting specific luminosity. Pretzel constraints on the horizontal tune severely limit control of the momentum compaction. Simulations, both with artificially low synchrotron tune and reduced bunch length suggest that the beam-beam parameter would climb from 0.03 to 0.055 when either is reduced to half nominal values. However, we were not able to find a practical option to mitigate this effect.

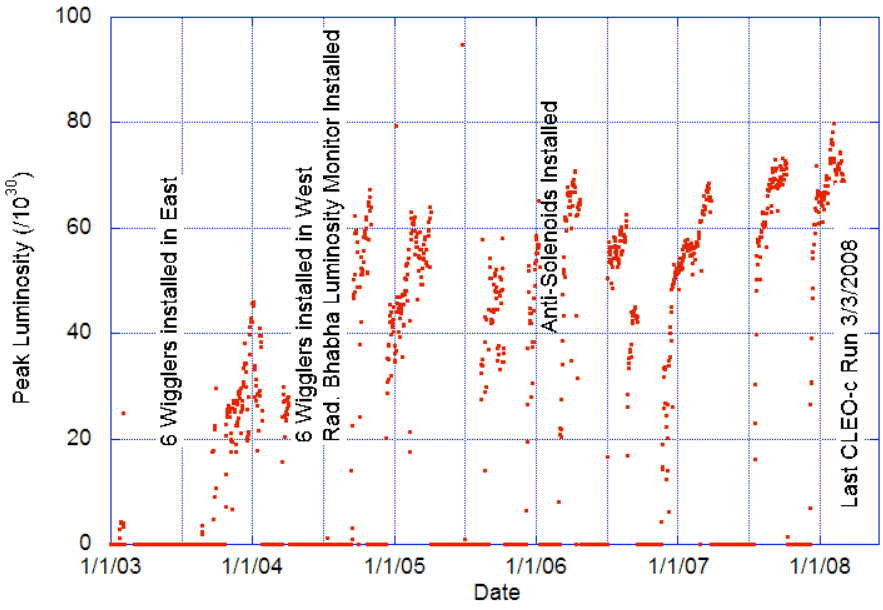


**Figure 6:** Peak Luminosity during CESR-c Operation. Gaps in data are either CHESS dedicated runs or machine shutdown periods.

CESR-c performance relied heavily on expert knowledge and tuning to maintain and improve performance, even more so than higher energy operation, in part because of the variation of conditions with current and bunch-to-bunch.

### 3.15.7 Performance Overview

The growth from a luminosity of 0.003/nb/sec reached in initial configuration 20 months after startup to nearly 1.3/nb/sec achieved with 45 bunches per beam, micro-beta IR, SC RF cavities, and numerous other changes is a remarkable and detailed story of continuous perseverance and resourcefulness that is representative of the accelerator community. The table below lists performance parameters reported at conferences in the period from 1987 through 2007, capturing the upgrade and changes in the growth period from 1988 through 2002.

**Table 1:** CESR parameters as reported at accelerator conferences.

| *Date* | *Luminosity /nb/sec* | *Cur/beam mA* | *XiV* | *RF* |
|---|---|---|---|---|
| 7/2007 | 0.075 | 75(7x4) | .03 (1.9 GeV) | 4-scrf |
| 6/2002 | 1.25 | 370 (9x5) | 0.06 | 4-scrf |
| 5/2001 | 1.1 | 310 (9x4) | 0.065 | 4-scrf |
| 5/1999 | 0.83 | 225 (9x4) | 0.05 | 2-5cell, 2-scrf |
| 6/1998 | 0.56 | 200 (9x3) | 0.044 | 3-5cell, 1-scrf |
| 5/1997 | 0.41 | 180 (9x2) | 0.04 | 4-5cell |
| 6/1996 | 0.35 | 160 (9x2) | 0.04 | 4-5cell |
| 5/1995 | 0.33 | 160 (9x2) | 0.036 | 4-5cell |
| 3/1994 | 0.29 | 112 (7x1) | 0.04 | 4-5cell |
| 5/1993 | 0.25 | 100(7x1) | 0.04 | 1-14cell,2-5 cell |
| 5/1991 | 0.18 | 82(7x1) | 0.028 (1 IP) | 2-14cell |
| 5/1989 | 0.09 | 73(7x1) | 0.017 (2 IP) | 2-14cell |
| 5/1987 | 0.025 | 37(3x1) | 0.018 (2 IP) | 1-14cell |
| 5/1985 | 0.026 | 37(3x1) | | 1-14cell |

### 3.15.8 Acknowledgements

The list of people who have contributed to the development of CESR over the years is long and extends outside the Cornell laboratory to collaborators, visitors, and those who have engaged in stimulating conversation with members of the CESR operations team. This is a list too large to include here, and with great risk of leaving out important contributors. However, we do wish to explicitly mention a few whose contributions have been pivotal.

- Boyce D. (Mac) McDaniel, Laboratory Director at the time of CESR's conception, worked tirelessly to secure funding and guide the project through construction and the early years. He gave the initial push to go beyond a single bunch after a holiday conversation with his son, being challenged to explain why we could NOT put additional bunches in CESR. In his retirement years Mac kept in touch with the laboratory, his last project being to put precision, yet

simple rotators on North area quads to test the Möbius machine concept. We miss him greatly.

- Maury Tigner, former director and present Chair of CLASSE Directorate, tirelessly managed the design, construction and commissioning of CESR and conceived the positron coalescing scheme that was critical to obtaining funding and saw CESR through the first few years of operation.
- Al Abashian and Marcel Bardon of the NSF Physics Division in the late 1970's had the vision of CESR and provided unwavering support leading to NSF approval of the project in 1977.
- Raphael Littauer conceived and developed the Pretzel scheme to successfully separate the counter-rotating beams. He has conceived the basic designs of many critical diagnostic systems, including the first beam position monitor processing and betatron phase measurement schemes for CESR.
- Bob Meller designed the ultra-stable timing systems used in CESR and made a convincing argument for a crossing angle / bunch train configuration to go beyond the 7 bunches per beam of the initial Pretzel scheme.
- John Hylas coupled intimately to CESR through thousands of hours of tuning and noting responses and correlations. He continually challenged the machine physicists to make good their theories of beam dynamics and tuning. John rescued the machine from performance minima on many occasions and could always coax an extra 10-15% in performance.

### 3.15.9 References


1. K. Berkelman, "A Personal History of CESR and CLEO: The Cornell Electron Storage Ring and Its Main Particle Detector Facility," World Scientific (January, 2004).
2. D. Hartill, D. Rice, "The CESR Magnet Power Supply System," IEEE Trans. Nucl. Sci., NS-26, No. 3, 4078 (1979) available at web site http://accelconf.web.cern.ch/accelconf/.
3. E.B.Blum, "Performance of the Cornell High Intensity Linac Injector," Proceedings of the 12th International Conference on High Energy Accelerators, August 1983, pp. 262-264., FNAL.
4. R Littauer, "Multibunch Operation of CESR", IEEE Trans. Nucl. Sci., .NS-32, No. 5, 1610 (1985) also http://accelconf.web.cern.ch/accelconf/.
5. R. Siemann, "CESR RF Window Summary," Internal note CON 86-9, August, 1986.
6. D. Rice, "High Luminosity Operation of the Cornell Electron Storage Ring," Proceedings of the 1989 IEEE Particle Accelerator Conference, Chicago, IL, p.444, March, 1989.
7. S. Herb, J. Kirchgessner, "Operation of CESR with Permanent Magnet Interaction Region Quadrupoles," Proceedings of the 1987 IEEE Particle Accelerator Conference, Washington, D.C., p.130 March, 1987.
8. Studies of "Delta-E" separation of bunches were documented in several internal "Cesr Operations Notes".
9. D. Rubin, "Magnetic Separation of Multiple bunch Beams," CON 90-2.
10. L. Schick, "Delta E Machine Studies," CON 90-10.
11. R. Littauer, "Orbit Measurement in the Delta-E Scheme," CON 90-13.
12. R. Littauer, "South IR Layout: A First Look at Delta E Implications," CON 90-14.
13. R. Meller, "Proposal for CESR Mini-B," CON 90-17 July, 1990.

14. T. Chen, D. Rice, D. Rubin, D. Sagan, M. Tigner, “Experimental Study of Crossing Angle Collision,” Proceedings of the 1993 IEEE Particle Accelerator Conference, Washington, D.C., p.3479 March, 1993.
15. D. Sagan, R. Siemann, S. Krishnagopal,”Resonances in the Beam-Beam Interaction Due to a Finite Crossing Angle,” Proceedings of the 1990 European Particle Accelerator Conference, p. 1649, Nice, France June, 1990.
16. M. Billing, S. Belomestnykh, “Observations of a Longitudinal Coupled Bunch Instability in CESR,” Proceedings of the 1999 Particle Accelerator Conference, TUA19, New York, NY March, 1999.
17. S. Belomestnykh, et al., “Commissioning of the Superconducting RF Cavities for the CESR Luminosity Upgrade,” Proceedings of the 1999 Particle Accelerator Conference, MOP135, New York, NY (1999).
18. J. Crittenden, M. Billing, “Compensation Strategy for Optical Distortions Arising from the Beam-Beam Interaction at CESR,” Proceedings of the 2007 Particle Accelerator Conference, TUPAS056, Albuquerque, NM June, 2007.
19. M. Palmer, V. Crede, D. Rubin, J. Smith, M. Cravey, J. Napolitano, H. Volgel, K. Dooley, “Design and Operation of a Radiative Bhabha Luminosity Monitor for CESR-c,” Proceedings of the 2005 Particle Accelerator Conference, RPAT062, Knoxville, TN May, 2005.
20. J. Crittenden, A. Mikhailchenko, E. Smith, K. Smolenski, A. Temnykh, “Field Modeling for the CESR-c Superconducting Wiggler Magnets,” Proceedings of the 2005 Particle Accelerator Conference, MPPT034, Knoxville, TN May, 2005.
21. D. Rice, “CESR-c: A Wiggler-Dominated Collider,” Proceedings of the 2007 Particle Accelerator Conference, MOZBKI01, Albuquerque, NM June, 2007.
22. A.B. Temnykh, “CESR-c Wiggler & Beam Measurements,” at Wiggle 2005 Mini-Workshop, Frascati, Italy Feb. 2005 http://www.lnf.infn.it/conference/wiggle2005/talks/Temnyk.pdf.
23. D. Rubin, http://www.lns.cornell.edu/~dlr/beambeam_simulation/index.html.

## 3.16 Study of Beam Dynamics during the Crossing of Resonance in the VEPP-4M Storage Ring

S. Glukhov, V. Kiselev, E. Levichev, O. Meshkov, S. Nikitin, I. Nikolaev,
P. Piminov, A. Zhuravlev
BINP, Novosibirsk, Russia
Mail to: P.A.Piminov@inp.nsk.su

### 3.16.1 Introduction

The passage of a beam in synchrotron or storage ring through the betatron resonance and the corresponding loss of particles or the beam distribution degradation were extensively studied in the past [1-3]. Recently, this issue has again become popular mainly because of the FFAG synchrotron projects [4]. We would like to point out that this issue could be important for electron-positron accelerators with an extremely low emittance such as linear collider damping rings or particles super-factories based on the crab-waist collision approach. In both machines the beam is injected with a relatively large emittance and then damps to the values as low as 1÷2 pm. During the damping two effects provide the resonance crossing mechanism:

- The betatron tune moves (predominantly for the vertical motion) by a considerably large value ~0.1÷0.2 due to the space charge force: $\Delta\nu_{sc} \sim (\gamma\varepsilon)^{-1}$.
- As the low emittance strong focusing lattice requires strong chromatic sextupoles yielding rather large amplitude dependent tune shift, the betatron frequency of each individual particle changes with the amplitude decrease according to the nonlinear detuning. It is worth mentioning that the space charge also produces the nonlinear tune shift depending on the beam emittance and it should be taken into account together with the external (magnet) nonlinearities.

These two effects in combination can increase or decrease the resonance crossing speed providing either particle trapping (in the adiabatic limit) or the beam size growth.

In this paper we discuss the results of experimental study of the resonance passage at the VEPP-4M collider. The third-order resonance $3\nu_z = 23$ was traversed by the electron beam with the variable speed. During the experiment the resonance strength could be changed by a single skew-sextupole magnet while the nonlinear detuning was controlled by a number of the octupole lenses. Different parameters such as particles loss rate, beam size and transverse distribution, space phase trajectories, amplitude dependent tune shift, etc. were measured.

### 3.16.2 Measurement Setup

The VEPP-4M electron-positron collider with a maximum energy of 5.5 GeV is operating now at ~1.8 GeV in the region of the $\psi$-meson family. The collider is equipped with a number of beam diagnostics, which allow the measurement of different parameters and the study of nonlinear motion.

The phase space trajectories are registered by the excitation of the coherent beam motion with the help of the fast electromagnet kicker with 50 ns 30 kV pulse. To measure the beam centroid motion, BPMs in the turn-by turn mode are used. The BPM resolution is ~50 μm.

Particles loss and the beam distribution tails are measured by a set of scintillator counters inserted into the vacuum chamber. The counter can be moved by a step-motor in and out of the beam with the accuracy better than 0.1 mm.

To measure a single-turn transverse beam distribution during tens of thousands of turns we have developed a unique device [5] based on the multi-anode photomultiplier R5900U-00-L16 HAMAMATSU. This device is capable of recording a transversal profile of a beam at 16 points at one turn during $2^{17}$ turns of a beam.

The optical arrangement (Fig. 1) allows us to change the beam image magnification on the cathode of MAPMT from 6× to 20×, which is determined by the experimental demands. The set of remote controlled grey filters, included into optical diagnostics, allows selecting a suitable level of the light intensity with the dynamic range of about $10^3$.

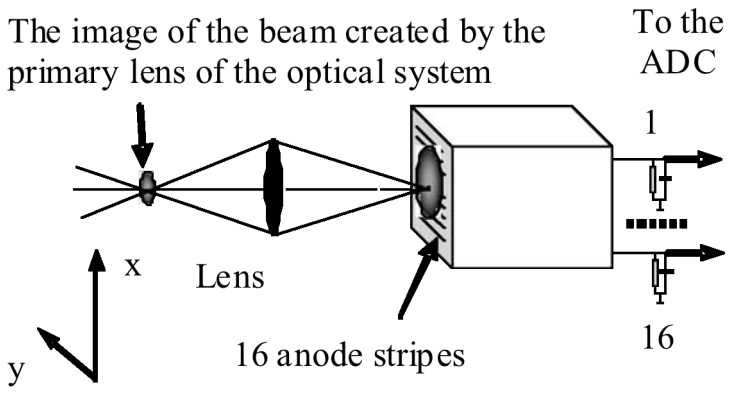


**Figure 1:** Optical layout of the diagnostics. The lens sets up a beam image on the photocathode of the MAPMT. The radial profile measurement is shown.

### 3.16.3 Theory Overview

In this section we briefly overview the main results of the resonance crossing theory. Let us start with a standard isolated resonance Hamiltonian in the action-angle variable

$$H = \delta(\theta) \cdot I + \alpha_0 \cdot I^2 + A_n \cdot I^{n/2} \cos m\varphi , \qquad (1)$$

with the nonlinear tune shift coefficient $\alpha_0$, the driving term strength $A_n$ and the distance from the resonance $\delta(\theta)$ that depends on the time (azimuthal angle) $\theta$. A sketch of the phase space portrait corresponding to the Hamiltonian (1) is plotted in Fig. 2.

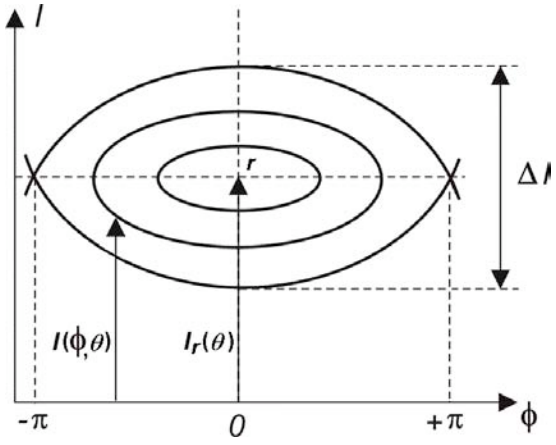


**Figure 2:** Isolated resonance phase space trajectories.

Two cases corresponding to the slow (adiabatic) and the fast crossing should be distinguished. A condition for the adiabatic crossing can be obtained by comparing the maximum rate of the amplitude (action) change

$$(I')_{\max} = -(\partial H / \partial \varphi)_{\sin m\varphi = 1} = mA_n \cdot I^{n/2}, \tag{2}$$

with the rate of the resonance island motion. The latter is found from the resonant action equation

$$\delta(\theta) + 2\alpha_0 \cdot I_r = 0$$

as

$$\frac{dI_r}{d\theta} = \frac{1}{2\alpha_0}\frac{d\nu}{d\theta}. \tag{3}$$

A particle motion at amplitude $I$ is considered adiabatic if its amplitude is such as

$$I_r' < I_{\max}' \qquad \text{or} \qquad mA_n I^{n/2} > \frac{\nu'}{2\alpha_0}. \tag{4}$$

In other words, a particle with the amplitude

$$I_a > \left(\frac{\nu'}{2m\alpha_0 A_n}\right)^{1/n},$$

will be captured by the resonance island and remained inside the island as it moves.

If the adiabatic criterion is not fulfilled, the particle is not trapped in resonance but its amplitude increases as

$$\Delta I / I_0 \approx A_n I_0^{n/2-1}\sqrt{2\pi m/|\nu'|},$$

and the faster the particle passes the resonance, the smaller is the growing of its amplitude. The explanation of this fact is evident: resonance can change the particle oscillation energy by a small fraction during the fast passage.

### 3.16.4 Experimental Estimation of the Adiabatic Criterion

At first we tuned the system parameters to observe the third-order resonance $3\nu_z = 23$ at the phase space plot by the turn-by-turn equipment. The tuning was performed by a single skew-sextupole magnet controlling the driving term in the Hamiltonian (1) and by a set of octupole magnets regulating the amplitude dependent tune shift. Turn-by-turn pick-up electrodes allow measuring the nonlinear behaviour of the betatron tune. Fig. 3 shows the vertical tune as a function of the amplitude for different excitation currents of two octupole magnets SEOQ and NEOQ placed symmetrically to the IP at the azimuth with $\beta_z >> \beta_x$.

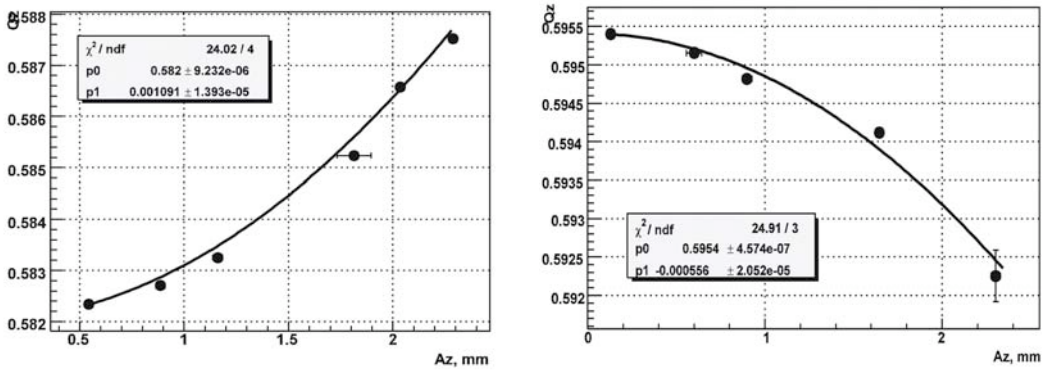


| *Octupole current = – 23 A* | *Octupole current = + 23 A* |
|---|---|

**Figure 3:** Vertical tune vs. amplitude for different currents in the octupoles. Polarity changing yields change of the tune shift term from $C_{zz} = 1 \times 10^{-3}$ mm$^{-2}$ to $C_{zz} = -0.5 \times 10^{-3}$ mm$^{-2}$.

Table 1 lists the nonlinear coefficients determined by the following expressions for different operation modes:

$$\Delta\nu_x = C_{xx}A_x^2 + C_{xz}A_z^2 \quad \text{and} \quad \Delta\nu_z = C_{zx}A_x^2 + C_{zz}A_z^2$$

**Table 1:** Tune-amplitude dependence coefficients (*O* is the octupoles current).

| $10^4 \cdot C_{nm}$ (mm$^2$) | *O = 0 A* | *–21.3 A* | *+21.3 A* | *Nominal* |
|---|---|---|---|---|
| $C_{xx}$ | 1.6 | 4.4 | –0.4 | 1.4 |
| $C_{xz}$ | 0 | –6.6 | 2.2 | 3.7 |
| $C_{zx}$ | 0 | –11.6 | 6.6 | 1.2 |
| $C_{zz}$ | 0 | 11 | –5.6 | –1.6 |

Besides, a turn-by-turn technique provides the measurement of the phase space trajectories for different kick amplitude, nonlineriry and resonance driving term. Two examples of such trajectories are shown in Fig. 4. The study of the vertical space curves allows the estimation of the resonance driving term from the following considerations.

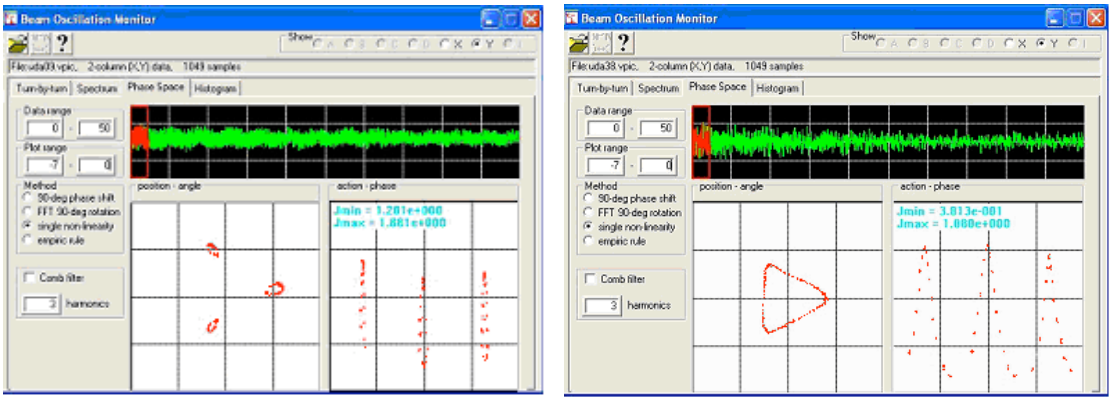


**Figure 4:** Phase trajectories at the resonance (left) and before the resonance creation. Each plot shows the trajectories in the variables $(z, z')$ and $(I_z, \varphi_z)$. The tune is $\nu_z = 0.6621$ and the amplitude of the island center is 0.9 mm.

For the resonance $3\nu_z = n$ a perturbated term of the Hamiltonian

$$H_1 = (2J_z)^{3/2} \sum_n A_{3n} \cos(3\varphi_z - n\theta), \tag{5}$$

where $A_{3n}$ are the relevant Fourier harmonics of the sextupole perturbation, allows us to obtain a second order invariant

$$\bar{J}_z \approx J_z + a_{3n} J_z^{3/2} \cos 3\varphi_z \approx const, \qquad a_{3n} = 3\sqrt{8}\frac{A_{3n}}{3\nu_z - n}, \tag{6}$$

which gives the following estimation of the main perturbation harmonic from the measured curve $J_z(\varphi_z)$

$$a_{3n} \approx \frac{J_{\max} - J_{\min}}{J_{\max}^{3/2} + J_{\min}^{3/2}}. \tag{7}$$

In our case the estimation of the resonance driving term from the experimental data gives the value of $A_{3,2}$ = 0.03÷0.07 mm$^{-1/2}$ depending on the operation mode and lattice tuning.

Having measured the values of the nonlinear detuning coefficients and the resonance driving term, we can estimate adiabatic condition of the resonance crossing. In practical units we have the following:

- For the resonance $3\nu_z = 2$ $n = m = 3$
- $\alpha_0[mm^{-1}] = C_{zz}[mm^{-2}] \cdot \beta_{z0}[mm] = 13300[mm] \cdot C_{zz}[mm^{-2}]$
- $\frac{d\nu}{d\theta} = \frac{R[m]}{c[m/s]} \frac{\Delta\nu}{\Delta t[s]} = \frac{60[m]}{3 \cdot 10^8 [m/s]} \frac{\Delta\nu}{\Delta t[s]}$, where $R$ is the average radius of VEPP-4M and $c$ is the speed of light

- $I_z^{3/2}[mm^{3/2}] = \left(\frac{N_z \varepsilon_z[mm]}{2}\right)^{3/2} = N_z^{3/2} \cdot \left(\frac{25 \cdot 10^{-8}[mm]}{2}\right)^{3/2}$, where $N_z$ is the particle action variable in term of the vertical emittance, $\varepsilon_z = 1\% \varepsilon_x$, $\varepsilon_x = 25$ nm

Taking into account the above notations, the following adiabatic criterion for our resonance can be found

$$\frac{\Delta\nu}{\Delta t[s]} < 20 \cdot C_{zz}[mm^{-2}] \cdot A_{3,2}[mm^{-1/2}] \cdot N_z^{3/2}. \quad (8)$$

For $C_{zz} = 10^{-3}[mm^{-2}]$ (corresponding to the octupole current of –21.3 A) and the driving term $A_3 = 0.05[mm^{-1/2}]$, traverse of the resonance discussed above with the crossing rate of $\Delta\nu / \Delta t = 0.01/10s = 10^{-3} s^{-1}$ provides the adiabatic conditions for the particles starting with the amplitudes (in term of the vertical emittance) $N_z \approx 1$.

### 3.16.5 Measurement Results

All measurements were performed at a low electron current of ~0.5 mA to avoid coherent effects. We changed the vetical betatron tune by the increasing or decreasing of the quadrupole magnet current with the variable rate. The minimal rate provided by the quadrupole power supply is $\Delta\nu_z = 0.01$ at 30 ms.

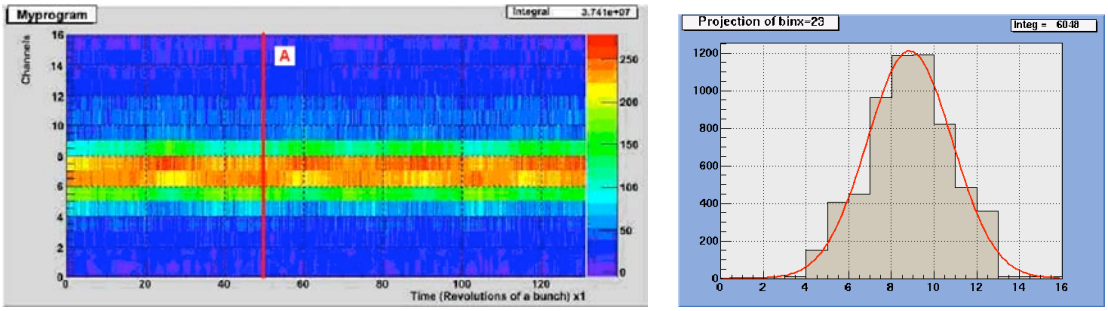


**Figure 5:** The vertical beam profile vs. revolution number (left plot). *Octupole* = 0 A, $\nu_z = 0.661 \rightarrow 0.672$, $\Delta t = 30$ ms. Colors indicate the beam intensity. Single shot vertical beam profile fitted by the Gauss function (right plot).

During the measurement we varied the strength of the resonance driving term and the amplitude dependent tune shift. During the resonance passage we have registered turn-by-turn the vertical beam profile by the fast 16-channel photomultiply tube and the particle loss with the help of the scintillator counter inserted in the vacuum chamber vertically. The example of the vertical beam profile measurement as a function of the turn number during the resonance crossing with the maximum speed and the nonlinear detuning close to zero is shown in Fig. 5, left. A cross-section of the plot along the line *A* is depicted in Fig. 5, right.

The following conclusions can be made from the estimation results of the previous section:

(1) For the switched off octupoles, the vertical nonlinear detuning is zero (see Table 1); no resonance islands exist and particle trapping can not occur. The third-order resonance is intrinsically unstable and particle loss should be observed for a slow resonance passing. Qualitative picture of the 3rd-order unstable resonance crossing is given in Fig. 6.

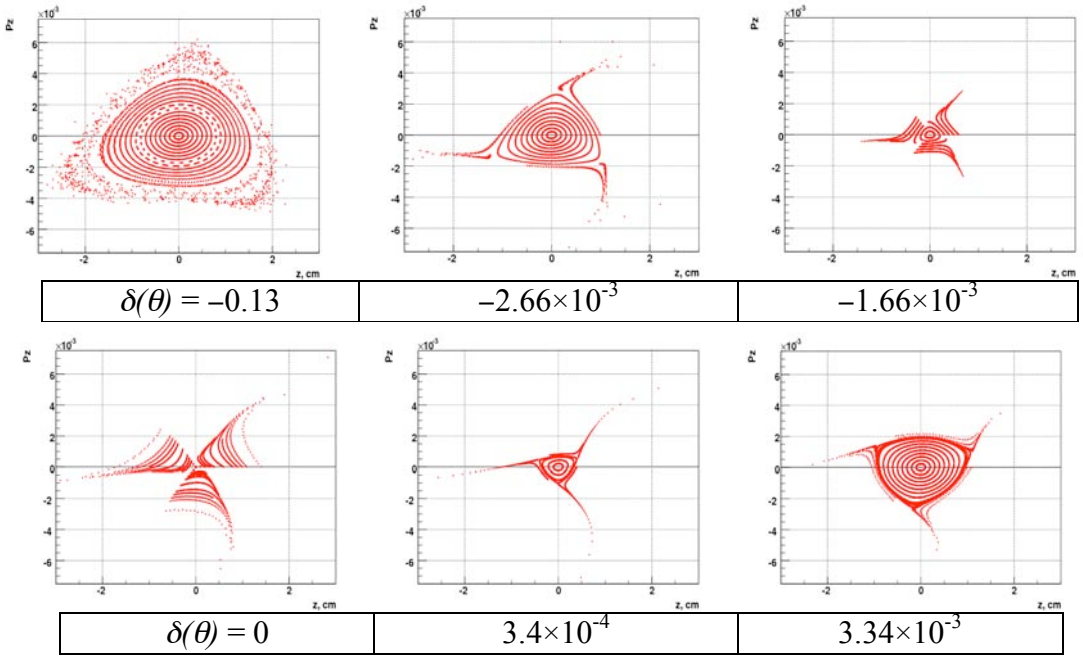


**Figure 6:** Phase trajectories evolution during the unstable resonance crossing.

And, indeed, the following plots of the beam profile during the resonance crossing at zero current of the octupole magnets were measured experimentally (see Fig. 7-1 and 7-2):

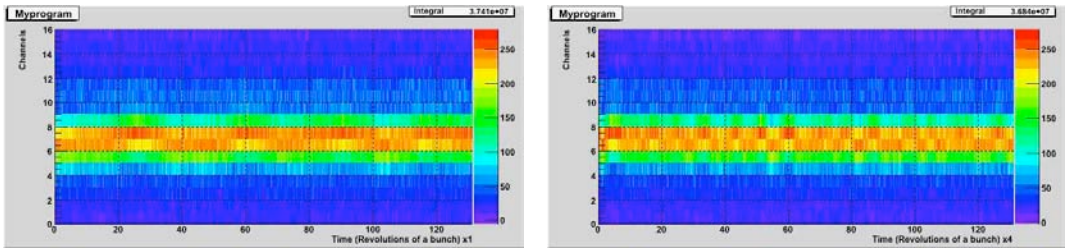


**Figure 7-1:** Tune range is $Q_z = 0.6611 \div 0.6720$, $\Delta Q_z = 0.0109$; time for the whole tune range crossing is 40 ms; $O = 0$ A. The left plot corresponds to the crossing with the tune increase, the right one to the tune decrease. Neither beam size change nor intensity loss is observed.

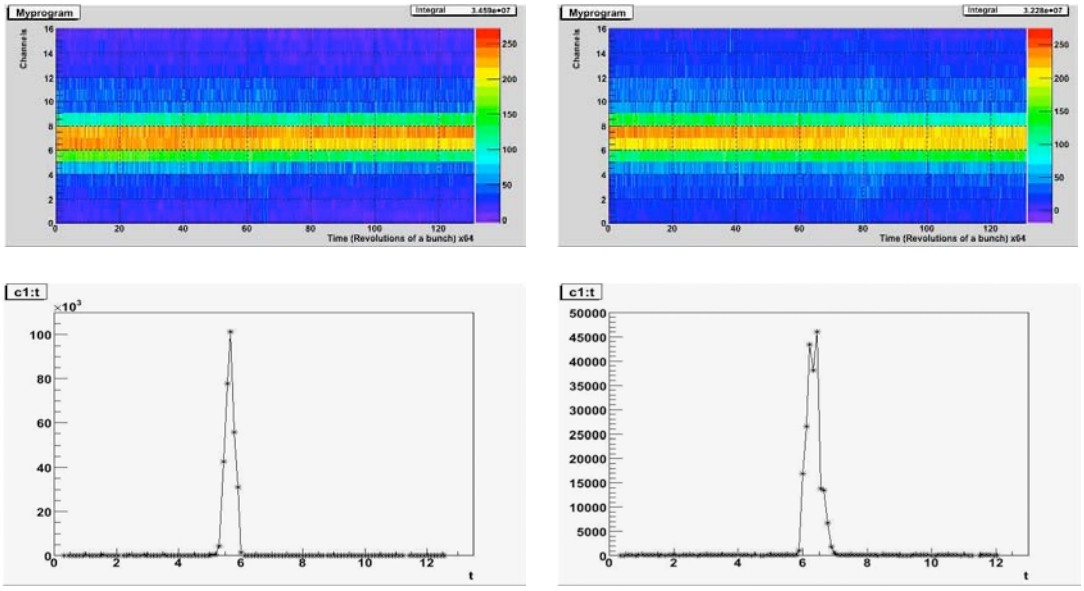


**Figure 7-2:** Same as in Fig. 7-1 but the tune range crossing time is 1 s. No beam size change is still observed but the beam loss during the resonance crossing is registered by the counters (bottom pictures).

(2) If the relevant tune-amplitude dependence is introduced, three stable resonance islands are created at the phase space plot when the betatron tune crosses the resonance value (Fig. 8). The sign of nonlinearity should correlate with the tune variation direction: for the positive nonlinearity the tune should be decreased to generate the islands at the exact resonant value.

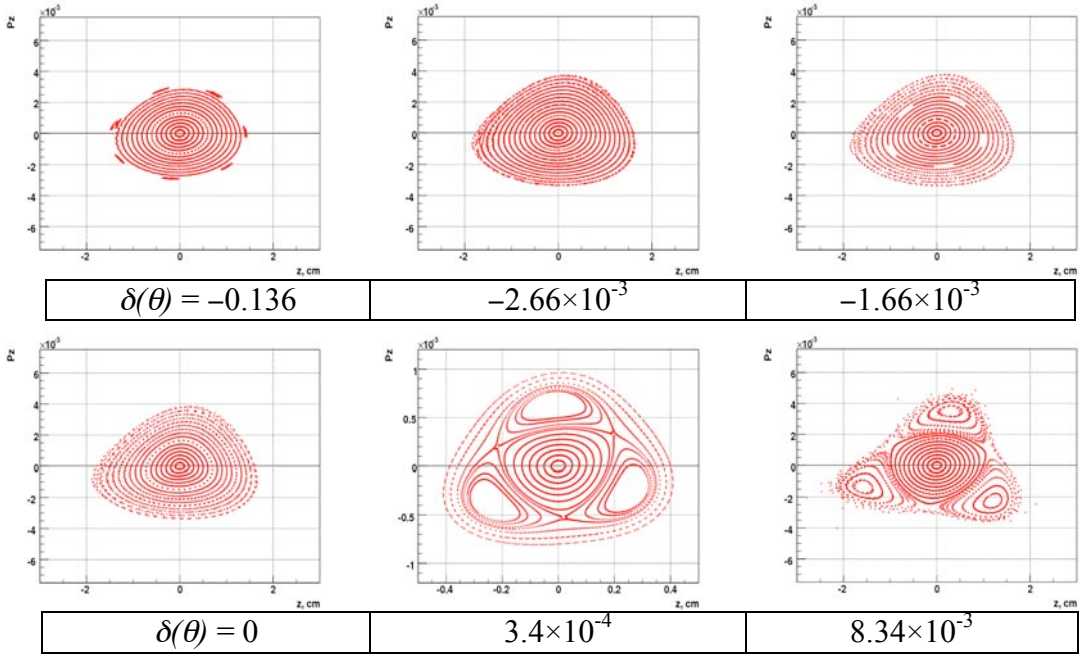


| $\delta(\theta) = -0.136$ | $-2.66\times10^{-3}$ | $-1.66\times10^{-3}$ |
|---|---|---|
| $\delta(\theta) = 0$ | $3.4\times10^{-4}$ | $8.34\times10^{-3}$ |

**Figure 8:** Phase trajectories evolution during the stable resonance crossing.

In our case the maximum value of the vertical nonlinearity $C_{zz} = 1.1 \cdot 10^{-3}$ corresponds to the octupole current of $O = -21.3$ A; and as the sign of the nonlinearity is positive, the particles capture in the resonance islands should be observed for the tune decrease. The measurement results are represented in the figures below.

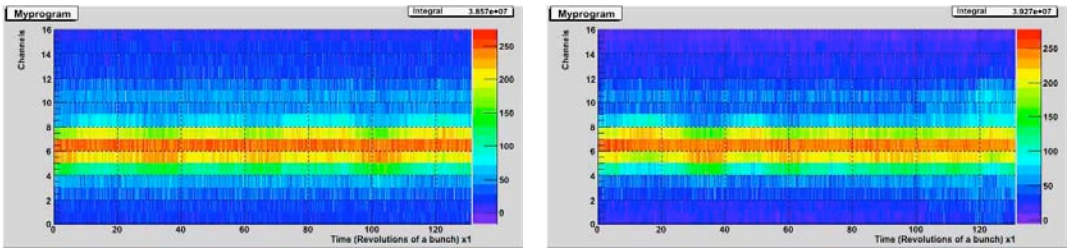


**Figure 9-1:** Tune range is $Q_z = 0.6608 \div 0.6717$, $\Delta Q_z = 0.0109$; crossing time is 40 ms; $O = -21.3$ A. The left plot is for the tune increase, the right one is for the tune decrease. For such high crossing rate neither beam size change nor particles capture is seen.

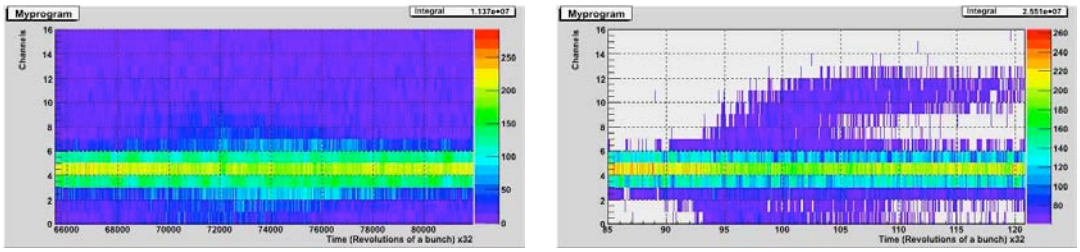


**Figure 9-2:** Same as in Fig. 9-1 but the crossing time is 3 s. At the left plot with the tune increasing a small beam blow-up is seen while at the right plot with the tune decreasing one can see the generation of the resonance island and particle trapping.

Process of particles trapping in the resonance is shown in details in Fig. 10 and Fig. 11. In Fig. 10 the vertical beam profile vs. the revolution number demonstrates the moment of the resonance island creation and moving outwards. This case relates to the adiabatic resonance traversing. The vertical beam distribution corresponding to the different times (cross-sections lines *A*, *B*, *C* and *D* in Fig.6) is shown in Fig. 11.

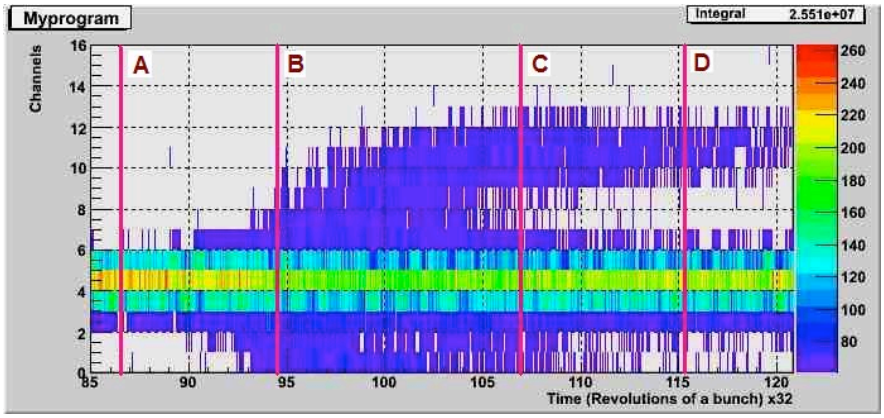


**Figure 10:** Time evolution of the vertical beam distribution in the case of the particle trapping in the resonance island ($O$ = –21.3 A, $\nu_z = 0.6717 \rightarrow 0.6608$, $\Delta t = 3$ s).

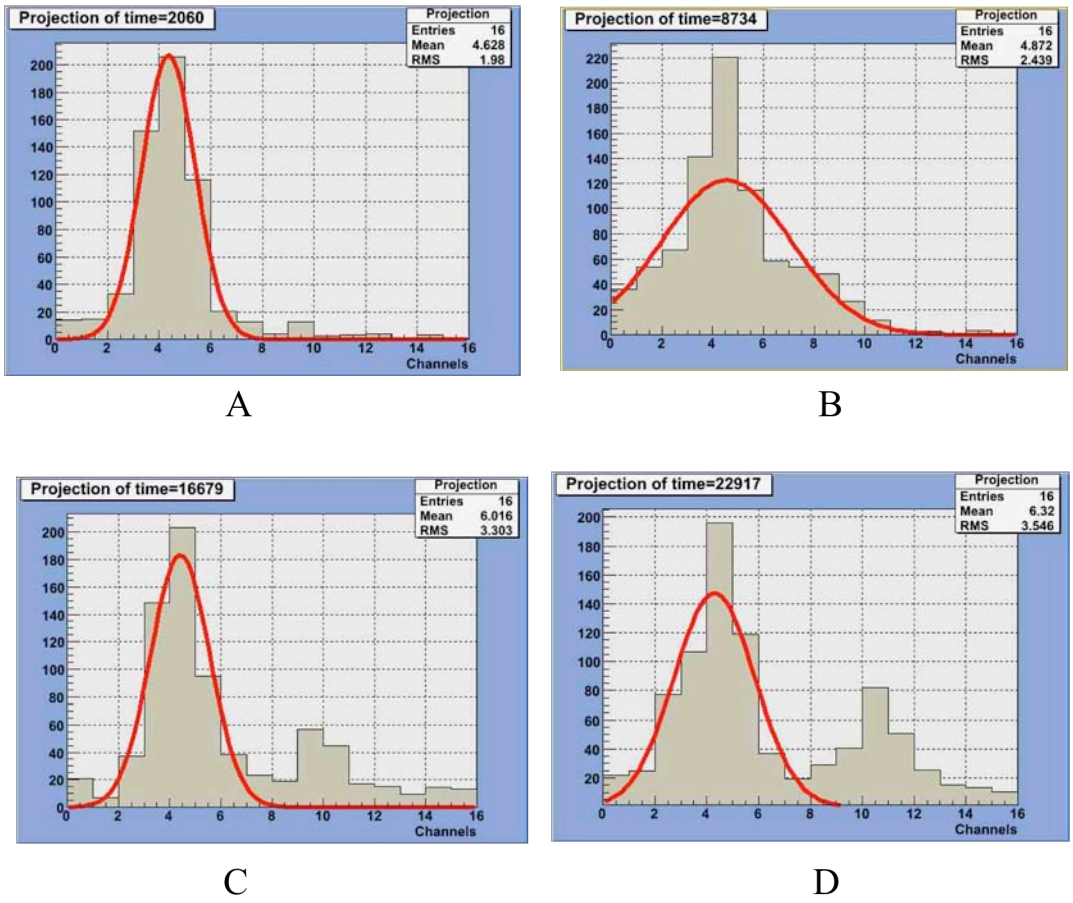


**Figure 11:** Creation of the resonance island and particles trapping in the adiabatic limit. The beam core is fitted by Gaussian function.

It is worth mentioning that with the changing of the resonance passage direction (the left plot in Fig. 9-2) we could see, instead of particles trapping, an insignificant

blow-up of the beam size. Such “hysteresis” of the nonlinear resonance behaviour is well-known and was studied theoretically in the past.

(3) Changing of the nonlinearity sign by assigning the octupole current of $O$ = +21.3 A reverses the situation. Now the particles trapping and moving out of the beam take place when the vertical betatron tune increases. However, as the absolute value of the tune-dependent coefficient in this case is less than that for the negative octupole current, $C_{zz} = -0.6 \cdot 10^{-3}$, the adiabatic condition (4) comes for the particles with a larger amplitude and less population, so the particles capture in the resonance is not so clearly seen.

### 3.16.6 Conclusions

The passing of the beam through the vertical sextupole resonance has been studied experimentally at the VEPP-4M storage ring. It was shown that under the adiabatic condition and the relevant resonance parameters particles are captured in the resonance island and may be brought away from the beam center. Turn-by-turn beam profilometer has shown itself as a powerful tool to observe fast processes in circular accelerators.

### 3.16.7 References


1. C.Pellegrini, A,M.Sessler, “Crossing of an incoherent integral resonance in the electron ring accelerator”, NIM 84, (1970), 109-116.
2. A.Chao and M.Month, “Particle trapping during passage through a high-order nonlinear resonance”, NIM 121, (1974), 129-138.
3. G.N.Kulipanov, S.Popov, G.Tumaikin, “Experimental study of particles loss in circular accelerator due to the nonlinear resonance passage”, Proc. of All-Union workshop on particle accelerators, 1968, 374-378.
4. S.Y.Lee, “Emittance dilution in resonance crossing of FFAG accelerators”, ICFA Beam Dyn.Newslett.43, 2007, 51-53.
5. O.I.Meshkov et al. “VEPP-4M optical beam profile monitor with one-turn temporal resolution”, Proc.of EPAC’04, Lucerne, 2004, 2733-2735.


## 3.17 Beam Energy Measurements at VEPP-4M Collider by Resonant Depolarization Technique


V.E. Blinov, A.V. Bogomyagkov, V.P. Cherepanov, V.A. Kiselev, E.B. Levichev, A.S. Medvedko, S.A. Nikitin, I.B. Nikolaev, A.G. Shamov, E.I. Shubin
BINP SB RAS, Novosibirsk
Mail to: A.V.Bogomyagkov@inp.nsk.su


### 3.17.1 Introduction

Since 2002 experiments are performed with the universal magnetic detector KEDR [1] at the electron-positron collider VEPP-4M [2] at BINP. The VEPP-4M collider consists of booster ring VEPP-3 with energy from 300 MeV to 2000 MeV and the main ring operating in the beam energy range from 1 GeV to 5.5 GeV. The physics program of the detector is focused on the study of ψ-, Y-mesons and γγ-physics. The

goal of the first series of the experiments was precise mass measurements of J/ψ, ψ(2s), ψ(3770), D mesons and τ lepton. The resonant depolarization technique [3] was used for precise instantaneous energy calibration. Continuous energy measurements were performed by determination of the utmost energy of the γ-quanta obtained from the Compton backscattering of laser photons against the electron beam [4, 5]. The present paper describes both methods, realization characteristics, achieved precision in experiments with the KEDR detector at the VEPP-4M collider.

### 3.17.2 Resonant Depolarization Technique

The resonant depolarization technique (RD) was proposed at BINP in 1975 [6, 7] and used in precise mass measurement of various particles: ϕ [8], $K^{\pm}$ [9], J/ψ and ψ(2s)-mesons [10], Υ(1s), Υ(2s)-, Υ(3s) mesons [11, 12, 13, 14, 15], Z-boson [16]. The relative accuracy of mass measurements in these experiments was $10^{-4} \div 10^{-5}$. The method itself is similar to the phenomena of electron or nuclear magnetic resonances. Spin of the electron traveling in the magnetic field precesses around the direction of the field. In the storage ring with a flat orbit without torsion the spin precession frequency Ω depends on the Larmor revolution frequency of the particle $\omega_0$ and Lorentz factor γ:

$$\Omega = \omega_0 \left( 1 + \gamma \frac{\mu'}{\mu_0} \right), \qquad (1)$$

where $\mu'/\mu_0$ — ratio of anomalous and normal parts of electron magnetic moment known with a relative accuracy of $3.3 \cdot 10^{-9}$ [17]. The average particle revolution frequency $\omega_0$ is completely determined by frequency of the accelerating RF field and could be set and measured with high accuracy. Thus, energy measurement is reduced to spin frequency measurement Ω, which is convenient to represent in units of revolution frequency and in the coordinate basis related to the particle velocity vector: $\nu = \gamma\mu'/\mu_0$. In order to measure spin precession frequency, resonant influence of an external electromagnetic field on spin motion is used [6, 7]. The spin precession frequency is measured at the moment of depolarization during scan of the external electro-magnetic field frequency. Depolarization happens when the resonant condition is satisfied:

$$\omega_d \pm \Omega = k\omega_0, \qquad (2)$$

where k — any integer, $\omega_d$ — electromagnetic field frequency. The external electromagnetic field could be created in the form of the alternating longitudinal magnetic field or transverse TEM wave propagating against the beam with the magnetic field direction perpendicular to the polarization vector. The moment of depolarization is detected by the process, which cross section depends on the polarization degree.

Since there is an energy spread in the beams of the electron-positron collider, the instantaneous spin tune spread $\sigma_\nu$ is proportional to the energy deviation RMS $\sigma_E$: $\sigma_\nu = \sqrt{2}\,\sigma_E \approx 10^{-3}$.

There is one more characteristic of the spin frequency distribution in the beam — an intrinsic spin line width ($\varepsilon_\nu \ll \sigma_\nu$) which corresponds to averaging of the spin motion over synchrotron and betatron oscillations. The synchrotron oscillations yield a shift and

widening of the spin line at the level $\Delta\Omega/\Omega \sim 10^{-8}$. Practically, the spin line width is determined by nonlinear effects of particle motion in the storage ring fields. The RD process is very slow as compared with any period of the orbital motion. It allows us to consider the spin frequency spectrum as a set of narrow isolated lines and to measure the spin frequency with an error much smaller than the instantaneous spin tune spread $\sigma_\nu$. The spin frequency spectrum due to the modulation effect of the orbital motion consists of the main and sideband lines. The synchrotron oscillation sideband lines are distant from the main line at the value $\nu_{synch} \approx 0.01$, which is equivalent to a 4.4 MeV bias for VEPP-4M. Therefore, a special care has to be taken to avoid depolarization at the synchrotron sideband line. The sidebands from the betatron oscillations are about 200 MeV apart from the main line and practically never crossed during the usual frequency scan.

Pulsations of the guiding field will change the revolution frequency as well as the energy of the individual particles. Therefore, there will be additional sidebands in the spin precession frequency spectrum at the magnetic field pulsation frequencies. These side bands might be very close to the main line, for instance a 50 Hz pulsation is only 26 keV away from the main line. Hence, one needs to keep an amplitude of pulsations small enough (<15 ppm) in order not to depolarize the beam at the wrong frequency and keep the depolarizer amplitude as small as possible (so depolarization does not happen at sidebands but is still possible at the main line).

The spread of particle horizontal trajectories in the presence of sextupole fields is responsible for associated spin tune width, which is estimated to be $\Delta\nu/\nu \approx 5 \cdot 10^{-7}$. This effect is the primary source of uncertainty of the spin tune measurements.

#### *3.17.2.1 Touschek Polarimeter*

The various methods for measurement of the electron/positron beam polarization in the storage rings were developed and used in BINP during the last thirty years [18, 19, 20]. Most effective of them applied to the low energy range of VEPP-4M including J/ψ, ψ(2s) mesons as well as τ lepton production threshold is the observation of spin dependence in the intra-beam (Touschek) scattering. The cross section of the intra-beam scattering of polarized electrons is smaller than for unpolarized. The registered counting rate of scattered electrons will experience jump at the moment of depolarization proportional to squared level of polarization $P^2$. Numerous variations of beam parameters change the counting rate hampering observation of the true moment of depolarization. Therefore scattered electrons are registered from two electron bunches separated by half a turn, one beam is polarized the other one is not. In such an approach, the relation $1-N_2/N_1$ (this ratio is less sensitive to the change of the beam parameters) will experience jump at the moment of depolarization, where $N_1$ and $N_2$ are the counting rates of the polarized and unpolarized beams respectfully (Figure 1).

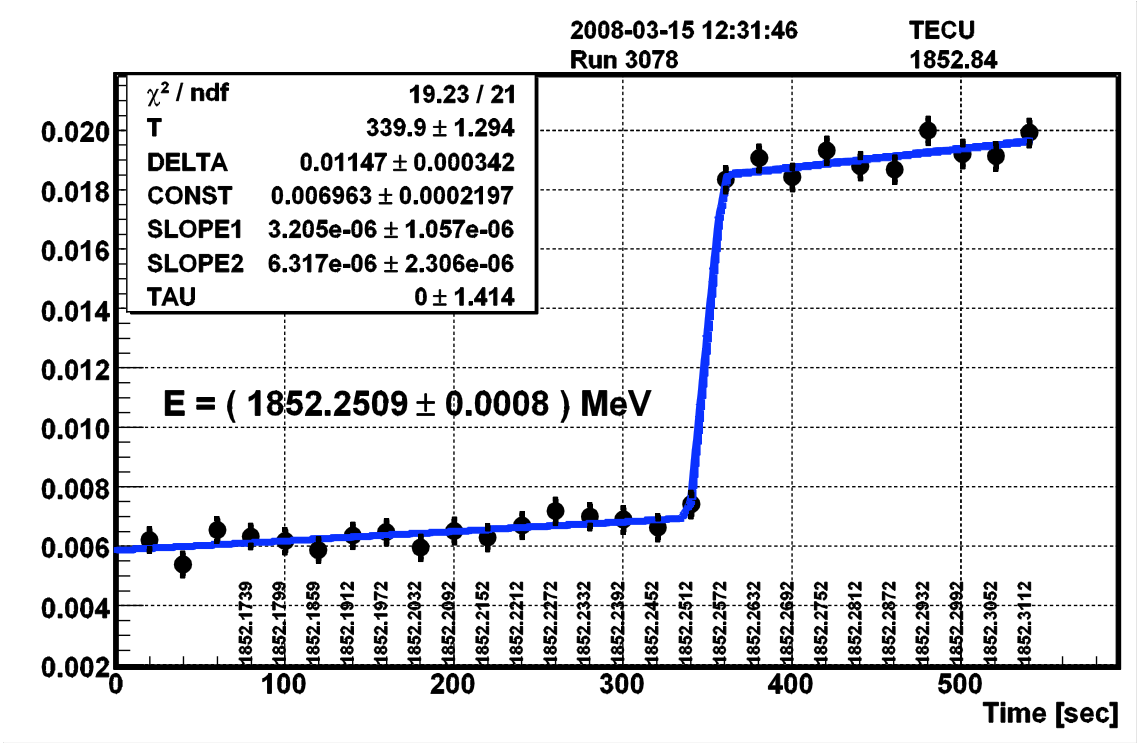


**Figure 1:** The ratio of counting rates from polarized and unpolarized beams during depolarization. The statistical error for Ebeam is 0.8keV.

The polarimeter system consists of several scintillator counter groups installed in the technical and experimental section of VEPP-4M (Figure 2). Every group consists of a pair of scintillation counters on opposite sides of the vacuum chamber in horizontal plane. Each counter could be moved inside the aperture in order to optimize counting rate. The range of counters motion could limit dynamic aperture.

The signal processing from the counters is destined to distinguish counting rate of Touschek electrons and briefly described below. The counting rate of the counters consists of correlated (two electrons from the same act of Touschek scattering) and uncorrelated events. Signals coincidence from the counters is summation of correlated events and random coincidence of uncorrelated events. Solving the obtained system of equations one yields the dependence of counting rate of correlated events on measured counting rates and theirs coincidences.

Special studies showed that in energy range of 1.5÷1.8 GeV 80÷60% of counting rate belongs to Touschek electrons, therefore counters were operated without coincidence circuits. However, at different energies coincidence circuits should be used. At the present time counting rate of the polarimeter system reaches 1 MHz at the beam current of 2÷4 mA and at the distance from the counters to the beam of 1 cm (at this distance beam life time is not yet significantly affected). The jump of the observed ratio is 2.5÷3.5% at energy region from 1.5÷1.8 GeV being in a good agreement with the calculation (at P=80%).

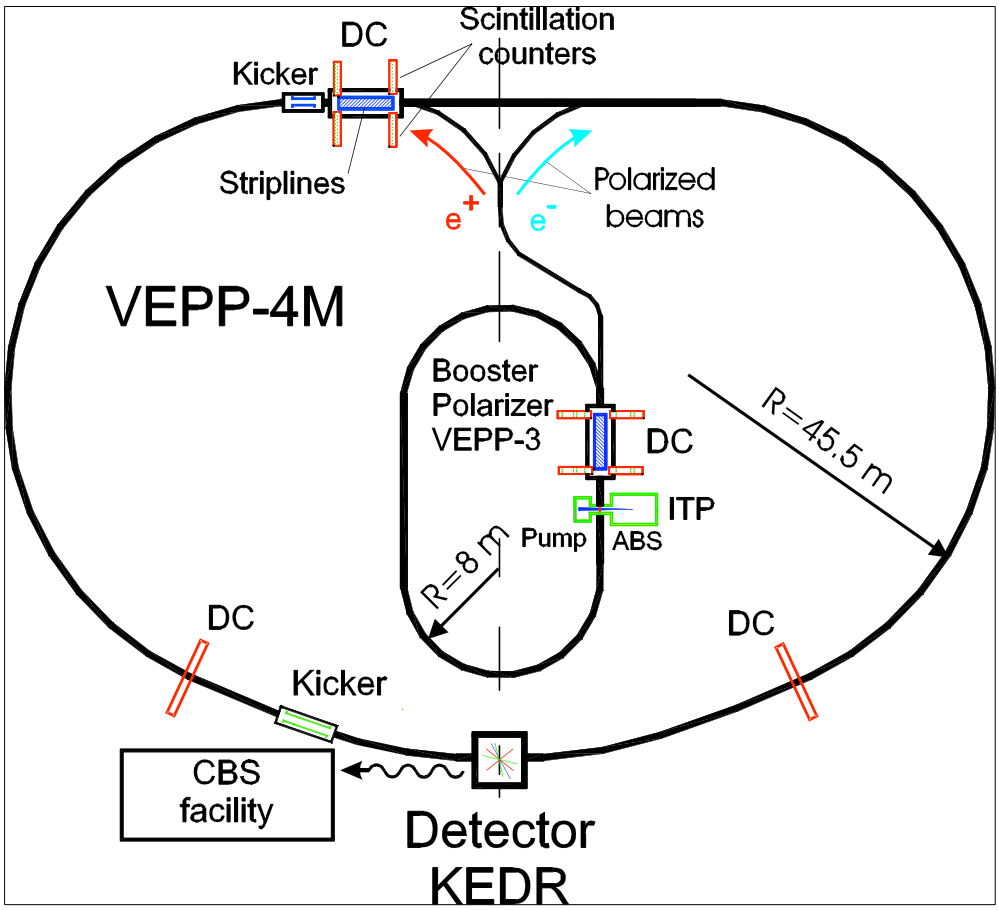


**Figure 2:** VEPP-4M layout.

### *3.17.2.2 Depolarizer*

The two matched strip lines of the VEPP-4M kicker (Figure 2) are used to create TEM wave propagating towards the beam. The signal source is a frequency synthesizer with the minimal frequency step of 0.35 mHz. For VEPP-4M, 1 keV in the beam energy scale corresponds to 1.85 Hz in the depolarizer frequency $f_d$. The power wide-band amplifier can provide an amplitude of the voltage across strip lines up to $U_d \approx 200$ Volts. The rate $\tau_d^{-1}$ of forced depolarization with the transverse field crucially depends on the absolute value of the spin response function $|F^\nu|$ [18] at the place of the depolarizer location: $\tau_d^{-1} \propto U_d^2 \cdot |F^\nu|^2/\Delta f_d$. For VEPP-4M, the design depolarization time $\tau_d$ is about 2 seconds at E=1550 MeV with $U_d \propto 15$ V, $\Delta f_d \propto 4$ Hz, $|F^\nu|^2=130$. The typical depolarizer parameters in the J/ψ experiment were: the rearrangement step of the depolarizer frequency 2 Hz; the band width (due to modulation at the frequency $f_m$=2 Hz) $\Delta f_d$ =4 Hz; the voltage amplitude 12 V; the average rate of the frequency rearrangement 0.2 Hz/sec. The corresponding accuracy in the current energy determination is $\delta E \approx \pm 1$ keV.

There are several kicker strip lines at different azimuths of VEPP-4M, which allows choosing of the most efficient with respect to the spin response function at the given energy.

### *3.17.2.3 Calibration of Particle Absolute Energy*

At the energy range of J/ψ , ψ(2s) - mesons and τ lepton VEPP-3 booster storage ring serves as a source of polarized beams for VEPP-4M (Figure 2). Due to Sokolov-Ternov effect the electron/positron beams become polarized in VEPP-3 with the characteristic time $\tau_p \approx 80$ minutes at E=1550 MeV (J/ψ) and $\tau_p \approx 30$ minutes at E=1840 MeV (ψ(2s)). Very large polarization time in VEPP-4M (~$10^2$ hours) does not allow to obtain polarized beams immediately in the main ring. Polarized beam is than injected in VEPP4-M and about 10 minutes later unpolarized beam is added as a second bunch. The regime of VEPP-4M during energy calibration is slightly different from the one with luminosity (all electrostatic separation is off). This is done to minimize possible errors associated with electron positron energy differences.

Formula (1) allows to calculate beam energy after measurement of spin precession frequency only for ideal accelerator with absolutely flat orbit. Vertical orbit distortions, local orbit bumps, errors of detector longitudinal field compensation are responsible for bias of beam average energy from calculated one by formula (1). Corrections that are applied during energy calibration at VEPP-4M and associated uncertainties have been well described in [21, 22, 23]. One of the RD calibration results is shown on Figure 1. The statistical error for the beam energy is 0.7 keV. The total correction due to orbit distortion is $\Delta E \approx 3 \div 5$ keV.

Due to the depolarizer (Sec. 1.1.2.2) and the spin line (Sec.1.1.2.2) widths the measured beam energy is biased with the value about ±1.5 keV. The sign is determined by the frequency scan direction — up or down. This bias can be measured and corrected with two opposite scans, which can be done with the same beam within short time.

The total systematic error for instantaneous beam energy is about 2 keV [23]. The whole process of energy calibration by RD consumes about 2 hours and was performed once a day for J/ψ, ψ(2s) scans and once in a few days for τ lepton, ψ(3770) mass measurement experiments. Since 2002 more than 1500 calibrations have been performed.

### *3.17.2.4 Assignment of Energy to Data Acquisition Runs*

The energy calibration technique described above is impossible to perform during the data acquisition. Large energy variations can occur between the calibrations, therefore additional measures has to be taken to assign RD energy to the data acquisition runs.

In the experiments [12, 13, 14, 16] the guide field measurements were used to calculate the beam energy assuming that

$$E_{beam} = \alpha_H \cdot H_{NMR}, \qquad (3)$$

with the field strength $H_{NMR}$ measured in a reference dipole powered in series with the main ring magnets and the $\alpha_H$ is a coefficient determined using nearby calibrations. The simple relation (3) implies the absence of orbit variations. The direct orbit measurements are usually not accurate and comprehensive enough to be used for a correction of the $\alpha_H$ value. In VEPP-4M, there are ten independent bending magnet power supplies, sixty radial correctors and only fifty-four beam position monitors. However, the empiric improvement of (3) is possible using observable parameters such

as magnet and machine tunnel temperatures, magnet currents and the explicit time dependence to take into account the parameters, which cannot be observed.

In the J/ψ and ψ (2s) mass experiment [23] the following extension of (3) was suggested:

$$E_{beam} = \alpha_H \cdot H_{NMR} \cdot \left(1 + \alpha_T \left(T_{ring} - T_{NMR}\right)\right) \cdot f(T_{ring}, T_{cool}, T_{tunnel}) + \\ + A(t) \cdot \cos\left(\frac{2\pi t}{\tau_{day}} - \varphi(t)\right) + \delta E_{on} \exp\left(-\frac{t_{on}}{\tau_{on}}\right) + \delta E_{cycle} \exp\left(-\frac{t_{cycle}}{\tau_{cycle}}\right) + E_0(\Delta i, t), \quad (4)$$

where $T_{NMR}$ is the temperature of the reference dipole, $T_{ring}$ and $T_{cool}$ are the average values of the ring and the cooling agent (air or water) temperatures, the temperature $T_{tunnel}$ is measured in some depth of the machine tunnel walls; t is current time, $t_{on}$ and $t_{cycle}$ denote time elapsed since the last switching of the collider and the last magnetization cycle, respectively.

The $\alpha_H$, $\alpha_T$, $\delta E_{on}$, $\delta E_{cycle}$, $\tau_{on}$ and $\tau_{cycle}$ are free parameters to be determined by the fit of all energy calibrations performed in a certain operating mode of the collider. The simplest (linear or step-like) functions f(T), A(t), φ(t) and $E_0(\Delta i,t)$ have additional free parameters.

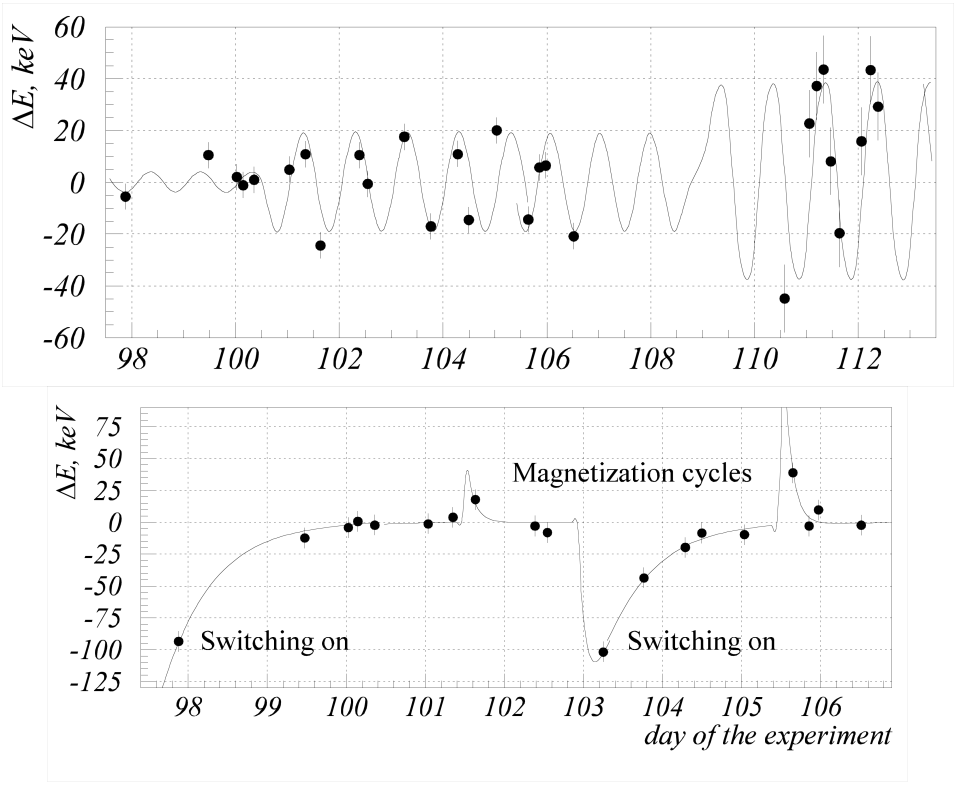


**Figure 3:** The example of the beam energy behaviour. Upper plot shows periodic dependence on time, lower — aperiodic energy dependence on time due to switching on the ring and the magnetization cycles. All dependences but presented ones are taken into account in ΔE, the error bars show the mean deviation from the fit.

In this parameterization, the difference of the reference dipole and the ring magnet conditions is accounted. Also the variations of the ring circumference and the corresponding shift of the orbit position relative to the magnets due to temperature variations is accounted partially by the linear function f(T). The significance of this effect at the VEPP-4M is known since 1982 [11]. The residual temperature effect is described by the day-to-night oscillations. In general, the amplitude A and the phase $\varphi$ are not constant due to season variations of properties of the ground surrounding the machine tunnel. The fitted value of A depends on the quality of the tunnel temperature monitoring. During the experiment [23] it was not monitored at all.

The exponential terms introduce the magnetic field relaxation; ignoring this effect results in a bias in the parameters $\alpha_H$, $\alpha_T$, etc.. The term E0($\Delta$i,t) serves to take into account the energy variation due to adjustments of the current $\Delta$i in some machine elements and thus to increase the number of calibrations which can be fitted together.

The results of the energy fit for May 2002 are illustrated on Figure 3. Fourteen free parameters are used to fit 28 points shown in the figure. The value of the $\chi$-squared per degree of freedom is employed to estimate the (mean) error of the energy interpolation by requiring $\chi^2/N_{dof} = 1$.

The appearance of strong day-to-night oscillations (the 100th day of the experiment on (Figure 3) and their further growth (between 107th and 110th days) can be probably explained by the change of the thermo-mechanical properties of the ground surrounding the VEPP-4M tunnel. These properties can change abruptly at the moment when the melting front reaches the tunnel (in Novosibirsk it occurs in May). According to the $\chi^2$ criterion, the sudden growth of the oscillation amplitude on the 100th day is much more probable than the gradual one.

During the whole experiment [23] (218 calibrations) the quasi-statistical accuracy of the interpolation varies from 6 to 8 keV. Various choices of the functions f(T), A(t) and $\varphi$(t) was tried to estimate the systematic uncertainties of the resulting J/$\psi$ and $\psi$(2s) mass values.

To apply the parameterization (4) in its full form, the large number of calibrations is required without essential change of the collider operating mode. In the measurements of the $\psi$(2s), D mesons and $\tau$ lepton masses [24, 25] the simplified forms of (4) were employed at the relatively short time intervals. The number of free parameters varies from 4 to 7. The interpolation accuracy achieved is 10÷15 keV for the narrow resonance scans and 15÷30 keV for the $\tau$ lepton threshold and $\psi$(3770) mass measurement experiments.

#### *3.17.2.5 Study of Applicability of Touschek Polarimeter at High Energies*

After completion of VEPP-4M activities at the low energies we plan to start a data acquisition with KEDR detector in the region of the Y-mesons at the 4.5÷5 GeV beam energy range for precision mass measurement of these states. For clarification of the Touschek polarimeter applicability at these energies, we have measured a dependence of Touschek particle counting rate on the beam energy and compared it with our theoretical estimate. Measurements have been performed at several energy points in the range from 1850 up to 4000 MeV.

With the aim to decrease errors, the following measures have been applied:

a) We performed studies of the counting rate with subtraction of random coincidence background at the beam energy of 3.87 GeV versus bunch current and vertical beam size. Results were in a good agreement with IBS properties, i.e. dependence on the squared bunch current and on the inverse beam vertical size.

b) Touschek particles were registered in the coincidence mode by two scintillation counters entered inside the vacuum chamber on opposite sides at the median plane. Since the conjugate Touschek, particles move symmetrically regarding to the beam center the positions of counters were set by equalizing their counting rates. The distance between the counters was the same at all energy points.

c) The vertical and horizontal beam sizes were measured. The synchrotron tune was controlled to provide a constant longitudinal beam size. Since the longitudinal size also depends on the bunch current, the experiment at different energies was carried out at close values of the beam current. All this allowed correct normalization of the measured counting rate to the beam volume.

d) Coincidence counting rate was normalized to the squared bunch current.

Results of the first in one's way experiment performed in the season of 2008 are presented on Figure 4. The degree of energy dependence measured is (-2.2± 0.2) for the counting rate normalized to the bunch current squared and multiplied by a ratio of the reference beam volume (at 1.85 GeV) to an actual one. Our theoretical estimate in the non-relativistic approximation for the Moller’s cross section with consideration of the geometrical factor of the counters and their distance to the beam yields the corresponding degree of 3.5. In spite of an obvious discrepancy and necessity to repeat the experiments as well as to specify estimates the first preliminary conclusion can be made. In accordance to the experiment, one can rely on 12 kHz load of the Touschek particle counter at 5 GeV and the beam current of 10 mA. Theoretical estimate reduces the predictable counting rate down to 9 kHz. In both cases, the rate is enough to apply the Touschek polarimeter for the RD technique.

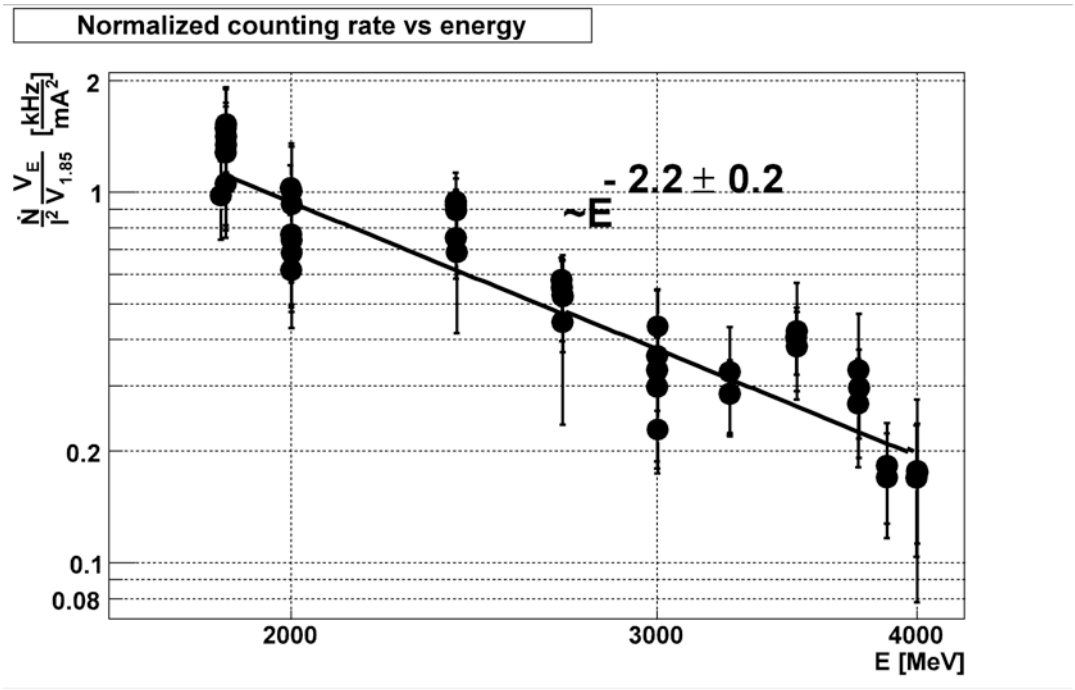


**Figure 4:** Counting rate normalized to a squared unit of the bunch current and multiplied by the ratio of the actual beam volume to the reference one (at 1.85 GeV). Data were obtained in several runs with the help of three scintillation counter pairs placed at the different azimuths of VEPP-4M.

### 3.17.3 References


1. V.V. Anashin et al., Nucl.Instrum.Meth. A 478 (2002) 420.
2. V.V. Anashin et al., proceedings of EPAC 1998, v. 1, p. 400.
3. V.E. Blinov et al., Nucl.Instrum.Meth. A 494 (2002) 81.
4. N.Yu. Muchnoi, S.A. Nikitin, V.N. Zhilich (Novosibirsk, IYF). European Particle Accelerator Conference (EPAC 06), Edinburgh, Scotland, 26-30 Jun 2006, Published in ``Edinburgh 2006, EPAC'', 1181-1183.
5. N.Yu. Muchnoi et al.,“Beam Energy and Energy Spread Measurement by Compton Backscattering of Laser Radiation at the VEPP-4M Collider”, published in this issue.
6. A.D. Bukin et al., In *Warsaw 1975, Proceedings, International Symposium On High Energy Physics*, Dubna 1975, 138-147 and Novosibirsk Inst Nucl Phys - IYAF 75-64
7. A.N. Skrinsky and Yu.M. Shatunov, Sov.Phys.J. 32(1989) 548 (Usp.Fiz.Nauk 158(1989) 315 - in Russian).
8. A.D. Bukin et al., Yad. Phys. 27 (1978) 985 (in Russian).
9. L.M. Barkov, et al., Nucl. Phys. B 148 (1979) 53.
10. A.A. Zholentz, et al., Phys. Lett. B 96 (1980) 214.
11. A.S. Artamonov et al., Phys. Lett. B 118 (1982) 225.
12. A.S. Artamonov, et al., Phys. Lett. B 137 (1984) 272.
13. S.E. Baru et al., Z. Phys. C 30 (1986) 551 [Erratum-ibid. C 32 (1986) 622].
14. W.W. MacKay et al., Phys.Rev.D29 (1984) 2483.
15. D.P. Barber et al., Phys.Lett.B135 (1984) 498.
16. L. Arnaudon et al., Phys. Lett. B 307 (1993) 187.

17. W.-M. Yao et al., ``Review of particle physics" [Particle Data Group], J.Phys.G 33 (2006).
18. Ya.S. Derbenev et al., Particle Accelerators, v.8, p.115, 1978.
19. A.E. Bondar et al., Proc.of 12th Intern. Conf. on High Energy Acc.,FNAL, Batavia, Illinois, 1983, p.240.
20. S.I. Mishnev et al., SPIN 2000, 14th Intern. SPin Phys. Symp.,AIP, v.570, p.892. 2001.
21. V.E. Blinov et al., NIM A 494 (2002) 81.
22. V.E. Blinov et al., NIM A 494 (2002) 68.
23. V.M. Aulchenko et al., Phys. Lett. B 573 (2003) 63.
24. K.Y. Todyshev et al. [KEDR Collaboration], PoS HEP2005 (2006) 115.
25. V.V. Anashin et al., JETP Lett. 85 (2007) 347.

## 3.18 Commissioning of the VEPP-4M Longitudinal Feedback System

G.Ya. Kurkin, V.N. Osipov, V.M. Petrov, E.A. Rotov, S.A. Krutikhin,
S.V. Motygin, S.E. Karnaev, V.V. Smaluk
Budker Institute of Nuclear Physics, Novosibirsk, Russia
Mail to: Smaluk@inp.nsk.su

### 3.18.1 Longitudinal Multi-Bunch Instability

Frequency characteristics of accelerating RF cavities usually include a number of parasitic high-order modes (HOM) in addition to the fundamental mode. The impedance of $m$-th HOM can be written as

$$Z_m^{HOM}(\omega) = \frac{R_m}{1 + iQ_m\left(\frac{\omega_m}{\omega} - \frac{\omega}{\omega_m}\right)}, \qquad (1)$$

where $\omega_m$ is the resonant frequency, $Q_m$ is the quality factor, and $R_m$ is the shunt resistance of the mode. Fig. 1 represents the normalized amplitude spectrum of the high-order modes for one of the VEPP-4M accelerating cavities.

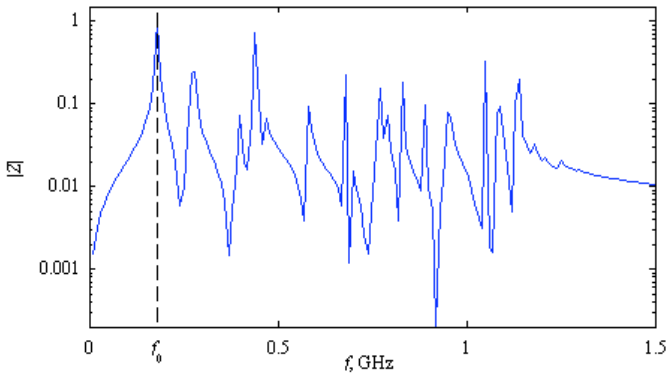


**Figure 1:** Frequency characteristic of the VEPP-4M RF cavity.

Quality factors of some of the high-order modes can be rather large, and the bunched beam passing through the RF cavity can excite long-lived wake-fields

influencing the following bunches. These wake-fields can result in longitudinal multi-bunch instability. If $N_b$ bunches are uniformly distributed along the accelerator perimeter, $k$-th oscillation mode is raised when the resonant condition is satisfied:

$$\omega_m^{HOM} = (lN_b + k + \nu_s)\omega_0, \tag{2}$$

where $\omega_0$ is the revolution frequency, $\nu_s$ is the synchrotron tune, and $l$ is an integer.

Since the impedance of each of the high-order modes is characterized by its own values of the resonant frequency, shunt resistance, and quality factor, the rise time of the instability should be estimated separately for each mode [1]:

$$\tau_m^{-1} = \frac{\alpha N_b I_b}{4\pi\nu_s E/e} R_m \omega_m, \tag{3}$$

where $\alpha$ is the momentum compaction factor, $E$ is the beam energy, and $I_b$ is the current of one bunch.

For the stable beam motion, the radiation damping time of longitudinal oscillation should be less than the rise time (3) of any HOM in the full operation range of the beam current. If this condition is not satisfied, the longitudinal multi-bunch instability occurs. For the VEPP-4M electron-positron collider, this instability is one of the principal efficiency decreasing factors during the high-energy physics experiments.

### 3.18.2 Mode-by-Mode Feedback System

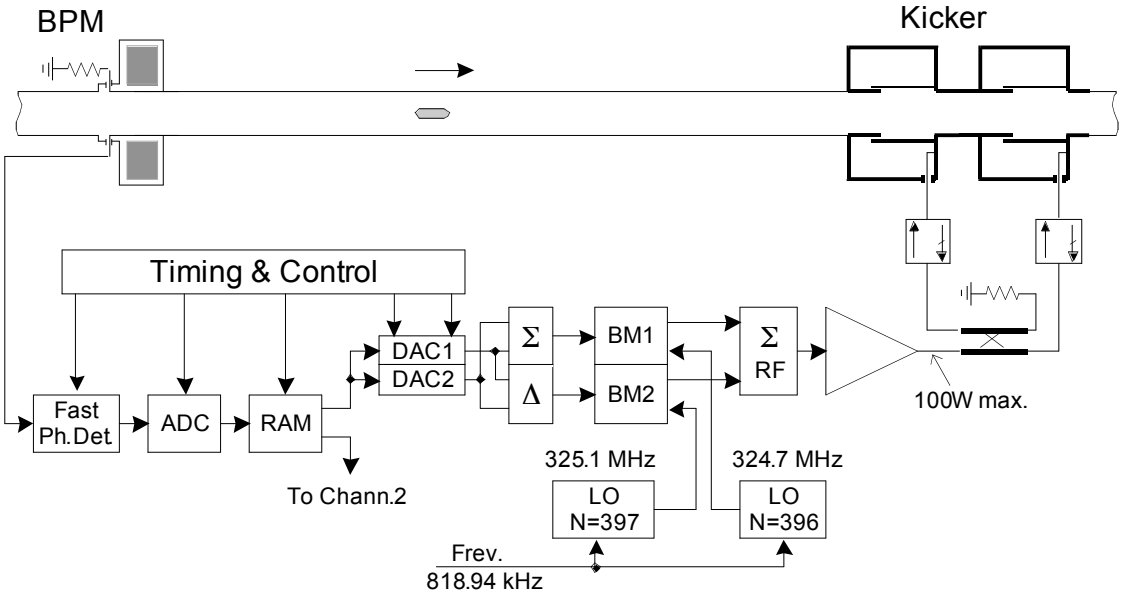


**Figure 2:** Mode-by-mode feedback system.

The mode-by-mode feedback system has been developed at VEPP-4M to suppress the longitudinal multi-bunch instability [2]. The block diagram of the system is presented in Fig. 2, only one channel of the feedback system for one sort of particles is shown. Since there are two pairs of equidistant bunches ($e^+$ and $e^-$), four coupled modes should be damped – two for electrons and two for positrons. In order to identify these

modes, the sample-and-hold technique is used. For all 4 bunches, a fast phase detector produces signals each revolution period. After sampling, the fast ADC digitizes the signals and stores the information in the digital memory (RAM). 4 DACs read the digital information from the memory and convert it into analogue signal again, so these 4 signals represent the instantaneous phases of all 4 bunches. Two of them are for electrons and two – for positrons. The sum signal of each pair identifies the in-phase coupled mode and the difference signal identifies the anti-phase mode. These signals are used to modulate RF voltage of the kickers. To suppress the in-phase mode, the even 398-th harmonic of the revolution frequency is used; to suppress the anti-phase mode – the odd 397-th harmonic.

Two local oscillators (LO) phase locked to the reference signal of the revolution frequency are connected to the corresponding balanced modulators BM1 and BM2. The output signals of the balanced modulators are summed up and the result is used to drive the RF power amplifier.

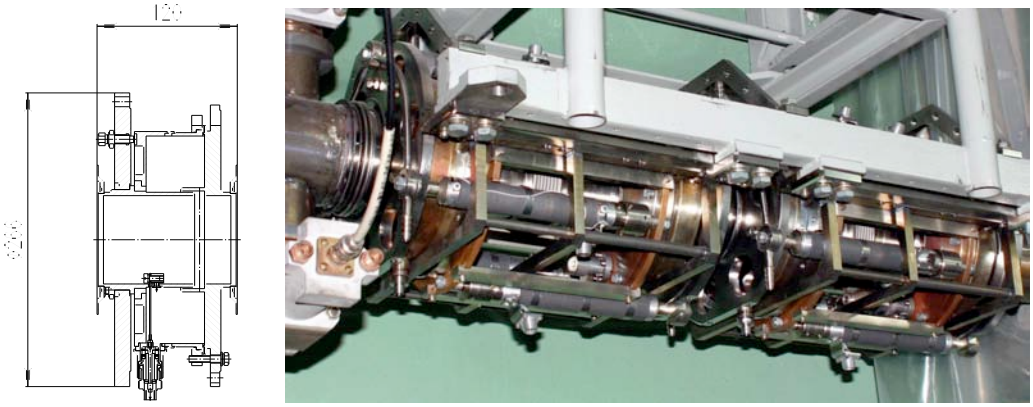

a) b)

**Figure 3:** (a) Cavity design, and (b) kicker photo.

There are two kickers in the system. One is for electrons and the other is for positrons. Each kicker consists of a pair of cavities. The main parameters of one cavity are given in Table 1. The cavity design is shown in Fig. 3a, and the photo of the kicker installed at VEPP-4M is shown in Fig. 3b.

**Table 1:** Main parameters of the kicker RF cavity.

| *Parameter* | *Symbol* | *Value* |
|---|---|---|
| central frequency | $f_c$ | 325.5 MHz |
| unloaded Q value | $Q_0$ | 7000 |
| loaded Q value | $Q_L$ | 1000 |
| characteristic impedance | $R/Q$ | 15 Ω |
| maximal RF voltage | $V_c$ | 1100 V |
| number of RF amplifiers | $N$ | 2 |
| RF amplifier power | $P_{max}$ | 100 W |

The high-order modes (HOM) of the kicker RF cavity are above the critical frequency of the vacuum chamber (2500 MHz). Therefore, there are no problems with the HOM-induced voltage.

The cavities are tuned to the frequency $f_c$ that is set in the middle between the operational harmonics. The distance between the cavities of each pair is 230 mm, which is a quarter-wavelength of $f_c$. The output power of the RF amplifier is divided by the 3 dB directional coupler and supplied to the cavities via the cables of an equal length. The connection is made so that for the particles of certain polarity ($e^+$ of $e^-$) moving in their proper direction, the RF voltage in the last cavity of the pair is delayed by $\pi/2$ relative to the first cavity. So, the particles of this polarity get a double kick, while for the particles moving in the opposite direction the effect of the kicker is zero. Therefore, the kickers for different sorts of particles are not coupled.

### 3.18.3 Commissioning Results

The decrement introduced by the feedback loop was measured using two methods. In both methods we excited the forced coupled mode oscillation by adding a signal of an external low-frequency (LF) generator into the feedback loop. By the adjustment of the LF generator frequency it is possible to achieve a rather stable oscillation of the mode.

In one method, the feedback loop was disabled by disconnecting the fast phase detector. Small amplitude $A_1$ of the excited mode oscillation was obtained with the output voltage $V_1$ of the LF generator. Then the feedback loop was closed and, as a result, the amplitude of oscillation was dropped to $A_2<A_1$. The voltage of the LF generator signal was increased to a certain value $V_2$ in such a way that the initial amplitude $A_1$ of the oscillation was obtained. The $V_2/V_1$ ratio determines a change of the oscillation decrement.

In the other method, we have measured the decay time of the mode oscillation by switching off the LF generator after the forced oscillation was excited. The frequency of the LF generator is 10.2 kHz. There are two electron bunches in the ring, each with the current of 0.5 mA. The oscillograms illustrating the decay time measurement are shown in Fig. 4. The LF generator voltage is displayed by trace 1, the phase of the anti-phase mode is displayed by trace 2. If the feedback is on, the decay time of the anti-phase mode is about 4 msec (Fig. 4a), if the feedback is off, the decay time is about 40 msec.

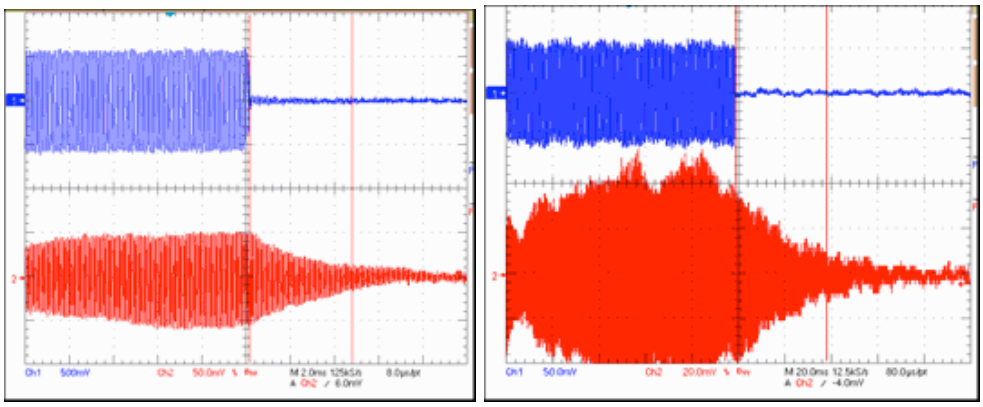

a) b)

**Figure 4:** Decay time measurement: (a) feedback on, (b) feedback off.

Practical test of the feedback system has been done with the real multi-bunch instability excited by special HOM tuning of the accelerating RF cavities. Fig. 5a shows

the oscillogram of the longitudinal profiles of the positron (upper graphs) and electron (lower graphs) beams with the excited oscillation and the feedback switched off, and Fig. 5b – with the feedback switched on. One can see the oscillation damping provided by the feedback.

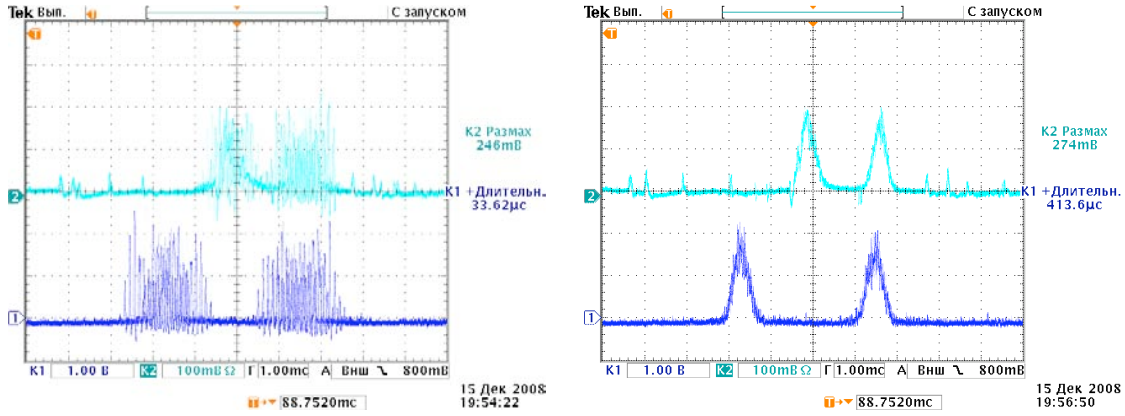


a) b)

**Figure 5:** Longitudinal beam profiles measured by the dissector tube:
(a) feedback off, (b) feedback on.

### 3.18.4 References

1. H. Wiedemann, “Particle Accelerator Physics II”, Springer-Verlag, 1995.
2. V.S. Arbuzov, et al. Feedback System for Damping of Longitudinal Bunch Oscillation in VEPP-4M Collider. Proc. of RuPAC 2006, Novosibirsk, Russia.

## 3.19 Beam Energy and Energy Spread Measurement by Compton Backscattering of Laser Radiation at the VEPP-4M Collider

V.E. Blinov, V.V. Kaminsky, E.B. Levichev, N.Yu. Muchnoi, S.A. Nikitin,
I.B. Nikolaev, A.G. Shamov, Yu.A. Tikhonov, V.N. Zhilich
Budker Institute of Nuclear Physics, Novosibirsk, Russian Federation
Mail to: N.Yu.Muchnoi@inp.nsk.su

### 3.19.1 Introduction

The accurate beam energy calibration in HEP experiments with colliders is important for particle mass measurements. In the “c-τ” energy region the masses of τ lepton, charmonium and charmed mesons are a matter of interest. Under the certain conditions the energy scale can be calibrated using the resonant depolarization technique (RD) [1]. This technique was implemented at the VEPP-4M collider [2] for experiments with the KEDR detector [3], allowing to measure particles masses with an ultimate accuracy [4]. However, RD can not measure the beam energy continuously along with the luminosity runs, so the beam energy behavior in time should be taken from the interpolation of the RD data points.

The beam energy calibration system described below is based on Compton backscattering of monochromatic laser radiation on the electron beam. It was implemented before at the SR storage rings BESSY-I and BESSY-II in Berlin [6, 7].

**The approach is based on the following items:**

**I.** The maximal energy of the scattered photon $\omega_{max}$ is strictly coupled with the electron energy ε due to the kinematics of Compton process:

$$\omega_{\max} \approx \frac{\varepsilon^2}{\varepsilon + \frac{m_e^2}{4\omega_0}},$$

where $m_e$ is an electron rest mass, $\omega_0$ is the laser photon energy. If one measures $\omega_{max}$, then the electron energy could be calculated:

$$\varepsilon = \frac{\omega_{\max}}{2}\left[1 + \sqrt{1 + \frac{m_e^2}{\omega_0 \omega_{\max}}}\right]$$

**II.** An ultimate energy resolution of contemporary commercial High Purity Germanium (HPGe) detectors provides the statistical accuracy in the beam energy measurement at the level of $\Delta\varepsilon/\varepsilon \approx (1 \div 2) \cdot 10^{-5}$ .

**III.** The systematical uncertainty is mostly defined by calibration of the detector energy scale. The accurate calibration is performed by monochromatic γ-rays from γ-active isotopes.

The system for precise beam energy and beam energy spread based on Compton scattering was built at VEPP-M to provide accurate data for the experiment in the τ lepton mass measurement, which was held by the KEDR team in 2005-2007 [3]. The method was verified using the multiple simultaneous measurements with the RD technique: both methods agree within $\Delta\varepsilon/\varepsilon \leq 3 \cdot 10^{-5}$ accuracy.

## 3.19.2 The Detailed Description of the Approach

### *3.19.2.1 Compton Scattering Kinematics*

Kinematics of photon-electron scattering is defined by the equation:

$$p + k_0 = p' + k, \tag{1}$$

where $p = [\varepsilon, \vec{p}]$, $k_0 = [\omega_0, \vec{k}_0]$ are the four-momenta of the initial and $p' = [\varepsilon', \vec{p}']$, $k = [\omega, \vec{k}]$ of the final electron and photon, respectively.

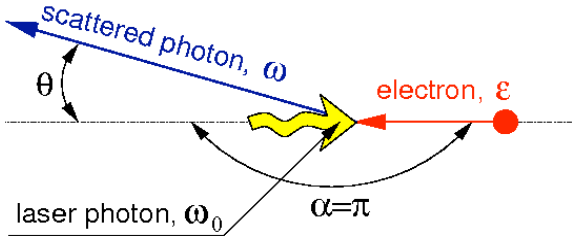


**Figure 1:** Compton scattering kinematics.

From equation (1) the scattered photon energy can be written as follows:

$$\omega = \omega_0 \frac{1-\beta\cos\alpha}{1-\beta\cos\theta+\frac{\omega_0}{\varepsilon}\left(1-\cos\Theta\right)}, \tag{2}$$

where β is the electron velocity in units of c, α is the angle between initial electron and initial photon, θ is the angle between initial electron and final photon, Θ is the angle between initial and final photons.

When the angle between momenta of initial electron and final photon is equal to zero (θ = 0 and Θ = α), the energy of the scattered photon becomes maximal:

$$\omega_{\max} = \omega_0 \frac{1-\beta\cos\alpha}{1-\beta+\frac{\omega_0}{\varepsilon}\left(1-\cos\alpha\right)}, \tag{3}$$

When low-energy photon is scattering on relativistic electron ( $\varepsilon >> m_e >> \omega_0$ ):

$$\omega_{\max} \approx \frac{\varepsilon^2 \sin^2\left(\frac{\alpha}{2}\right)+\frac{m_e^2}{4}\cos\alpha}{\varepsilon \sin^2\left(\frac{\alpha}{2}\right)+\frac{m_e^2}{4\omega_0}}. \tag{4}$$

For head-on collision (α is close to π):

$$\omega_{\max} \approx \frac{\varepsilon^2}{\varepsilon+\frac{m_e^2}{4\omega_0 \sin^2\left(\frac{\alpha}{2}\right)}}. \tag{5}$$

The energy spectrum of scattered photons has a sharp edge at maximal energy $\omega_{max}$.

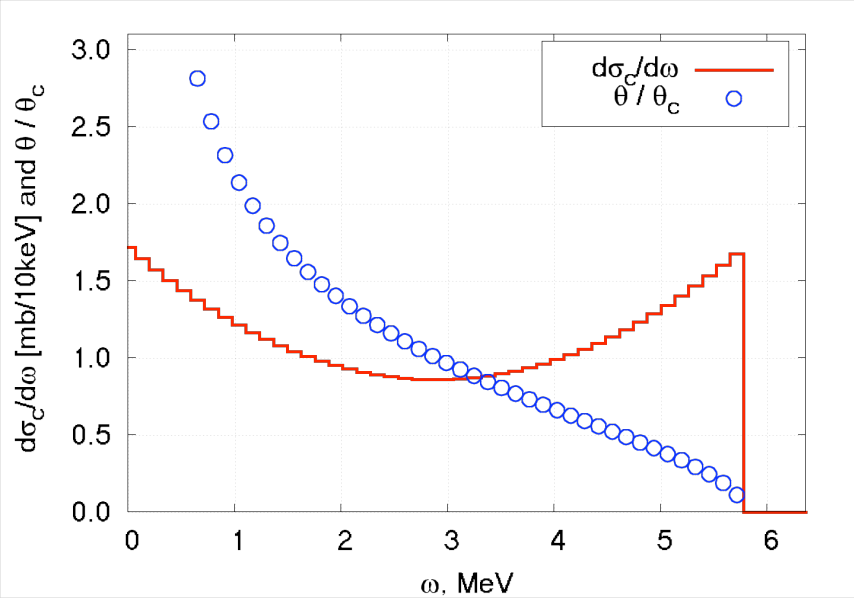


**Figure 2:** Red solid line shows the photon energy spectrum. Blue circles are the photon scattering angle θ in units of $\theta_c$ ($\theta_c \sim 1/\gamma \equiv m/\varepsilon$) versus its energy. Photon energy $\omega_0 = 0.12$ eV, electron energy $\varepsilon = 1777$ MeV, scattering angle $\alpha = \pi$.

From Figure 2 one can see that the scattered photons with the energies close to $\omega_{max}$ propagate along the initial electron trajectory.

### *3.19.2.2 Measurement of the Beam Energy and Beam Energy Spread*

It is possible to obtain the initial electron energy by measuring the maximal energy of the scattered photon:

$$\varepsilon = \frac{\omega_{\max}}{2}\left[1 + \sqrt{1 + \frac{m_e^2}{\omega_0 \omega_{\max} \sin^2(\alpha/2)}}\right]. \qquad (6)$$

Under the actual experimental conditions the abrupt edge of the scattered photons energy distribution is smeared due to the following effects:

- energy spread in the electron beam $\delta\varepsilon/\varepsilon$,
- the width of laser radiation line $\delta\omega_0/\omega_0$,
- energy resolution of the e detector $\delta r/r$,
- angular distribution of initial particles.

Taking into account these contributions the visible edge width can be written as:

$$\sigma_\omega \equiv \frac{\delta\omega_{\max}}{\omega_{\max}} \approx 2\frac{\delta\varepsilon}{\varepsilon} \oplus \frac{\delta\omega_0}{\omega_0} \oplus \frac{\delta r}{r} \oplus \frac{\delta\alpha}{\tan(\alpha/2)}. \qquad (7)$$

The last term is negligible when $\alpha \sim \pi$. It will be shown below that the laser radiation bandwidth is also very small. The relative accuracy is then:

$$\frac{\Delta\varepsilon}{\varepsilon} \approx \frac{1}{2}\left(\frac{\Delta\omega_0}{\omega_0} \oplus \frac{\Delta\omega_{\max}}{\omega_{\max}}\right). \tag{8}$$

The energy spread of the electron beam could be determined if the width of the spectrum edge is measured and the detector energy resolution is known:

$$\sigma_\varepsilon \equiv \frac{\delta\varepsilon}{\varepsilon} \approx \frac{1}{2}\sqrt{\left(\frac{\delta\omega_{\max}}{\omega_{\max}}\right)^2 - \left(\frac{\delta r}{r}\right)^2}. \tag{9}$$

The statistical accuracy for the beam energy spread measurements is defined as:

$$\frac{\Delta\sigma_\varepsilon}{\sigma_\varepsilon} \approx \frac{\sigma_\omega d\sigma_\omega \oplus r dr}{\sigma_\omega^2 - r^2}. \tag{10}$$

### 3.19.3 Experimental Setup

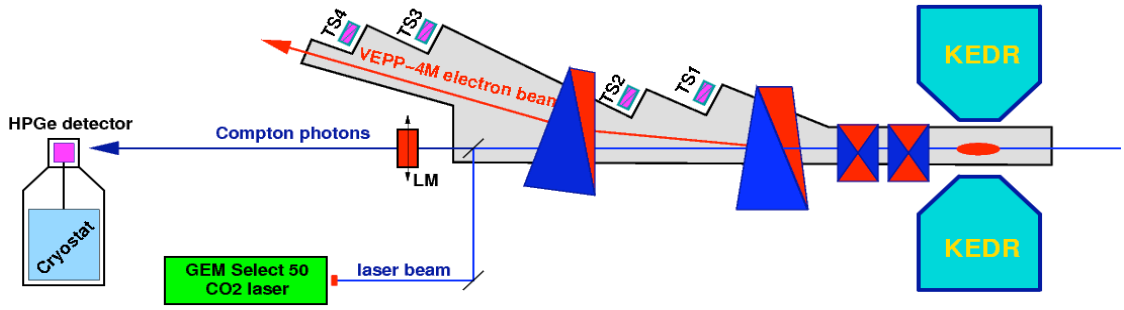


**Figure 3:** Layout (not in scale) of the beam energy monitoring system at the VEPP-4M collider. TS1-TS4 are the modules of the KEDR registration system of scattered electrons.

The experiment layout is shown in Figure 3. The laser beam propagates through the system of focusing lenses and enters the VEPP-4M vacuum chamber through the infrared transparent ZnSe window. It interacts with the electron beam in the 12 m length straight section of the VEPP-4M collider. The backscattered high-energy photons propagate towards the HPGe detector. The laser spot size in the interaction area is about 2 mm, approximately 10 times larger than the electron beam horizontal transverse size. This was done to ensure that all of the beam electrons have equal probability to scatter on the laser target and we measure *the average energy of beam electrons*.

This location was chosen as it has already been used for the laser-electron interactions [7, 8], the laser-to-vacuum insertion module already existed, so only minor changes were necessary to adopt it for the IR laser radiation. However, it is evident that the electron-positron collisions inside the KEDR detector will produce a huge background of high-energy photons to the HPGe detector.

The LM module shown in Figure 3 is the KEDR luminosity monitor. It is the lead-plastic scintillation sandwich with the overall radiation length of 13.5 $X_0$. The unit is mounted on a movable support with two positions: a) when there is no electron-positron

collisions the unit is out of the beam allowing the backscattered photons to hit the HPGe-detector; b) in a collision mode the luminosity monitor intersects the beam line and registers high-energy bremsstrahlung γ-rays. In b) mode the HPGe detector is well protected from high-energy γ-rays, but a small amount of backscattered γ-rays with a few MeV energies survives and this amount is sufficient to measure the beam energy during the luminosity runs.

The mirror outside the vacuum chamber in Figure 3 is mounted on the special support, so that its X- and Y- angles can be precisely adjusted by two stepping motors. The control over the mirror is in feedback with the HPGe counting rate measurement system. This feedback system always keeps the maximum counting rate of backscattered photons via fine angular adjustments in order to guarantee that the laser and electron beams collide centrally.

#### *3.19.3.1 $CO_2$ Laser as a Source of Reference Energy Rradiation*

The most convenient source of photons for the beam energy calibration system is the infrared $CO_2$ laser [9]. $CO_2$ lasers typically emit photons with $\lambda$=10.6μm, but there are other lines in the region of 10-11 μm (see Figure 4). Usually, the laser can radiate photons spontaneously at different neighboring lines or even at several lines simultaneously.

As the relative distance between the neighboring lines $\Delta\nu/\nu \sim 0.2$ %, it is essential to have the laser operating at only one vibration-rotation transition in $CO_2$ molecule. The width of each line is formed by Doppler and collision widening with ~ 100 MHz bandwidth ($\Delta\nu/\nu \sim 3$ ppm). Homogenization of the radiation wavelength occurs due to several longitudinal cavity modes and, finally, the average laser photon energy is as stable as $\mathbf{\Delta\nu/\nu < 0.1}$ **ppm**.

The GEM Selected 50$^{TM}$ laser by COHERENT Inc., USA, was chosen for our facility. It is a 50 W CW power, single line $TEM_{00}$ laser ($M^2$ <1.1) operating at 10P20 optical transition with $\lambda$ = 10.591035 μm ($\omega_0$ = 0.117065223 eV).

The laser was put into operation in April 2005. Since then it has been switched on for an integral of ~ 18.000 hours, and no parameter degradation has been observed yet.

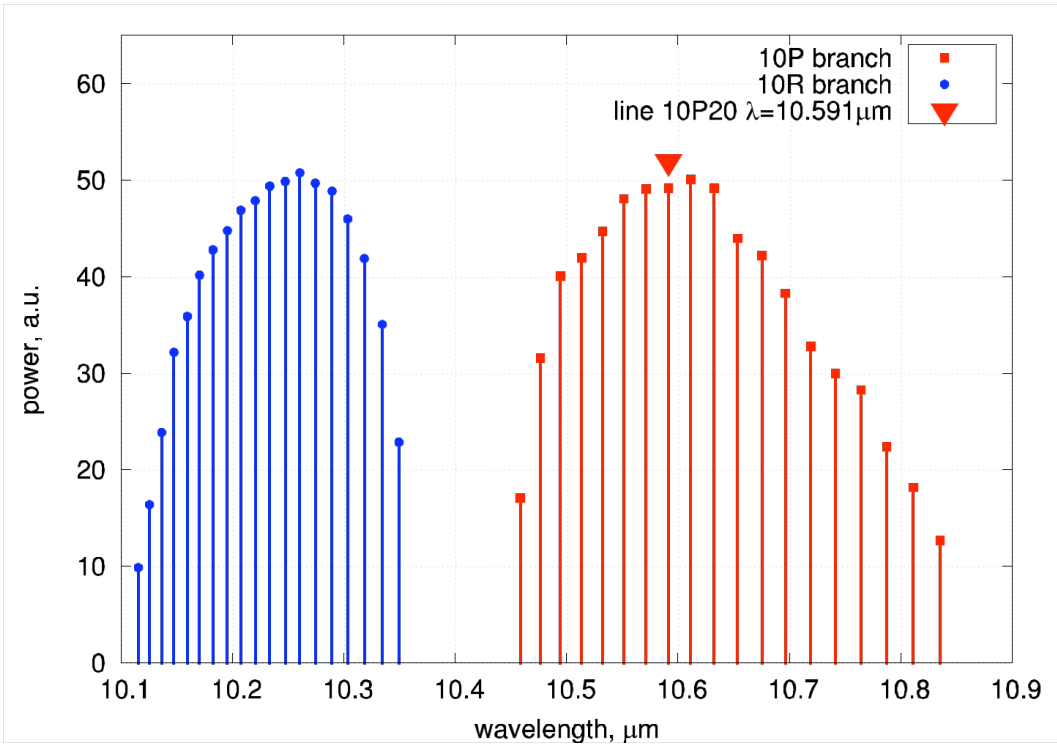


**Figure 4:** Spectrum of $CO_2$ molecule transitions.

### *3.19.3.2 HPGe Semiconductor Detector*

HPGe detector is a large germanium diode of the p-n or p-i-n type operating in the reverse bias mode [10]. At a suitable operating temperature (normally 85 K), the barrier created at the junction reduces the leakage current to acceptably low values. Thus, an electric field can be applied that is sufficient to collect the charge carriers liberated by the ionizing radiation.

The energy lost by ionizing radiation in semiconductor detectors ultimately results in the creation of electron-hole pairs. The average energy $\xi$ , necessary to create an electron-hole pair in a given semiconductor at a given temperature, does not depend on the type and the energy of the ionizing radiation. The value $\xi$ is 2.95 eV in germanium at 80 K. The low value of $\xi$ compared with the average energy necessary to create an electron-ion pair in a gas (typically 15 eV to 30 eV) results in the superior spectroscopic performance of semiconductor detectors.

We used the coaxial type HPGe detector with ~ 120 $cm^3$ active volume. It has ~ 5% total photo-absorption efficiency for γ-rays with the energies from 5 to 6 MeV.

### *3.19.3.3 Reference γ-Rays used for HPGe Detector Calibration*

In Table 1 there is a list of γ-ray sources used for calibration of the HPGe detector energy scale and resolution in the range from 0.5 MeV to 3 MeV [11]. For the energy calibration at higher energies of the detector a $^{238}Pu/^{13}C$ - source was ordered. The α-particles from the $^{238}Pu$ decay lead through the $^{13}C(\alpha,n)$-$^{16}O$ reaction to $^{16}O$ in an excited nuclear state. The 6.12863(4) MeV γ-decay line of this excited state would help to perform the energy scale calibration at higher energies.

**Table 1:** γ-ray isotopes used for calibration.

| *Source* | *Half-life* | $E_\gamma$, *keV* | $\pm\Delta E_\gamma$, *eV* | $I_\gamma$, *%* |
|---|---|---|---|---|
| $^{24}$**Na** | 14.96 h | 1368.625<br>2754.008 | 5<br>11 | 99.99<br>99.86 |
| $^{60}$**Co** | 5.2714 y | 1173.228<br>1332.492 | 3<br>4 | 99.86<br>99.98 |
| $^{137}$**Cs** | 30.07 y | 661.657 | 3 | 85.1 |
| $^{228}$**Th**<br>with decay daughter isotopes | 1.9131 y | 583.187<br>2614.511 | 2<br>10 | 30.6<br>35.86 |

### 3.19.4 Data Taking and Analysis

The HPGe signal pulses from the charge sensitive preamplifier are processed by the spectrometry station, including DSP and a spectrum storage buffer. Then the spectrum data are transferred into PC for further analysis. The analysis is performed with ROOT software package [12]. In the real experimental conditions we require not less than $10^6$ events in the measured spectrum of Compton backscattered γ-rays to have enough statistics near the spectrum edge for further processing.

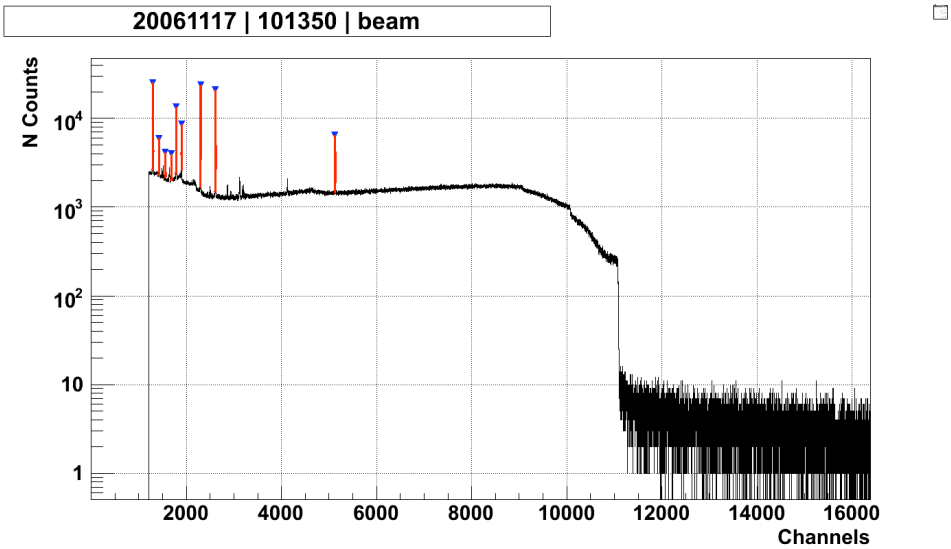


**Figure 5:** Energy spectrum of backscattered photons measured by coaxial HPGe detector Canberra GC2518 (November 17, 2006). Electron beam energy $E_{beam}$ = 1777 MeV, acquisition time t ~ 1 hour, spectrum integral I=1.5*$10^7$ counts.

On the left of the spectrum one can see calibration peaks, the edge is also clearly seen near 11000 channel.

#### *3.19.4.1 HPGe Detector Energy Scale Calibration*

The available γ-ray calibration sources provide photons with a maximum energy of 2750 keV (see Table 1). The photon energies at the spectrum edge are close to 6000 keV. Calibration of the energy scale near the edge can be done in two ways: by extrapolation of the low energy data or by using the RD data of the VEPP-4M beam

energy. It was found that extrapolation leads to ~ 100 keV difference between the beam energy measurements by Compton scattering and RD. To reduce this error, the RD measurements were used to determine nonlinear terms in HPGe energy scale calibration for different time periods. To avoid this problem in future applications we suppose to use 6.13 MeV γ-quanta source, which we do not have yet. Another promising possibility of the HPGe energy scale calibration is an application of the precise pulse generator [13]. In the nearest future we hope to solve the problem of the independent energy scale calibration using both the source and the pulse generator, which we are waiting to obtain soon.

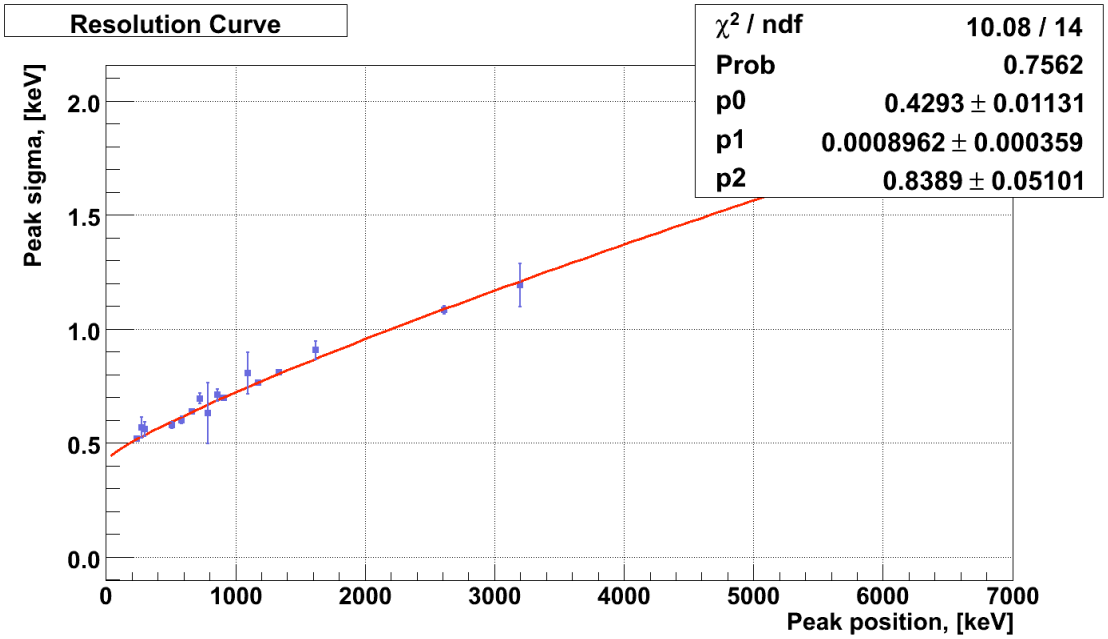


**Figure 7:** Energy resolution of the HPGe detector vs. photon energy.

The energy resolution of the HPGe detector is defined by the calibration peaks width (σ). The dependence of the resolution from the photon energy is shown in Figure 7. It is well described by a power function:

$$R(x, p_{0..2}) = p_0 + p_1 \cdot x^{p_2}. \tag{11}$$

### *3.19.4.2 Edge Parameters Determination*

The determination of the edge parameters is performed via fitting the spectrum shape by the following function:

$$g(x, p_{0...5}) = \frac{p_4(x - p_0) + p_2}{2} erfc\left[\frac{x - p_0}{\sqrt{2}p_1}\right] - \frac{p_1 p_4}{\sqrt{2\pi}} \exp\left[-\frac{(x - p_0)^2}{2p_1^2}\right] + \tag{12}$$

$$+ p_5(x - p_0) + p_3$$

The parameters meanings are: $p_0$ is the edge position, $p_1$ is the edge width, $p_2$ is the edge height, $p_3$ is the left slope, $p_4$ the background level, $p_5$ is the background slope.

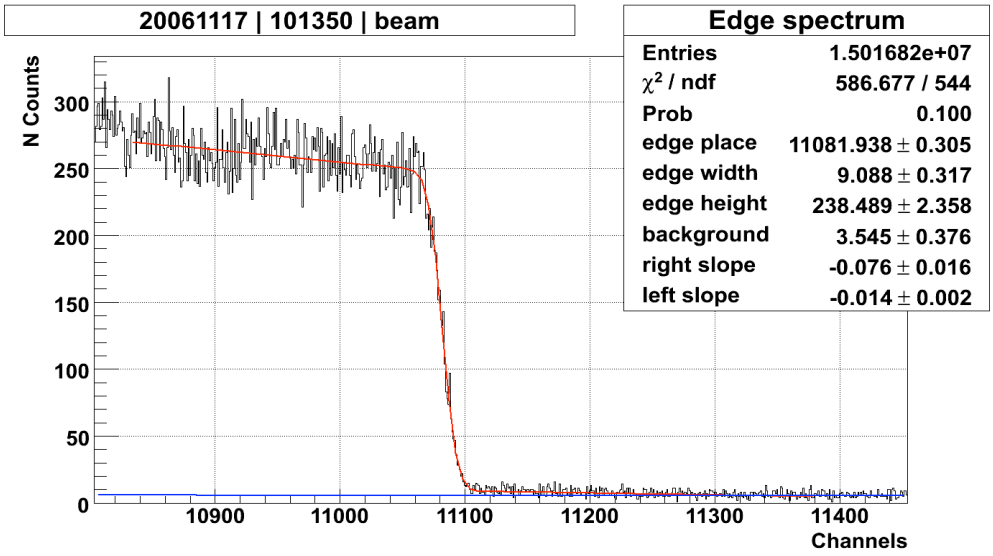


**Figure 8:** Energy spectrum of backscattered photons measured by the HPGe detector.

In Figure 8 the experimental spectrum is shown with the fitting applied to its edge. From the fit parameters one can see that the "edge place" parameter is determined with a relative statistical accuracy $<3\cdot10^{-5}$, while the "edge width" parameter has a statistical uncertainty of about 3%. These parameters are used to obtain on-line data about the VEPP-4M beam energy and beam energy spread.

### *3.19.4.3 VEPP-4M On-Line Beam Energy Monitor*

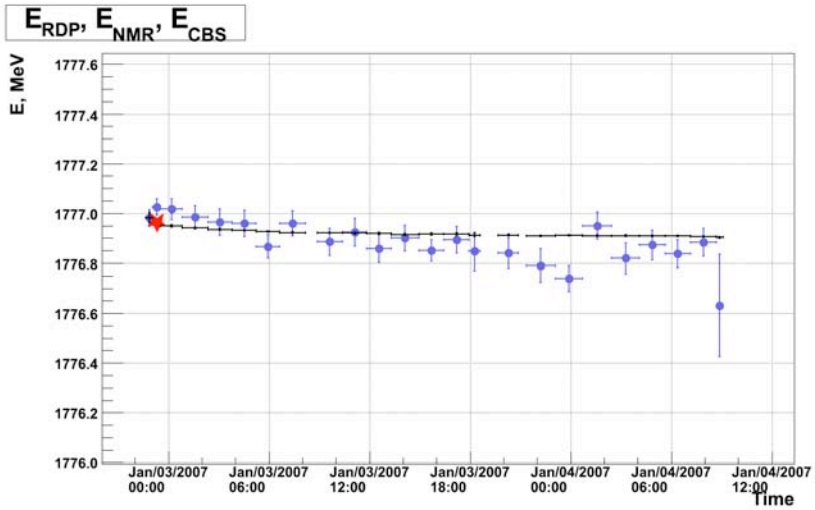


**Figure 9:** Beam energy vs time on-line

During the τ lepton mass measurement experiment the Compton beam energy monitor was providing the on-line information like it is shown in Figure 9. The red star

at the beginning of the plot is the RD measurement. The blue circles with error bars are the Compton energy monitor results. The black lines are RD extrapolation by the NMR probe measurements of the VEPP-4M guide field.

### 3.19.5 Results and Discussion

The luminosity taking for the τ lepton mass measurement experiment was performed in several runs during the time period from 2005 to 2007. Along the whole experiment there were more than 150 simultaneous energy measurements by the RD technique and the Compton beam energy monitor (further – CBS approach) in the beam energy range $E_{beam}$ = 1777 ± 10 MeV (near the threshold of the $e^+e^- \rightarrow \tau^+\tau^-$ reaction).

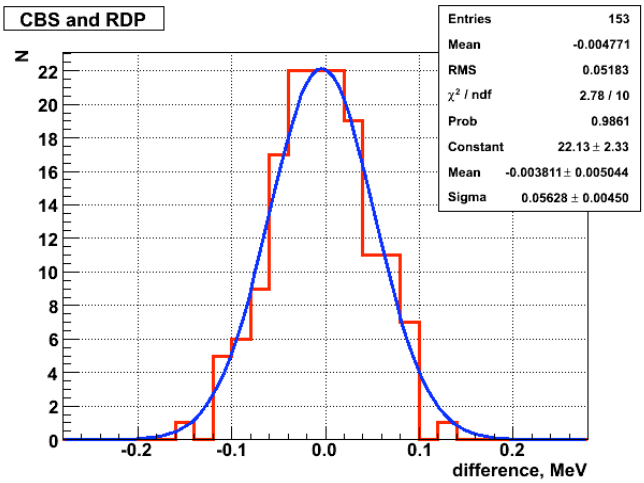


**Figure 10:** The difference ($E_{RD}$-$E_{CBS}$) between two approaches for 153 simultaneous measurements performed during the 2005-2007 at $E_{beam}$ = 1777 ± 10 MeV.

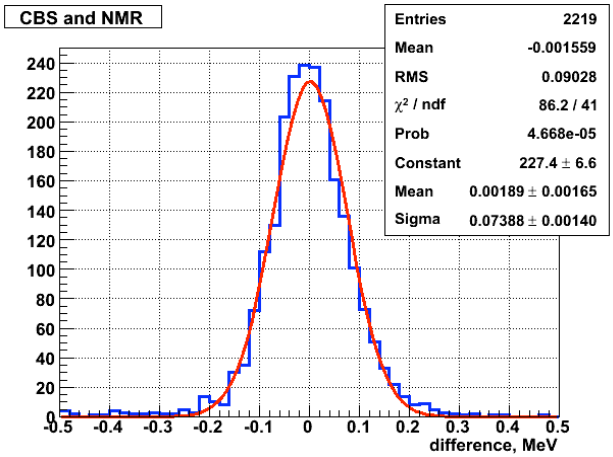


**Figure 11:** The difference ($E_{interpolation}$-$E_{CBS}$) during the 2005-2007 run at $E_{beam}$ = 1777 ± 10 MeV.

The histograms in Figures 10, 11 may be used to estimate the systematical errors in the beam energy measurement by Compton backscattering of laser light (CBS

approach). The RD measurements may be considered as reference values, since their uncertainties are much smaller than for the CBS approach. The total uncertainty for Compton measurements consists of its statistical and systematical components:

$$s_{histogram} = \sqrt{s_{stat}^2 + s_{syst}^2} \tag{13}$$

The average statistical error of the Compton energy measurement, included to the histogram in Figure 10, is about 40 keV. Estimation of the CBS approach systematic uncertainty from equation (13) gives $\sigma_{syst} \sim 30$ keV. At the beam energy $E_{beam} \sim 1777$ MeV this gives the relative error $\Delta E_{beam} / E_{beam} \sim 2 \cdot 10^{-5}$.

However, histogram in Figure 11 has larger RMS value, giving the upper-level estimation for systematical uncertainty in the beam energy determination during the KEDR luminosity runs. This uncertainty is about 60 keV, or $\Delta E_{beam} / E_{beam} \sim 3.4 \cdot 10^{-5}$.

Every beam energy measurement by CBS approach provides the value of the beam energy spread. These values for the same conditions ($E_{beam} = 1777 \pm 10$ MeV) and same period of time (2005-2007) are presented in a histogram on Figure 12.

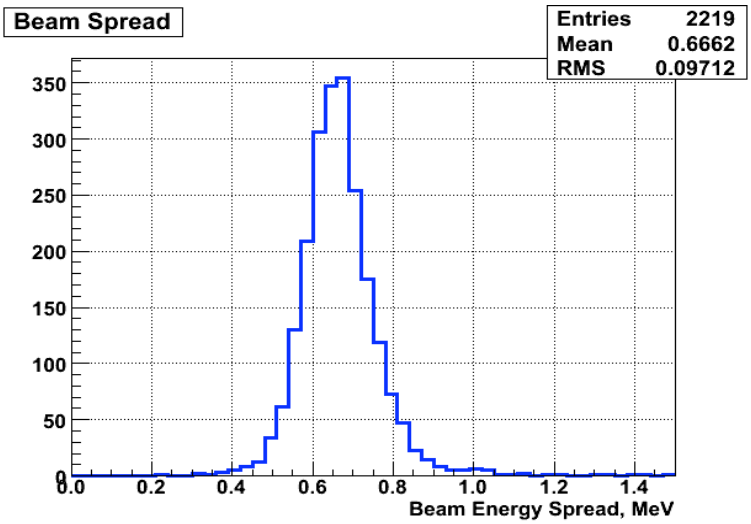


**Figure 12:** Beam energy spread was measured by determination of the edge width in the energy spectrum of backscattered laser photons.

### 3.19.6 References

1. A.N. Skrinsky, Yu.M. Shatunov, "Precision measurements of masses of elementary particles using storage rings with polarized beams", Sov. Phys. Usp. 32 : 548-554, 1989, Usp. Fiz. Nauk 158 : 315-326, 1989
2. V.E.Blinov, A.V.Bogomyagkov, V.P.Cherepanov, V.A.Kiselev, E.B.Levichev, A.S.Medvedko, S.A.Nikitin, I.B.Nikolaev, A.G.Shamov, E.I.Shubin "Beam Energy Measurements at VEPP-4M Collider by Resonant Depolarization Technique", this issue.
3. By KEDR Collaboration (V.V. Anashin et al.), "Measurement of the tau lepton mass at the KEDR detector", JETP Lett. 85 : 347-352, 2007.

4. By KEDR Collaboration (V.M. Aulchenko et al.), “New precision measurement of the J / psi and psi-prime meson masses” Phys. Lett. B 573 : 63-79 , 2003.
5. R. Klein, R. Thornagel, G. Ulm, T. Mayer, P. Kuske “Beam diagnostics at the BESSY I electron storage ring with Compton backscattered laser photons: Measurement of the electron energy and related quantities” Nucl. Instrum. Meth. A384 : 293-298, 1997.
6. R. Klein, R. Thornagel, G. Brandt, G. Ulm, P. Kuske, R. Gorgen. “Measurement of the BESSY II electron beam energy by Compton-backscattering of laser photons” Nucl. Instrum. Meth. A486 : 545-551, 2002
7. G.Ya. Kezerashvili, A.M. Milov, N.Yu. Muchnoi, A.P. Usov. “A Compton source of high-energy polarized tagged gamma-ray beams. The ROKK-1M facility.” Nucl. Instrum. Meth. B145:40-48, 1998.
8. V.M. Aulchenko et al. “Detector KEDR tagging system for two photon physics” Nucl. Instrum. Meth. A379 : 360-362, 1996.
9. http://www.rp-photonics.com/co2_lasers.html
10. http://www.ortec-online.com/
11. Gamma-ray Energy and Intensity Standards.
12. http://root.cern.ch
13. http://www.berkeleynucleonics.com/products/model-pb5.html

## 3.20 Study of the Possibility of Increasing the Accuracy of CPT Invariance Test at Electron-Positron Storage Rings

V. Blinov, A. Bogomyagkov, G. Karpov, V. Kiselev, E. Levichev,
S. Nikitin, I. Nikolaev, E. Shubin, G. Tumaikin
BINP, Novosibirsk, Russia
Mail to: nikitins@inp.nsk.su

### 3.20.1 Introduction

This work is devoted to preparation of the experiment for the CPT invariance test at an electron-positron storage ring. CPT theorem [1, 2] is one of the most fundamental regulations of the quantum field theory. This theorem predicts that the g-factors, masses, charges, and absolute values of magnetic and electric dipole moments of particle and anti-particle are equal [3]. Despite the fact that all present models of particles are CPT invariant, now and then the experiments on increasingly accurate testing the CPT theorem are carried out. In the experiment under consideration, the CPT invariance test will be based on a precise comparison with an accuracy of ~ $10^{-10}$ of spin precession frequencies of electrons and positrons simultaneously circulating in a storage ring. At that, the spin precession frequency is determined through the combination of the anomalous magnetic moment, charge $e$ and mass $m$. Therefore, at one time just three fundamental parameters of electron and positron are compared in only one measurement. Resonant depolarization technique (RD) proposed and for the first time realized at BINP [4] is used to measure the spin precession frequency of particle.

In our experiments at the VEPP-4M storage ring we set ourselves to study a principle possibility to make the CPT invariance test at the electron-positron storage rings with the error mentioned above and realize it with an accuracy, at the least, of ~$10^{-8}$. The first results with a record accuracy of $2 \cdot 10^{-8}$ obtained in comparison of depolarization frequencies of two electron bunches (“electron-electron comparison”)

were reported in [5]. Some sources of systematic errors, which can affect the comparison of spin frequencies of electrons and positrons, were considered.

In the present paper we describe the new record advantages in our experiments on electron-electron comparison including minimization of a statistic error and the measures on some storage ring parameter stabilization required to decrease a systematic error. More information is given about the instrumentation. Preliminary results on measurement of the dependence of spin frequency on the bunch current are presented. The status of the "electron-positron comparison" experiment being as yet at the primary stage is described.

### 3.20.2 Method for CPT Invariance Test

In an ideal storage ring an anomalous part of the spin precession frequency relates to the guide field averaged over the machine azimuth $< H >$ through the equation $\Omega = \nu\Omega_0 = q' < H >$, $q'=(g-2)/2\cdot(e/mc)$. If the electron and positron bunches circulate simultaneously in the same ring, they anyway have the same revolution frequency $\Omega_0 = \Omega_0^+ = \Omega_0^- = e^{\pm}c < H/E >_{\pm}$ imposed by the RF system (here $E$ is a beam energy, $\pm$ is a sign of particle). The closed orbits of electrons and positrons are not coincident, even in an ideal storage ring not containing any static electric fields but having mirror symmetry of its magnetic structure relative to an axis passing through the RF cavity. Just in this case the orbits are reciprocally symmetrical. The reason is in a presence of distributed energy losses and a local energy recovery in the RF cavity. Ideally, in the case of the CPT invariance the equalities $< H/E >_+ = < H/E >_-$ as well as $< H >_+ = < H >_-$ take a place. Generally, under the assumption that the electron charge and mass are not identical with positron ones ( $e^- \neq e^+$ and $m_- \neq m_+$), the closed orbits of electrons and positrons differ from the reciprocally symmetrical orbits noticed above. Thus, the average fields along the orbits of opposite in sign particles also mismatch: $< H >_+ \neq < H >_-$. Besides, it is not improbable that $q'_+ \neq q'_-$. Therefore, it is possible to examine CPT invariance by measuring the frequency difference $\Delta\Omega = \Omega_+ - \Omega_- = q'_+ < H >_+ - q'_- < H >_-$. But the question is: what an accuracy of the mirror symmetry for the storage ring must one provide to exclude systematic errors in $< H >_{\pm}$? This problem is partially discussed in [5].

There are two known experiments, in which the highest accuracies were obtained in comparison of anomalous magnetic moments of electron and positron. The results are shown in Table 1 where $\Delta_q = 2\cdot|q'_+ - q'_-|/(q'_+ + q'_-)$.

**Table 1:** Accuracy of the AMM experiments at 95% CL.

| *Year* | *Group* | $\Delta_q$ |
|---|---|---|
| 1987 | BINP, VEPP-2M | $< 10^{-8}$ |
| 1987 | R Van Dyck et al. | $< 3\cdot10^{-9}$ |

Methods applied in these experiments differ from a direct comparison of depolarization frequencies. In [6] the final polarization a degree of the electron and

positron bunches was compared after the adiabatic spin resonance crossing (with flipping of spins). The authors interpreted their results as the anomalous magnetic moment (AMM) comparison with an accuracy of $10^{-8}$ assuming equality of charges and masses of electron and positron. In [7] the ratio $(g-2)/2$ was measured separately for electron and positron captured in the Penning trap. Their result corresponds to the $3\cdot 10^{-9}$ relative accuracy in AMM comparison.

### 3.20.3 Resonant Depolarization Technique at VEPP-4M

The system of absolute calibration of the particle energy at VEPP-4M by measuring the average spin precession frequency in the beam includes a polarimeter based on IBS (Intra-Beam-Scattering) effect and TEM wave-based depolarizer [5, 8-10].

#### *3.20.3.1 Transverse Field Depolarizer*

TEM wave is generated with the help of two parallel, vertically-spaced conductive plates connected to a variable-frequency RF generator (see Figure 1). The type of connection corresponds to a stationary wave formation at the plates; this provides a concurrent action of the depolarizer with an equal efficiency on electrons and positrons. The frequency is set by a BINP-developed computer-controlled synthesizer with an ultimate resolution for a frequency step better than $6\cdot 10^{-7}$ Hz. The reference frequency signal for the synthesizer is generated by the rubidium frequency standard with frequency stability better than $10^{-10}$.

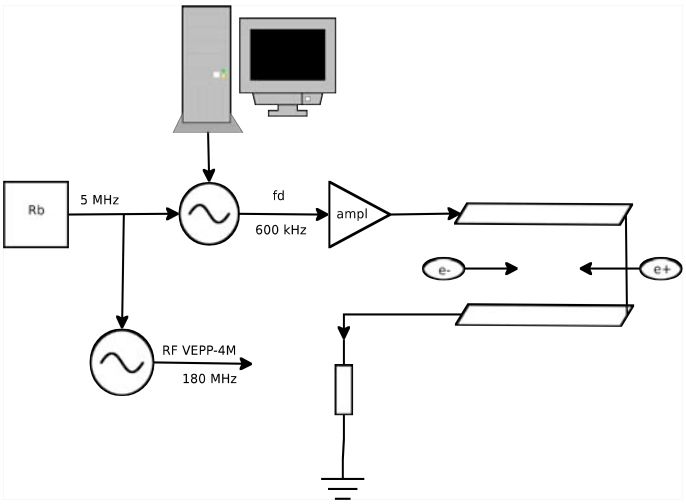


**Figure 1:** Control of the depolarizer.

To examine the intrinsic line width of synthesizer we performed the special experiment with two identical synthesizers on measurement of their phase noises close to the carrier. The scheme of the experiment is shown in Figure 2. Output frequency of both synthesizers = 1MHz. Direct digital synthesizers DDS1 and DDS2 use a common reference source of 30 MHz frequency. Internal multiplier of each synthesizer raises the reference frequency from 30 to 180 MHz. Orthogonal signals of DDS2 are used for quadrature mixing with the DDS1 signal. Output low frequency signals of mixer enter two 20-bit Analog-to-Digital Converters integrating over 320 millisecond time interval. The result of the experiments is represented in Figure 3 as a spectrum of noise power

per 1 Hz band normalized to the carrier-frequency power in dBc/Hz. In particular, this quantity is -30 dBc at $10^{-4}$ Hz offset from the carrier. If the depolarization process lasts more than ten seconds, like in our case, the relative noise power becomes even smaller: less than -40 dBc. It is rather small. In our case of the so-called "super-fine scan" experiments, we scan the depolarizer frequency $f_d$ with a rate $\dot{f}_d = df_d / dt = 10$ mHz/sec and a step of 20 mHz, which formally corresponds to a relative frequency resolution of $5 \cdot 10^{-9}$. A “dynamic” broadening of the depolarizer line is $\delta f_d \sim \sqrt{\dot{f}_d} \sim 10^{-1}$ Hz or 50 eV or $2.5 \cdot 10^{-8}$ in relative units. Because of the broadening of spin and depolarizer line widths we compare the related depolarization frequencies rather than the spin ones. This does not contradict our aims because of the same conditions for electrons and positrons. In practice, the mentioned dynamic broadening of the depolarizer line also does not matter since its width proves to be much less than the spin line one.

#### *3.20.3.2 IBS-based Polarimeter*

The quantity $S = 1 - (dN_1 / dt)/(dN_2 / dt)$ denoted in the figures below as *Delta* is determined through the ratio between the counting rates of scattered electrons from a unpolarized bunch $(dN_2 / dt)$ and a polarized one $(dN_1 / dt)$. In the simplest configuration of the registration system, the counting rates are measured with the help of two scintillation counters entered inside the vacuum chamber from its opposite sides at the median plane. Every counter registers mainly the Touschek particles i.e. electrons (positrons) experienced IBS. The fraction of such registered particles achieves a great extent: 70-80%. By this reason we can use just a simple sum of counter data to increase statistics. The beam depolarization event is observed by the related jump in *S*, which is practically proportional to a square of the polarization degree and is of an order of 1%. Recently we started two new Touschek registration systems at VEPP-4M forming together with the old one a distributed detecting system. The total counting rate of the counters increased from 0.1-0.2 MHz with the old system up to 1-2 MHz with the new one per a 2 mA bunch current. We use the following combinations of simultaneously circulating bunches of the same sign. "Two bunches" or “1+1” mode is the case of one polarized and one unpolarized electron bunches, which are equalized in current. "2+1" mode is the case of two polarized and one unpolarized bunches. The latter serves for normalization of the counting rate. Two pairs of electron bunches are used in the "2+2" mode. Each pair represents the "1+1" case. The "2+2" mode is suitable to study the systematic error depending on bunch current if the pairs differ in this parameter.

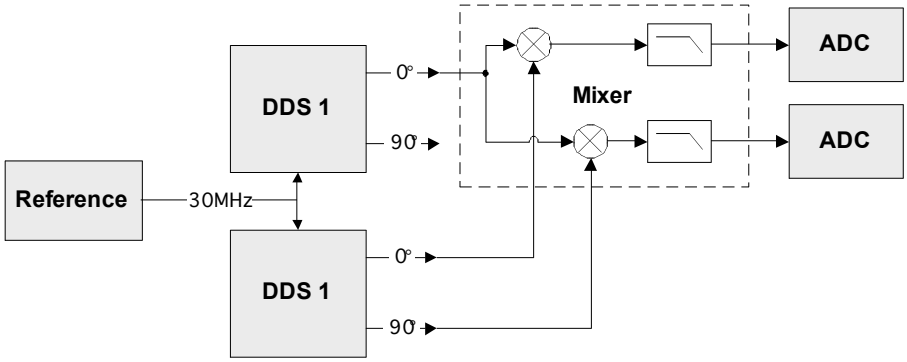


**Figure 2:** Measurement of the synthesizer noise performance (bench-test scheme).

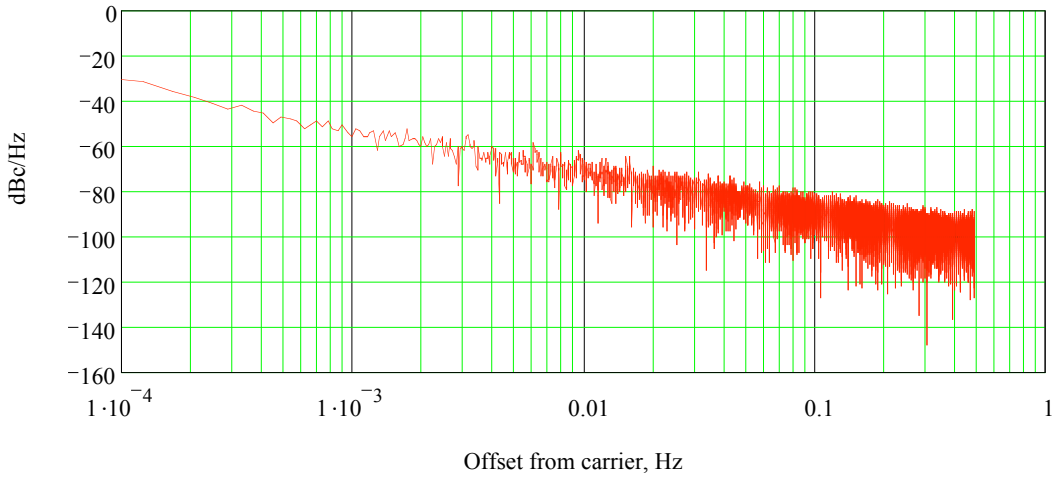


**Figure 3:** Residual phase noise of the DDS synthesizer at 1 MHz output frequency (without reference oscillator noise contribution).

### 3.20.4 NMR Magnetometer-based Field Stabilization System

With the purpose to increase stability of the bend magnet field at VEPP-4M, an additional feed back loop including the precision NMR magnetometer has been created. NMR magnetometer measures a field in the reference magnet, which is similar to the main arc bend magnets and connected in series with them. The relative accuracy of the magnetic field measurement by the NMR magnetometer is of the order of several unities by $10^{-7}$. The field stabilization feedback loop, besides the NMR magnetometer, includes a digital-analog converter (DAC) and a direct current transformer (DCCT). When the system is on, the magnetometer measures a deviation of the field from a reference value and forms an error signal by issuing a corresponding voltage to the DAC. This error voltage enters the DCCT of the bend magnet power supply and causes such a change in the current, which compensates the field deviation from the reference value. Owing to the additional feedback loop, the control field band is about $\pm 10^{-4}$; the feedback band is about 0.1 Hz, i.e. the ripples of a period more than 10 seconds are

suppressed. The developed stabilization system enables a long-term field non-stability to be reduced to a level of $10^{-6}$ (see Figure 4). Day-to-day beam energy drift with the field feedback loop turned on is of an order of 1 keV as it has been shown in our long-term energy stability runs using RD. Earlier the similar field stabilization systems using NMR magnetometer were applied at CERN and VEPP-2M. But an accuracy of $10^{-6}$ in comparison of the field and actual beam energy stabilities is achieved only at VEPP-4M.

### 3.20.5 Super-fine Scan Experiments

In the recent experiments we have improved the system of Touschek particle registration and started using the NMR magnetometer-based field feedback loop. As result, the depolarization frequency resolution is raised to a level of $10^{-9}$.

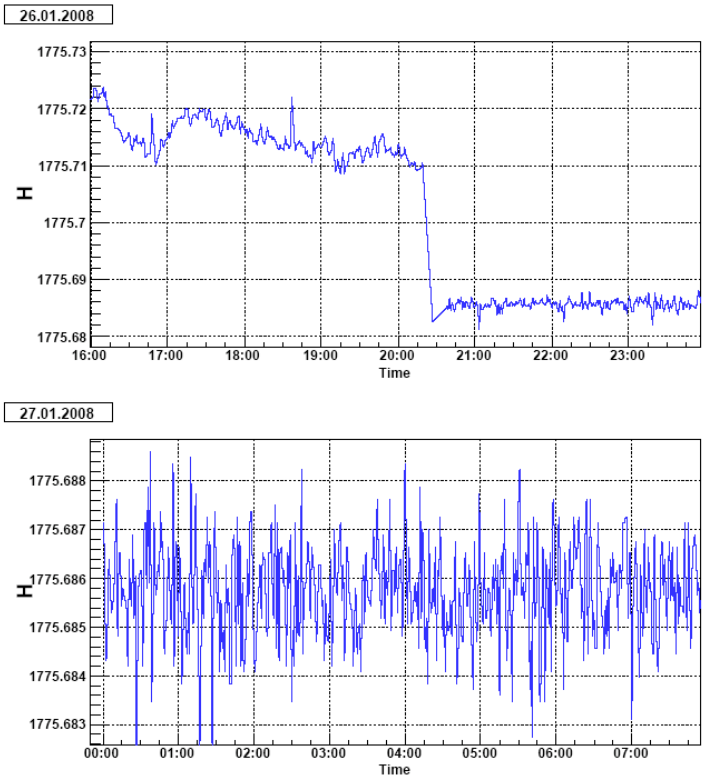


**Figure 4:** NMR magnetometer monitoring data on the VEPP-4M reference magnet field at the additional feedback loop switched off (before 20:30, 26 Jan 2001) and switched on (beginning from 20:30, 26 Jan 2001). The guide field values given in Oersted approximately correspond to the beam energy in MeV. NMR data were read with a period of several seconds.

#### *3.20.5.1 "Long-drawn Jump" Model*

We have developed two super-fine scan models to understand the results of our experiments. One of the models is a phenomenological one describing a spin resonance crossing with the help of formal parameters and using the Monte Carlo methods for simulation of the measurement process. Another model is analytical. It follows from the kinetic theory of spin resonant diffusion [11] and includes the main physical parameters

of the experiment. Depolarization mechanism is based on fast crossings by the beam particles the spin resonance in a characteristic time equal to the radiation damping time over the spin tune range of the order of spin line width [12]. In the given case the spin tune spread is due to quantum fluctuations and determined by an average product of the guide field quadratic non-linearity and the radial beam size squared. In the super-fine scan experiment the depolarizer line width is much less than the spin line width and is about 0.1 Hz (50 eV) even taking into account its dynamic broadening at scanning. At the same time the relative spin line width is of several units times $10^{-7}$ or about 1 Hz (1 keV). Therefore, the depolarizer line width does not exert an essential influence upon the experiment accuracy. Depending on the spin line width and on a relative rate of retuning the spin resonance detuning, one can observe a smooth change of the relative Touschek particle counting rate $S$ during the depolarization process, which looks like a long-drawn jump. Both models enable us to explain a long-drawn jump shape and its deformations caused by the guide field ripples (see Figure 5.).

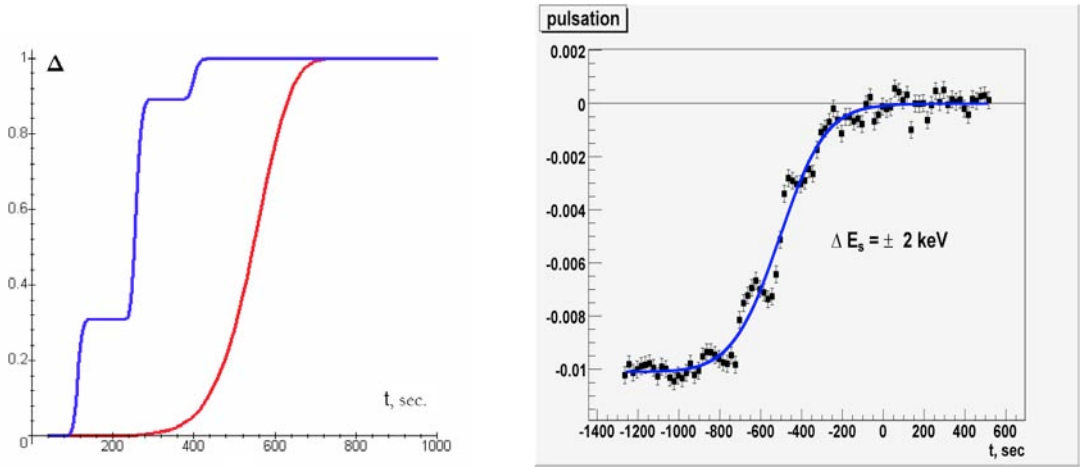


**Figure 5:** Model influence of the field ripples on a shape of the "long-drawn jump". Left: the kinetic model at the scan rate=5 eV/s, the spin line width=1 keV; the cases without and with ripples of the 150 sec period and the 2.5 keV amplitude are presented. Right: the phenomenological model at 200 second ripples (the energy interval of scan occupied by the jump is about 2 keV).

### *3.20.5.2 Accuracy of Depolarization Frequency Determination*

The bending field stabilization described above allows the super-fine scan interval to be limited by a several keV range. Otherwise, a preliminary "crude and fast scan" energy calibration with a partial depolarization is required before a super-fine scan starts or the energy interval for scanning must be notably expanded (up to about 10 keV). Besides, that feedback loop suppresses the ripples in the lowest region of the spectrum: from 0 to 0.1 Hz. Above 0.1 Hz the bending field ripples broaden the spin line. If there is no ripples the spin line width is determined only by a particle trajectory spread at the presence of a quadratic field non-linearity and is estimated at about 2 Hz. Super-fine scan seizes a depolarizer frequency range of several Hz. Taking into account that the field feedback loop suppresses the ripples with the frequencies < 0.1 Hz, one can consider a band from 0.1 to several Hz as a deleterious one affecting the long-drawn depolarization jump. Nevertheless, an influence of these quick ripples on the spin line

broadening descends due to the averaging during a time of data taking by the Touschek particle registration system. Typically, this time is 20 seconds per one point. Depolarization time at the super-fine scan is a few tens of seconds. The achieved depolarization frequency resolution is $10^{-9}$. In such conditions, one can count on the electron and positron spin frequency comparison accuracy of $10^{-8}$. Earlier, before the registration system improvement, we obtained the accuracy of $2 \cdot 10^{-8}$ in the electron-electron comparison experiment [5].

#### *3.20.5.3 Record-high Resolution Experiments*

Efficiency of the new Touschek particle registration system is ten times higher in comparison with the old one. The combined measures for providing stable conditions of the super-fine scan experiments include the following. First is the field stabilization feedback loop described above. It reduces the field ripples with a period of more than 10 seconds by a factor of approximately ten. Another is the stabilization of the VEPP-4M revolution frequency as well as the reference frequencies of the depolarizer and the NMR magnetometer devices by means of the frequency standard with stability better than $10^{-10}$. This eliminates systematic errors caused by a difference in directions of the respective generator frequency drifts. All these methodical techniques together enable us to achieve in most cases a $(1 \div 3) \times 10^{-9}$ resolution in determination of the depolarization frequency, which is an absolute record.

Experiments were being conducted at the beam energy $E$=1.85 GeV in the "1+1" mode with electrons. In Figures 6-8 behaviour of the relative counting rate $S$ in a time during some super-fine scans is plotted. The duration of the jump formation related to the depolarization time depends on the spin line width and a relative drift rate of the spin tune. The spin line width is determined by the field quadratic non-linearity distribution along the closed orbit and weakly changes at similar adjustment of the storage ring. In the conditions when the slow field ripples are suppressed and regular fast ripples are averaged over a period of data taking, a shape of the depolarization jump may depend on manifestations of the sporadic fast ripples. In typical case the jump looks like in Figure 6. Depolarization times in the most performed scans are within 15-75 seconds. For comparison, this interval was 150-450 seconds and the frequency resolution was $(3 \div 8) \times 10^{-9}$ when the developed field feedback loop was not in action. If a fast shift of the spin line occurs against the scan running, the jump may become abrupt as in Figure 7. This effect can increase a systematic error in the electron-positron comparison. In an opposite case when the spin line suddenly and quickly moves from the scanning depolarizer line one can observe two successive partial depolarization jumps like in Figure 8.

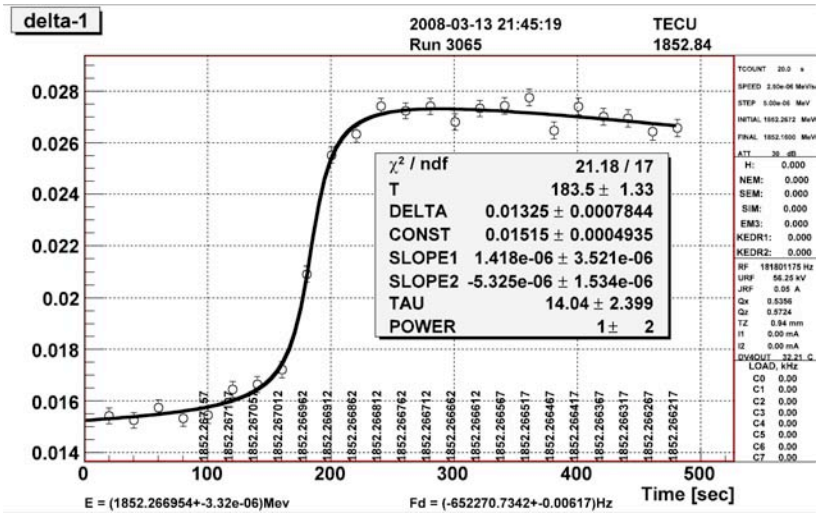


**Figure 6:** Typical case of the "long-drawn jump". Scan rate is 2.5 eV/s. Characteristic time of the jump formation, or the depolarization time, is $14 \pm 3$ sec. Resolution on the depolarization frequency determination is found by the ratio of the experimental data fit error ~3 eV to the beam energy 1852 MeV and is about $1.5 \cdot 10^{-9}$.

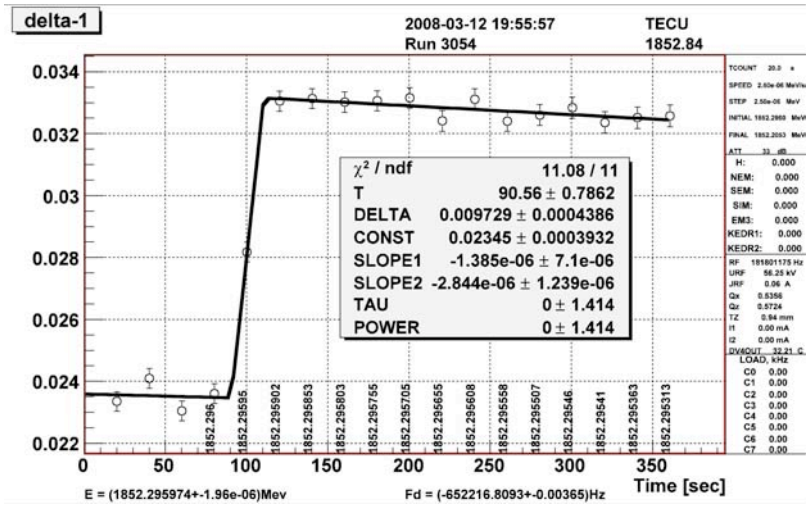


**Figure 7:** Abrupt jump case. Depolarization frequency resolution is ~$10^{-9}$.

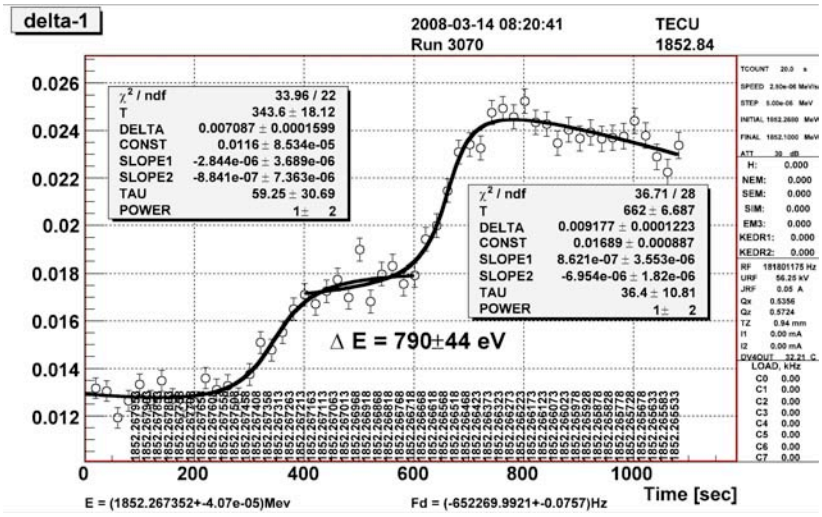


**Figure 8:** Rare case of two jumps. After partial depolarization by the time of 400 seconds a very fast change of the main field of 800 eV in energy units occurs. Further scanning discovers a destruction of residual beam polarization.

#### *3.20.5.4 Bunch Current Dependence*

Difference between the electron and positron energies (spin tunes) can depend on a difference in the electron and positron bunch population. The possible mechanisms of such dependence are related to specific distortions of the closed orbit. These distortions arise due to the deflection effect of EM fields induced by a bunch in the vacuum chamber walls as well as due to non-mirror symmetry distribution of coherent losses [3]. If to compare the energies of two bunches of the same sign (electron) but of the different current, the measured difference can be unambiguously treated as a existence proof of the current dependence. We have started conducting such experiments in different conditions. In particular, the electron-electron comparison is made with the electro-static orbit separation system turned on in one case and turned off in another. According to the preliminary data the difference in the bunch current must be smaller, at the worst, than 1% to provide the spin frequency comparison experiment accuracy of $\sim 10^{-8}$.

### 3.20.6 Status of the Electron-Positron Comparison Experiments

The pulse solenoids in the VEPP3-VEPP4M beam line have been put into operation to restore the vertical polarization of injected positrons at 1.85 GeV, the energy of experiment. This allowed the VEPP-4M energy measurement using the resonant depolarization technique with positrons to be realized. The series of alternate energy calibrations with electrons and positrons has been performed with the aim to study a systematic error in the J/Ψ- and Ψ' - masses measured in the experiments with the KEDR detector at VEPP-4M [9]. A limitation on their energy difference about 1 keV has been obtained in conditions when their orbits are separated at the parasitic interaction points. Simultaneous measurement of the electron and positron spin frequencies has been carried out in the "2×2" mode of four circulating bunches. Two of them are electron bunches (polarized and unpolarized) and two are positron ones (polarized and unpolarized). A study of the systematic error in the electron and positron

energy difference caused by a dependence of spin precession frequency upon the bunch current, by an influence of nonlinear magnet corrector, a skew sextupole, as well as of the electrostatic orbit separation system has been started.

### 3.20.7 Discussion

The counting rate of 1-2 MHz/mA was achieved with the new Touschek counters distributed along the VEPP-4M orbit. In operating with stabilization of the main reference frequencies (RF, the depolarizer synthesizer and the NMR magnetometer) and suppression of the guide field slow ripples, the record resolution ($10^{-9}$) of the depolarization frequency was obtained experimentally for electrons. Now, as we found, the accuracy is limited by the fast, seldom and tiny (less than 1 G) field jumps in the storage ring magnets. The nature of these jumps is not clear yet.

Taking into account present systematic errors [5] we estimate the accuracy of the $e^+e^-$ spin precession frequency comparison, achievable in the experiments at VEPP-4M as $\leq 10^{-8}$.

In ideal conditions, the achieved counting rate 1-2 MHz/mA allows us to obtain a statistical accuracy of $10^{-10}$ in comparison of the spin precession frequencies. To decrease a systematic error to this level it is required to design and create a special storage ring at low beam energy – about 300 MeV. Characteristic features of such machine must be: the low radiation losses [5], affecting the mirror symmetry of the electron and positron orbits, and a high stability of the guide field; the latter can be provided using superconducting magnets.

### 3.20.8 Acknowledgements

We would like to thank our colleagues V. Cherepanov, S. Karnaev, E. Starostina, E. Simonov, V. Smaluk, S. Sinyatkin for help in the performance of the experiments.

### 3.20.9 References

1. O.G. Lüders, Ann. Phys. (NY) 2 (1957) 1.
2. R.F. Streater and A.S. Wightman, “CPT, Spin and Statistics, and All That” (Benjamin, New York, 1964).
3. G.Gabrielse et al., Phys. Rev. Lett. 65, 1317 (1990)
4. A.D.Bukin, et al., Vth Int.Symp. on High Energy Phys. and Elementary Part.Phys., Warsaw, 1975, p.139.
5. O. Anchugov et al., Proceedings of EPAC 2006, THOBFI03, p.2787.
6. I.B.Vasserman et al., Phys. Lett. 198B (1987) 302.
7. R. van Dyck et al., Phys. Rev. Lett. 59, 26 (1987)
8. V.E.Blinov, et al., EPAC 2002, pp.1954-1956.
9. V.M. Aulchenko et al., Physics Letters B 573 (2003) 63-79.
10. V.E.Blinov, et al., NIMA 598 (2009) 23-30.
11. Ya.S. Derbenev and A.M. Kondratenko, DAN SSSR 217,2 (1974) 311-314.
12. S.A. Nikitin, BINP Preprint 2005-54.

## 3.21 Study of Electron Beam Profile with Multi-Anode Photomultiplier

V. F. Gurko, A. N. Zhuravlev, P. V. Zubarev, V. A. Kiselev, O. I. Meshkov,
N. Yu. Muchnoi, A. N. Selivanov, V. V. Smaluk, A. D. Khilchenko.
Budker Institute of Nuclear Physics, Novosibirsk 630090, Russia
Mail to: Meshkov@inp.nsk.su

### 3.21.1 Introduction

In the physics of particle accelerators and beams, there is a number of interesting beam dynamics tasks, such as study of beam instabilities, beam-beam effects, non-linear beam motion, etc., which requires turn-by-turn measurement of transverse beam size along with the beam center-of-mass position. Moreover, routine machine operation for the high-energy physics experiments, which are performing now at the VEPP-4M electron-positron collider [1], requires measurement and control of such parameters as betatron and synchrotron frequencies, beam energy spread, etc. Some of these tasks, such as beam energy spread measurement, should be done with a beam current of several microamperes to avoid undesirable collective effects, while the usual value of the VEPP-4M bunch current in the routine operation mode is several milliamperes. Ideally, the proper beam diagnostics should provide turn-by-turn beam profile measurements during several tens of thousands of the beam turns within a wide dynamic range. For all the above-mentioned purposes, we have designed a new Fast beam Profile Meter (FPM). This device is based on the Multi-Anode Photomultiplier Tube (MAPMT) and provides turn-by-turn measurement of transverse beam profile. The dynamic range of the MAPMT allows us to study turn-by-turn beam dynamics within the beam charge range of 1 pC – 10 nC. The Fast Profile Meter is a part of the VEPP-4M optical diagnostic system [2]. We have successfully applied the FPM to a number of beam dynamics investigations, such as study of synchro-betatron resonances, beam energy spread measurement, study of beam-beam effects, phase oscillation monitoring, resonance crossing .

### 3.21.2 Design and Characteristics of the FPM

The principal part of the Fast Profile Meter is the Hamamatsu R5900U-00-L16 Multi-Anode Photomultiplier Tube with single anode size of 0.8 mm. Overall dimensions of the FPM including MAPMT and signal processing electronics are 250/100/100 mm. In addition to the MAPMT, the device includes a 12-bit ADC, a controller module, an internal memory of 4 Mb and 100 Mbit Ethernet interface. The memory capacity is enough to store $2^{17}$ 16-point samples of a transverse beam profile. Sampling period can vary within 1 - $2^8$ periods of beam revolution $T_0$ ($T_0$ =1220 ns for the VEPP-4M), so the total recording time can last between 0.16 s and 20 s. As a result, beam oscillation can be analyzed in the frequency range of 10 Hz - 1 MHz.

The optical arrangement (Fig. 1) allows us to change the beam image magnification on the MAPMT cathode from 6× to 20×, which is determined by the experimental demands. High sensitivity of the photomultiplier tube in combination with a set of

remote controlled grey filters, included into the optical diagnostics, provides selecting a suitable level of light intensity within the dynamic range about $10^3$.

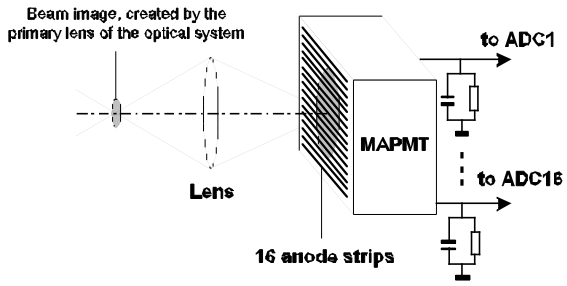


**Figure 1:** Optical layout of the diagnostics. The lens sets up a beam image on the MAPMT photocathode.

This optical scheme can be easily transformed for overcoming the diffraction limit in case of a small beam dimension. The X-ray obscura with the necessary magnification should be applied as the first part of the projection system. The beam image can be projected on the fast decay phosphor (say, Hamamatsu J9758, decay time is 500 ps). The beam image from the phosphor screen is easy to adapt to the MAPMT dimension with a lens.

Block diagram of the FPM signal processing electronics is shown in Fig. 2. The operating cycle of the device is as follows: after a single start pulse, a series of trigger pulses starts 16 ADCs in parallel, MAPMT signals are measured by the ADCs and recorded into the internal memory. The ADC triggering is synchronized with the beam revolution frequency. Sampling period and data array length are set by a user, the starting moment is either chosen by the user or synchronized with a beam kick, injection, moment of beam convergence at the interaction point, etc.

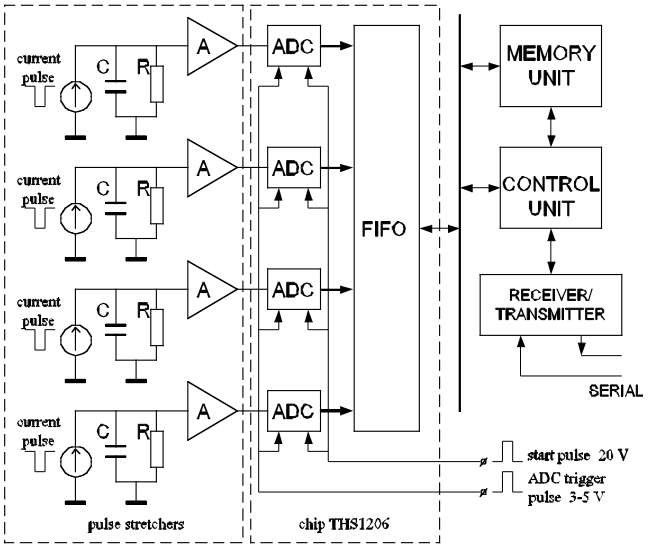


**Figure 2:** Block diagram of the FPM electronics.

The data stored in the internal memory is transferred out to a control computer via Ethernet interface. The data processing includes the Gaussian fitting of every single profile measured, calculation of turn-by-turn arrays of the beam center-of-mass position

and r.m.s. beam size, and Fourier transformation of these arrays. The relative sensitivity of the MAPMT channels is taken into account. Typical single-measured beam profile is shown in Fig. 3.

One of the principal advantages of the FPM in comparison with other beam diagnostic instruments is the possibility to measure single-turn beam profiles during a lot of successive beam turns. There are a number of instruments such as dissector tubes or CCD cameras providing high-resolution measurement of a time-averaged beam profile. Such complicated and expensive device as a streak camera can register only several beam images [3]. On the other hand, for long-range turn-by-turn measurement of a beam position, electrostatic pickups are widely used. A standard four-electrode beam position monitor (BPM) can measure only the center-of-mass position of a beam. To give information about the beam size oscillation, the electrostatic pickup should consist of at least 8 electrodes. Such devices are very exotic. Thus, to provide a long-range turn-by-turn measurement of a beam center-of-mass position simultaneously with the beam size, the FPM is the most proper device.

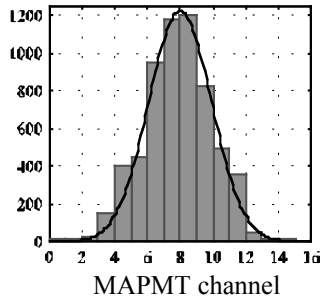


**Figure 3:** Example of the single-measured beam profile with the Gaussian fit.

The second principal advantage of the FPM is extremely high sensitivity provided by the photomultiplier tube, which is the most sensitive optical recorder. Use of the FPM with a set of removable optic filters provides a wide dynamic range of the order of $10^3$. To estimate the FPM sensitivity in comparison with the BPM one, a signal-to-noise ratio in dependence of the beam current has been measured. For a various beam current in the range of 3 mkA - 3 mA, coherent betatron oscillation of the VEPP-4M electron beam is excited by a short kick, then turn-by-turn beam position is measured both by the FPM and the VEPP-4M turn-by-turn BPM [4]. The signal-to-noise ratio is estimated as $20\lg(a_m \; a_n)$, where $a_m$ is the betatron oscillation amplitude obtained from the oscillation spectrum and $a_n$ is the average amplitude of noise harmonics.

An example of spectra of the oscillation measured both by the FPM and by the BPM is presented in Fig. 4.

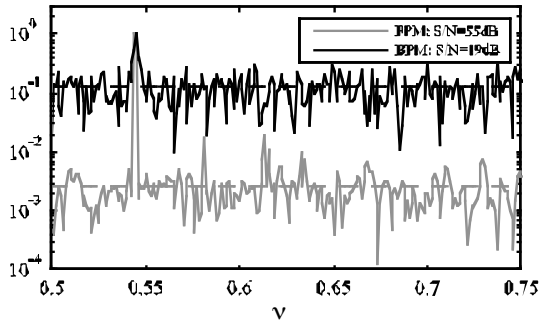


**Figure 4:** Spectra of beam oscillation measured by the FPM and by the BPM. *I*=0.3 mA, $a_m = 1$ mm.

Beam current is 0.3 mA, amplitude of the oscillation is about 1 mm. Fig. 5 shows the measured signal-to-noise ratio of the FPM and the BPM in dependence of the VEPP-4M beam current. As one can see in the figures, the FPM is substantially more sensitive than the electrostatic pickup, besides, the FPM provides turn-by-turn beam size measurements.

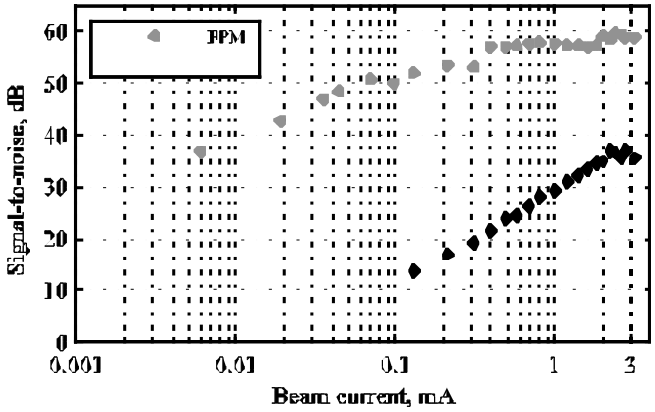


**Figure 5:** Measured signal-to-noise ratio of the FPM and the BPM.

## 3.21.3 Experimental Results

### *3.21.3.1 Beam Decoherences*

An example of the device using is presented in Fig. 6. The vertical turn-by-turn beam position $y_{c.m.}$ and size $\sigma_y$ are measured after a short kick exciting betatron oscillation. Beam current is of 3 mA, unperturbed vertical beam size is $\sigma_y = 0.2$ mm, the vertical chromaticity is $C_y \cong 3.5$.

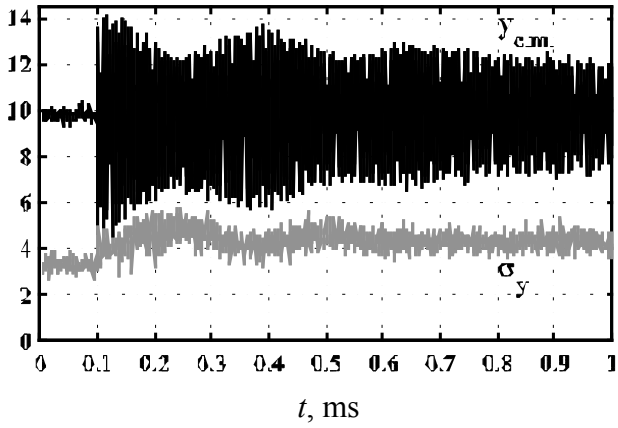


**Figure 6:** Betatron oscillation chromatic decoherence. Oscillations of the beam center of mass and beam size are shown.

One can see that, just after the kick, the beam center-of-mass oscillation damps with $\tau \cong 0.12$ ms while the beam size $\sigma_y$ increases. The time of decoherence could be obtained from these data as well [5]. Then an amplitude modulation caused by chromaticity occurs, and it is also seen, that increase of amplitude of the center-of-mass oscillations causes decrease of the $\sigma_y$ and vice versa.

### *3.21.3.2 Beam-Beam Effects*

During the beam injection procedure, electron and positron bunches are separated vertically at the VEPP-4M beam interaction point by electrostatic strip-line separators. To switch on the beam colliding mode, the electron and positron bunches are converged by zeroing of the separators voltage. Interaction of colliding beams is quite complicated, because each beam acts on another one as a strong non-linear force. So, an experimental study of the beam-beam effects is an object of interest.

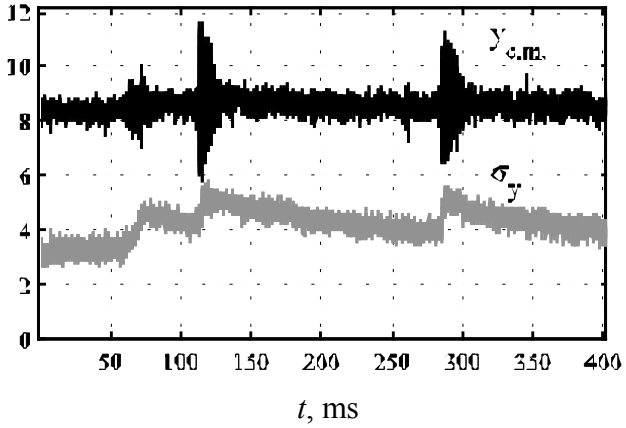


**Figure 7:** Beam-beam instability. Oscillations of the beam center of mass and beam size are shown.

Figure 7 presents the beam size and center-of-mass position behavior in the case of beam-beam instability, obtained from the FPM data. Currents of the electron and

positron beams are limited by the beam-beam effects ( $I_e = 3.0$ mA, $I_p = 3.4$ mA), the positron beam is the "strong" one in this measurement. Both the dipole oscillation amplitude and the beam size increase during the evolution of instability. Every "flash" of the oscillations is accompanied by beam losses.

Sometimes beam convergence is accompanied by an instability, which looks like beam "twinkling". It can be observed by a TV camera included into the optical beam diagnostics. The image looks like a small periodical kick applied to the beam. As a matter of fact, this "twinkling" is caused by the oscillation of the vertical beam size as Fig. 8 demonstrates.

### *3.21.3.3 Beam Energy Spread Measurement*

The high-energy physics experimental program of the VEPP-4M collider with the KEDR detector consists of precise measurement of the $\tau$ -lepton mass, and experiments to improve measurement accuracy of mass of the $J/\psi$ , $\psi$ (2s) and $\psi$ (3770) mesons. Value of the beam energy spread $\sigma_E$ is directly included into accuracy of the particles mass measurement. Knowledge of the beam energy spread enables us to reduce significantly a systematical error in the experiment of $\tau$ -lepton mass measurement. It is also an essential supplement to precision measurement of the average beam energy. Clear understanding of the effects influencing the beam energy spread and ability to control it are important tasks for our experiments.

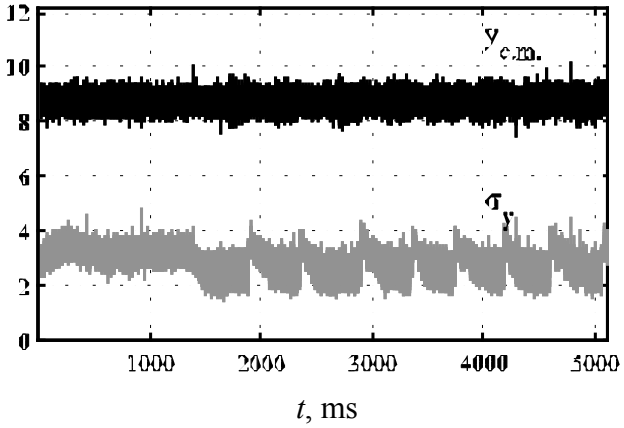


**Figure 8:** Convergence of the beams, accompanied by a quadrupole instability.

Measurements of the energy beam spread were carried out with changes of the vertical chromaticity. Chromaticity of a storage ring causes appearing of synchrotron sideband peaks in a spectrum of beam oscillation. The amplitude of the central betatron peak and the synchrotron satellites are [6]:

$$R_m(y) = \frac{1}{y^2}\int_0^\infty J_m^2(x) e^{-\frac{x^2}{2y^2}} x dx , \qquad (1)$$

where $y = \left(\frac{\omega_\beta \alpha}{\omega_s} + \frac{\omega_0 C_y}{\omega_s}\right)\delta_E$ , $m$ is the number of harmonic, $\delta_E$ is the relative energy spread. Determination of energy spread is based on the measurement of the ratio of

synchrotron satellites to the main peak height. Experimentally, the beam oscillation was excited by a short kick with amplitude $b \geq \sigma_y$. An example of measured spectrum is presented in Fig. 9. Three synchro-betatron satellites are clearly seen.

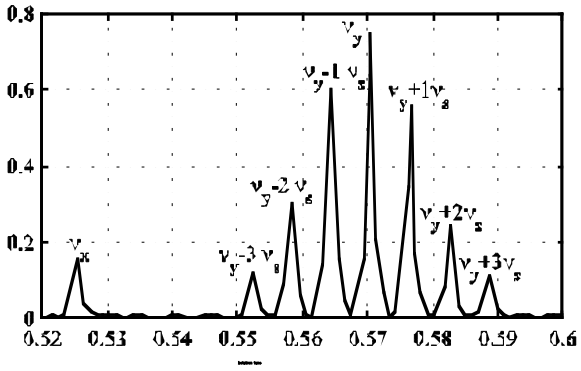


**Figure 9:** A spectrum of vertical synchrobetatron oscillations.

This measurement should be carried out with a low intensity beam to avoid collective effects. The FPM sensitivity provides sufficient accuracy of the measurement performed with a beam of 10-30 $\mu$A.

Figure 10 demonstrates the motion of the center-of mass of the beam following this kick. The envelope of the oscillations is described as [5]:

$$A(t) \propto \exp\left(-\frac{t^2}{2\tau^2}\right) \cdot \exp\left(-\left(\frac{\partial \omega_y}{\partial E}\frac{\sigma_E}{\omega_s}\right)^2 \cdot (1-\cos(\omega_s t))\right), \text{ where } \tau = \left(2\frac{\partial \omega_y}{\partial a^2} b \cdot \sigma_y\right)^{-1} \qquad (2)$$

and allows us to determine the beam energy spread as well.

Experimentally, the energy spread can be determined by fitting of the measured betatron oscillation envelope with the theoretical curve $A(t)$. The problem of such a measurement is a deformation of beam oscillation envelope by the fast damping resulted from the beam interaction with the vacuum chamber resistive impedance. The fast damping decrement is proportional to the beam current, therefore the measurement should be done with a low-intensity beam. To increase the accuracy, a digital filter based on Fourier transform has been applied to the measured data. For envelope analysis, the oscillation is calculated by inverse Fourier transform of spectrum of the measured betatron oscillations but only $\nu_y \pm m\nu_s$ harmonics are taken into account. An example of this operation is shown in Fig. 10. More information can be obtained in [7].

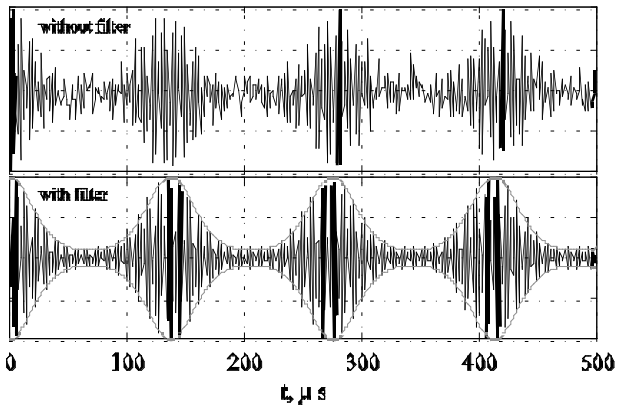


**Figure 10:** Digital filtering of betatron oscillation measured.

### *3.21.3.4 Study of Beam Profile Behavior during Resonance Crossing*

The influence of resonances on the beam dynamics in the storage rings is of a substantial interest for the accelerator physics. For example, a fast crossing of resonances occurs in the damping rings of future linear colliders during the beam damping due to the space charge tune shift that can result in a loss of particles. We have studied experimentally the crossing of resonance nearby the working point of the VEPP-4M storage ring.

For these experiments [8] the ability of FPM to record about $10^5$ beam profiles during several seconds was extremely useful. It enables us to smooth effectively the experimental data and to study in detail the beam profile behavior during the vertical resonance crossing ($3\nu_z = 23$), as Fig. 11 presents.

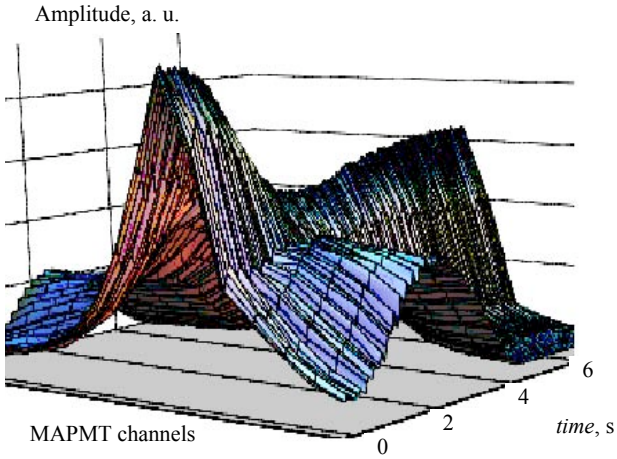


**Figure 11: B**ehavior of the vertical beam profile during the vertical resonance crossing. The vertical betatron tune changes proportional to the time.

## 3.21.4 Conclusion

New Fast Beam Profile Monitor has been developed in Budker Institute of Nuclear Physics. This monitor is based on the Hamamatsu multi-anode photomultiplier with

16 anode strips and provides turn-by-turn measurement of transverse beam profile. The device is equipped with the internal memory, which capacity is enough to store 131072 samples of the beam profile. The dynamic range of the beam profile monitor allows us to study turn-by-turn beam dynamics within the bunch charge range from 1 pC up to 10 nC. The device provides a possibility to measure single-turn beam profiles during a lot of successive beam turns. Along with the high sensitivity and wide dynamic range of the device, this enables study of beam center-of-mass and beam size oscillation under various experimental conditions. The FPM is now used at the VEPP-4M for accelerator physics research and routine machine service. Using this instrument, we have investigated at the VEPP-4M electron-positron collider a number of beam dynamics effects which can not be observed by other beam diagnostics tools.

### 3.21.5 References


1. V. Smaluk, Status of the VEPP-4M Collider, Proceedings of the 2006 Russian Particle Accelerators Conference, Novosibirsk,2006, http://www.jacow.org/.
2. O.I. Meshkov et al., The upgraded optical diagnostics of the VEPP-4M collider, Proceedings of the EPAC-2004, Lucerne}, 2739-2741.
3. A.W. Chao, M.Tigner, Handbook of Accelerator physics and Engineering, World Scientific, 1998.
4. A.S. Kalinin et al., Beam Diagnostic System for Storage Rings, Proceedings of the EPAC-1996, Barcelona.
5. N.A. Vinokurov et al., The influence of chromaticity and cubic nonlinearity on kinematic of betatron oscillations, Budker INP 76-87, Novosibirsk, 1976 (in Russian).
6. T. Nakamura et al., Chromaticity for energy spread measurement and for cure of transverse multi-bunch instability in the SPRING-8 storage ring, 2001 Particle Accelerator Conference, Chicago, 1972-1974.
7. V.A. Kiselev et al., Beam energy spread measurement at the VEPP-4M Electron-Positron Collider. J. Inst. 2 No 06 (June 2007) P06001
8. S. V. Glukhov et al., Study of Beam Dynamics during the Crossing of Resonance in the VEPP-4M Storage Ring, this issue.


## 3.22 Progress on Commissioning of BEPCII


J.Q. Wang, L. Ma and C. Zhang for the BEPCII Commissioning Team
Institute of High Energy Physics, Beijing China
Mail to: wangjq@ihep.ac.cn


### 3.22.1 Introduction

The BEPCII is the upgrade project of BEPC, serving continuously the dual purpose of high energy physics experiments and synchrotron radiation applications. The design goals and its construction is described in Ref. [1,2]. As an $e^+e^-$ collider, it consists of an electron ring (BER) and a positron ring (BPR), respectively. The two rings cross each other at the southern interaction point (IP), where the BESIII (Beijing Electron Spectrometer) detector is located, with a horizontal crossing angle of 2×11mrad. A pair of superconducting insertion magnets (SIMs) are used to squeeze the $\beta$ function at the IP, compensating the detector solenoid and to serve as the bridge connecting two outer

half rings for synchrotron radiation (SR) operation, respectively. For the dedicated SR mode, electron beam circulates in the ring made up of two outer half rings. 5 wigglers were installed in the outer rings to generate stronger SR.

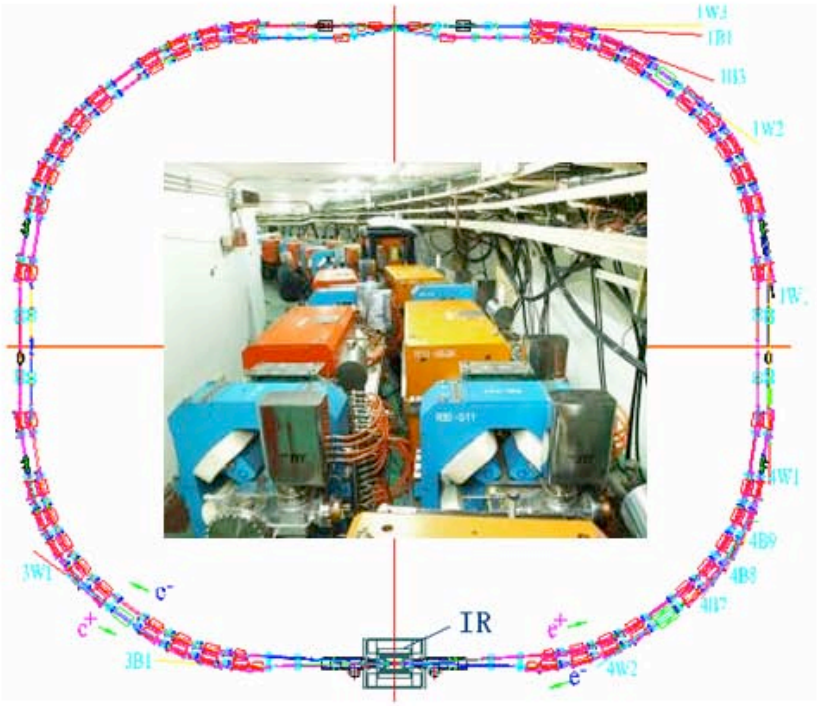


**Figure 1:** Layout and the installed two rings in tunnel.

In accordance to keep the progress of construction and to meet the demands from the SR users community as well, the beam commissioning of BEPCII is carried out in 3 phases: Phase 1, with the backup scheme which adopted the conventional magnets in the interaction region (IR) instead of SIMs; Phase 2, with SIMs in the IR; Phase 3, joint commissioning with detector.

The phase 1 commissioning was from November 13, 2006 to August 3, 2007. In this phase, 100mA by 100mA beam collision was achieved with $\beta_y^*$=5cm, while the estimated luminosity reached to the level of BEPC. Two rounds of dedicated synchrotron radiation operation were arranged during that period. The beam performance and commissioning results have been reported on the APAC07 [3] and PAC07 [4].

After the superconducting magnets SIM's and corresponding vacuum chambers were installed into the IR in the summer of 2007. The second phase commissioning was carried out from October 24, 2007 to March 28, 2008. The maximum beam current in each ring exceeded 550mA and the luminosity was estimated to be $1\times10^{32}cm^{-2}s^{-1}$ by the zero degree luminosity detector. In this phase, the dedicated SR mode was run for about one month, with peak beam current of 250mA. The beam lifetime reached to the designed value of 10hrs at 200mA while the gap of the in-vacuum wiggler 4W2 was set to 18mm. The beam performance and main commissioning was reported on the Factory08 workshop [5] and EPAC08 [6].

The third phase commissioning started out from June 22, 2008 after the detector was moved into the IR. Up to now, the beam current for each ring achieved was more than

700mA and 650mA for BPR and BER, respectively. The luminosity exceeded $1.0\times10^{32}cm^{-2}s^{-1}$ when the $e^+$ and $e^-$ beam reached to about 350mA at collision in September 2008. However, the luminosity did not increase proportionally when the beam current became higher. The record luminosity achieved was $1.3\times10^{32}cm^{-2}s^{-1}$ at 486mA×523mA by the end of 2008. Severe longitudinal oscillation sidebands were observed in BPR. After systematic study, a reused screen monitor (SM) on BPR was suspected as the source causing the instability. Then it was decided to remove these two SMs during the winter shutdown. Beam commissioning resumed on February 1, this year. The longitudinal oscillation of positron beam was significantly reduced and the luminosity was steadily improved with collision beam current increase. The latest record was $1.85\times10^{32}cm^{-2}s^{-1}$ at 393mA×447mA. From March 1, 2009, physics running at ψ(2S) started.

This paper summarizes the beam commissioning progresses in 3 phases, while focusing on the effort done to improve the beam performance in the third phase

## 3.22.2 Single Beam Performance

### *3.22.2.1 Orbit and Optics Correction*

The closed orbit and optics correction was done based on the response matrix and its analysis using LOCO (Linear Optics from Closed Orbits) method [7]. As the result, the measured beam optics functions are in good agreement with theoretical prediction with discrepancy within ±10% at most quadrupoles [8].

The LOCO analysis results indicated that the quadrupole strengths are mostly lower than the design set within 1~2%. One contribution to this systematic component was from the short distance between the quadrupole and its adjacent sextupole. Another may from the fringe filed effect. Other origin of these errors is still pursued.

### *3.22.2.2 Detector Solenoid Compensation & Optics Correction*

After the detector moved into the IR in the 3rd phase commissioning, one key issue is to compensate the effect due to the Superconducting Solenoid Magnet (SSM) of the BESIII detector. To have perfect compensation for particles with any momentum, a scheme with three anti-solenoids (AS1~3) and a skew quadrupole was designed in the SIM package of coils. The combined magnetic field measurement of SIM and SSM was done in July 2007. All the field components met the specifications, particularly, the 3 Anti-Solenoids AS1 AS2 AS3 to compensate detector solenoid field works very well. The integral $\int B_z ds$ between the IP and the Superconducting Quadrupole (SCQ), which is used to squeeze the $\beta_y$ at IP, is nearly zero. $\int B_z$ over the SCQ is also nearly zero, and the $\int B_z ds$ after the SCQ is zero too. For fine tuning over the SCQ region, the coils serving as skew quadrupoles can be used. The beam measurement results confirmed this scheme, with natural coupling less than 1% measured from tune split method. The only residual effect is additional focusing in both x and y planes. Then, the strength of SCQ has to be reduced 0.32% to cancel this, thus the $\beta$ functions can be well restored as that without the SSM and ASM.

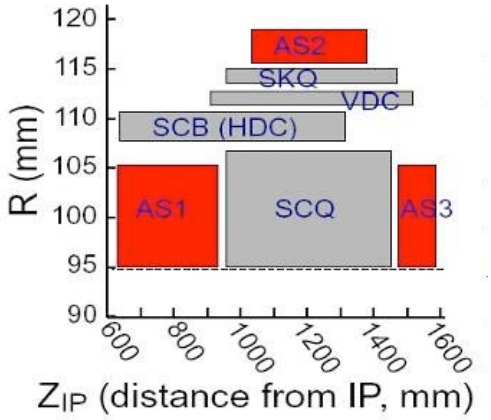


(a) Schematic drawing of the coils on the (SIM) with AS1-3 to compensate the effect of SSM.

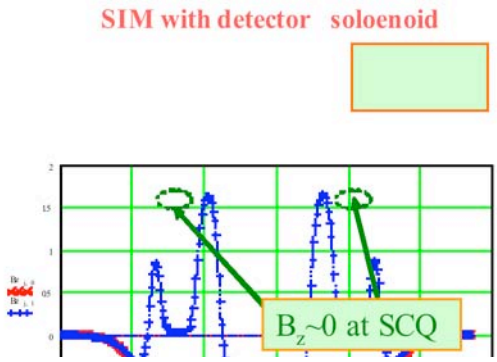


(b) The measured field distribution of magnetic field.

**Figure 2:** Coils of SIM and the field measurement result.

#### *3.22.2.3 Injection*

For beam injection, a two-kicker system is adopted. Thus the betatron phase advance between the two kickers is designed as 180 degree to form a local bump during injection. However, to reduce the residual orbit oscillation of the stored beam during injection, it's tricky to set the right timing and amplitude of the two kickers. This was done using the Libra BPM system [9]. Thanks to the sameness between the waveforms of the two kickers, after the time delay and amplitude of the two kickers was optimized for the injecting bunch, the residual orbit oscillation of all the other bunches during injection can be reduced to around 0.1mm, corresponding to about $0.1\sigma_x$. This made it possible to inject beam during collision, as well as to get uniform filling of all the buckets.

#### *3.22.2.4 Beam Current Growth of BER and BPR*

The growths of the beam current in the BER and BPR in the phase 3 commissioning are shown in Figure 3 and the beam parameters achieved are listed in Table 1. However, during the phase 2 commissioning, a multipacting effect near the RF window of SC cavities (SCC) occurred when the beam current in both BER and BPR exceeded 100mA. Thus, a DC bias voltage was applied on the power coupler of the SC cavities to suppress it. This worked very effectively and the beam current of both rings could be improved steadily. Nevertheless, transverse feedback system has to be employed for smooth injection and stable operation at high beam current.

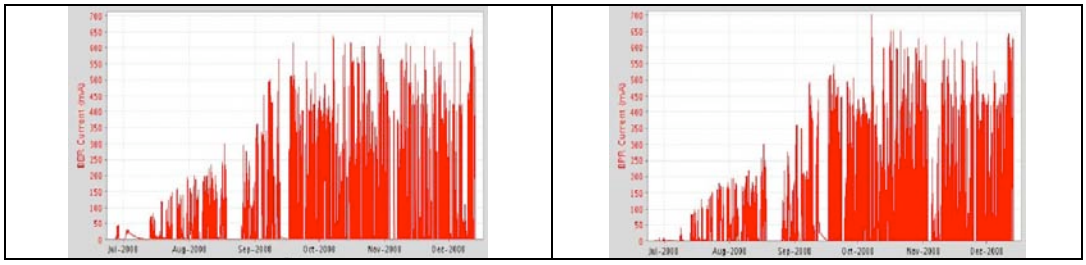

**Figure 3:** Current growth during the phase 3 commissioning in 2008, BER (left) and BPR (right).

**Table 1:** The main parameters of the BER and BPR.

| ***Parameters*** | ***Design*** | ***Achieved*** | |
|---|---|---|---|
| | | BER | BPR |
| Energy (GeV) | 1.89 | 1.89 | 1.89 |
| Beam current (mA) | 910 | 650 | 700 |
| Bunch current. (mA) | 9.8 | >10 | >10 |
| Bunch number | 93 | 93 | 93 |
| RF voltage | 1.5 | 1.6 | 1.6 |
| Tunes ($\nu_x/\nu_y$) | 6.54/5.59 | 6.54/5.61 | 6.54/5.61 |
| $*\nu_s$ @ $V_{RF}$= 1.5MV | 0.033 | 0.032 | 0.032 |
| $\beta_x^*/\beta_y^*$ (m) | 1.0/0.015 | ~1.0/0.016 | ~1.0/0.016 |
| Injection Rate (mA/min) | 200 $e^-$<br>50 $e^+$ | >200 | >50 |

$*\nu_s$ is extrapolated from the measurement at RF voltage of 1.69MV for BER and 1.61MV for BPR, respectively.

### *3.22.2.5 Instabilities & Feedback*

The single bunch beam dynamics as well as collective effects are described in detail in ref. [10]. An analog bunch-by-bunch transverse feedback (TFB) system has been adopted to cure the instabilities [11].

In transverse, coupled bunch instability was observed in both BER and BPR. In the BER, vertical sidebands near the rf frequency was observed on the spectrum analyser. These may be due to resistive wall impedance. In the BPR, a broadband distribution of vertical sideband spectrum was observed, which can be attributed to the electron cloud effect, as shown in Figure 3. With the TFB carefully tuned, the sidebands of couple bunch instabilities in both BER and BPR can be well suppressed at the beam current up to 600mA.

Besides, the streak camera and gated camera were used to measure the bunch lengthening and the blow up of the vertical beam size due to ECI, respectively. Up to now, no obvious grow up of the bunch size at the tail of the bunch train has been observed with only single beam of positron. However, ss prevention to further ECI, solenoid was winded on the vacuum chamber and can be put into use when needed.

In longitudinal, since SC cavity is adopted, the beam behaves fairly stable. However, synchrotron oscillation sideband was sometime observed along with beam current increase, so longitudinal feedback system is being developed.

### 3.22.3 Luminosity Tuning

#### *3.22.3.1 Single Bunch Collision*

Electron and positron beams in two rings were brought to collision at the IP by Beam-Beam Scan (BBS) [12]. A luminosity monitor (LM) based on the detection of zero degree $\gamma$ from irradiative bhabha process was installed. It can distinguish the luminosity bunch by bunch with a response time fast enough to be used in the tuning procedures. Thus the beam parameters such as tune, coupling and local optics at IP were optimized to maximize the specific luminosity given by the LUM.

To get the best luminosity, tunes of each ring were scanned around the region of the designed tune of (6.54, 5.59) obtained from beam-beam simulation. Then the tunes for the BER and BPR were set near (6.54, 5.61).

Optimization is also on the x-y coupling or vertical beam size. This was done by adjusting the local vertical orbit in one sextupole in the arc. It is found that 1% coupling gives the best specific luminosity.

The vertical dispersion measured at IP was small and its contribution to the beam size at IP can be neglected. The local optical functions at the IP such as coupling and $\beta_y$ waist were also adjusted with a set of quadrupoles around the IP according to the luminosity.

With the above beam parameters optimized iteratively, the maximum bunch current achieved in stable collision with high luminosity is 11mA×11mA, which is higher than the design of 9.8mA. However, the specific luminosity at high bunch current is lower due to beam-beam blow-up, so there is still room for further optimization.

#### *3.22.3.2 Multi -Bunch Collision*

Multi-bunch collision was practiced in two ways, one with relative high bunch current but small number of bunches, say above 7mA/bunch with 70 bunches, the other is with moderate bunch current, but 93 bunches as designed. At the same total beam current, it's expected that a higher luminosity can be obtained in the former case. However, in 3rd phase commissioning in September 2008, it was found that the luminosity for each pair of colliding bunches decreases along the bunch train, as shown in Figure 4. Thus the luminosity does not increase proportional to the bunch number.

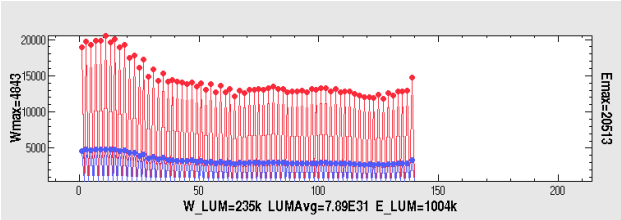


**Figure 4:** Luminosity decrease along the bunch train.

To identify the cause of the phenomenon, systematic study was done. First, a comparison was done by colliding the beam with a long train of 70 electron bunches vs two short trains of 5 positron bunches. The two trains of positron bunches are positioned to collide with the first 5 and last 5 electron bunches in the long train respectively. In this case, the luminosity of the last 5 bunches is almost equal to the first 5 bunches. But in contrast, with 70 positron bunches colliding to 10 electron bunches, the luminosity of 5 bunches in tail part of the train give much lower luminosity. So it indicates that the positron beam is the cause for luminosity degradation.

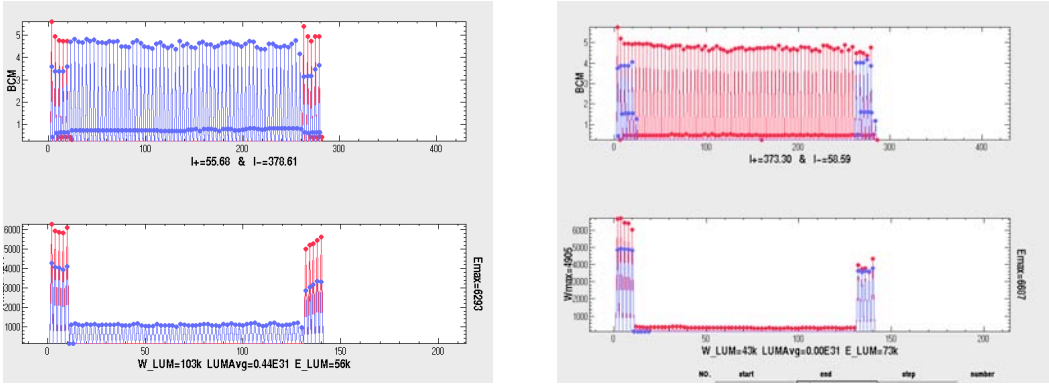


70 electrons vs 10 positron bunches  10 electrons vs 70 positron bunches

**Figure 5:** Comparison of luminosity vs intensity of electron and positron beam current.

Is this caused by ECI? However, the increase of the transverse beam size did not observed by gated camera in the case of single positron beam. So it seems the problem not caused by the electron cloud similar to other machines such as KEKB and PEP-II.

During the study of ECI, it was observed from the streak camera that positron bunches are lengthened and more look like they are oscillating. Observation from the oscilloscope confirmed this and the amplitude of oscillation increases along the bunch train. From the amplitude of bunch lengthening and the dipole oscillation, it's estimated that the bunch luminosity in the tail of the bunch train can be reduced to less than 70% of that in the head [13].

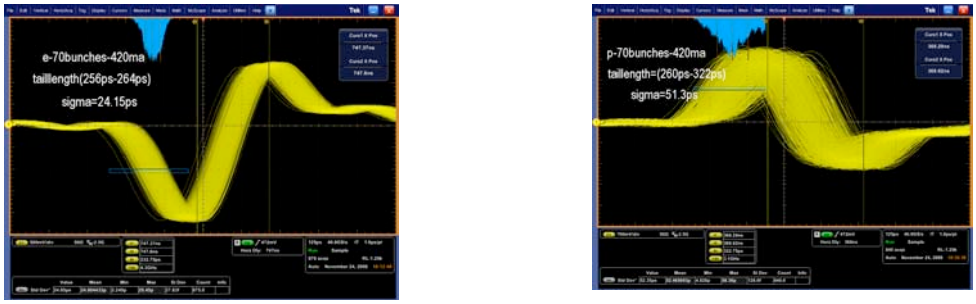


(a) Electron bunches  (b) Positron bunches

**Figure 6:** Longitudinal oscillation observed for the tail part of bunch train.

Then the possible sources can be HOM. We look at the components which can generate the HOMs. From the difference on the amplitude of longitudinal oscillation between positron and electron ring, the two screen monitors, which were only

temporarily used for the first turn injection of positron beam, became the most suspicious. It's found [14] that there are gap between flange and HOM can be trapped, as shown in Figure 7.

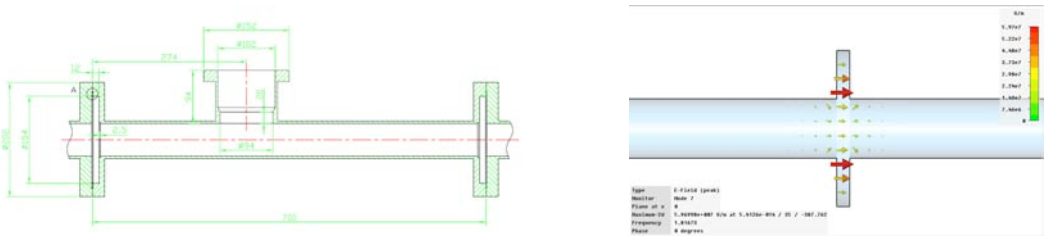

(a) 2D view of screen monitor (b) Trapped mode at the flange gap.

**Figure 7:** The structure of the screen monitor and the trapped mode at the flange gap.

From the impedance calculation, a mode with resonant frequency around 1.8GHz and shunt impedance of 80,000Ω was found. Calculation shows that the field decay time is about 200ns which is shorter than the time span of the bunch train and its frequency can be allayed to some of the longitudinal oscillation modes. Then it was decided to remove the screen monitor during the winter shutdown time.

The commissioning resumed this Febuary 1. As expected, the longitudinal oscillation in the positron ring became much weaken and the amplitude is same to that in electron ring, as shown in Figure 8.

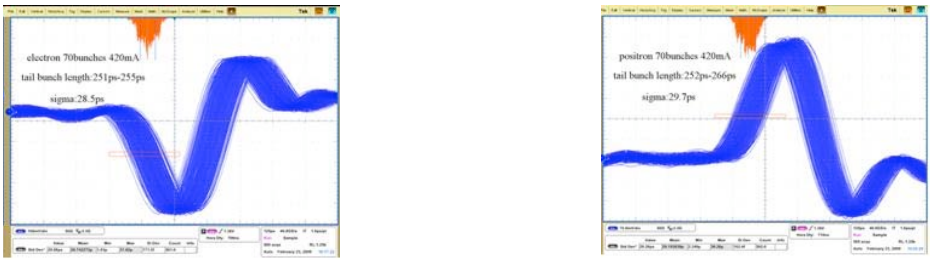


(a) Electron bunches (b) Positron bunches

**Figure 8:** After the screen monitor removed, the longitudinal oscillation of BPR reduced.

Correspondingly, luminosity decrease from head to tail along the bunch train mitigated as shown in Figure 9. The luminosity in 2009 vs 2008 is shown in Figure 10 with 40% improvement at the same beam current. However, there are still some drops along the bunch train and the specific luminosity of multi-bunch case is still lower than that in the single bunch case with same bunch current. Systematic study on the longitudinal as well as transverse instability is underway.

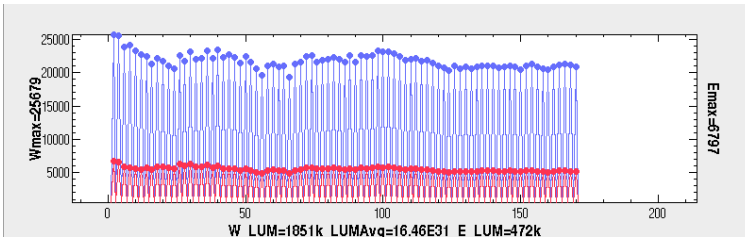


**Figure 9:** After the screen monitor in BPR removed, the luminosity along the bunch train.

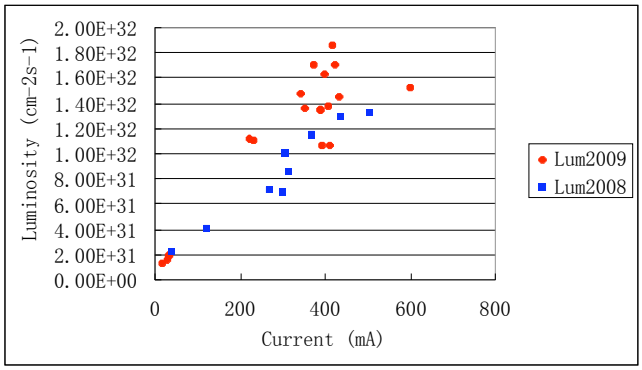


**Figure 10:** The luminosity achieved in 2009 compared to that in 2008.

### 3.22.4 Background

Optimization has been done to reduce the dose rate in the IR during injection to protect the BESIII detector. To reduce the backgrounds during steady runs for data taking, collimators were used. Experiment [15] shows that most of the background can be attributed to Touschek effect. For higher beam operation, it still needs further study on the aperture limit to improve the beam lifetime and to reduce the beam loss generated background.

### 3.22.5 Summary

The optimization methods to achieve high beam current as well as high luminosity have been practice systematically. The beam current has reached more than 1/2 of design and most devices performed stably as expected. The luminosity has reached the record of $1.85\times10^{32}cm^{-2}s^{-1}$ and the collider has already provided stable operation for high energy physics experiment.

However, there are still lots of issues for further studies, particularly to improve the specific luminosity at high beam current, the transverse feedback system needs better tuning, and the longitudinal feedback system has to be developed. Besides, the beam parameters need further optimization to avoid the blow-up due to beam-beam effect.

There is still long way to approach the design luminosity.

### 3.22.6 Acknowledgement

The authors thank all the members of the BEPCII team for the supporting of commissioning. Colleagues from BNL, DESY, KEK, LBNL, SLAC provided much help on the SIM, cryogenic system, SRF system etc. Thanks also go to the BEPCII IMAC members for their advice.

### 3.22.7 References

1. BEPCII Group, BEPCII Design Report, Aug. 2001.
2. C. Zhang, Factories08, Russia, Apr. 2008.
3. C. Zhang et al, Proc. of APAC'07, India, Jan. 2007.
4. J. Q. Wang et al, Proc. of PAC'07, U.S.A, July. 2007.
5. J. Q. Wang et al, Factories08, Russia, Apr. 2008.
6. J. Q. Wang et al, Proc. of EPAC'08, Italy, June. 2007.
7. J. Safranek et al, Proc. of EPAC'02, France, 2002.
8. Y.Y. Wei et al, Proc. of Factories08, Russia, Apr. 2008.
9. H.Z. Ma et al, internal report, Mar. 2008.
10. Q. Qin et al, Factories08, Russia, Apr. 2008.
11. J.H. Yue et al, Factories08, Russia, Apr. 2008.
12. C.H. Yu et al, internal report, Jan. 2009.
13. J.Q. Wang et al, internal report, Jan. 2009.
14. T.M. Huang et al, internal report, Jan. 2009.
15. D.P. Jin et al, internal reprot, Dec. 2008.

## 3.23 First Commissioning Results of VEPP-2000

D.Berkaev, A.Kirpotin, I.Koop, A.Lysenko, I.Nesterenko, A.Otboev,
E.Perevedentsev, Yu.Rogovsky, A.Romanov, P.Shatunov, Yu.Shatunov, D.Shwartz,
A.Valkovich, I.Zemlyansky
BINP, Novosibirsk, Russia
Mail to: I.A.Koop@inp.nsk.su

### 3.23.1 Introduction

The new $e^+e^-$ collider VEPP-2000 [1] based on round beams approach was constructed at BINP and now is in commissioning stage. It will operate in the energy range from pion-production threshold up to 2 GeV. First luminosity $10^{31}cm^{-2}s^{-1}$ at phi-meson energy was successfully achieved in a single bunch mode. At the moment two detectors are in final preparation for data taking. Below a brief activity report and first results of a commissioning are presented.

### 3.23.2 Layout, Lattice and Design Parameters

VEPP-2000 complex consists of high-intensity 3 MeV electron linac ILU, 250 MeV pulsed synchrotron B-3M, 900 MeV booster storage ring BEP and 1 GeV collider storage ring VEPP-2000.

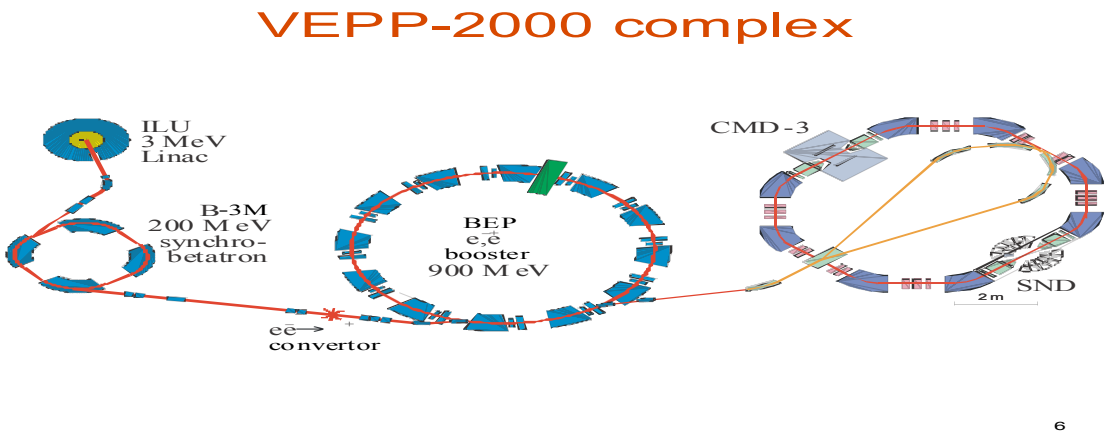


**Figure 1:** Layout of VEPP-2000 complex.

**Table 1:** Main Parameters of VEPP-2000 at 1 GeV.

| | |
|---|---|
| Circumference | 24.38 m |
| RF frequency | 172 MHz |
| RF voltage | 100 kV |
| RF harmonic number | 14 |
| Momentum compaction | .036 |
| Synchrotron tune | .0035 |
| Energy spread | $6.4 \cdot 10^{-4}$ |
| Beam emittances (in round mode) | $1.29 \cdot 10^{-7}$ m·rad |
| Dimensionless damping decrements (x,y,s) | $2.19 \cdot 10^{-5}$, $2.19 \cdot 10^{-5}$, $4.83 \cdot 10^{-5}$ |
| Betatron tunes (x,y) | 4.1, 2.1 |
| Betatron beta-functions at IP | 10 cm |
| Number of bunches per beam | 1 |
| Number of particles per bunch | $1 \cdot 10^{11}$ |
| Beam-beam space charge parameter (x,y) | 0.075, 0.075 |
| Luminosity per IP (at 1 GeV) | $1 \cdot 10^{32}$ $cm^{-2}s^{-1}$ |

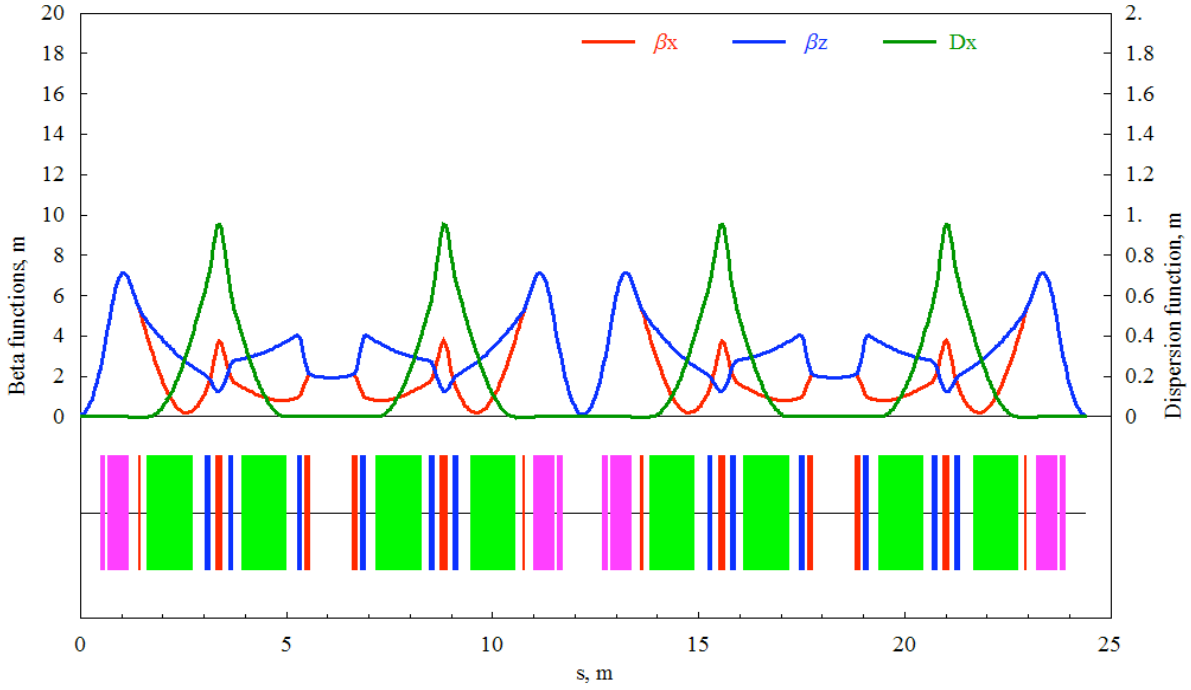


**Figure 2:** Lattice functions of VEPP-2000 storage ring.

### 3.23.3 Single Beam Studies

Commissioning of a collider started in the fall of 2007. First injection of electrons and positrons was performed at the beam energy 508 MeV. A temporary optics with switched off solenoids was prepared for that. This simplified optics has provided the functionality test of all the beam diagnostics. Besides, an extensive beam scrubbing was performed in optics with switched off solenoids. The vacuum chambers walls were subjected to irradiation by the synchrotron light with the total electron current exposure of about 20 Ampere*hours in both circulation directions.

Sixteen CCD cameras and the four pickups have shown 1 micron sensitivity to the orbit distortions at few milliamperes of the stored current. Besides, these fast pickups provided the tune measurements, sampling the signal of coherent oscillations induced by the kicker pulse.

By measuring the orbit responses to small changes of field gradients in quads ( $\Delta G$ wobbling method) the closed orbit was determined in all 20 quads and then the orbit was corrected with accuracy to about 0.1 mm.

Subsequently, by measuring the orbit responses to dipole correctors and then applying SVD analisys the actual optics reconstructrion was achieved.

Then the beam based alignment of solenoids was performed. The orbit responses to changes of currents in solenoids were measured and then the solenoids transverse displacements and inclinations were deduced using the optics theoretical model. After realignement the solenoids were powered with required currents and electrons were captured in almost nominal optics with the temporary working point $\nu_x = 4.4,\ \nu_y = 2.4$, which was shifted as far as possible from the integer resonances. Finally, after making a

set of orbit corrections, it was possible to shift the working point down to optimal for getting of high luminosity values: $\nu_x = 4.125,\ \nu_y = 2.125$.

Significant efforts were undertaken for the cancellation of the dynamical orbit distortions caused by the stray fields generated by a pulsed septum magnet. These distortions were successfully damped and stacking of positrons and electrons was achieved. The beam transfer efficiency from the booster storage ring BEP to VEPP-2000 has reached 80-90%.

To avoid the developing of head-tail instability the natural chromaticity was slightly overcompensated by two families of sextupole lenses. No coherent instabilities were observed up to 150 mA of the stored beam current.

Damping time of horizontal oscillations and its dependence versus the revolution frequency were found in perfect agreement with the theoretical model: $\tau_x = 21\ \text{ms},\ d(\tau_x^{-1})/df_0 = 0.0098\ \text{ms}^{-1}\text{kHz}^{-1}$.

It was interesting to investigate of how close to integer tunes we can brought the working point. For this we made a 2D tune scan, measuring tunes and checking that the single beam life time exceeds 100 s. Results are presented in the Fig. 3. Clearly, the widths of integer resonances are in the order of: $\Delta\nu_x = 0.05,\ \Delta\nu_y = 0.025$.

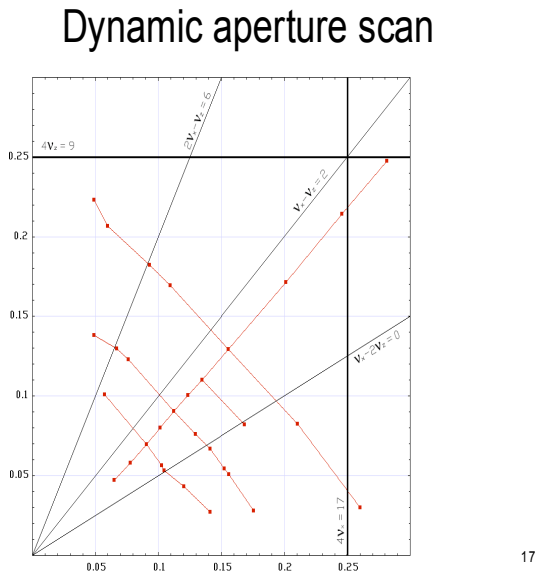


**Figure 3:** Experimental points show the accessible region of tunes in vicinity of integer resonances (no collisions, single beam).

### 3.23.4 Beam-Beam Experiments

It was decided to perform the first beam-beam study in a mode having the zero field integrals in both - SND and CMD detectors straight sections, i.e. having opposite polarities of longitudinal fields in two solenoids of each straight section, see the Fig. 4. In such decoupled optics the roundness of beams was organized by placing the tune

working point exactly on the main coupling resonance $\nu_x - \nu_y = 2$. The minimal residual coupling was reached $|\nu_1 - \nu_2| = 0.004$.

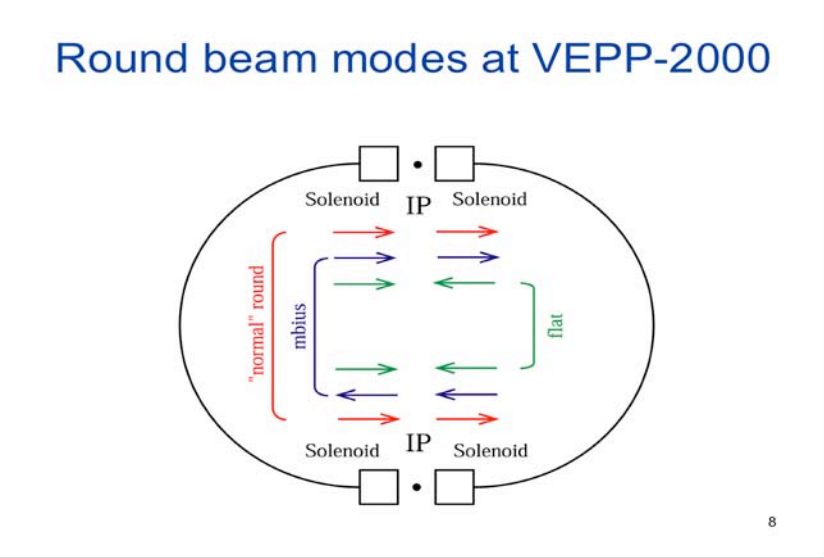


**Figure 4:** Three possible optics schemes with different polarities of longitudinal field in solenoids. Green arrows show the polarities used in first commissioning run.

The tune scan across the main coupling resonance $\nu_x - \nu_y = 2$ reveals a drastic decrease of the beam-beam current threshold in case of large detuning from the diagonal line. We have found that allowable by beam-beam effects detuning should not exceed of $|\nu_1 - \nu_2| = 0.01$, or less.

The results of a tune scan along the diagonal line $\nu_x - \nu_y = 2$ are presented in the Fig. 5. Many resonances are seen there and the node: $\{\nu\} = 1/6$ is the strongest one. Seems, the reduction of dynamic aperture, when the working point approaches too much the integer tunes node, limits the observed beam-beam current threshold.

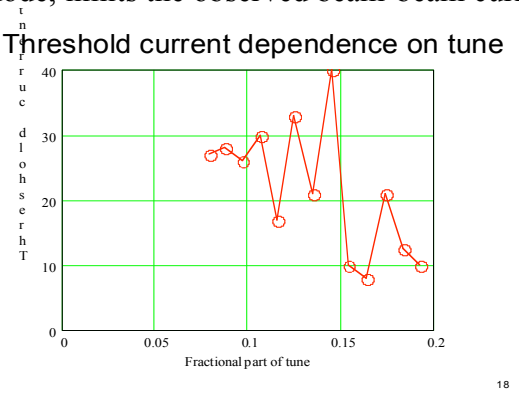


**Figure 5:** Beam-beam limit on a strong beam current versus the fractional part of tunes: $\{\nu\} = \{\nu_x\} = \{\nu_y\}$.

Also the beta-function at IP was varied by a special knob. Results are presented in the Fig. 6. The optimum around $\beta^* = 5$ cm is not very sharp.


**Figure 6:** Beam-beam limit on a strong beam current versus the beta-function value at IP.

We also have measured the dependence of sizes of a weak positron beam on the strong electron beam current, see the Fig. 7.

Beam sizes were measured by four CCD cameras located at different places. The large semi-axis corresponds to the vertical direction and the small one to the horizontal direction. This plot was obtained at the nominal working point and with $\beta^* = 4.5$ cm. At $I^- = 41$ mA the positron beam-beam parameter reaches $\xi = 0.08$! This value of $\xi$ exceeds the design number of $\xi = 0.075$, which was assumed to be achieved only at highest beam energy 1 GeV. In somewhat better conditions the strong beam current threshold has reached $I^- = 53$ mA. This corresponds to $\xi = 0.1$ per one crossing!

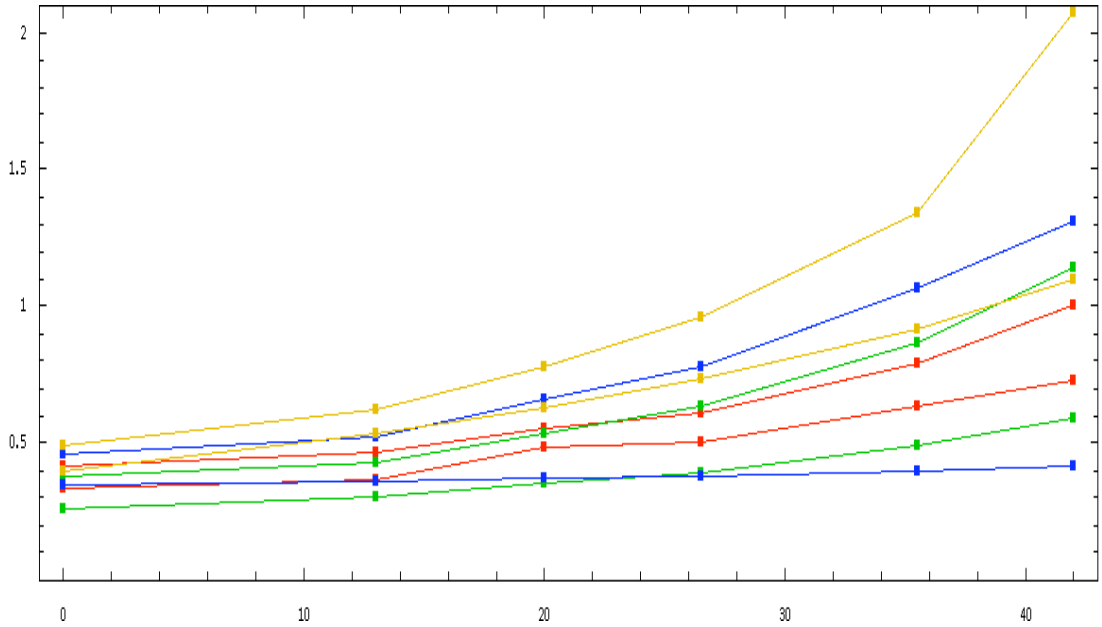


**Figure 7:** Dependence of sizes of a weak positron beam on the strong electron beam current.

In the Fig. 8 one can see how the positron beam looks like at 3 different CCD cameras. Practically everywhere the vertical beam size is larger than a horizontal one, because of larger vertical beta-function value there. Therefore some ellipses are stretched mainly in the vertical direction.

In January 2008 a short run with the full intensity colliding beams was made. The best luminosity $L = 1 \cdot 10^{31}\ \mathrm{cm}^{-2}\mathrm{s}^{-1}$ was achieved with equal stored currents $I^+ = I^- = 42\ \mathrm{mA}$, ($\xi = 0.08$). The luminosity was monitored by the SND detector, which has identified the events of $e^+e^-$ scattering at large angles.

Unfortunately, a burning of one superconducting current lead happens just the next day after this success and the collider operation was stopped for repairing of this current lead. Later on, it was decided to upgrade the suspension system of all four solenoids with the aim to reduce the liquid helium consumption. This goal was achieved: the helium consumption was improved roughly by a factor of 2. Commissioning was restored in January 2009 and new results are expected soon.

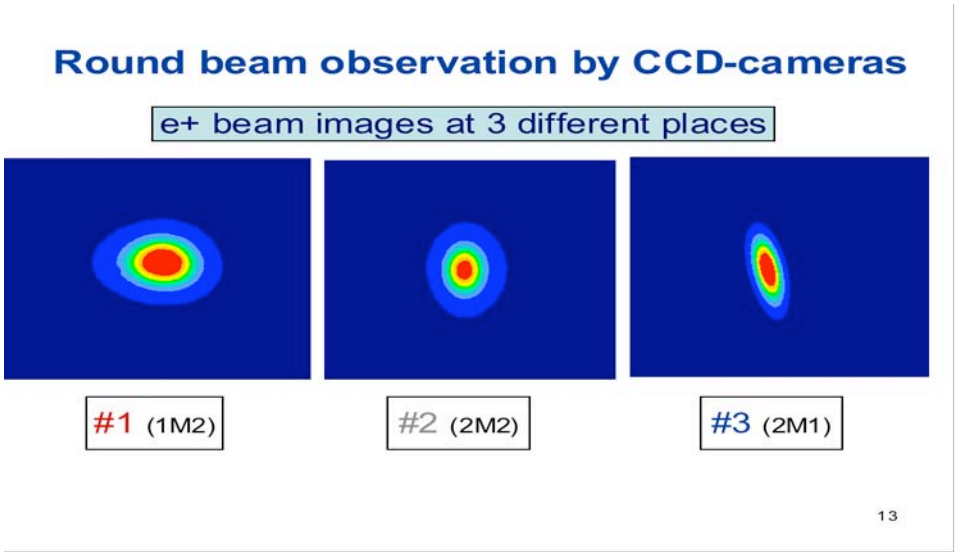


**Figure 8:** Beam profile measured in 3 different azimuths. The transverse motions are fully coupled due to choice of tune point sitting exactly at the linear coupling resonance $\nu_x - \nu_y = 2$.

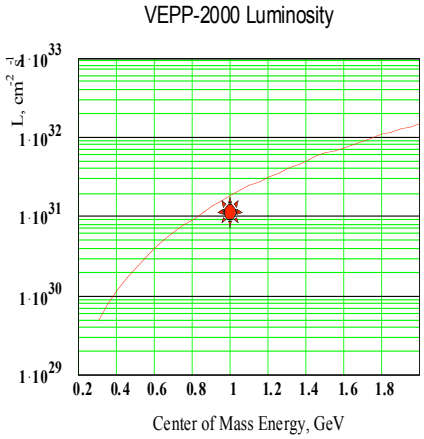


10

**Figure 9:** The luminosity theoretical curve and one experimental point measured at $\phi-$meson energy.

### 3.23.5 Conclusion

Round beams mode approach was successfully tested at VEPP-2000 collider. The maximum luminosity was observed $L=1\cdot10^{31}$ cm$^{-2}$s$^{-1}$ at $\phi-$meson energy. The space charge beam-beam parameter has reached $\xi=0.08$ per each of two crossings. Potentially $\xi=0.1$ could be expected and, correspondingly, the luminosity could reach $2\cdot10^{31}$ cm$^{-2}$s$^{-1}$ at this energy. At 2 GeV of centre of mass energy we expect to reach $1.6\cdot10^{32}$ cm$^{-2}$s$^{-1}$.

### 3.23.6 References

1. Yu.M.Shatunov et al. In Proc. of the 2000 European Particle ACC. Conf., Vienna, 2000, p.439.

## 3.24 The SuperB Accelerator Project

A. Alesini, M.E. Biagini, R. Boni, M. Boscolo, T. Demma, A. Drago, S. Guiducci, G. Mazzitelli, P. Raimondi, M. Serio, A. Stella, S. Tomassini, M. Zobov
INFN Laboratori Nazionali Frascati, Italy
K. Bertsche, M. Donald, Y. Nosochov, A. Novokhatski, M. Pivi, J. Seeman, M. Sullivan, G. Yocky, U. Wienands, W. Wittmer
SLAC, USA
S. Bettoni, D. Quatraro, CERN, Switzerland
E. Paoloni, G. Marchiori, Pisa University, Italy
A. Bogomyagkov, I. Koop, E. Levichev, S. Nikitin, P. Piminov, D. Shatilov
BINP, Russia
G. Bassi, A. Wolski, Daresbury, UK
A. Variola, LAL, Orsay, France
Mail to: marica.biagini@lnf.infn.it

### 3.24.1 Introduction

A Super B-Factory, an $e^+e^-$ collider at the center of mass B pairs production energy (10.58 GeV), with a luminosity of order $10^{36}$ $cm^{-2}s^{-1}$, can provide a uniquely sensitive probe of New Physics in the flavour sector of the Standard Model.

The PEP-II and KEKB asymmetric colliders [see Reports in this Issue] have produced unprecedented luminosities, above $10^{34}$ $cm^{-2}$ $s^{-1}$, taking our understanding of the accelerator physics and engineering demands of asymmetric $e^+e^-$ colliders to a new parameter regime. The study of New Physics effects in the heavy quark and heavy lepton sectors, however, requires a data sample two orders of magnitude larger, hence the luminosity target of $10^{36}$ $cm^{-2}$ $s^{-1}$ for *SuperB*, an asymmetric (7 GeV HER, 4 GeV LER) $e^+e^-$ collider.

A collider like *SuperB* will open a unique window on this physics because it will allow a high statistics study of the current hints of new aggregations of quarks and gluons. Besides the physics one can study in running at the Y(4S) resonance, the following alternative energies are of interest: Y(3S) (at least 0.3 $ab^{-1}$) and a high luminosity scan between 4-5 GeV (5 MeV steps of 0.2 $fb^{-1}$ each would require a total of 40 $fb^{-1}$). While this is not huge statistics, this scan is only feasible with *SuperB*. The only possible competitor, BES-III, is not planning to scan above 4 GeV, since their data sample would, in any case, be lower than that of the B-Factories alone. Finally, the search for exotic particles among the decay products of the "bottomonia" can probe regions of the parameters space of non-minimal supersymmetric models that cannot be otherwise explored directly, for instance at LHC. These studies are particularly efficient when producing Y(nS) mesons with $n < 4$.

The superiority of *SuperB* with respect to the planned upgrade of KEKB lays both in the higher statistics, which broadens the range of cross sections the experiment is sensitive to, but also in the flexibility to change center of mass energy. Moreover collisions with a longitudinally polarized electron beam for producing polarized $\tau$ leptons will be a unique feature of this project, opening an entirely new realm of exploration in lepton flavour physics,.

The design of *SuperB* combines extensions of the design of the past and present B-Factories with new linear collider concepts to produce an extraordinary leap in B-Factory luminosity without increasing beam currents or power consumption.

The implementation of a new colliding scheme [1, 2] with the combination of "large Piwinski angle", low $\beta_y$*, ultra low emittances and "*crab waist*" transformation opened new possibilities, hence allowing for a target luminosity two orders of magnitude higher than presently achieved, by overcoming some of the issues that have plagued earlier "super" $e^+e^-$ collider designs, such as very high beam currents and very short bunches. This scheme has being firstly tested at the upgraded DAΦNE Φ-Factory in Frascati, with very exciting results [4, and also C. Milardi's Report in this Issue]. Details on the scheme features and principles, as well as comparison between simulations and measurements, can be found in M. Zobov's Report in this Issue.

This scheme has been also taken into consideration for the new design of the Super KEKB accelerator [see Y. Ohnishi's Report in this Issue], as a solution to overcome possible difficulties related to the high currents (9.4 x 4.1 Amps), short bunches (3 mm) approach.

A Technical Design Report (TDR) will be started in spring 2009 to define the accelerator design and to clarify R&D activities before to proceed with construction, possibly already in 2011.

## 3.24.2 The *SuperB* Accelerator

### *3.24.2.1 Design Strategy*

The construction and operation of modern multi-bunch $e^+e^-$ colliders have brought about many advances in accelerator physics in the area of high currents, complex interaction regions, high beam-beam tune shifts, high power RF systems, controlled beam instabilities, rapid injection rates, and reliable uptimes (~90%).

A Conceptual Design Report (CDR) [5] was issued in May 2007, with about 200 pages dedicated to the accelerator design. This report discusses site requirements, crab waist compensation, parameters optimization in order to save power, IP quadrupole design, Touschek backgrounds, spin rotator scheme, and project costs. The ring lattices have been modified to produce very small horizontal (a few nm-rad) and vertical emittances (a few pm-rad). Crab waist sextupoles near the interaction region introduce a left-right longitudinal waist position variation in each beam allowing a vertical beta function which is much smaller than the bunch lengths.

*SuperB* consists of two rings of different energy (electrons in HER, 7 GeV, positrons in LER, 4 GeV) colliding in one Interaction Region (IR) at a large (60 mrad total) horizontal angle. Spin rotator sections in the HER will provide helicity of a polarized electron beam. The two rings each have two arcs and two long straight sections. One straight will house the IR, the other will be used for the diagnostics, RF, and injection lines. The crab waist scheme, with a couple of sextupoles per ring in a dispersive section near the IR, and an appropriate betatron phase with respect to the IP, will create a longitudinal waist shift over the width of the beam, so providing suppression of betatron and synchrobetatron resonances arising from the crossing angle geometry. To save on costs the design is based on the reuse of the PEP-II (SLAC)

hardware, including magnets, beam pipe, RF. A possible layout at Tor Vergata University campus near Rome (Italy) is shown in Figure 1.

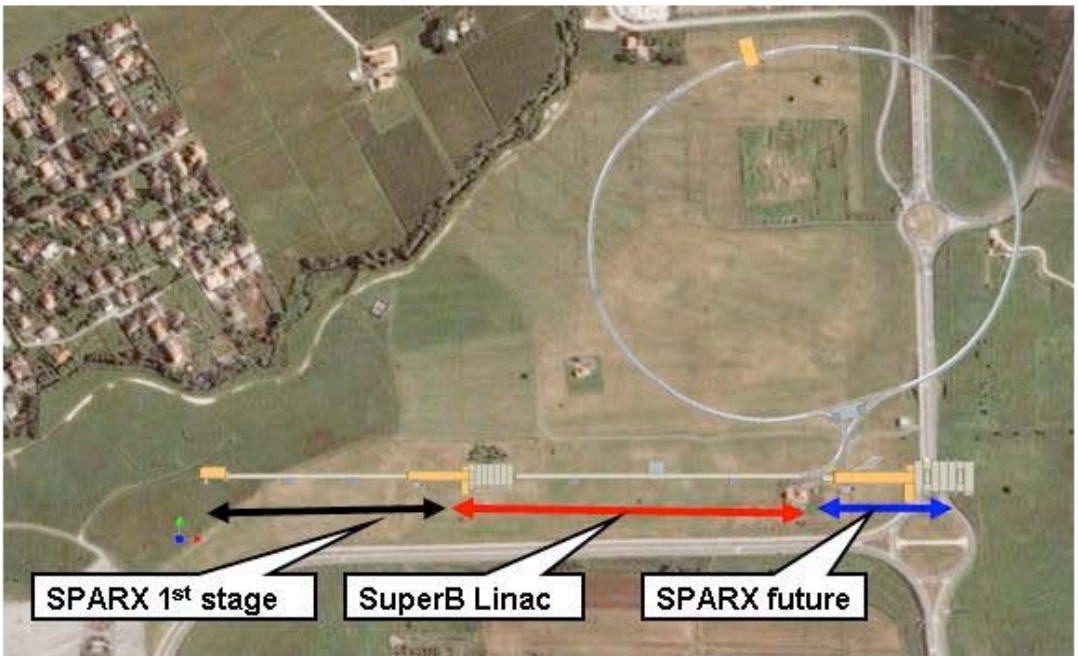


**Figure 1:** Possible *SuperB* location at Tor Vergata University campus, with a ring circumference of 1800 m and an injector located adjacent to the future SPARX FEL.

Recently the *SuperB* parameters have been slightly modified in order to decrease the vertical tune shifts, while maintaining the goal peak luminosity: this is possible by slightly increasing the beam currents and consequently the RF wall plug power. Also, parameter flexibility in reaching the design luminosity is desirable. In Table 1 are reported for comparison the previous parameters (column 3, June 2008) and the most recent ones (column 4, January 2009). Two additional scenarios have been considered in order to further relax the vertical beam-beam tune shifts: double number of bunches with bunch current decreased by a factor √2 (column 5), double number of bunches and vertical emittance increased by a factor of 4 (column 6). In the RF wall plug calculations the bunch lengthening effect has been taken into account.

**Table 1:** *SuperB* rings main parameters.

| ***Parameter (LER/HER)*** | ***Unit*** | ***June 2008*** | ***January 2009*** | ***2xN$_b$, I$_b$/√2*** | ***2xN$_b$, 4xε$_y$*** |
|---|---|---|---|---|---|
| Energy | GeV | 4/7 | 4/7 | 4/7 | 4/7 |
| Luminosity | $cm^{-2}s^{-1}$ | $1x10^{36}$ | $1x10^{36}$ | $1x10^{36}$ | $1x10^{36}$ |
| Circumference | m | 1800 | 1800 | 1800 | 1800 |
| No of bunches, $n_b$ | | 1250 | 1250 | 2500 | 2500 |
| $F_{RF}$ | MHz | 476 | 476 | 476 | 476 |
| No of particles/bunch | | $5.5x10^{10}$ | $6x10^{10}$ | $4.23x10^{10}$ | $6x10^{10}$ |
| Current/beam | A | 1.85/1.85 | 2/2 | 2.82/2.82 | 4/4 |
| Current/bunch | mA | 1.48 | 1.6 | 1.13 | 1.6 |
| $\beta_x$* | mm | 35/20 | 35/20 | 35/20 | 35/20 |
| $\beta_y$* | mm | 0.22/0.39 | 0.21/0.37 | 0.21/0.37 | 0.21/0.37 |
| Emittance $\varepsilon_x$ | nm·mrad | 2.8/1.6 | 2.8/1.6 | 2.8/1.6 | 2.8/1.6 |
| Emittance $\varepsilon_y$ | pm·mrad | 7/4 | 7/4 | 7/4 | 28/16 |
| rms hor. size $\sigma_x$ | μm | 9.9/5.7 | 9.9/5.7 | 9.9/5.7 | 9.9/5.7 |
| rms vert. size $\sigma_y$ | nm | 39/39 | 38/38 | 38/38 | 77/77 |
| rms nat. bunchlength $\sigma_z$ | mm | 5/5 | 5/5 | 5/5 | 5/5 |
| Full crossing angle $\theta_{cross}$ | mrad | 50 | 60 | 60 | 60 |
| Damping times $\tau_{x,y}/\tau_s$ | msec | 40/20 | 40/20 | 40/20 | 40/20 |
| Theoretical H-tune shift | | 0.007/0.002 | 0.005/0.0017 | 0.004/0.0012 | 0.005/0.0017 |
| Theoretical V-tune shift | | 0.14/0.14 | 0.125/0.125 | 0.09/0.09 | 0.06/0.06 |
| RF AC power | MW | 16.2 | 18 | 25.5 | 39.3 |

The injection system needed for the *SuperB* is similar to the one of PEP-II. A preliminary design is shown in Figure 2. Since the beam lifetimes are of the order of 10-30 minutes, continuous injection will be needed. A polarized electron gun, similar to the SLAC one, will provide polarized electrons. Two small damping rings will reduce $e^+$ and $e^-$ emittances.

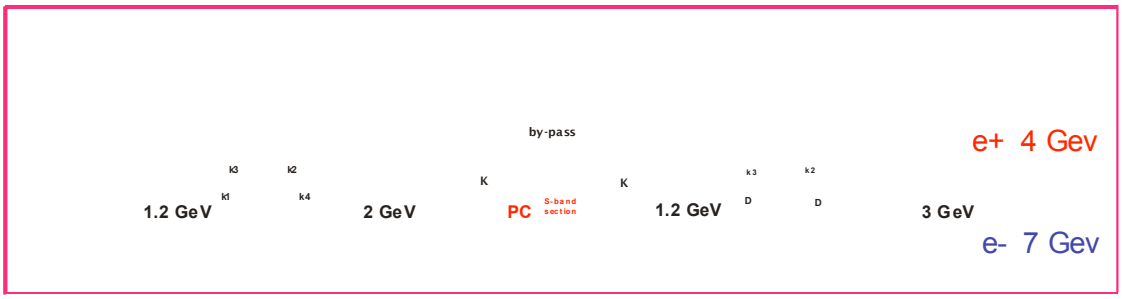


**Figure 2:** Schematic of the *SuperB* injector.

The power required for this collider is the sum of power for the magnets, RF system, cooling water, controls, and the accelerator operation. These values do not include the campus power requirements or that of the particle physics detector. Due to the advantages of the very low emittances and the crab waist with this design, the power requirements are significantly lower than those of the present B-Factory colliders. The present estimates indicate about 20 MW is needed for the nominal luminosity goal.

### *3.24.2.2 Lattice Design*

The optimization of the ring lattices, performed after the CDR completion, aimed to minimize the intrinsic emittance so that nominal values can be obtained even without wigglers and the ring circumference is shortened, better fitting the proposed construction site. When increasing the horizontal phase advance $\mu_x$ in the *Super*B arc cell, the intrinsic emittance naturally decreases. The damping time increases by 30% but the RF power decreases, with a net operational costs saving. Beam-beam simulations have studied the degree to which an increase in the damping time affects the luminosity and beam-beam induced tails: an increase by a factor of 2.5 does not lead to any substantial luminosity degradation. In the new lattice the longitudinal damping times are of the order of 20 msec in both rings, about 1.3 times larger than the CDR values and still below the threshold of beam tail growth. Moreover the design emittances can be reached without the insertion of wiggler magnets.

LER and HER lattices [6] are very similar, and based on the reuse of most PEP-II magnets. The arcs have an alternating sequence of two different cells: a $\mu_x = \pi$ cell that provides the best dynamic aperture, and a $\mu_x = 0.72$ cell that has a much smaller intrinsic emittance and provides a phase slippage for the sextupoles pairs, in such a way that one arc corrects all the phases of the chromaticity. As a consequence, the chromatic functions $W_x$ and $W_y$ are lower than 20 and the second order dispersion is almost zero everywhere except in the IR). With this arrangement, the number of arcs can be reduced to 4, with two 40 m long straight sections. With 14 cells in each arc a horizontal emittance of 1.6 nm in HER and 2.8 nm in LER are obtained, the LER lattice having still room for further reduction. Fig. 3 shows the beta functions for the HER and LER arc cells.

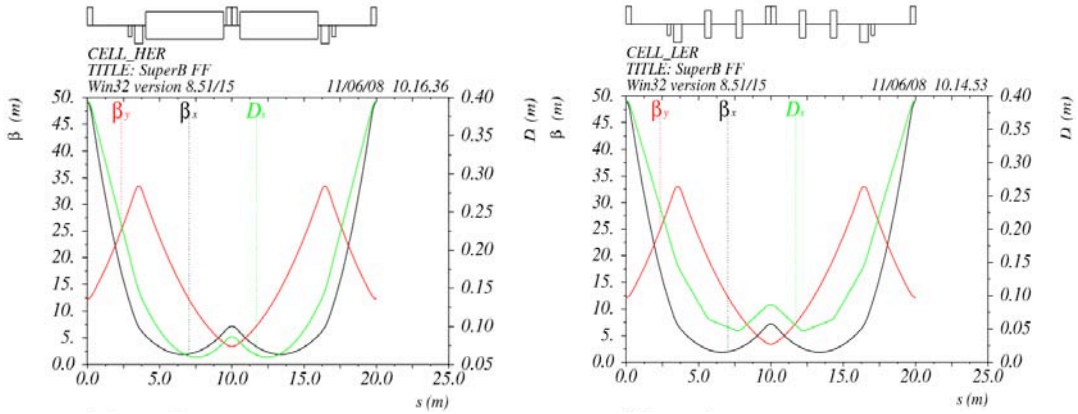


**Figure 3:** Optical functions in HER (left) and LER (right) arc cells.

### *3.24.2.3 Interaction Region*

The IR (see Figure 4) is designed to be similar to that of the ILC and to leave about the same longitudinal free space for the detector as that presently used by BABAR or BELLE, but with superconducting quadrupole doublets QD0/QF1 as close to the interaction region as possible [7, 8].

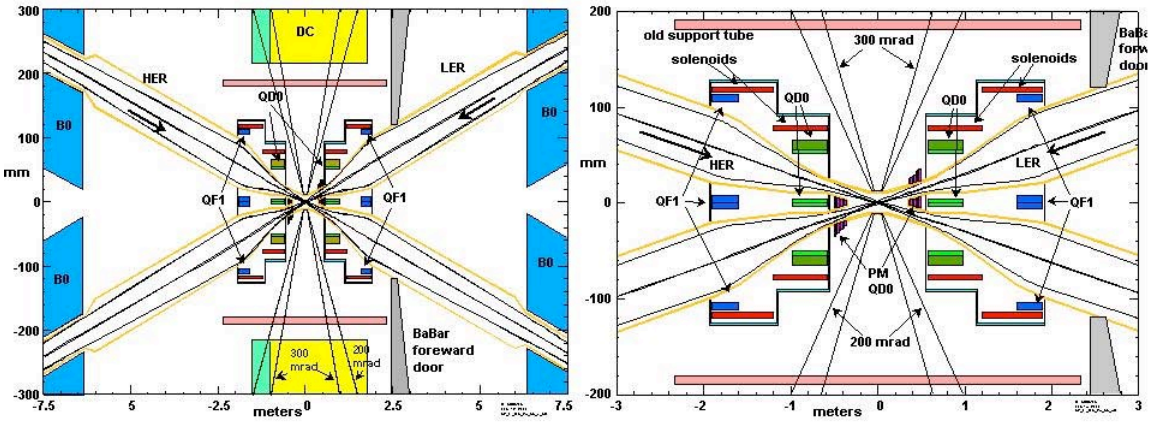


**Figure 4:** IR for two asymmetric beams (left) and close up of the IP zone (right).

The total Final Focus (FF) length is about 160 m and the final doublet is at 0.4 m from the IP, with the beams horizontally crossing at 60 mrad. A plot of the optical functions in the incoming half of the FF region is presented in Figure 5, while Figure 6 shows the optical functions in all the LER (HER being very similar).

The choice for a finite crossing angle at the IP greatly simplifies the IR design, naturally separating the beams at the parasitic collisions. The resulting vertical beta is about 0.2-0.3 mm and the horizontal 35 mm. These beta values are much closer to a linear collider design than a traditional circular collider. The beams enter the IP nearly straight to minimize synchrotron radiation and lost particle backgrounds and are bent more while exiting the IR to avoid parasitic collisions and the resulting beam-beam effects.

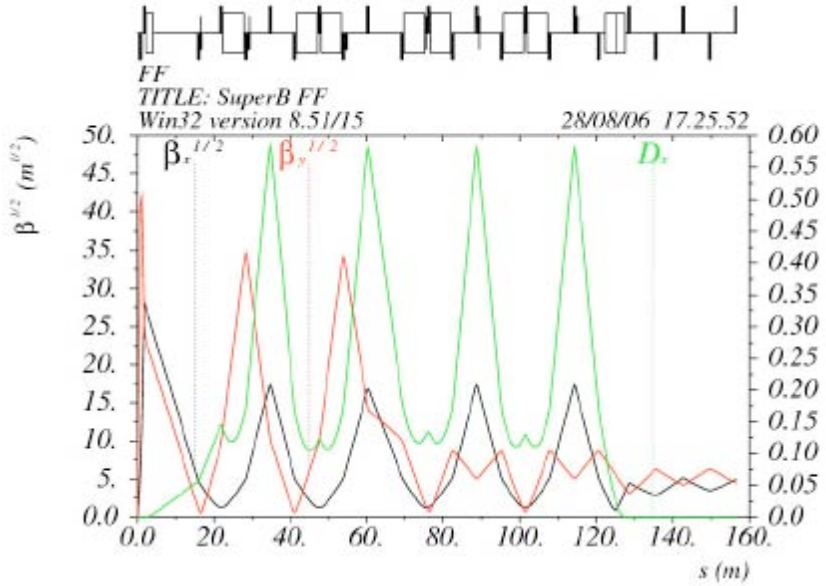


**Figure 5:** Optical functions for half Final Focus.

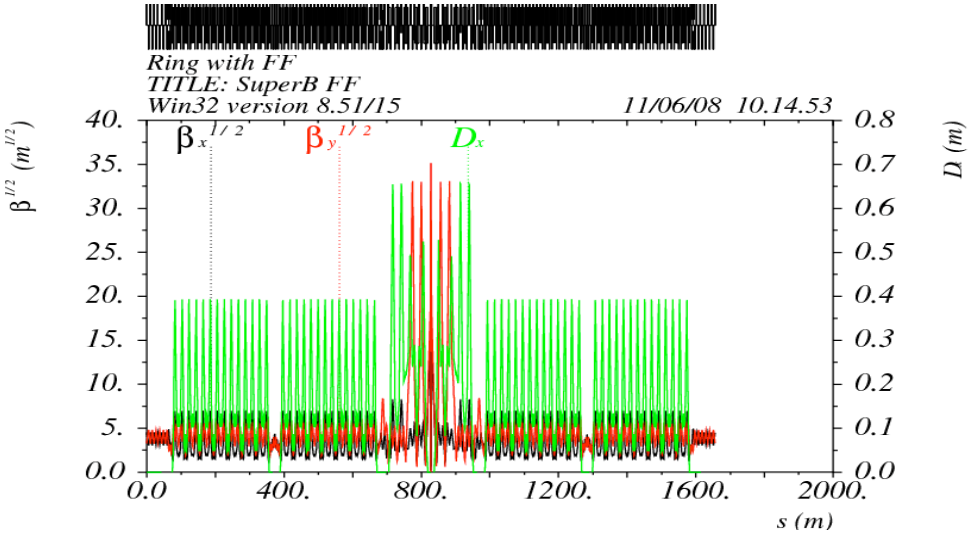


**Figure 6:** Optical functions in LER with Final Focus included.

The challenge for the magnets of the final doublet is to provide a good quadrupole field with gradients in excess of 50T/m, separately for each beam line. The final vertically focusing quadrupole (QD0) was initially thought as a magnetic element shared by both beams. However, although the bending of the off-axis beam was minimized in the IR design, the bending was still significant and caused several concerns. The radiative Bhabha beam particles, which had too low an energy, were swept out of the beam by the off-axis bending in QD0, and can cause a significant background in the detector. In addition, the bending can create high power synchrotron radiation (SR) fans that can be managed but do cause more exotic magnet designs for the outgoing beam magnets. The final concern was emittance growth from the high field bending in these shared quads. In order to eliminate some of these concerns and further improve the IR design, a new layout and a new concept to compensate the cross-talk among the two QD0's core and fringe fields has then been studied [8]. The limited amount of space available in between the two beam stay clear (~1cm) together with the required field strength make extremely difficult all the conventional designs. A novel approach, a "Siamese Twin" quadrupole based on the double-helix coils [9], has been proposed and is now under active development.

This new QD0 is a double quadrupole in that it has two magnetic centers with a septum of super-conducting coils. The magnet bores are cold in order to minimize the material between the two beams, thereby maximizing the beam-stay-clear (BSC). In addition, the crossing angle has increased to ±30 mrad and the QD0 magnet face has moved back from the IP. The magnets are composed by two double-helix coils, each one surrounding a single beam line (see Figure 7). All the coils are properly deformed with respect to the ideal sin (2π) shape, in such a way that undesired multipoles on the left (right) beam line, produced by the leaking field of the right (left) nearby magnet, are canceled out by counter-multipoles generated by the left (right) coils.

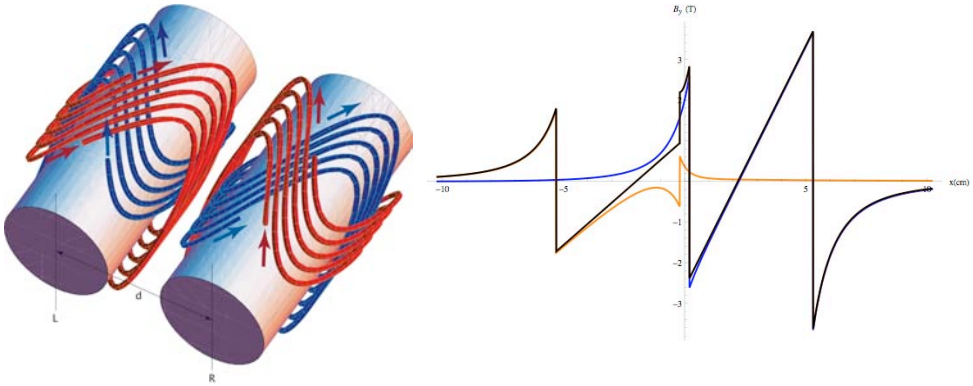


**Figure 7:** On the left side: a schematic view of the "Siamese Twin" quadrupoles. On the right side is the component $B_y$ of the field as a function of the radial coordinate x. (The left coils contribution in orange, the right one in blue and their sum in black.)

Attainable errors are in the $10^{-5}$ range and the required gradients seem achievable with conventional NbTi wires at 1.8 K.

This design strongly reduces the rate of off-energy particle losses near the IP, thus reducing the background rates seen in the detector with respect to a conventional design with a shared QD0. An additional small D-quadrupole will provide the necessary focusing to the HER beam.

#### *3.24.2.4 Polarization Scheme*

At *SuperB* energies, Sokolov-Ternov polarization takes too long and polarized electrons will be injected. The injector will have the necessary spin handling, and polarized sources with the required intensity exist (e.g. the SLC gun). At the IP, the desired polarization is longitudinal; this can be provided in principle either by 90° spin rotators up and downstream of the IP or by a Siberian Snake (180° rotator) diametrically opposite in the ring, thus avoiding the need for spin rotators matched to the critical IR optics. The rotators or Snake(s) can be designed either using solenoids or vertical dipoles together with horizontal dipoles. The overall spin matching in *SuperB* will be less critical than in facilities like HERA or LEP because of the short beam lifetime. This causes frequent injection of freshly polarized beam, thus reducing the effect of depolarization in the ring, so that maintaining above 90% of the injecting polarization is an achievable goal, provided rotators are spin-matched across the whole energy spread of the beam. It is still important to avoid integer spin tunes (and their synchrotron sidebands) as the spin orientation will move away from longitudinal at the IP for such values. Solenoid spin rotators tend to be more compact than pure dipole rotators, however for first-order spin matching they need to be anti-symmetric about the IP, leading to a horizontal "dog leg" in the IR layout causing a distortion of the ring geometry. The orbital coupling introduced by the solenoids is compensated by inserting a plane twister between two half-solenoids [10]. A pure dipole spin rotator has been designed that avoids this, i.e. its dipoles become part of the overall 360° bending, however, the vertical bends will raise the minimum vertical emittance achievable [11]. Figure 8 shows the HER half IR optical functions, with the spin rotator inserted [12].

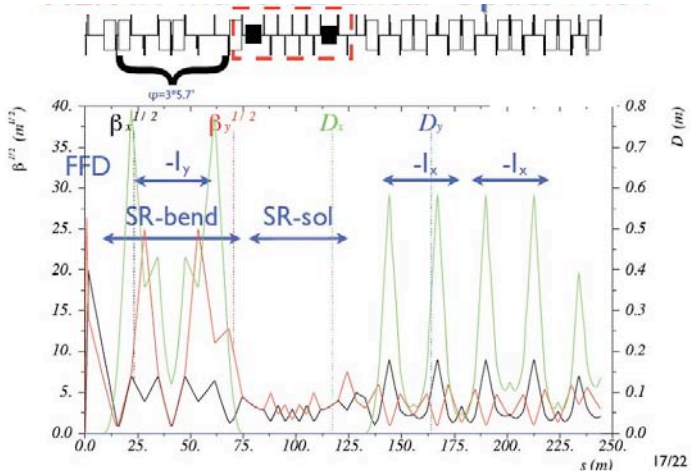


**Figure 8:** HER half IR optical functions, with the spin rotator inserted.

### 3.24.3 Summary

Accelerator studies have continued after the completion of the CDR, in order to optimize the rings performances while simplifying their designs, and including unique features as the polarization scheme of the electron beam. The *SuperB* lattice, based on the reuse of PEP-II hardware, fits in the Tor Vergata University campus site near Frascati. The new cell layout is more flexible in terms of emittance, and wigglers are no longer needed for the nominal operation scenario, with a net gain in wall plug power and costs. The rings are shorter and less costly, since the total number of magnets has been reduced. Spin rotator sections have been matched into the HER lattice.

In 2008 the *SuperB* accelerator design has been scrutinized by an International Review Committee (IRC) and by a Machine Advisory Committee (MAC).

The IRC, formed by 8 international experts chaired by J. Dainton (Daresbury, UK), was established in 2007 to review the whole project. It has closed its works in April 2008 with a very positive statement:

*"We recommend strongly that work towards the realization of a SuperB, taken to be an asymmetric $e^+e^-$ collider with luminosity at least $10^{36}$ $cm^{-2}s^{-1}$, continues. The SuperB concept is at an important stage. The significance of the physics program at such a machine continues to be developed, increasing in both scope and importance. It motivates an even more concerted effort to meet many technical challenges, in particular concerned with the design of storage rings which meet the physics specification. So far there has been no "showstopper"; rather there have emerged a number of innovative and noteworthy developments at the cutting-edge of contemporary technique in accelerator physics and of detector technology."*

The Machine Advisory Committee (MAC) for the accelerator, chaired by J. Dorfan (SLAC) and formed by 10 international accelerator experts from US and EU, has met for the first time in July 2008. The outcome from this first look at the accelerator design was highly positive. The MAC has issued a list of topics which will require further attention and study in order to fully validate the design. Work in the second half of 2008

has been focused on these topics. The next MAC review will take place at LNF the last week of April 2009.

In 2008 the *SuperB* project has also been presented to the CERN Strategy Group, to be included in the list of the European projects. Final decision will probably take place in Fall 2009.

### 3.24.4 References


1. P. Raimondi, 2nd LNF Workshop on *SuperB*, Frascati, 16-18 March 2006, http://www.lnf.infn.it/conference/superbf06/
2. P. Raimondi, "Crab waist collisions in DAΦNE and *SuperB* design", Proc. of EPAC08, June 2008, Genoa, Italy.
3. P. Raimondi and M. Zobov, "DAΦNE Technical Note G-58," April 2003; D. Shatilov and M. Zobov, ICFA Beam Dyn. Newslett. 37, 99 (2005). P. Raimondi, D. Shatilov, M. Zobov, "Beam-beam issues for colliding schemes with large Piwinski angle and crab waist", LNF-07/003 (IR), January 2007.
4. P. Raimondi et al, "DAΦNE crab waist beam tests", proceedings of 11th European Particle Accelerator Conference (EPAC 08), Genova, Italy, June 2008.
5. "SuperB Conceptual Design Report", INFN/AE-07/2, SLACR-856, LAL 07-15, arXiv:0709.0451.v2 [hep-ex] March 2007.
6. M.E. Biagini et al, "New low emittance lattice for the *SuperB* accelerator", Proc. of EPAC08, June 2008, Genoa, Italy.
7. M. Sullivan et al, "*SuperB* interaction region design", proceedings of 11th European Particle Accelerator Conference (EPAC 08), Genova, Italy, June 2008.
8. E. Paoloni et al, "IR SC quadrupole design for *SuperB*", proceedings of 11th European Particle Accelerator Conference (EPAC 08), Genova, Italy, June 2008.
9. C. Goodzeit, R. Meinke, M. Ball, Combiner Function Magnets Using Double-Helix Coils, Proceedings of the 2007 Particle Accelerator Conference, Albuquerque, New Mexico, USA
10. A. Zholents, P. Litvinenko, BINP Report 81-60, Novosibirsk, Russia.
11. I. Koop, Proc. of 40$^{th}$ ICFA Advanced Beam Dynamics Workshop 2008, BINP, Russia, 2008.
12. W. Wittmer, SLAC, private communication.


## 3.25 Recent Report on Design of SuperKEKB


Y. Ohnishi
High Energy Accelerator Research Organization (KEK), Tsukuba, 305-0801, Japan
Mail to: yukiyoshi.onishi@kek.jp


### 3.25.1 Consideration of Machine Parameters

#### *3.25.1.1 History of Machine Parameters*

The target luminosity of SuperKEKB is more than $5x10^{35}$ $cm^{-2}s^{-1}$ that is given by tentative machine parameters as shown in Table 1. The beam energy is 3.5 GeV (LER) for positrons and 8 GeV (HER) for electrons that is optimized by a physics requirement. Polarization of a colliding beam is not included as an option so far. In order to satisfy

the requirement, we have designed SuperKEKB with a short bunch length for both rings and high beam currents until the end of 2008. The parameters are shown in Table 1 which are indicated by "2008". However, a serious problem due to a coherent synchrotron radiation (CSR) arises from a computer simulation study. The CSR effect in SuperKEKB has been studied by T. Agoh since 2004, which is found in Letter of Intent for KEK Super B Factory [1]. Recently, an independent calculation that includes a realistic shape of a beam pipe and most of impedance sources considered in the SuperKEKB ring has been done by K. Oide in 2008 [2]. This realistic estimation is consistent with those of T. Agoh in principle. The wake fields come from accelerating cavities, ante-chambers, masks, bellows, pumps, BPMs, and so on are considered in the calculation. The longitudinal wake field due to the CSR is found to be much larger than the other wake fields. The height of the beam pipe does not help to reduce the CSR effects so much with the range of 90 to 50 mm. In the case of LER, the initial bunch length of 3 mm becomes 5.5 mm and the energy spread increases by 65 % due to the CSR. On the other hand, the CSR effect is negligible in HER. Therefore, we have decided to make the bunch length in LER longer than 3 mm. In this analysis, we also compare the case of a positive momentum compaction with a negative momentum compaction. The negative momentum compaction is slightly better than the positive. The optimized bunch length is 4.5 mm in LER and 3 mm in HER for the zero bunch current, respectively. The bunch length for the design current is estimated to be 5.3 mm in LER and 3.1 mm in HER. The energy spread increases by 20 % at most.

In order to compensate an hourglass effect due to the longer bunch length, we adopt a *travel waist* [3] in LER. The parameters for the travel waist are shown in Table 1. The luminosity is obtained from the strong-strong simulation with the travel waist, however, the travel waist is not considered to calculate the beam-beam parameters in the table. We use a combination of crab cavities and sextupole magnets to realize the travel waist at IP. In this travel waist scheme, a HER beam always collides a LER beam at the LER vertical waist.

Both case of the crab-crossing scheme with the short bunch and the travel waist scheme is called *a high current scheme*. A characteristic of the high current scheme is an extremely high beam-beam parameter that is a level of 0.3 or more. We have invested the crab-crossing scheme to improve the beam-beam parameter, however, the achieved beam-beam parameter is 0.09 at KEKB in 2008 [4]. Since the beam-beam simulation for the ideal case still suggests a feasibility of the high beam-beam parameter [5], we continue to investigate the reason of the present result and to reduce machine errors for the improvement of the luminosity performance in the experiment.

In contrast, *a Low beta and a Low emittance scheme with a Large crossing angle* (LLL scheme) has been proposed to achieve a higher luminosity for SuperB [6]. This scheme is also called a super-bunch scheme. The super-bunch scheme has a feasibility to achieve the same or larger geometric luminosity than the high current scheme with a smaller beam-beam parameter and smaller beam currents. The super-bunch scheme for SuperKEKB is also shown in Table 1. The machine parameters indicated by "Super-bunch (T)" is a tentative parameters with an assumption that the beam-beam parameter is less than 0.1. If the beam-beam parameter can achieve 0.14, the target luminosity can be $10^{36}$ $cm^{-2}s$-1 as indicated by "Super-bunch (H)".

A *crab waist scheme* [7] is proposed for SuperB by P. Raimondi together with the super-bunch scheme because the large Piwinski angle might induce a beam-beam blowup. The crab waist scheme has a capability to mitigate the beam-beam blowup. In

the crab waist scheme, the waist point moves along the x position. In order to make this possible, sextupole magnets with an appropriate phase advance to IP are installed, then a particle in a bunch collides with other beam at the waist point. The hourglass effect is further reduced. The crab waist scheme has been tested at DAΦNE and successfully works to improve the beam-bean performance [8].

**Table 1:** Machine parameters for SuperKEKB. Left is LER and right is HER. The parenthesis indicates a half finite-crossing angle for a crab crossing. *1beam-beam simulation. *2geometrical calculation.

| *Parameter LER/HER* | *Unit* | *2008* | *Travel Waist* | *Super-bunch(T)* | *Super-bunch(H)* |
|---|---|---|---|---|---|
| Energy | GeV | 3.5/8.0 | | | |
| Circumference | m | 3016 | | | |
| Current | A | 9.4/4.1 | | 2.70/1.55 | 2.65/1.55 |
| No of bunches | | 5018 | | 2500 | 1200 |
| No of particles (x$10^{10}$) | | 11.8/5.13 | | 6.78/3.89 | 13.9/8.11 |
| Horizontal emittance | nm | 12/12 | 24/18 | 1/10 | 1/10 |
| Vertical emittance | pm | 60/60 | 240/90 | 3.5/25 | 3.5/25 |
| Horizontal beta | mm | 200/200 | 200/200 | 35/20 | 35/10 |
| Vertical beta | mm | 3/3 | 3/6 | 0.35/0.22 | 0.35/0.22 |
| Bunch length | mm | 3/3 | 5/3 | 6/6 | 6/6 |
| Half crossing angle | mrad | 0 (15) | 0 (15) | 30 | 30 |
| Piwinski angle | | 0/0 (0.92/0.92) | 0/0 (1.1/0.75) | 30/13 | 30/18 |
| Horizontal beam-beam | | 0.272/0.272 | 0.182/0.138 | 0.003/0.001 | 0.006/0.002 |
| Vertical beam-beam | | 0.295/0.295 | 0.295/0.513 | 0.067/0.068 | 0.139/0.139 |
| Luminosity (x$10^{35}$) | $cm^{-2}s^{-1}$ | 5.5*1 | 5.3*1 | 5.0*2 | 10*2 |

#### *3.25.1.2 Travel Waist Scheme*

The travel waist with the crab crossing is realized by using crab cavities and sextupole magnets. Two sextupole magnets (SX1) are located with a phase advance with IP at π in the x plane and at π/2 in the y plane, on both sides of IP. Two sextupole magnets (SX2) are placed at –I' transformation with SX1 to eliminate a crab waist term for each. Crab cavities are located between SX1 and SX2 with IP at π/2 in the x plane. A schematic view of the travel waist scheme is shown in Figure 1.

Hamiltonian generated by a sextuple magnet is expressed by

$$H_I = k_x X^3 + k_y X Y^2, \tag{1}$$

where X and Y is a normalized coordinate with Twiss parameters,

$$X = \frac{x}{\sqrt{\beta_x}} \quad P_X = \frac{\beta_x}{\sqrt{\alpha_x}} x + \frac{p_x}{\sqrt{\beta_x}} \quad Y = \frac{y}{\sqrt{\beta_y}} \quad P_Y = \frac{\beta_y}{\sqrt{\alpha_y}} y + \frac{p_y}{\sqrt{\beta_y}} \quad Z\phi = \frac{z\phi}{\sqrt{\beta_x}} \tag{2}$$

where ϕ is a half crossing angle at IP and

$$k_x = \frac{\beta_x^{3/2} K}{6} \quad k_y = -\frac{\beta_x^{1/2} \beta_y K}{2}. \tag{3}$$

The strength of the sextupole magnet is denoted by K. The second term of the Eq. (1) for a transformation from the sextupole magnet (SX1) to IP is written by

$$\begin{aligned} H_{I,SX1} &= k_y \left( X \cos\Delta\psi_x + P_X \sin\Delta\psi_x + Z\phi \right) \left( Y \cos\Delta\psi_y + P_Y \sin\Delta\psi_y \right)^2 \\ &= k_y \left( -XP_Y^2 + \phi Z P_Y^2 \right) \end{aligned}, \tag{4}$$

where $\Delta\psi_x=\pi$ and $\Delta\psi_y=\pi/2$. On the other hand, SX2 to IP is

$$\begin{aligned} H_{I,SX2} &= k_y \left( X \cos\Delta\psi_x + P_X \sin\Delta\psi_x \right) \left( Y \cos\Delta\psi_y + P_Y \sin\Delta\psi_y \right)^2 \\ &= k_y X P_Y^2 \end{aligned}, \tag{5}$$

where $\Delta\psi_x=2\pi$ and $\Delta\psi_y=3\pi/2$.Therefore,the crab waist term, $XP_Y^2$ and $X^3$ terms are cancelled by SX2. The remaining term, $\phi Z P_Y^2$ is the travel waist term comes from the pair of sextupole magnets. The total Hamiltonian at IP from the both pairs is

$$\begin{aligned} H_I &= 2k_y \phi Z P_Y^2 \\ &= -\beta_y \beta_y^* \sqrt{\frac{\beta_x}{\beta_x^*}} \phi K \cdot z p_y^2 . \\ &= -\frac{1}{2} z p_y^2 \end{aligned} \tag{6}$$

In order to make the travel waist, the required strength of the sextupole magnet is

$$K = \frac{1}{2\phi\beta_y\beta_y^*} \sqrt{\frac{\beta_x^*}{\beta_x}}. \tag{7}$$

In the case that the horizontal beta at IP is 20 cm and 15 m at the travel waist sextupole and the vertical beta at IP is 3 mm and 350 m at the sextupole, the K value becomes 3.7 $m^{-2}$ for 15 mrad half crossing angle. The K value is within the range used in KEKB. Two sets of sextupole magnets and the crab cavity are necessary to localize the travel waist in the interaction region (IR).

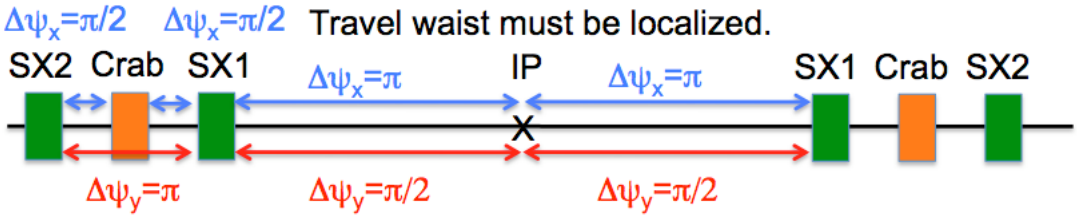


**Figure 1:** A schematic view of the travel waist.

#### *3.25.1.3 Super-Bunch Scheme*

The luminosity is expressed in general by

$$L = \frac{N_p N_e f_{col}}{2\pi\sqrt{\sigma_{xp}^2 + \sigma_{xe}^2}\sqrt{\sigma_{yp}^2 + \sigma_{ye}^2}} R_L, \tag{8}$$

where $N_{p,e}$ is a number of particles per a bunch for a positron and an electron, $\sigma_x$ and $\sigma_y$ is a beam size in the horizontal and the vertical plane, respectively. The luminosity reduction is indicated by $R_L$. The beam-beam parameters for a positron are written by

$$\begin{aligned} \xi_{xp} &= \frac{r_e}{2\pi\gamma_p}\frac{\beta_{xp}N_e}{\sigma_{xe}\left(\sigma_{xe}+\sigma_{ye}\right)}R_{\xi x} \\ \xi_{yp} &= \frac{r_e}{2\pi\gamma_p}\frac{\beta_{yp}N_e}{\sigma_{ye}\left(\sigma_{xe}+\sigma_{ye}\right)}R_{\xi y} \end{aligned}, \tag{9}$$

where $R_\xi$ is a reduction factor, the beam-beam parameters for an electron are similar to those of Eq. (9) except for replacing p with e. When the super-bunch which is a small transverse beam size and a large crossing angle satisfies a condition of the hourglass suppression, the horizontal beam size can be replaced by a bunch length by a product of a half crossing angle at IP which is a projected beam size in the x direction. The requirement to suppress the hourglass effect,

$$\beta_{yp} \geq l_e = \frac{\sigma_{xe}}{\phi} << 2\sigma_{ze} \quad \beta_{ye} \geq l_p = \frac{\sigma_{xp}}{\phi} << 2\sigma_{zp}, \tag{10}$$

where $l_e$ and $l_p$ is an overlapped length for the electron and the positron. The beta function at IP can be smaller than the bunch length. Consequently, the longer bunch is applicable compared with the high current scheme and a HOM heating can be reduced. Then, the luminosity can be written by

$$L = \frac{N_p N_e f_{col}}{2\pi\phi\sqrt{\sigma_{zp}^2 + \sigma_{ze}^2}\sqrt{\sigma_{yp}^2 + \sigma_{ye}^2}} R_L, \tag{11}$$

and the beam-beam parameters are

$$\xi_{xp} = \frac{r_e}{2\pi\gamma_p}\frac{\beta_{xp}N_e}{(\phi\sigma_{ze})^2}R_{\xi x}$$
$$\xi_{yp} = \frac{r_e}{2\pi\gamma_p}\frac{\beta_{yp}N_e}{\sigma_{ye}(\phi\sigma_{ze})}R_{\xi y} \quad (12)$$

From Eq. (11), the luminosity depends on the vertical beam size at IP with less dependence on the horizontal beam size. The beta function should be squeezed at IP and the extremely low vertical emittance, namely, a small X-Y coupling is necessary to realize the higher luminosity. The higher luminosity can be achieved by a smaller beam size with keeping a similar beam current to the present B factory. Since the vertical beam-beam parameter is proportional to $\beta_y/\sigma_y$, the beam-beam parameters can be kept to be the same amount what we have achieved even though the low beta and low emittance are adopted.

### 3.25.2 Lattice Design

The lattice design of SuperKEKB is based on that of KEKB. The arc cell adopts 2.5π non-interleaved chromaticity correction scheme. The flexibility of the emittance and the momentum compaction in the arc cell is 7 nm < $\varepsilon_x$ < 30 nm and $-8\times10^{-4} < \alpha_p < 8\times10^{-4}$ by changing magnetic field of quadrupole magnets. Another advantage is that the dispersion, the X-Y coupling, and the beta function can be corrected independently by using an orbit offset at the sextupole magnets in the arc section in principle.

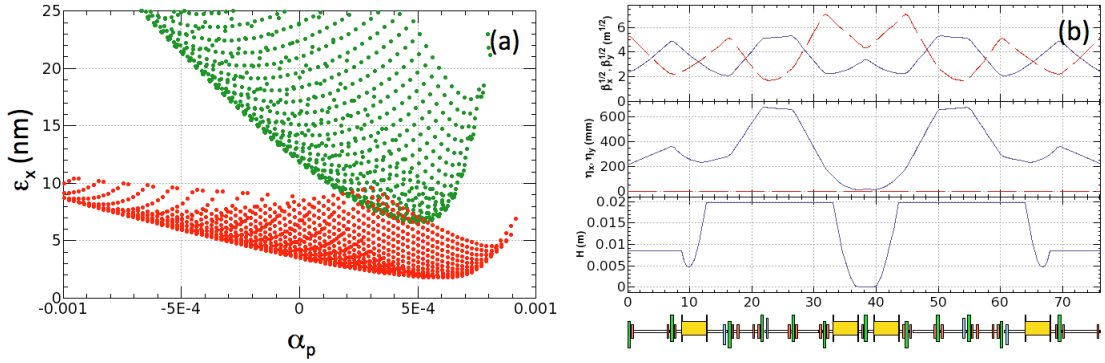


**Figure 2:** (a) Lattice flexibility for the emittance as a function of the momentum compaction. Bending magnet of 0.89 m length is shown as green, 4 m long as red. (b) Lattice of the arc cell in LER. The emittance is 2 nm and the momentum compaction is 4.4x10-4 in this case.

In the case of the super-bunch scheme, the bending magnets in the arc has to be replaced with 4 m long magnets to achieve 1 nm emittance together with the wiggler section in LER. The present effective length of the bending magnet in LER is 0.89 m. Figure 2 shows the lattice flexibility and the arc cell of the 4 m bending magnet in LER.

The whole lattice for the travel waist in LER [9] is shown in Fig. 3. The sextupole magnets, SCTO and SCTN, are used for the travel waist. Each crab cavity is located between the pair of sextupole magnets. On the other hand, when we adopt the crab waist, one of two sextupole magnets in a family and the crab cavities are turned off.

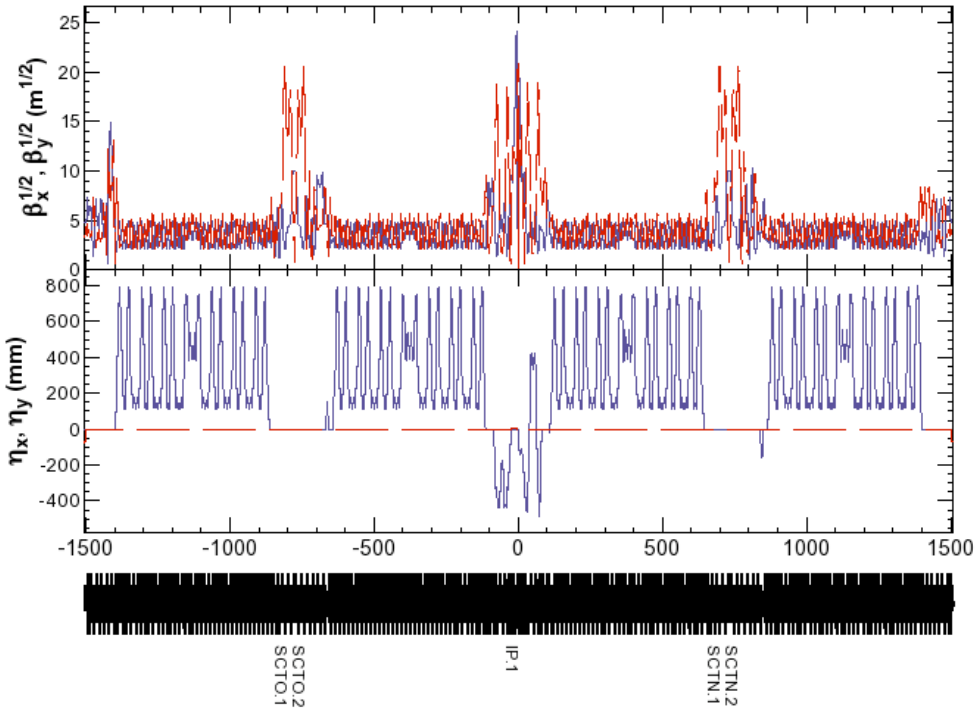


**Figure 3:** Lattice of LER with the travel waist scheme. SCT is the sextupole magnet for the travel waist.

### 3.25.3 IR Design

The parameters related to the IR design for the high current scheme are the horizontal beta function of 20 cm, the vertical beta function of 3 mm, and the half crossing angle of 15 mrad as the nominal values. Since the high beam-beam parameter is assumed in the high current scheme, beam-beam effects on a dynamic beta and a dynamic emittance are considered in the design. The requirements are physical apertures, SR fan and power deposition, realistic magnetic strength and magnet locations for a beam separation. However, there is no realistic solution to realize the 20 cm horizontal beta so far, though we found a solution of the 40 cm horizontal beta. The work is still on going.

The recent lattice design needs a set of new quadrupole magnets. One is a superconducting magnet working at 1.9 K [10], the other is a permanent magnet. Figure 4 shows the IR lattice with the horizontal beta of 40 cm for the high current scheme.

On the other hand, the target beta functions are 20 mm in the horizontal and 0.2 mm in the vertical plane for the super-bunch scheme. Local chromaticity corrections in the vicinity of IP for both rings are necessary to correct the large chromatic effect induced at IP. In order to make this possible, a SuperB final focus or an ILC type final focus becomes a candidate for the lattice design.

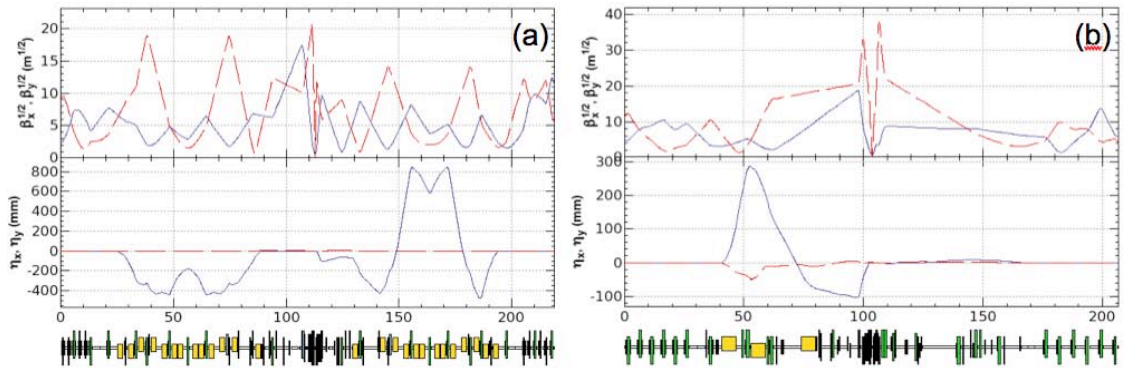


**Figure 4:** (a) Lattice of LER and (b) HER in the IR region.

### 3.25.4 Summary

The key issues for the SuperKEKB are a dynamic aperture and a physical aperture related to the injection system, a SR fan at the IR region, detector backgrounds consist of synchrotron radiation, a radiative Bhabha, Touschek effects, and a feasibility of the low emittance and the low beta lattice. Especially, a design of special IR magnets and an assembly of beam pipes become difficult due to tight space. The injection scheme includes a damping ring for a positron injection, however, an electron damping ring might be necessary for the super-bunch scheme to satisfy the injection aperture.

Both of the high current scheme and the super-bunch scheme will be evaluated to realize the SuperKEKB machine and it will take a few months.

### 3.25.5 References

1. SuperKEKB Task Force, KEKB-Report 2004-4, June 2004.
2. K. Oide, The 14th KEKB Accelerator Review Committee, February 2009.
3. V.E. Balakin, N.A. Solyak, NIM A355 (1995) 142-149.
4. Y. Funakoshi et al., EPAC08-WEXG01, June 2008.
5. K. Ohmi et al., KEK-PREPRINT-2005-42, PAC05-TPPP004, July 2005.
6. SuperB, Conceptual Design Report, INFN/AE-07/2, SLAC-R-856, LAL 07-15, March 2007.
7. P. Raimondi et al., EPAC08-WEXG02, June 2008.
8. C. Milardi et al., Int. J. Mod. Phys. A24, 360-368, January 2009.
9. H. Koiso et al., private communications.
10. N. Ohuchi, The 14th KEKB Accelerator Review Committee, February 2009.

## 3.26 Study of Various Collision Schemes for Super KEKB

K. Ohmi
KEK, 1-1 Oho, Tsukuba, Ibaraki, 305-0801, Japan
Mail to: ohmi@post.kek.jp

### 3.26.1 Introduction

KEKB will achieve the integrated luminosity of 1 $ab^{-1}$ this or next year. We are planning an upgrade of KEKB. The integrated luminosity should target 10 $ab^{-1}$ next 5-10 years. The peak luminosity should be 10 times higher than the present value of $1.7x10^{34}$ $cm^{-2}s^{-1}$. Various collision schemes are proposed to boost the luminosity performance. Every collision schemes should be studied for the upgrade. Here we present the trials for the collision schemes.

### 3.26.2 Collision Schemes for B Factories

#### *3.26.2.1 Crossing Angle*

Various collision schemes are proposed for high luminosity B factories. In recent colliders, multi-bunch collision is crucial to get gain the multiplicity of the number of bunches. The crossing angle is introduced to avoid parasitic encounters.

An essential of crossing angle is expressed by transformations as shown in Figure 1. The electro-magnetic field is formed perpendicular to the traveling direction. The transformation which particles in the beam experience is expressed by [1, 2]

$$\begin{aligned}\Delta p_x &= -F_x(x+2s\phi, y)\\ \Delta p_y &= -F_y(x+2s\phi, y)\\ \Delta\delta &= -\phi F_x(x+2s\phi, y)\end{aligned} \tag{1}$$

where $s=(z-z_c)/2$ and $\phi$ is the half crossing angle. The transformation is separated by three parts.

$$e^{\phi p_x z} \circ e^{-:H_{bb}:} \circ e^{-\phi p_x z} \tag{2}$$

where $H_{bb}$ is Hamiltonian for the beam-beam interaction. The first transformation is given by

$$e^{-\phi:p_x z:} x = x - \phi[p_x z, x] = x + \phi z$$

$$e^{-\phi:p_x z:}\delta = \delta - \phi[p_x z, \delta] = x - \phi p_x \tag{3}$$

The residual of the first and third transformations gives the transformation for δ in Eq.(1). This expression, which is called Lie operator expression, is presented in [3]. Note the operator order; ∘ denotes the multiplication of transformations, which is inverse order of Lie operator multiplication.

Both beams are transferred by the same transformation. The term $\phi z_c$ appears from $2s\phi$ in Eq.(1). This transformation is actually equivalent to the appearance of z dependent dispersion ($\zeta_x$) at the collision point: i.e., the revolution matrix including the crossing transformation is expressed by

$$M = e^{\phi p_x z} \circ M_0 \circ e^{-\phi p_x z} \tag{4}$$

where $M_0$ is the revolution matrix of the lattice. Now the beam envelope matrix has a finite element of $\langle xz \rangle = \zeta_x \sigma_z = \phi \sigma_z$ [4], for the weak limit of the beam-beam interaction. The collision is now regarded as head-on collision with tilt beams in x-z plane as shown in Figure 2. Electro-magnetic field is the perpendicular to the moving direction now.

Another important point of the crossing angle is that the collision area in the two beams is limited. For long bunch compare than beta function, tune shift enlargement due to the hourglass of the beta function is avoidable. The long bunch scheme is called superbunch scheme [5]. This feature is great merit for collision with extreme small beta function. The bunch length and beta function can be chosen independently in this scheme. The relations of optics and beam-beam parameters are summarized in as follows.

**Table 1:** Parameter comparison.

| | ***Short bunch*** | ***Long bunch*** |
|---|---|---|
| Requirement 1 | $\sigma_x/\phi > \sigma_z$ | $\sigma_x/\phi < \sigma_z$ |
| Requirement 2 | $\sigma_z < \beta_y$ | $\sigma_x/\phi < \beta_y$ |
| $L\left(\frac{f_{rep}}{4\pi}\times\right)$ | $\frac{N^2}{\sqrt{\varepsilon_x\beta_x\varepsilon_y\beta_y}}$ | $\frac{N^2}{\phi\sigma_z\sqrt{\varepsilon_y\beta_y}}$ |
| $\xi_x\left(\frac{r_e}{2\pi\gamma}\times\right)$ | $\frac{N}{\varepsilon_x}$ | $\frac{N\beta_x}{\left(\phi\sigma_z\right)^2}$ |
| $\xi_y\left(\frac{r_e}{2\pi\gamma}\times\right)$ | $N\sqrt{\frac{\beta_y}{\varepsilon_x\beta_x\varepsilon_y}}$ | $\frac{N}{\phi\sigma_z}\sqrt{\frac{\beta_y}{\varepsilon_y}}$ |

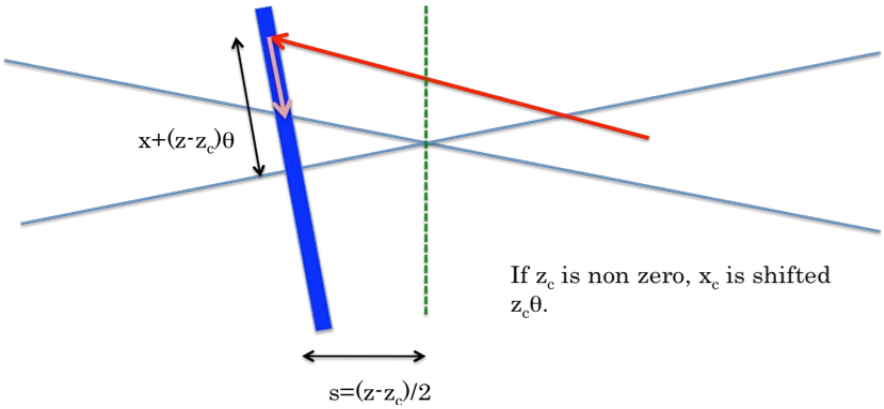


**Figure 1:** Transformation for crossing angle.

**Figure 2:** Collision with crossing angle is equivalent to head-on collision with tilt beam.

### *3.26.2.2 Crab Crossing*

The crab crossing [1, 6] is basically meaningful for the short bunch scheme. A transformation, which is equivalent to the crossing angle, is applied before and after the collision,

$$e^{-\phi p_x z} \circ e^{\phi p_x z} \circ e^{-:H_{bb}:} \circ e^{-\phi p_x z} \circ e^{\phi p_x z} = e^{-:H_{bb}:}, \tag{5}$$

Thus the effective transformation is the same as that for the head-on collision. To realize the transformation, crab cavities, which gives the transformation, $e^{-V':xz:/E_0}$, are placed at locations where linear transformation $T_A$ is satisfied to,

$$e^{\phi p_x z} = T_A \circ e^{-V':xz:/E_0} \circ T_A^{-1} = e^{-(V'/E):T\circ xz:}, \tag{6}$$

where

$$T_A \circ x = \sqrt{\frac{\beta_x^*}{\beta_{x,c}}} x \cos\varphi_x + \sqrt{\beta_x^* \beta_{x,c}}\, p_x \sin\varphi_x \tag{7}$$

$\varphi_x$ is the horizontal betatron phase difference between the collision point and crab cavity position, and $\beta_x^*$ and $\beta_{x,c}$ are horizontal beta functions at the collision point and crab cavity position.

The well-known formula for crab angle and voltage is given by choosing the betatron phase difference of $\pi/2$.

$$\phi = \frac{\omega_{crab} V}{cE_0} \sqrt{\beta_{x,c} \beta_x^*} \tag{8}$$

Only one crab cavity can be possible to realize the transformation

$$e^{\phi p_x z} \circ M_0 \circ e^{-\phi p_x z} = T_B \circ e^{-V' :xz: / E_0} \circ T_B^{-1} \circ M_0 \tag{9}$$

Basically this procedure is really 6 × 6 optics matching for the dispersion $\zeta_x$.

#### *3.26.2.3 Crab Waist Scheme*

A transformation with the form exp(-a:$p_y^2$:/2) controls the vertical waist position with keeping minimum beta function. The transformation is represented by matrix as

$$\begin{pmatrix} y \\ p_y \end{pmatrix} = T_a \begin{pmatrix} y \\ p_y \end{pmatrix} \qquad T_a = \begin{pmatrix} 1 & a \\ 0 & 1 \end{pmatrix} \tag{10}$$

Twiss parameters at the collision point are transferred by

$$\begin{pmatrix} \beta & -\alpha \\ -\alpha & \gamma \end{pmatrix} = T \begin{pmatrix} \beta & 0 \\ 0 & 1/\beta \end{pmatrix} T_a^t = \begin{pmatrix} \beta + a^2/\beta & a/\beta \\ a/\beta & 1/\beta \end{pmatrix} \tag{11}$$

This transformation is equivalent to shift the waist position of *a*.

The waist position is shifted so as to linearly depend on the horizontal coordinate x under the presence of the crossing angle in the crab waist scheme [7]. The transformation at the collision point is expressed by

$$e^{axp_y^2} \circ e^{\phi p_x z} \circ e^{-:H_{bb}:} \circ e^{-\phi p_x z} \circ e^{-axp_y^2} \tag{12}$$

The transformation is rewritten as

$$e^{\phi p_x z} \circ e^{-\phi p_x z} \circ e^{a x p_y^2} \circ e^{\phi p_x z} \circ e^{-:H_{bb}:} \circ e^{-\phi p_x z} \circ e^{-a x p_y^2} \circ e^{\phi p_x z} \circ e^{-\phi p_x z}$$

$$= e^{\phi p_x z} \circ e^{a(x-\phi z) p_y^2} \circ e^{-:H_{bb}:} \circ e^{-a(x-\phi z) p_y^2} \circ e^{-\phi p_x z} \qquad (13)$$

Choosing a=1/2f, the waist position is s=z/2-x/2f. Beam particles satisfying x=zf, which collide with central axis of another beam at s=0, have the waist at s=0. Particles with x=zf +Dx, which collide with the centre at s=–Dx/2f, have the waist s=–Dx/2f. This feature minimizes the beam-beam effect for colliding particles. The transformation $\exp(-:xp_y^2:/2f)$ is realized by sextupole magnet: that is, at least two sextupole magnets are located at both side of the collision point. The betatron phase difference is np for x and (1/2+n)p for y, and the strength is determined by Eq. (7).

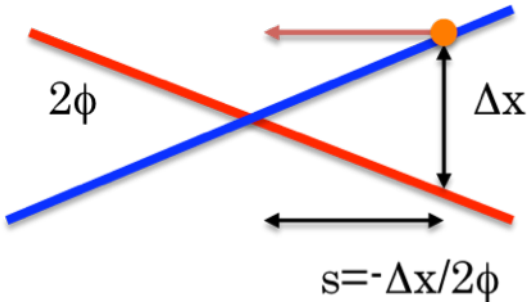


**Figure 3:** Deviation of collision point for x and waist position in crab waist scheme.

Characteristic of the crab waist scheme can be seen following Figure 3. Coordinates x and y are transferred by the crab waist action near the collision point as follows,

$$y(s) = y_0 + x p_y / 2\phi + p_y s \approx x p_y / 2\phi + p_y s$$

$$x(s) = x_0 + p_x s \approx x_0 \qquad (14)$$

Beam distribution is Gaussian except for the collision point. Near the collision point, the distribution is distorted by Eq.(14). The distribution is roughly given by

$$\exp\left[-\frac{x^2}{2\varepsilon_x \beta_x} - \frac{\beta_y p_y^2}{2\varepsilon_y}\right] = \exp\left[-\frac{x^2}{2\varepsilon_x \beta_x} - \frac{\beta_y y^2}{2\varepsilon_y (x/2\phi + s)^2}\right], \qquad (15)$$

where $\exp(-y_0^2/2\varepsilon_y\beta_y)$ is neglected, because $p_y$ is dominant for $s>\beta_y$. Figure 4 shows the contour of the distribution. Particles located at x collide with another beam at their waist position as shown in Figure 4.

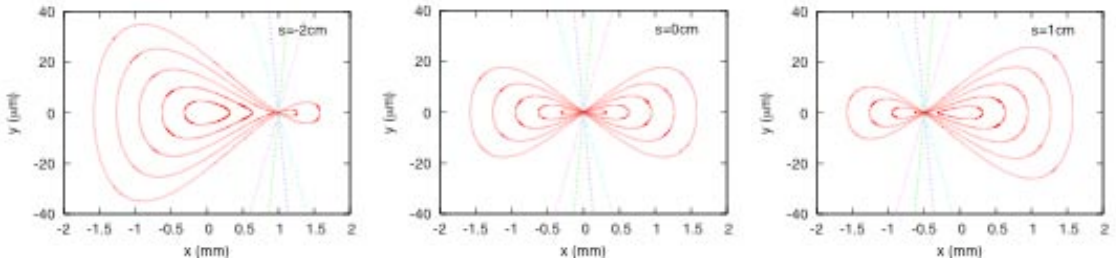


**Figure 4:** Particle distribution of colliding beam in the crab waist scheme. Collision arises at the point with the minimum y size. Another beam distributes symmetric for x.

#### *3.26.2.4 Travel Focus Scheme*

Beam particles with z collide with the center of another beam at s=z/2 in the travel focus scheme [8]. The particles with z should have the waist position at s=z/2 to minimize the beam-beam effect. The transformation $\exp(-p_y^2 z/4)$ realizes the travel focusing:

$$e^{zp_y^2/4} \circ e^{-:H_{bb}:} \circ e^{-zp_y^2/4} \tag{16}$$

RF focusing is used for the transformation. However heavy development works are necessary for the RF device. We know the crab cavity exchanges x and z.

$$e^{-\phi p_x z} \circ e^{xp_y^2/4\phi} \circ e^{\phi p_x z} \circ e^{-:H_{bb}:} \circ e^{-\phi p_x z} \circ e^{-xp_y^2/4\phi} \circ e^{\phi p_x z}$$

$$= e^{(x-\phi z)p_y^2/4\phi} \circ e^{-:H_{bb}:} \circ e^{-(x-\phi z)p_y^2/4\phi} \tag{17}$$

The first and last operator $\exp(+\text{-}fp_x z)$ at the first line of Eq.(17) are actions of the crab cavities, while 3rd and 5th are the crossing angle. The 2nd and 6th operators are from two sextupole magnets located at the both sides of the collision point. Additional two sextupole magnets in both sides are added to cancel the residual nonlinear term [9].

$$e^{xp_y^2/4\phi} \circ e^{-(x-\phi z)p_y^2/4\phi} \circ e^{-:H_{bb}:} \circ e^{-(x-\phi z)p_y^2/4\phi} \circ e^{xp_y^2/4\phi}$$

$$= e^{zp_y^2/4} \circ e^{-:H_{bb}:} \circ e^{-zp_y^2/4} \tag{18}$$

Realistic arrangement of IR is given by chosen betatron phase so as to realize the transformation as is done in Eq. (7). Two pairs of crab cavities, which are inserted between two sextupole magnets, are located at the horizontal betatron phase difference of (1/2+n)p. The sextupole magnets are located at the vertical betatron phase difference

of (1/2+n)p. The phase difference of two sextupole magnets is p or 2p depending on the sign of magnets. In this scheme two crab cavity is necessary.

In the travel focus scheme, the waist position shifts for z but does not for s: that is, particles at z have waist position for the variation of s, and the waist position is located at the centre (z=0) of the colliding beam. The hourglass effect is not avoidable even in the travel waist scheme.

### 3.26.3 Study of the Collision Schemes in Super KEKB

These collision schemes have to be studied to upgrade KEKB. The crab cavity has been studied since 2007 at KEKB. The crab cavity was expected to boost the luminosity twice higher [10]. Figure 5 shows the beam-beam parameter as a function of the bunch population of HER, where the transparency condition is assumed.

The beam-beam parameter, which is regarded as a normalized luminosity, is defined by

$$\xi_n = \frac{2r_e\beta_{y,\pm}L}{N_\pm\gamma_\pm f_{col}} \ . \tag{19}$$

The luminosity is $4.5\times10^{35}$ $cm^{-2}s^{-1}$ for the nominal parameter, $N(HER)=5.5\times10^{10}$ and 2ns collision repetition.

Figure 6 shows the beam-beam parameter as a function of the travel focus strength. The beam-beam parameter does little depend on the strength. The vertical beam size, which is simple 2nd order moment, has a minimum at the optimum strength. The tail distribution should be improved by the travel focus, while the luminosity performance is not remarkable.

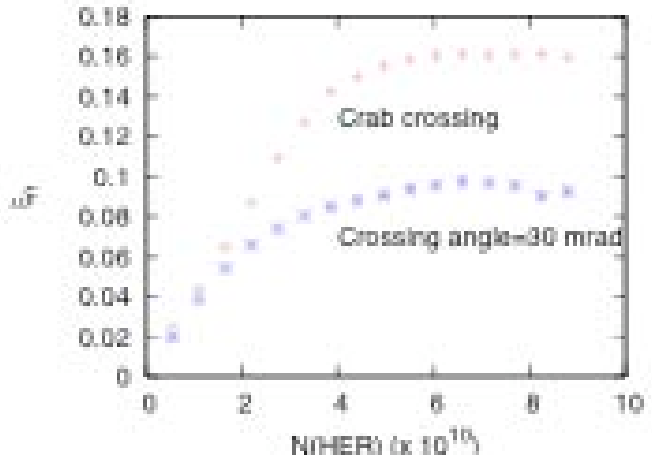


**Figure 5:** Beam-beam parameter with and without crab cavity given by a strong-strong simulation. Number of the longitudinal slice in the simulation is 5.

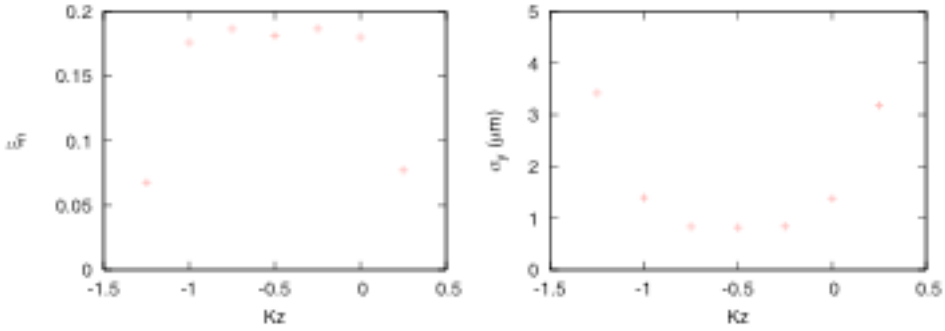


**Figure 6:** Effect of travel focusing in the simulation. The optimum is Kz=-0.5, where exp(Kz:$p_y^2$z/2:)

Using the travel-focusing scheme, higher luminosity is targeted. Figure 7 shows the beam-beam parameters as a function of the bunch population of HER beam given by both of strong-strong and weak-strong simulations. The corresponding luminosity is $8.0\times10^{35}$ $cm^{-2}s^{-1}$ for the nominal parameter, N(HER)=$5.5\times10^{10}$ and 2ns collision repetition.

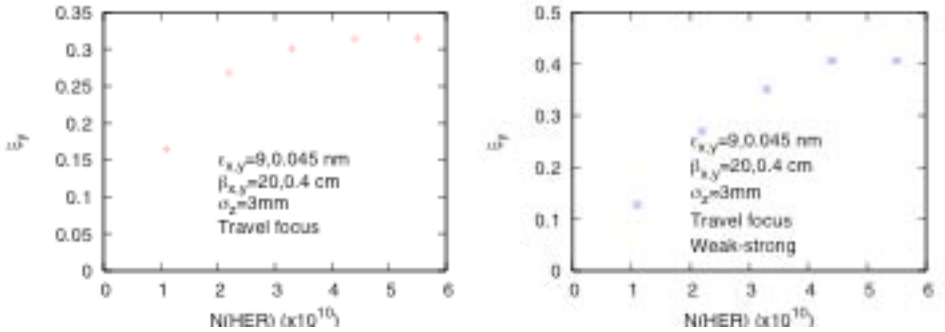


**Figure 7:** Beam-beam parameters given by strong-strong and weak-strong simulations.

Superbunch and crab waist scheme have been studied. The simulation for superbunch scheme is very hard; because a bunch has to be sliced into many pieces and a number of collisions between slices, square of the number of slices, have to be calculated per one revolution. Figure 8 shows the luminosity evolution in a strong-strong simulation for Super B parameters [11]. This luminosity is given for the collision repetition of 2 ns. Since it is 4 ns for the present design of Super B, the luminosity is $0.7\times10^{36}$ $cm^{-2}s^{-1}$. The simulation, which is preliminary, is very hard and can contain numerical difficulties. Since better simulations will give better luminosity, this result can be considered as a lower bound for an ideal machine. The beam-beam parameter is 0.08 using Eq. (19), where $\beta_y$=0.22/0.39 mm, N=$5.52\times10^{10}$ and E=4/7 GeV.

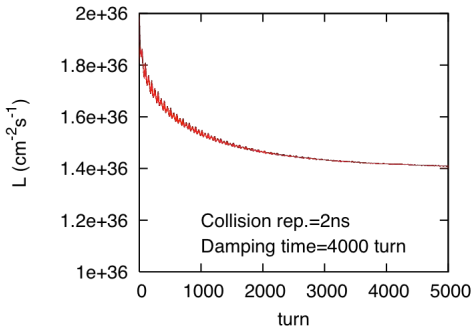


**Figure 8:** Luminosity evolution in a strong-strong simulation for Super B parameters.

### 3.26.4 References


1. K. Oide and Y. Yokoya, “Beam-beam collision scheme for storage-ring colliders”, Phys. Rev. A40, 315 (1989).
2. K. Hirata, "Analysis of beam-beam interactions with a large crossing angle", Phys. Rev. Lett., 74, 2228 (1995).
3. A. J. Dragt, “Lecture on nonlinear orbit dynamics”, AIP Conf. Proc. 87:147-313 (1982).
4. K. Ohmi, K. Hirata and K. Oide, “From the beam envelope matrix to synchrotron radiation integrals”, Phys. Rev. E49, 751 (1994).
5. K. Takayama, “Superbunch hadron colliders”, Phys. Rev. Lett. 88, 144801 (2002).
6. R. B. Palmer, “Energy scaling, crab crossing and the pair problem”, SLAC-PUB-4707 (1988).
7. P. Raimondi, “Suppression of beam-beam resonances in crab waist collision”, Proceedings of PAC2007, WEPP045.
8. V.E. Balakin and N.A. Solyak, “Status of electron accelerators for linear colliders”, Nucl. Instru. & Methods in Phys. Res. A355, 142 (1995).
9. K. Oide and H. Koiso, private communications.
10. K. Ohmi et al., “Luminosity limit due to the beam-beam interactions with or without crossing angle”, Phys Rev. ST-AB. 7, 104401 (2004).
11. SuperB conceptual Design report, INFN/AE-07/2, SLAC-R-856, LAL 07-15, March 2007.


## 3.27 The Project of Tau-charm Factory with Crab Waist in Novosibirsk


A. Blinov, A. Bogomyagkov, A. Bondar, V. Kiselev, I. Koop, G. Kurkin,
E Levichev, P. Logachev, S. Nikitin, I. Okunev, V.M. Petrov, P. Piminov, Yu. Pupkov,
D. Shatilov, S. Sinyatkin, V. Smaluk, A. Skrinsky, P. Vobly
BINP, Novosibirsk, Russia
Mail to: levichev@inp.nsk.su



*Abstract*

The project of a new-generation t-charm factory is now under consideration in Novosibirsk. A novel approach of the Crab Waist collision scheme allows reaching the luminosity of $1\div2\times10^{35}$ $cm^{-2}s^{-1}$. The other features of the facility are: variable energy from 2 GeV to 4.5 GeV (c.m.), longitudinal polarization of electrons at IP, usage of

damping wigglers to keep high luminosity for all energy levels, etc. We discuss some of the challenges and opportunities available with the development of the project.

### 3.27.1 Introduction

A tau-charm factory can study the issues concerning the tau leptons, charmed particles, and light quark spectroscopy in a unique manner. Many of these issues can only be addressed to a t-charm factory and may not be substituted by the successfully operating B-factories.

A number of different projects of TCF were discussed in the '90s of the last century [1-6]. All these projects had more or less similar features: the maximum luminosity around $10^{33}$ $cm^{-2}s^{-1}$ and the single beam energy variable in the range ~1÷3 GeV. One of the representatives of this family, the Beijing Tau Charm Factory, has already started its operation.

In 1995 BINP also released a conceptual design of t-charm factory [7]. In the framework of the BINP TCF project, a new $e^+e^-$ injection facility has been launched. An excavation work of the TCF main halls and tunnels was started in 1996 but then it was frozen. However, recently we decided to revive the TCF project in Novosibirsk and this time our optimism was inspired by (a) the invention of the Crab Waist collision concept that allows increasing the luminosity by factor of 10÷100 and (b) the exciting results from the B-factories, which enhance significantly an interest to the physics of charmed particles.

The following task list was formulated for the new TCF project:

- D-Dbar mixing
- CP violation search in charm decays
- Study of rare and forbidden charm decays
- Standard Model tests in tau lepton decays
- Searching for lepton flavor violation
- CP/T violation search in tau lepton decays
- Production of polarized anti-nucleons

This experimental program can be carried out at a facility with the basic features listed below:

- Collision energy from 2 GeV to 4.5 GeV (anti-nucleons – J/psi – charm barions)
- The luminosity $\geq 10^{35}$ $cm^{-2}s^{-1}$
- Electrons polarized longitudinally at IP
- No energy asymmetry is required
- No beam monochromatization is required
- An accuracy of energy calibration $\sim 5\times10^{-4}$ can be achieved with the Compton back scattering technique realized at VEPP-4M [8], so the beam transverse polarization is not required.

Other constraints include the correspondence of the new factory performance with the capability of the injection facility, which is now entering the commissioning stage

and matching of underground tunnels and halls already constructed for the previous TCF design.

### 3.27.2 Crab Waist Collision Scheme

One of the key requirements of high luminosity colliders is extremely small $\beta_y$ at the IP. But $\beta_y$ cannot be made much smaller than the bunch length without encountering a "hourglass" effect, so this imposes a rigid limitation on the bunch length. But, unfortunately, it is very difficult to shorten the bunch length $\sigma_z$ in a high current ring without facing the instabilities.

This problem can be overcome with the recently proposed Crab Waist collision scheme [9], which can substantially increase luminosity without the bunch length decrease, since it combines several potentially advantageous ideas. The first idea is the use of a large Piwinski angle

$$\phi = \frac{\sigma_z}{\sigma_x} \tan\frac{\theta}{2} \approx \frac{\sigma_z}{\sigma_x}\frac{\theta}{2} \tag{1}$$

where $\theta$ is the horizontal crossing angle, $\sigma_z$ and $\sigma_x$ are the rms bunch length and the horizontal beam size, respectively.

For collisions at the crossing angle $\phi$, the luminosity $L$ and the tune shifts $\xi_x$ and $\xi_y$ scale as [10]:

$$L \propto \frac{N\,\xi_y}{\beta_y} \propto \frac{1}{\sqrt{\beta_y}} \tag{2}$$

$$\xi_y \propto \frac{N\,\beta_y}{\sigma_x\sigma_y\sqrt{1+\phi^2}} \propto \sqrt{\beta_y} \text{ and } \xi_x \propto \frac{N}{\varepsilon_x(1+\phi^2)}$$

where $N$ is the number of particles per bunch, $\varepsilon_x$ is the horizontal emittance and $\sigma_y$ is the vertical rms beam size at IP. We consider here the case of flat beams, small horizontal angle $\theta << 1$ and large Piwinski angle $\phi >> 1$.

In the Crab Waist collision scheme, the Piwinski angle is increased by decreasing the horizontal beam size and increasing the crossing angle. In this way, the luminosity grows, and the horizontal tune shift due to the crossing angle decreases.

The most important effect is that the overlap area of colliding bunches is reduced, as it is proportional to $\sigma_z/\theta$ and $\beta_y$ can be made comparable to the overlap area size (i.e. much smaller than the bunch length):

$$\beta_y \approx \frac{\sigma_x}{\theta} << \sigma_z \tag{3}$$

A smaller spot size at IP and reduction of the vertical tune shift can be achieved at the same time, providing an increase in luminosity inversely proportional to $\beta_y$.

The main advantage in such a collision scheme is that the bunch length must not be shortened to increase the luminosity. This will certainly ease the problems of HOM

heating, coherent synchrotron radiation of short bunches, excessive power consumption, etc.

However, a large Piwinski angle itself introduces new beam-beam resonances and may limit the maximum achievable tune shifts (see, for example, [11, 12]). This is where the Crab Waist innovation is required. The Crab Waist transformation boosts the luminosity, mainly by suppression of betatron (and synchrobetatron) resonances that usually arise through the vertical motion modulation by horizontal beam oscillations [13]. In this scheme the modulation becomes significantly smaller as compared to the head-on collision scheme, thus, the beam-beam limit $\xi_y$ increases by a factor of about 2-3.

A sketch of the Crab Waist scheme is shown in Fig. 1.

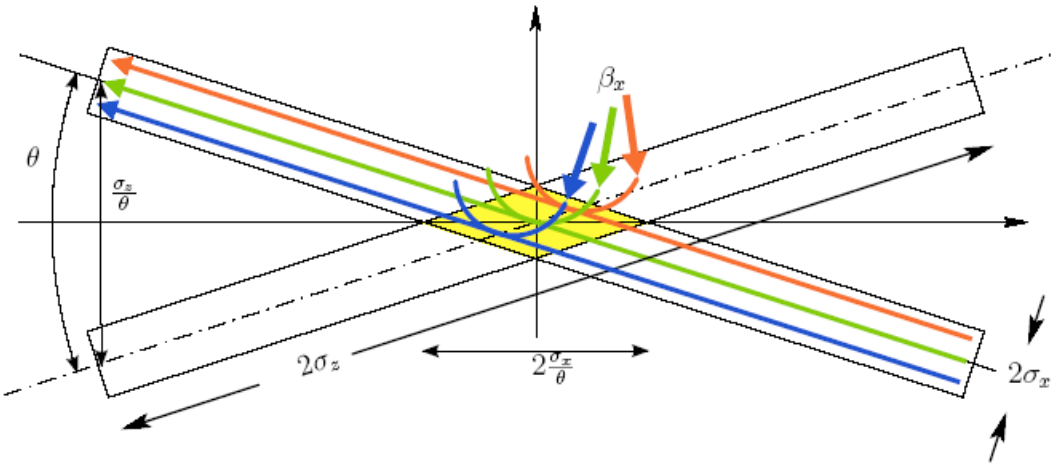


**Figure 1:** Sketch of large Piwinski angle and Crab Waist scheme. The collision area is shown in yellow.

The Crab Waist correction scheme is realized in practice with two sextupole magnets in phase with the IP in the x plane and at π/2 in the y plane, on both sides of the IP, as shown in Fig. 2.

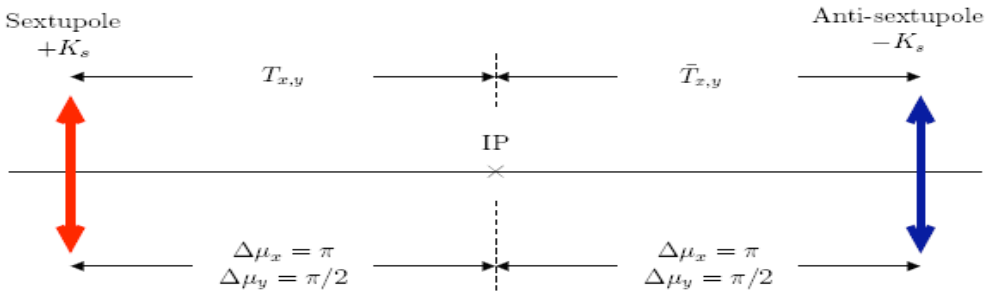


**Figure 2:** Scheme of Crab Waist correction by sextupoles.

The position of such sextupoles in the ring lattice has to be studied with great care, minimizing nonlinearities that may induce a reduction of the ring dynamic aperture.

Recently the Crab Waist concept was proven experimentally at DAΦNE in Italy [14].

### 3.27.3 Physics Challenges

A schematic view of the TCF layout is shown in Fig. 3. A two-ring configuration with the racetrack rings, single collision point and a system of the emittance damping and excitation wigglers is considered. A circumference of the machine is around 850 m, a straight section length is ~150 m and the arcs radius is ~90 m. In the design of the injection complex we use the already existing facilities and engineering infrastructures.

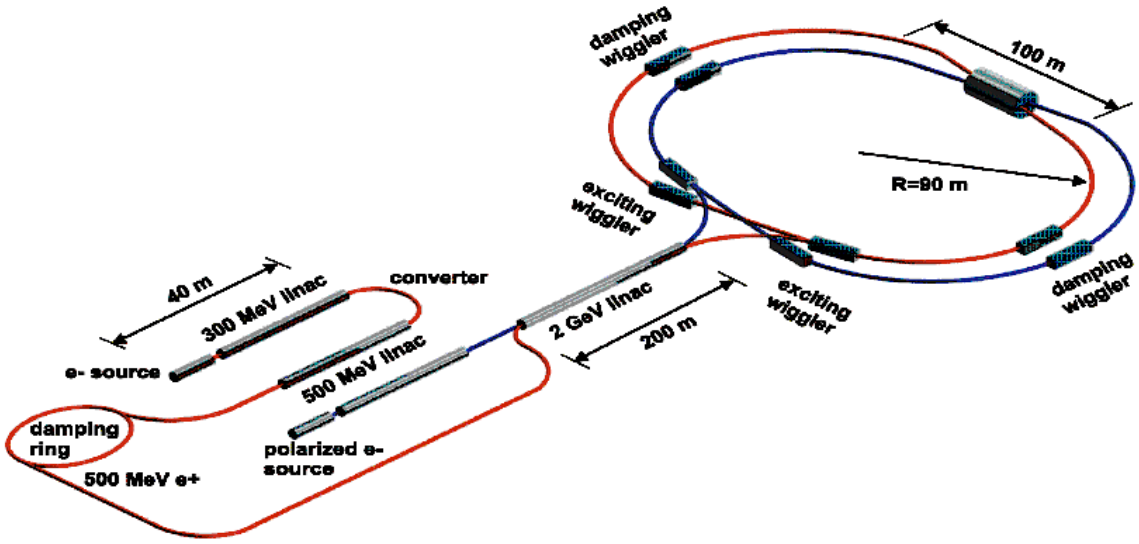


**Figure 3:** Schematic view of the Novosibirsk TCF.

The design of a high-luminosity TCF leads to physics challenges primarily in the areas of lattice design, IR design, $e^-$ polarization technique, dynamic aperture optimization and the beam-beam interaction.

#### *3.27.3.1 Luminosity*

The peak luminosity has been optimized for the beam energy of 2 GeV. To reach the goal of $\geq 1\times10^{35}\text{cm}^{-2}\text{s}^{-1}$, the following essential parameters of the colliding beams should be met: small emittance $\varepsilon_x$ = 10 nm-rad, small betas at IP $\beta_x/\beta_y$ = 30 mm/0.75 mm and large crossing angle at IP $2\phi_x$ = 40 mrad.

Table 1 lists the main machine parameters and the TCF luminosity at three energy levels.

**Table 1:** Main parameters of the Novosibirsk TCF.

| *Energy, GeV* | *1.5* | *2.0* | *2.5* |
|---|---|---|---|
| Hor. emittance, nm | 10 | | |
| Coupling, % | 0.5 | | |
| Bunch length, mm | 10 | | |
| Bunch number | 400 | 400 | 300 |
| Particles/bunch | $5.1\times10^{10}$ | $6.8\times10^{10}$ | $8.5\times10^{10}$ |
| Bunch current, mA | 3.1 | 4.0 | 5.0 |
| Total current, A | 1.2 | 1.6 | 1.51 |
| Damping times, ms | 30/30/15 | | |
| Betas at IP, mm | 30/0.75 | | |
| Crossing angle, mrad | 40 | | |
| Parameter $\xi_y$ | 0.15 | | |
| Luminosity, $cm^{-2}s^{-1}$ | $7.8\times10^{34}$ | $1.4\times10^{35}$ | $1.6\times10^{35}$ |

It is worth mentioning that neither of the above parameters seems to be too excessive: even smaller emittance is typical for the latest generation synchrotron light sources; the total current of ~2 A was obtained in PEP II and DAΦNE; a few millimeter vertical beta, $\xi_y$ = 0.1 or 10 mm bunch length can be attributed to KEKB. Undoubtedly, reaching all these figures is a challenge but all the accelerator technologies required for that already exist.

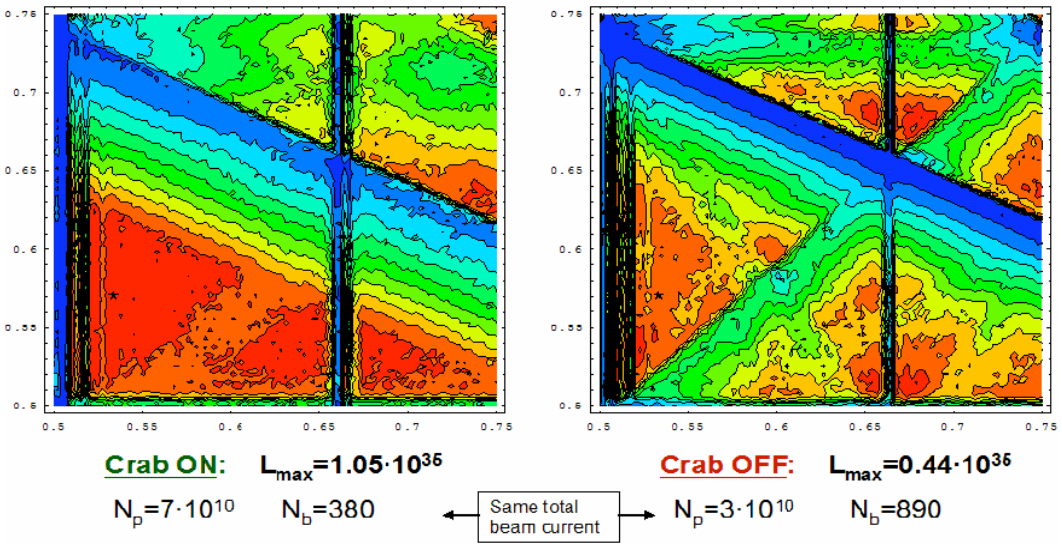


**Figure 4:** Luminosity scan with the Crab-on and -off. Axes are the betatron tunes. The red color corresponds to the highest luminosity while the blue is the lowest.

A sophisticated tracking of the beam-beam collision without and with the Crab Waist conditions by a LIFETRACK computer code [15] has shown the advantage of the last one.

At the luminosity scan presented in Fig. 4, a suppression of betatron coupling resonances with the Crab Waist optics is clearly seen. As a result, the betatron tune region available for high luminosity is opened substantially. One should note that direct

comparison in Fig. 4 is, to some extent, incorrect because, if we tune the Crab Waist to the maximum luminosity and switch off the sextupole, the beam-beam effects will kill the beam. That is why we had to reduce particles number per bunch and increase bunch number to plot the right diagram in Fig. 4.

### *3.27.3.2 Lattice Design*

Both rings of the TCF have the same racetrack design with two arcs (~280 m each) and two long straight sections (~150 m). The facility circumference (~850 m) is constrained by the tunnel that is now under construction at BINP. The lattice can be separated into the following sections: two arcs, producing the required emittance; IR with the Crab Waist optics and sextupoles; a long straight section opposite the IR intended to accommodate RF, injection and other technological equipment; several straights for wigglers to control the emittance with energy change and matching cells between all mentioned parts.

Key parts are the arcs producing the low emittance and the interaction region with the final focus and the Crab sextupoles.

Different cells (FODO, DBA, TME) have been considered as the candidates for the low emittance arcs and, finally, a simple FODO was selected because its focusing strength is enough to get the required emittance and, at the same time, to provide compact and reliable cell with a reasonable strength of chromatic sextupole.

An essential idea of the machine tuning is using the damping wigglers to control radiation parameters and to optimize the Crab Waist luminosity parameters in the whole energy range.

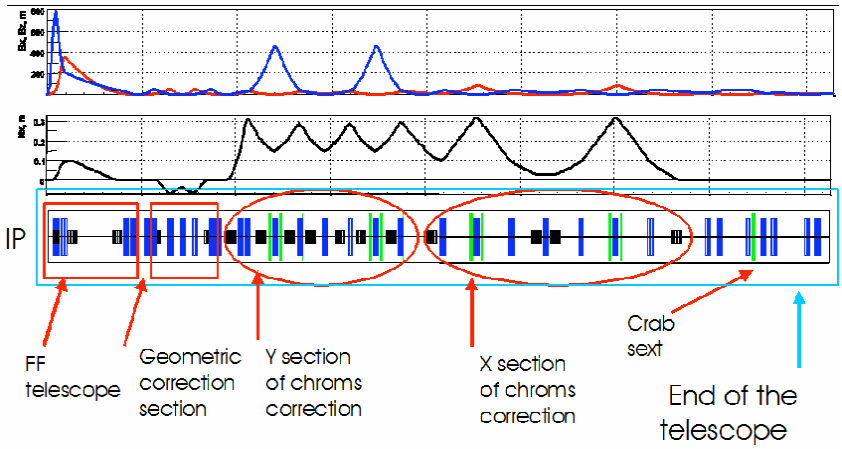


**Figure 5:** TCF FF lattice functions.

The design of the IR with the low beta final focus and the Crab Waist optics is a most challenging task in the TCF lattice development because the following restrictions should be kept in mind: very small spot sizes at the IP; local correction for the very high chromaticity due to the highly focused beam; keeping chromatic and geometric aberrations small; separation of two beams from the rings as soon as possible; preventing synchrotron radiation production from hitting the beam pipe and the detector. Presently we have a solution based on the telescope approach with sextupole pairs spaced by –I in phase and compensation of the chromatic and the geometry aberrations locally (Fig. 5). In our design a dispersion vector $(\eta,\eta')$ is zero at the IP and

at the Crab sextupoles location; and special dipoles introduce the dispersion to the location of the chromatic sextupoles. Such a design provides a rather large momentum bandwidth of ±2% (Fig. 6).

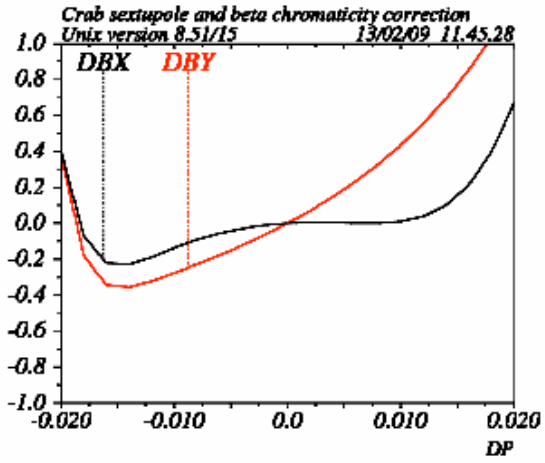


**Figure 6:** TCF bandwidth.

### *3.27.3.3 Dynamic Aperture and Beam Lifetime*

Due to the very strong focusing, almost 50% of the horizontal and 80% of the vertical chromaticity is induced and corrected in the FF region. It requires high-strength sextupole magnets and the study shows that they, together with the Crab sextupoles, are the main source of the dynamic aperture (DA) limitation. A special technique of the weak DA correction sextupole pair interleaved with the strong chromatic pair was developed and provided a rather large transverse DA (Fig. 7).

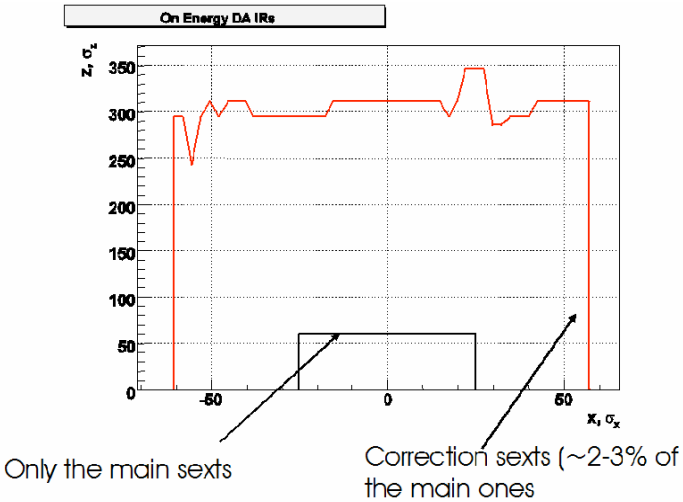


**Figure 7:** Correction sextupole pair opens the DA reduced by the strong chromatic sextupoles.

There are two sources of the beam life time degradation in the TCF: the Touschek effect and the loss of particles due to scattering at the interaction point at a rate

proportional to the machine luminosity. At the low energy the Toschek lifetime dominates (~1000 s) and this is an additional point for a further lattice optimization.

At the high energy the beam life time due to the Bhabha process (radiative and elastic), that scatters particles outside the ring acceptance, and the Touschek lifetime have approximately the same value of ~2000 s.

### 3.27.4 Technology Challenges

#### *3.27.4.1 Injection*

To reach the specified luminosity, we have to provide a top-up injection of $2 \div 4 \times 10^9$ particles at 50 Hz repetition frequency.

At present a new Injection Facility is commissioned at BINP. It consists of the 300-MeV electron linac, the conversion system, the 510-MeV $e^+e^-$ linac and the damping ring of the same energy (Fig. 8).

Today the Facility produces $2 \times 10^{10}$ $e^-$/pulse yielding at the 50 Hz repetition rate and with 1.5% conversion coefficient $1.5 \times 10^{10}$ $e^+$/s. In the future we plan to use the Facility to supply the TCF with positrons. The following upgrade is available: new electron gun can increase the electron intensity by factor 3; more effective focusing system in the positron linac may enhance the positron current by 1.5; installation of a debuncher at the exit of the positron linac provides a better matching of the beam energy spread with the energy acceptance of the damping ring and, hence, increase twice the injection efficiency.

**Figure 8:** Damping ring under commissioning.

Totally the positron production capacity can be enlarged up to $1.4 \times 10^{11}$ $e^+$/s.

Experimental performance of the TCF requires longitudinally polarized electrons. To deliver such electrons we plan to use a Polarized Electron Source (PES) that was developed by BINP and operated successfully at AmPS (Netherlands) for many years [16]. The polarized electrons are accelerated to 510 MeV by the linac identical to the one of the Injection Facility. Finally, a 200 m long 2 GeV linac will be shared in turn between positron and electron beams to inject the particles in TCF at the energy of the experiment.

### *3.27.4.2 Beam Polarization*

To obtain longitudinally polarized electrons at IP, several options were considered. At the moment it seems that the most appropriate way is to produce polarized electrons by the PES [16] and manipulate them in the TCF with the Siberian Snakes as it is shown in Fig. 9.

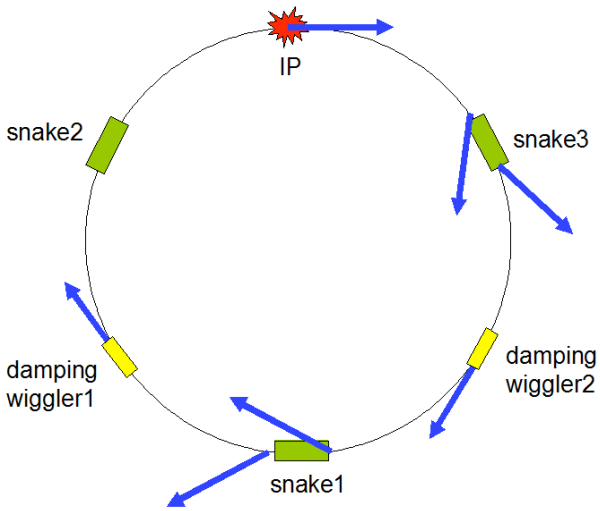


**Figure 9:** The odd-number Siberian Snakes spin manipulator.

In our project we use 5 Snakes 12-m-long each. The Snake consists of two superconducting solenoids ($L$ = 2.6 m, $B$ = 5 T), rotating the spin by 90° each around the beam velocity vector, and 7 quadrupoles providing condition for the local correction of the betatron coupling.

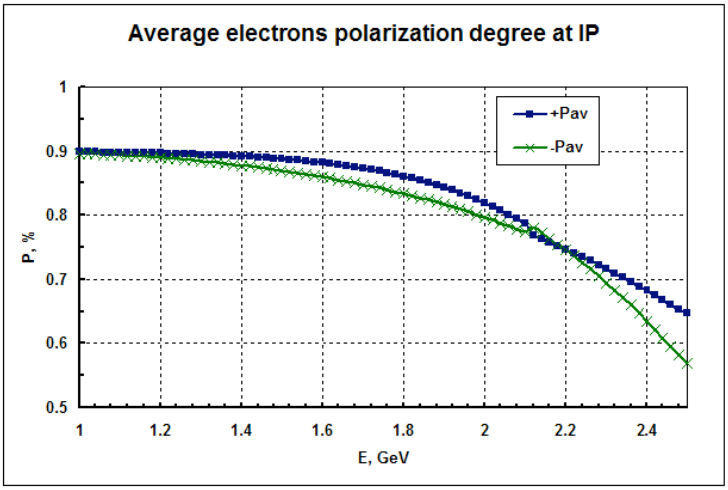


**Figure 10:** Average polarization degree (along and opposite the velocity vector) of the electron beam at IP vs. energy.

The Snakes provide smooth (without the gaps at the spin resonance values) behavior of the average polarization degree at IP in the whole energy range. Fig. 10 shows the polarization degree as a function of energy for the initial degree of 90% and the beam life time of 1000 s.

#### *3.27.4.3 Infrastructure*

One of the important constraints imposed on the new TCF project is using of the infrastructures already designed and partly constructed for the old TCF project. Besides the Injection Facility, it includes the underground tunnel for the longitudinally polarized source, 2.5 GeV linac injector (Fig. 11) and halls for the storage rings.

**Figure 11:** A 800 m tunnel for 2.5 GeV linac.

### 3.27.5 Conclusions and Outlook

Tau-charm factory with $L \geq 10^{35}$ $cm^{-2}s^{-1}$ seems to be an extremely attractive facility for HEP experiments. The Crab Waist crossing approach allows us to obtain this luminosity without going far beyond the present accelerator state-of-art with the already existing technology.

At BINP we have an advantage-ground to start the TCF project because the injection facility is under commissioning now, the tunnels for the linac and injection lines are ready, a lot of the solutions put in the core of the project are based on the existing wares and technologies.

Future plans for the project design include a further FF improvement, the dynamic aperture optimization, the beam-beam study, Touschek lifetime increase, etc.

### 3.27.6 References


1. E. Perelshtein et al. Proc. of the 3rd Workshop on the TC Factory, Marbella, Spain, 1-6 Jun 1993, 557-570.
2. M.V. Danilov et al. Int. J. Mod. Phys. A, Proc. Suppl. 2A (1993) 455-457.
3. E.Berger et al. ANL-HEP-TR-94-12, Feb 1994. 28pp.
4. Yu.Aleksahin, A.Dubrovin, A.Zholents. In EPAC 90 Proc., vol. 1, 398-400.
5. He-Sheng Chen. Nucl. Phys. Proc. Suppl. 59: 316-323, 1997.
6. A. Faus-Golfe and J. Le Duff. NIM A372:6-18, 1996.
7. C-Tau in Novosibirsk: Conceptual Design Report, BINP, Novosibirsk, 1995.
8. N.Yu. Muchnoi, S. Nikitin, V. Zhilich. Proc. of EPAC 2006, Edinburg, Scotland.

9. P. Raimondi, Status of the SuperB Effort, presentation at the 2nd Workshop on Super B Factory, LNF-INFN, Frascati, March 2006.
10. P. Raimondi and M. Zobov, DAΦNE Technical Note G-58, April 2003; D. Shatilov and M. Zobov, ICFA Beam Dyn. Newslett. 37, 99 (2005).
11. D.V.Pestrikov, NIM Phys. Res., Sect. A 336, 427 (1993).
12. K. Ohmi et al., Phys. Rev. ST Accel. Beams 7, 104401 (2004).
13. P. Raimondi, D. Shatilov, M. Zobov, LNF-07/003 (IR), 2007.
14. M.Zobov (INFN LNF), for DAΦNE Collaboration Team, DAΦNE Operation Experience With Crab Waist Collision, arXiv:0810.2211v1.
15. D.Shatilov, Part.Accel., 1996, Vol.52, pp. 65-93.
16. L.G. van Amersfoort et.al. Proc. PAC'97, v.1, pp. 1063-1065.

# 4 Workshop and Conference Reports

## 4.1 The 40th ICFA Advanced Beam Dynamics Workshop on High Luminosity e+e-Factories

Eugene Levichev
Budker Institute of Nuclear Physics, Novosibirsk, Russia
Mail to: levichev@inp.nsk.su

The 40th Advanced Beam Dynamics Workshop was held at Budker Institute of Nuclear Physics, Novosibirsk, Russia on April 14-16, 2008. The Workshop was dedicated to the high luminosity electron-positron colliders.

All the operating electron-positron colliders were presented at the Workshop:

- BEPC II (IHER, Beijing, China)
- CESR (Cornell University, Ithaca, USA)
- DAΦNE (LNF INFN, Frascati, Italy)
- KEKB (KEK, Tsukuba, Japan)
- PEP-II (SLAC, Stanford, USA)
- VEPP 2000 (BINP, Novosibirsk, Russia)
- VEPP 4M (BINP, Novisibirsk, Russia)

Besides the working facilities, two new projects, Super B Factory in Europe and Tau-Charm factory in Novosibirsk, were discussed together with the planned upgrade of the KEK B factory in Japan.

The total 30 talks at the Workshop were divided into three sections: status reports from the existing installations; reports describing the issues of beam dynamics on the high luminosity electron-positron colliders and experimental results; and talks on two future projects exploiting the Crab Waist collision approach (Super B and Tau-Charm).

It is worth mentioning that at the Workshop, the first results were presented illustrating the three existing directions in the luminosity increase including the round colliding beam concept applied on VEPP 2000 (Novosibirsk), the Crab Crossing

approach intensively employed at KEKB (Tsukuba) and the large Piwinsky angle (Crab Waist) collision scheme tested successfully on the DAΦNE storage ring (Frascati).

Besides, the workshop participants met enthusiastically the results of commissioning on VEPP 2000, BEPC II and DAΦNE (after the Crab Waist upgrade). Interesting experimental results describing the beam-beam study, machine resonance suppression, etc, from one of the $e^+e^-$ collider patriarch, CESR (Ithaca, USA), were presented.

The Workshop reports have been published at the Joint Accelerator Conference Website (JACoW).

## 4.2 Mini-Workshop on Laser Assisted $H^-$ Beam Stripping

John Galambos
ORNL, SNS, Tennessee, USA
Mail to: galambosjd@ornl.gov

A mini-workshop was held at the SNS in Oak Ridge TN, Feb. 18-19 2009, focused on the physics and technology of laser-assisted stripping of H- beams for use in high-power proton accelerators. Recent theoretical and experimental work suggests that lasers may be employed in the stripping of H- beams that is required for multi-turn charge-exchange injection in high power proton facilities. Laser-stripping methods hold the promise of eliminating limitations associated with conventional stripping foils, namely short foil lifetime at high beam powers, radio-activation of nearby accelerator components, beam loss associated with multiple foil traversals, and complications associated with foil inefficiency. The mini-workshop website is at https://wiki.ornl.gov/events/lahbsa/default.aspx. About 30 people participated, with representation from Asia, Europe and North America, and from both the accelerator community and laser experts.

The mini-workshop overall organization was:

- review of the proof-of-principle demonstration at SNS
- overview of proposed laser stripping injection concepts at SNS, FNAL (Project-X) and CERN (PS2) with an emphasis on laser requirements
- discussion of laser and light recycling state-of-the art status from laser experts
- discussion of the next step demonstrations

The presentations are available from the mini-workshop web site. One general conclusion from the mini-workshop is that the laser and recycling requirements estimated for the higher energy proposals (utilizing UV light) are not large extrapolations from present capabilities. A number of follow-up actions were discussed, as listed below:

- The requirements (and design impact) for laser stripping depend on the radiation environment. Presumably, with laser stripping the Ring Injection area will have lower radiation fields. SNS will estimate the level of radiation for a laser stripping design (J. Galambos)

- Create a Table of the laser light requirements for the three stripping proposals discussed at the workshop (SNS, Project-X and CERN PS2): (S. Danilov, D. Johnson and B. Goddard)
- Perform optimization studies of the laser stripping efficiency including more realistic stripping process modeling and tradeoffs (interaction point – magnet separation, field strength, etc.): T. Gorlov, M. Zolotorev, with interactions with D. Johnson, B. Goddard
- The capabilities of existing lasers to produce light for the macro-pulse lengths needed for Ring injection (typically ~ 1 msec) is an issue. It may be possible to "stitch" together multiple lasers with reduced pulse lengths to cover the required macropulse length. M. Laha will provide a table of laser capabilities (power, pulse length, etc. for different frequencies).
- An attractive option was discussed in which light from a pumped diode laser is recycled with the full msec pulse length. This "pumped – CW-like" operation is possible even with modest development of existing technologies for UV. R. Wilcox will provide an overview comparison of this possibility to the "stacked – pulsed" laser option. (Try to also get input from J-Lab on this for IR light systems).
- An intermediate laser stripping demonstration step is proposed at SNS, which uses permanent magnets to facilitate the stripping. The design and fabrication of these magnets is to be followed up with S. Aleksandrov, FNAL (D. Johnson contact) and CERN (B. Goddard).
- Create a more realistic of a laser stripping "injection design". Concepts were proposed for a variety of laser light angles (w.r.t. the H- beam), and injection chicane magnet spacing. As injection design concepts are being put forth now, a rough knowledge of the requirements for a dual system or at least retrofitting capability with a laser stripping setup would be useful. SNS, CERN.

# 5 Recent Doctorial Theses

## 5.1 The Study of Fringe Field Effects of Magnet in the Synchrotron

Yuan Chen
Graduate University of Chinese Academy of Sciences and
Institute of High Energy Physics, Beijing, China
Mail to: chenyuan@ihep.ac.cn

Graduation Date: July 1, 2008
Supervisors: Prof. Fang Shouxian and Prof. Wang Sheng

*Abstract*

Fringe field effect of magnet is getting more important for the present high intensity accelerator and high luminosity collider than ever. The fringe field effects in China Spallation Neutron Source (CSNS) accelerator and the upgrading project of Beijing Electron Positron Collider (BEPCII) are investigated and studied. The works consist of four parts: (1) the physical design of Lambertson septum magnet for the extraction system of CSNS is well performed. By detailed comparing the core materials, optimizing the design of the septum, circulating beam pipe and shielding, the ratio of stray field can be controlled under 1‰, which is much lower than that of SNS. (2) Calculations and Optimizations of fringe field interference between bump magnets for injection system of CSNS are completed. The influence of the shape of coil end to the distribution of fringe field is investigated by using the magnetic imaging method, and a formula on relation of coil end and the distribution of fringe field is given. Base on these theoretical analysis, the physical design of the bump magnets are worked out, and the induction of the magnetic field integral due to fringe field interference is controlled within 1%, which meet the requirements of injection system of CSNS. These theoretical methods can also be used in the other similar accelerators. (3) Systematical study on effects of fringe field interference in Quadrupole-Sextupole doublet is done. Based on 3-D simulations and measurements of magnetic fields, a scaling law is carried out, which describes effects of fringe field interference between the neighboring quadrupole and sextupole. The scaling law is checked by magnetic field measurement, and used in the study of the fringe filed interference effects in the BEPCII storage ring. (4) The detailed investigations of fringe field effect of single magnet and the effect of fringe field interference in BEPCII storage ring are completed. By adopting 3-D magnetic field simulations, magnetic field measurements, beam dynamics simulations and machine study, the impacts of fringe field effects, including single magnet fringe field and fringe field interference, to the beam dynamics are figured out. It is concluded that effects of fringe field is the most important reason, which induces the difference between designed beam optics and actual beam optics in the machine operation.

## 5.2 Application of the Frequency Map Analysis to Analyze Beam Dynamics in the Ring Accelerator

Yi Jiao
Graduate University of Chinese Academy of Sciences and
Institute of High Energy Physics, Beijing, China
Mail to: jiaoyi@ihep.ac.cn

Graduation Date: July 1, 2008
Supervisors: Prof. Shou-xian Fang and Prof. Jiu-qing Wang

*Abstract*

Frequency map analysis (FMA) is a useful tool to look insight to the beam dynamics and resonance structure in a global way by constructing one-to-one relationship between the space of initial conditions ($x$, $y$, $x' = y' = 0$) and the tune space ($Q_x$, $Q_y$). The method is used to analyze the beam dynamics of the Shanghai Synchrotron Radiation Facility (SSRF) and Beijing Electron and Positron Collider Upgrade Project (BEPCII).

Taking reference lattice based on the storage ring of the SSRF, FMA is used to verify the method of the super-periodic structural resonances analysis (SSRA). It shows that the first- and second-order SSR stopbands do exist and have significant effects on beam dynamics in a limited range. The author extends the SSRA to analyze higher order super-periodic structural resonances (SSR). FMA and Lie Algebra method are used to study the resonances. The mechanisms and features of the higher order SSR are described in detail. The tune diagram of SSR instead of general structure resonance is thought to be essential for tune choosing, which is proved by successfully applying the tune diagram of SSR to analyze other third generation light sources. Without considering magnetic errors, optimization study of the SSRF lattice is made.

The FMA method is systematically applied to the lattice of the BEPCII storage ring for the first time. The RF cavity and synchrotron radiation are turned on during the tracking, and synchro-betatron resonance $2Q_x - Q_s = 13$ is found responsible for the limit of DA for the BECPII collsion mode lattice specified for high luminosity. To minimize the growth time of the resonance by optimizing the sectupole parameters is proved to be beneficial to the improvement of the beam dynamics.

The turn-by-turn experiments, which are the necessary condition of experimental FMA, are carried out on the BEPC and BEPCII storage rings. The oscillation of the beam transverse position in each turn, the motion in phase space and transverse damping are acquired. The resonance phenomenon under special conditions are also observed and analyzed.

## 5.3 Emittance Control in High Power LINACs

Mohammad Eshraqi
CERN/IPM and
Institute for Studies in Fundamental Sciences (IPM), Tehran, Iran
Mail to: meshraqi@cern.ch

Graduation date: March 2009
Supervisors: Dr. Alessandra Lombardy, Prof. Hessam Arfaei

*Abstract*

Emittance as one of the main properties of the beams of charged particles has multiple effects on the performance and costs of any accelerator and in case of physics experiments have also enormous effects on the rate of events and background signals. The main purpose of this thesis is to demonstrate some recipes to maintain the emittance in RF cavities and magnetic solenoids of an accelerator.

Then the effect of errors in positioning of quadrupole in accelerators and transfer-lines will be addressed. It will be proved that the emittance increases with the forth power of radius in RF cavities and that the two perpendicular transverse planes are independent. In case of diverging beams it will be shown that the emittance increase is higher for beams with higher divergence which again is a result of higher average beam radius. For the magnetic solenoids, mainly used for focusing in low energy parts of the accelerators, it will be demonstrated that the emittance growth increases with the initial divergence of the beam.

It will be shown that the error on positioning of quadrupoles can cause an additional emittance increase which is proportional to the second power of positioning error and is

linearly dependent on the rms beam size. A series of statistical runs is performed on LINAC4 and the results are presented in addition to a scheme to reduce the losses.

# 6 Forthcoming Beam Dynamics Events

## 6.1 Workshop on the Future Directions of Accelerator R&D at Fermilab

Particle accelerators are a major invention of the 20th century. They are engines of discovery, the most powerful microscopes in existence, the brightest light sources, and an invaluable tool for research in material, chemistry and life sciences. Accelerators are also a driving force for the advancement of numerous technologies including superconductivity, vacuum, cryogenics, microwave devices, radiation-hard materials, instrumentation, remote operation and control, computing, data storage and global communication networks.

Accelerator R&D has played a crucial role in enabling scientific discovery in the past century and will continue to play this role in the years to come. In the U.S., the Office of High Energy Physics (OHEP) of DOE's Office of Science is developing a plan for national accelerator R&D stewardship. It is examining the uses of accelerators throughout society, the desired performance characteristics of these and future accelerators, and the R&D efforts in the private and government sectors. To support this effort, Fermilab will organize a *Workshop on the Future Directions of Accelerator R&D at Fermilab* (pending DOE approval). This will take place from **May 11 to 13, 2009 at Lake Geneva, Wisconsin** (about 60 miles north of Fermilab). The purpose of this workshop is to review the status of the current research and development in the field of accelerator science and advanced accelerator technology. The intent is to have open, friendly discussions of numerous proposals for experiments and programs at the lab. The objective of the workshop is to:

- Compose a coherent proposal for general accelerator R&D;
- Compose a coherent proposal for advanced R&D at the New Muon Lab (NML) for 2012-2017;
- Outline long term prospects for these activities.

The ILC Test and AARD Facility at the NML is currently under construction and is expected to provide first beam in late 2011. This facility will have an RF photoinjector providing 40 MeV $e^-$ beam to a string of (eventually) 6 SC RF cryomodules. There will be additional 40 MeV beamlines available for AARD. At the downstream end of the cryomodule string there will be a test area large enough to house a small storage ring and several test beamlines with beam energy up to 1.5 GeV. More information can be found on the Workshop web page:

http://apc.fnal.gov/ARDWS/index.html

This workshop will briefly review accelerator R&D activities around the world and devote most of the time to brainstorming. The attendance is by invitation with a maximum number of attendees of 50. There will be no registration fee.

The Organizing Committee members are:

Vladimir Shiltsev (Chair)
Michael Church
Panagiotis Spentzouris
Weiren Chou
Margaret Bruce

For more information please contact Vladimir Shiltsev e-mail: shiltsev@fnal.gov, phone: +1(630)840-5241 and cc Margie Bruce, e-mail: mbruce@fnal.gov, phone: +1(630)840-5680.

## 6.2 COOL09 - Workshop on Beam Cooling and Related Topics

August 31 – September 4, 2009
IMP, Lanzhou, China

The Institute of Modern Physics (IMP), affiliated to Chinese Academy of Sciences will be hosting the Workshop on Beam Cooling and Related Topics (COOL09). The workshop will take place at the campus of Institute of Modern Physics from August 31 to September 4, 2009.

Up-to-date information about the workshop is available on the COOL09 website at http://cool09.impcas.ac.cn.

**Workshop Layout**

The workshop will highlight the following topics:

- Electron cooling
- Stochastic cooling
- Laser cooling,
- Muon cooling,
- Ionization cooling
- Storage of particles in antiproton and heavy ion traps
- Other methods of phase space manipulation.

The workshop will include a reception evening, invited presentation, oral contribution, poster sessions, a conference banquet, a technical tour of the IMP facilities (including cyclotrons and storage rings), and a conference excursion to a local museum and riverside of the Yellow River in Lanzhou.

**Program and Proceedings**

The workshop will start on Monday morning, August 31 at 9 a.m. and finish on Friday, September 4 before lunch.

It is planned to present as many as possible contributions orally. Those contributions which cannot be considered for oral presentation will be shifted to a poster session on Thursday afternoon.

Main topics of invited talks:

- Status of New and Existing Accelerators
- Progress of Stochastic and Electron Cooling
- Cooling at High Energy Accelerators
- New Cooling Concepts
- Theoretical Studies of the Cooling Process and Parameters of Cooled Beams
- Application of Cooling for Secondary Beam Preparation
- Crystalline Beams

For an updated list of invited speakers please visit the workshop website.

The proceedings will be published with JACoW. The proceedings will be provided to the participants on a CD. If a sufficient number of participants express their interest, a printed copy will be provided which must be paid at the workshop. Please indicate your interest in the registration form.

**Abstracts**

Abstracts must be submitted to the SPMS system developed by the JACOW collaboration (http://spms.kek.jp/pls/cool2009/repository.html).Authors must register to the JACOW system before submitting an abstract.

For abstract submission please go to the COOL09 website.

**Workshop Venue**

The workshop will be held at the Institute of Modern Physics located near the downtown center of Lanzhou.

Lanzhou is the capital of Gansu province. The medium-sized city is located along the famous Silk Road (http://www.chinats.com/lanzhou/index.htm) with a history of more than thousand years. Lanzhou has a total area of about 14, 000 square kilometers and a population of 2.6million. There are more than 30 ethnic groups in Lanzhou.

Lanzhou stretches along the Yellow River as it snakes its way through the valley. The city is located on the loess plateau with an average elevation of 1520 meters. Its weather is comparatively good. Winters are not severe, nor is it extremely hot in summer. When most cities of China suffer from the intense heat of summer, the average temperature here is only 22.6ºC in the hottest month.

The weather at the beginning of September should be still pleasantly warm, but you should be prepared for cold and rainy days.

**Call for Contributions and Registration**

All colleagues interested in the related fields are cordially invited to participate in the workshop and present contributions in oral or poster format. If you would like to receive further information or intend to participate in the workshop, please visit the workshop webpage http://cool09.impcas.ac.cn/ and fill in the registration form at your earliest convenience. Because the registration in time is crucial for organization of the workshop, participant's cooperation will be highly appreciated.

**Workshop Registration Fee**

The reduced workshop fee is € 450 for payments which are received before July 31, 2009. After that date the fee is € 500. The workshop registration fee includes:

- Attendance at all sessions

- All materials of the workshop including the proceedings and the book of abstracts
- The workshop coffee breaks and lunch buffet through Monday to Thursday
- Get-together reception(Sunday evening), conference banquet (Wednesday)
- Technical tour of the IMP facilities
- Conference excursion to a local museum and riverside of the Yellow River
- Transport between the hotel and Lanzhou airport (70 km)

The reduced registration fee can only be paid by bank transfer. Payments must be made in Euros. Payments (late registration fee € 500) can be made at the conference desk on Sunday and Monday by cash or credit card (VISA or MASTER ).

The registration fee for each accompany person is 250- €, which includes get-together reception, conference banquet, lunch through Monday to Thursday, the conference excursion to a local museum and riverside of the Yellow River, transport between Lanzhou airport and the hotel, and a guided tour to nearby attractions.

Please note that any bank fees incurred as a result of electronically transferred payments are the sole responsibility of the participants. The workshop bank account is:

NAME: INSTITUE OF MODERN PHYSICS, CHINESE ACADEMY OF SCIENCES
BANK OF DEPOSIT: BANK OF CHINA GANSU BRANCH
ACCOUNT: 325127835688091038
SWIFT: BKCHCNBJ660

**Hotel**

A number of rooms have been reserved in the Ning-Wo-Zhuang Hotel(about 5 minutes walk to IMP) for the workshop participants at Registered Member rate. Two buildings are available for the workshop, the No.2 Building and VIP Building, The rate of different room rate is shown in the following table.

| NO.2 Building | | | | VIP Building | | | |
|---|---|---|---|---|---|---|---|
| Deluxe Standard Room | Grand King | Deluxe Suite | VIP suite B | Standard Room | Business Standard Room | Suite | Deluxe suite |
| ¥980 | ¥980 | ¥1990 | ¥2990 | ¥320 | ¥360 | ¥800 | ¥2400 |

All the participants are expected to make their hotel reservation through the Ning-Wo-Zhuang Hotel, http://www.gsnwzhotels.com/English/index.asp, there one can get the detail information of room.

No pre-payment for the hotel reservation is requested. The hotel payment can be made by credit card (VISA or MASTER) or cash when you arrive at the hotel or during your stay in the hotel. The hotel information is available on the workshop web site.

**Visa information**

Each registered COOL09 workshop participant will receive an invitation letter for the visa application from IMP with an official VISA APPLICATION FORM. The participants should apply for visa at Chinese Embassy or Consulate in their resident

countries. Please find the useful information of visa issue at the official website of Ministry of Foreign Affairs of China (http://www.fmprc.gov.cn/eng/ljzg/3647/default.htm).

The invitation letter does not imply any undertaking to support the participant financially.

**Insurance**

Attendants of the workshop have to take care of proper health and personal liability insurance. No responsibility can be taken by the organizers.

**Travel**

There are a number of flights from Beijing/Shanghai/Guangzhou/Chengdu to Lanzhou everyday. Participants are kindly requested to inform the local committee your flight number, date and landing time, our colleagues will pick you up in Lanzhou Zhongchuan airport and drive to Ning-Wo-Zhuang Hotel.

**Important Dates**

Abstract submission March 9 – June 12
Registration March 9 – August 21
Deadline for registration and room reservation August 26
deadline for early registration fee July 31

**International Program Committee**

Ilan Ben-Zvi (BNL), Brookhaven, USA
Håkan Danared (MSL), Stockholm, Sweden
Yaroslav Derbenev (TJNAF), Newport News, USA
Dan Kaplan (IIT), Chicago, USA
Kwang-Je Kim (ANL), Argonne, USA
Igor Meshkov (JINR), Dubna, Russia
Dieter Möhl (CERN), Switzerland
Yoshiharu Mori (KEK), Tokyo, Japan
Sergei Nagaitsev (FNAL), Batavia, USA
Akira Noda, Kyoto University, Japan
Vasily Parkhomchuk (BINP), Novosibirsk, Russia
Ralph Pasquinelli (FNAL), Batavia, USA
Dieter Prasuhn (IKP), Jülich, Germany
Andrew Sessler (LBNL), Berkeley, USA
Markus Steck (GSI), Darmstadt, Germany
Gérard Tranquille (CERN), Switzerland
Hongwei Zhao (IMP), Lanzhou, China

**Local Organizers at IMP**

Xiaohong Cai
Zhenguo Hu
Qiang Liang (Secretary)
Lijun Mao (Scientific Secretary)
Junxia Wu (Scientific Secretary)
Jiawen Xia

Ming Xie
Xiaodong Yang (Co-Chair)
Youjin Yuan (Editor)
Hongwei Zhao (Chair)

**Contacts**
Lijun Mao
Institute of Modern Physics
Chinese Academy of Sciences
509 Nanchang Road, Lanzhou
730000 - P.R.China
Tel:86-0931-4969221
Fax:86-0931-8272100
Email:cool09@impcas.ac.cn
Workshop Website: http://cool09.impcas.ac.cn

## 6.3 10th International Computational Accelerator Physics Conference (ICAP'09)

Robert D. Ryne, LBNL
Mail to: RDRyne@lbl.gov

The 2009 International Computational Accelerator Conference, ICAP'09, will be held from 31 August to 4 September, 2009 in San Francisco, California.

The conference venue will be the Mark Hopkins Intercontinental Hotel (http://www.markhopkins.net/) located at 1 Nob Hill in the heart of San Francisco.

ICAP'09 IS NOW OPEN FOR SUBMISSION OF ABSTRACTS

To submit abstracts, see the *author info* pages of the ICAP'09 web site, or go directly to http://appora.fnal.gov/pls/icap09/profile.html

The ICAP'09 web site is http://outreach.scidac.gov/icap09/

ICAP focuses on the latest advances in computational accelerator physics. ICAP'09 will be the 10th in the conference series following meetings in La Jolla, California (1988), Los Alamos, New Mexico (1990), Pleasanton, California (1993), Williamsburg, Virginia (1996), Monterey, California (1998), Darmstadt, Germany (2000), East Lansing, Michigan (2002), St. Petersburg, Russia (2004), and Chamonix, France (2006).

ICAP'09 is being organized by the Lawrence Berkeley National Laboratory and the SLAC National Accelerator Laboratory.

Important Dates:
Abstract Submission Available: Friday Feb 13
Abstract Submission Deadline: Friday May 1
Notification of Abstract Acceptance: Friday May 8
Registration Opens: Friday May 8

Early Registration Deadline: Monday June 29
Hotel Room Block Reservation Deadline: August 2
Conference begins: 8:00 AM, Monday August 30
Conference Ends: Noon, Friday Sept 4
Publication Submission Deadline: Friday Sept 4

## 6.4 LLRF09 Workshop

October 19 to 22, 2009
KEK, Japan

The LLRF09 workshop will be held from October 19 to 22, 2009 at KEK, Japan.

http://www-conf.kek.jp/llrf09/llrf-intro.html

Sophisticated Low-Level RF systems are essential to control RF structures and their power sources in modern particle accelerators for producing high-quality beams. The goals of the LLRF09 workshop are to share our experiences, to present the status of our work, and to discuss recent developments and future prospects in this field.

This four-day workshop will be the fourth in a series on low-level RF techniques, initiated at Jefferson Lab in 2001, and followed at CERN in 2005 and at SNS in 2007.

LLRF09 will take place at KEK, in Tsukuba. Tsukuba is located 60 km northeast of Tokyo.

Useful URL:
Access to KEK: http://www.kek.jp/intra-e/access/index.html

IMPORTANT DATES
Early March, 2009 First announcement
June 15, 2009 Abstract Submission and Conference Registration Open
August 7, 2009 Early Conference Registration Deadline
August 21, 2009 Abstract Submission Deadline
October 19-22, 2009 Workshop

CONTACT US
e-mail: llrf09@ml.post.kek.jp

## 6.5 The Physics and Applications of High Brightness Electron Beams 2009

November 16-19, 2009
Maui, Hawaii

Dear Colleague,

It is with pleasure that we invite your participation in the workshop entitled "The Physics and Applications of High Brightness Electron Beams", to be held in Maui, Hawaii, November 16-19, 2009. This workshop is presently being considered, as in the past, for endorsement by the ICFA Panels on Beam Dynamics and Advanced & Novel Accelerators. It represents the latest workshop in the joint tradition of the "Arcidosso" and High Brightness Beam series, and is the direct heir to the last workshop in the series, held in Erice, Sicily.

The workshop mission is given in the following statement:

High brightness electron beams are playing an increasingly critical role in two frontier fields that are now yielding results that provoke considerable excitement and activity across the scientific community: radiation generation methods and advanced acceleration schemes. Such cutting edge radiation production methods include variations on the revolutionary 4$^{th}$ generation device, the free-electron laser, as well as inverse Compton scattering of intense lasers. These diverse approaches are thus able to create high peak and high average power light sources, with applications in ultrafast sciences and the Å level, as well as in nuclear and high-energy physics. Likewise, high brightness beams are at the center of many future accelerator schemes, e.g. based on high gradient electron and laser wakefields. Indeed, laser wakefield accelerators are now entering the proof-of-application phase, where unique light sources based on advanced acceleration schemes are enabled. The goal of this workshop is to provide a comparative study of the generation, manipulating, modeling and measuring of high brightness electron beams, and the multitude of underlying, interdisciplinary methods linking the physics of these beam systems to the physics of advanced applications.

The preliminary web site for the workshop has been launched, and will be functional soon. Please bookmark

http://home.physics.ucla.edu/calendar/Workshops/index.html.

In the meantime, the following information is now available:

— Registration will be open soon. As the number of attendees will be limited, early registration is encouraged. The registration fee will be $450 US and will support the conference infrastructure, refreshments, attendance of young scientists and students, and publication of the conference proceedings.
— The workshop secretariat will be headed by Carly Nguyen. Communication with the workshop organization will be formally handled through the email address HBEB@physics.ucla.edu.
— The program is now being prepared, and will include invited and contributed plenary talks in the mornings, with the afternoons dedicated to working groups.
— We are at present examining proceedings options, as we will be looking to institute a review process. We are also weighing the option of publication a special issue of PRST-AB dedicated to the workshop is also planned.
— The following working groups are foreseen:
  1. Sources, including photoinjectors and plasma-based sources
  2. Manipulation and diagnosis of high brightness beams
  3. Theory and modeling, simulation challengers
  4. Applications of high brightness beams in advanced accelerators and light sources.
—The following committees are involved in organization and programming of the workshop:

Organizing committee
**Co-chairs**
**J. Rosenzweig (UCLA)**
**L. Palumbo (Univ. Roma "La Sapienza")**
**M. Uesaka (U. Tokyo)**
L. Serafini (INFN-Milano)
C. Brau (Univ. Vanderbilt)
H. Braun (PSI)
K-J. Kim (UC/ANL)
G. Dattoli (BNL)
S. Milton (Sinc. Trieste)
S. Chattopadhay (Cockroft Inst.)
P. Emma (SLAC)
J. Rossbach (DESY)
W. Leemans (LBNL)
V. Yakimenko (BNL)

Program committee
**M. Ferrario (INFN-LNF), Chair**
C. Pellegrini (UCLA)
W. Barletta (LBNL)
Z. Huang (SLAC)
G. Krafft (JLAB)
L. Giannessi (ENEA)
X. Wang (BNL)
R. Kishek (Univ. Maryland)
F. Stephan (DESY)
M. Eriksson (MAXLAB)
F. Gruner (LMU-Munich)
F. Stephan (DESY)
D. Giulietti (Univ. Pisa)
G. Hoffstaetter (Cornell)
T. Kamps (BESSY)
T. Shintake (SPring-8)

We hope to see as many of you as possible in Maui in November!

L. Palumbo J. Rosenzweig M. Uesaka

# 7 Announcements of the Beam Dynamics Panel

## 7.1 ICFA Beam Dynamics Newsletter

### 7.1.1 Aim of the Newsletter

The ICFA Beam Dynamics Newsletter is intended as a channel for describing unsolved problems and highlighting important ongoing works, and not as a substitute for journal articles and conference proceedings that usually describe completed work. It is published by the ICFA Beam Dynamics Panel, one of whose missions is to encourage international collaboration in beam dynamics.

Normally it is published every April, August and December. The deadlines are 15 March, 15 July and 15 November, respectively.

**Categories of Articles**

The categories of articles in the newsletter are the following:

1. Announcements from the panel.
2. Reports of beam dynamics activity of a group.
3. Reports on workshops, meetings and other events related to beam dynamics.
4. Announcements of future beam dynamics-related international workshops and meetings.
5. Those who want to use newsletter to announce their workshops are welcome to do so. Articles should typically fit within half a page and include descriptions of the subject, date, place, Web site and other contact information.
6. Review of beam dynamics problems: This is a place to bring attention to unsolved problems and should not be used to report completed work. Clear and short highlights on the problem are encouraged.
7. Letters to the editor: a forum open to everyone. Anybody can express his/her opinion on the beam dynamics and related activities, by sending it to one of the editors. The editors reserve the right to reject contributions they judge to be inappropriate, although they have rarely had cause to do so.

The editors may request an article following a recommendation by panel members. However anyone who wishes to submit an article is strongly encouraged to contact any Beam Dynamics Panel member before starting to write.

### 7.1.2 How to Prepare a Manuscript

Before starting to write, authors should download the template in Microsoft Word format from the Beam Dynamics Panel web site:

http://www-bd.fnal.gov/icfabd/news.html

It will be much easier to guarantee acceptance of the article if the template is used and the instructions included in it are respected. The template and instructions are expected to evolve with time so please make sure always to use the latest versions.

The final Microsoft Word file should be sent to one of the editors, preferably the issue editor, by email.

The editors regret that LaTeX files can no longer be accepted: a majority of contributors now prefer Word and we simply do not have the resources to make the conversions that would be needed. Contributions received in LaTeX will now be returned to the authors for re-formatting.

In cases where an article is composed entirely of straightforward prose (no equations, figures, tables, special symbols, etc.) contributions received in the form of plain text files may be accepted at the discretion of the issue editor.

Each article should include the title, authors' names, affiliations and e-mail addresses.

### 7.1.3 Distribution

A complete archive of issues of this newsletter from 1995 to the latest issue is available at

http://icfa-usa.jlab.org/archive/newsletter.shtml.

This is now intended as the primary method of distribution of the newsletter.

Readers are encouraged to sign-up for electronic mailing list to ensure that they will hear immediately when a new issue is published.

The Panel's Web site provides access to the Newsletters, information about future and past workshops, and other information useful to accelerator physicists. There are links to pages of information of local interest for each of the three ICFA areas.

Printed copies of the ICFA Beam Dynamics Newsletters are also distributed (generally some time after the Web edition appears) through the following distributors:

| | | |
|---|---|---|
| Weiren Chou | chou@fnal.gov | North and South Americas |
| Rainer Wanzenberg | rainer.wanzenberg@desy.de | Europe[++] and Africa |
| Susumu Kamada | susumu.kamada@kek.jp | Asia[**] and Pacific |

++ Including former Soviet Union.

** For Mainland China, Jiu-Qing Wang (wangjq@mail.ihep.ac.cn) takes care of the distribution with Ms. Su Ping, Secretariat of PASC, P.O. Box 918, Beijing 100039, China.

To keep costs down (remember that the Panel has no budget of its own) readers are encouraged to use the Web as much as possible. In particular, if you receive a paper copy that you no longer require, please inform the appropriate distributor.

### 7.1.4 Regular Correspondents

The Beam Dynamics Newsletter particularly encourages contributions from smaller institutions and countries where the accelerator physics community is small. Since it is impossible for the editors and panel members to survey all beam dynamics activity worldwide, we have some Regular Correspondents. They are expected to find interesting activities and appropriate persons to report them and/or report them by themselves. We hope that we will have a "compact and complete" list covering all over the world eventually. The present Regular Correspondents are as follows:

| | | |
|---|---|---|
| Liu Lin | Liu@ns.lnls.br | LNLS, Brazil |
| Sameen Ahmed Khan | Rohelakan@yahoo.com | SCOT, Oman |
| Jacob Rodnizki | Jacob.Rodnizki@gmail.com | Soreq NRC, Israel |
| Rohan Dowd | Rohan.Dowd@synchrotron.org.au | Australian Synchrotron |

We are calling for more volunteers as Regular Correspondents.

## 7.2 ICFA Beam Dynamics Panel Members

| *Name* | *eMail* | *Institution* |
|---|---|---|
| Rick Baartman | baartman@lin12.triumf.ca | TRIUMF, 4004 Wesbrook Mall, Vancouver, BC, V6T 2A3, Canada |
| Marica Biagini | marica.biagini@lnf.infn.it | LNF-INFN, Via E. Fermi 40, Frascati 00044, Italy |
| Yunhai Cai | yunhai@slac.stanford.edu | SLAC, 2575 Sand Hill Road, MS 26, Menlo Park, CA 94025, U.S.A. |
| Swapan Chattopadhyay | swapan@cockcroft.ac.uk | The Cockcroft Institute, Daresbury, Warrington WA4 4AD, U.K. |
| Weiren Chou (Chair) | chou@fnal.gov | Fermilab, P.O. Box 500, Batavia, IL 60510, U.S.A. |
| Wolfram Fischer | wfischer@bnl.gov | Brookhaven National Laboratory, Bldg. 911B, Upton, NY 11973, U.S.A. |
| Yoshihiro Funakoshi | yoshihiro.funakoshi@kek.jp | KEK, 1-1 Oho, Tsukuba-shi, Ibaraki-ken, 305-0801, Japan |
| Miguel Furman | mafurman@lbl.gov | Center for Beam Physics, LBL, 1 Cyclotron Road, Berkeley, CA 94720-8211, U.S.A. |
| Jie Gao | gaoj@ihep.ac.cn | Institute for High Energy Physics, P.O. Box 918, Beijing 100049, China |
| Ajay Ghodke | ghodke@cat.ernet.in | RRCAT, ADL Bldg. Indore, Madhya Pradesh, 452 013, India |
| Ingo Hofmann | i.hofmann@gsi.de | High Current Beam Physics, GSI Darmstadt, Planckstr. 1, 64291 Darmstadt, Germany |
| Sergei Ivanov | ivanov_s@mx.ihep.su | Institute for High Energy Physics, Protvino, Moscow Region, 142281 Russia |
| Kwang-Je Kim | kwangje@aps.anl.gov | Argonne Nat'l Lab, Advanced Photon Source, 9700 S. Cass Avenue, Argonne, IL 60439, U.S.A. |
| In Soo Ko | isko@postech.ac.kr | Pohang Accelerator Lab, San 31, Hyoja-Dong, Pohang 790-784, South Korea |
| Alessandra Lombardi | alessandra.lombardi@cern.ch | CERN, CH-1211, Geneva 23, Switzerland |
| Yoshiharu Mori | mori@kl.rri.kyoto-u.ac.jp | Research Reactor Inst., Kyoto Univ. Kumatori, Osaka, 590-0494, Japan |
| Mark Palmer | mark.palmer@cornell.edu | Wilson Laboratory, Cornell University, Ithaca, NY 14853-8001, USA |
| Chris Prior | c.r.prior@rl.ac.uk | ASTeC Intense Beams Group, STFC RAL, Chilton, Didcot, Oxon OX11 0QX, U.K. |
| Yuri Shatunov | yu.m.shatunov@inp.nsk.su | Acad. Lavrentiev, prospect 11, 630090 Novosibirsk, Russia |
| Junji Urakawa | junji.urakawa@kek.jp | KEK, 1-1 Oho, Tsukuba-shi, Ibaraki-ken, 305-0801, Japan |
| Jiu-Qing Wang | wangjq@mail.ihep.av.cn | Institute for High Energy Physics, P.O. Box 918, 9-1, Beijing 100049, China |
| Rainer Wanzenberg | rainer.wanzenberg@desy.de | DESY, Notkestrasse 85, 22603 Hamburg, Germany |